UNIVERSITY OF SOUTHAMPTON

Spin fluctuations in intermetallic cerium compounds

by

Andrew Neville

A thesis submitted for the degree of

Doctor of Philosophy

Department of Physics and Astronomy

November 1997

UNIVERSITY OF SOUTHAMPTON

ABSTRACT

FACULTY OF SCIENCE

PHYSICS

Doctor of Philosophy

Andrew Neville

This thesis contains the results of extensive measurements on CePdSb, alloys from the $CeRu_2Si_{2-x}Ge_x$ series, and some work on CePtSb. The main experimental techniques used in the investigation of these materials were neutron scattering and muon spin relaxation and rotation, with some additional magnetisation measurements.

Hexagonal CePdSb is a very interesting ferromagnet with quite a high Curie temperature, $T_c = 17.5K$. It displays large anisotropy between the basal plane and c-axis in many properties, arising from the crystal field. The most striking property is that there is little sign of any cooperative effect in the heat capacity at the ordering temperature, which is extremely unusual. Motivated by a desire for an explanation of these properties we have been able to determine several new pieces of information. Magnetisation measurements show that CePdSb has an anomalous magnetisation curve. Neutron scattering shows that CePdSb is not Kondo–like and is an exchange coupled paramagnet above the ordering temperature. Spinwaves appear at low temperatures but a diffusive inelastic component is apparent for temperatures above 6K. Small angle neutron scattering and μSR show curious results.

The $CeRu_2Si_{2-x}Ge_x$ alloys display a range of properties as the composition x is varied. $CeRu_2Si_2$ is a non-magnetic heavy fermion, while $CeRu_2Ge_2$ is a good local moment ferromagnet with Ising–like character. Expanding the lattice of $CeRu_2Si_2$ by substitution of Si by Ge gives an opportunity to examine the changing groundstate across the series as a result of altering the competing interactions. Three alloys in the composition range $1.25 < x < 1.75$ have been studied extensively with some other further work on $x = 1.0$ and 2.0 alloys. Magnetisation measurements reveal a rich magnetisation–field phase diagram for each alloy. Some of the alloys have two magnetic transitions and all exhibit metamagnetism. Above their ordering temperatures all alloys display quasielastic neutron scattering. Its linewidth shows that the Kondo temperature decreases only weakly as a function of increasing x. The single ion component of the linewidth is linear with temperature while the wavevector dependent linewidth is modulated and shows an unusual temperature dependence. At low temperatures there is a magnetic excitation for alloys $x < 1.5$ which cannot correspond to a standard spin wave mode. The excitation is a longitudinal spin fluctuation which appears only below $\sim$ 2K and must result from the interplay of the Kondo and RKKY interactions.

Contents

List of Figures

List of Tables

Preface

Chapters 1, 2 and 3 of this thesis contain introductory material which is based on various books and material from the literature. All sources are referenced.

The original material in this thesis is contained in chapters 4, 5 and 6. Some of the work from chapter 4 has been published in the papers

- "Spin dynamics in CePdSb" in Physica B **206 & 207**, 209 (1995).
- "Anomalous spin dynamics in CePdSb" in Physica B **224**, 271 (1996).

and some work from chapter 5 has been published in the paper

- "Low temperature excitations in $CeRu_2Si_{2-x}Ge_x$ alloys" in Physica B **223&224**, 163 (1996).

Acknowledgements

I would like to thank my supervisor Professor Brian Rainford for his help and guidance in the course of this research. I must also thank the EPSRC for the studentship, which basically means thanking the taxpayer for the opportunity to do this work. I would also like to thank Dr. D. T. Adroja for the many times he was prepared to answer questions and give help on all kinds of things no matter what he was doing.

Thanks to Dr. Keith Yates, my mentor, I wish my efforts at thesis writing were more like his. Thanks to Darren, "Iaaaaainnnn", Stef and Tim for their friendship over the past few years. Thanks to Zoe for patiently giving me time to get on with this thesis.

Finally, thanks to my family for waiting for this ... I hope they are satisfied now!

Chapter 1

Rare earth magnetism

The group of 14 elements from Ce to Lu, the rare-earth elements, sometimes called the Lanthanides, are very important in experimental magnetism research. For a number of decades these elements, and compounds containing these elements, have been a rich source of new and unexpected phenomena which are associated with new groundstates of the electronic system. As research continues it is likely that new materials will be uncovered which provide yet more interesting effects for the theorist and experimentalist to study.

In the following sections a brief outline of some important aspects of magnetism in rare–earth compounds is given.

1.1 Free atoms.

The energy levels of the free atom are filled in sequence. The groundstate configuration of electrons in the last unfilled subshell is given by Hund's rules. In Ce the last unfilled shell is the 4f. Hund's rules can be stated [1, 2]:

i. Arrange the electrons to maximise the total spin S.

ii. Arrange the electrons to maximise the total orbital angular momentum L, consistent with maximum total spin S, and the Pauli exclusion principle.

A filled shell has $S = 0$, $L = 0$, so that only the unfilled electron shells or unpaired electrons contribute to the magnetic moment of the free atom.

After this initial step it is necessary to consider what the ground state will be when extra perturbations are applied to the free atom. If the free atom is incorporated into a solid lattice the effects of the band structure, spin orbit coupling, crystalline electric fields, exchange interactions, the Kondo effect and possibly other effects should be taken into account.

1.2 Itinerant electron magnetism

In some compounds the magnetic electrons on each ion overlap considerably in the solid and they will form a band. When effects of different interactions between the electrons are taken into account it may be possible for the electron band to form a magnetically ordered groundstate. Chromium is a band antiferromagnet (more properly a spin density wave antiferromagnet) and nickel is band ferromagnet. The opposite limit to itinerant magnetism is that in which the magnetic electrons are more localised at the atomic sites. These localised electrons will retain some of their atomic character. Of course real materials often fall into a category intermediate between the two extremes. In this thesis the compounds studied are better described in terms of localised magnetic moments and so the following sections of this chapter focus on this aspect in greater detail.

1.3 The local moment picture

Atoms of the rare earths series have an electron configuration consisting of $[\mathrm{Xe}]4\mathrm{f}^n5\mathrm{d}^2 6\mathrm{s}^1$ where n is the number of electrons in the 4f level. As a starting point it is possible to assume that the local moment which exists on the free atom also exists on the ion incorporated into a lattice. The magnetic electrons of the rare earths are in the 4f level which is not close to the outer edge of the atom. Electrons of the $5\mathrm{d}^2$ and $6\mathrm{s}^1$ levels participate in bonding, or form the conduction bands in metals. The filled $5\mathrm{s}^2$ and $5\mathrm{p}^6$ shells have charge densities lying predominantly outside that of the 4f electrons so that the 4f electrons are well screened from the local environment, and retain much of their atomic-like character [3]. Typical rare earth 4f shell radii are in the range $\sim 0.2 \rightarrow 0.3$Å [4] whereas lattice spacing are of the order of 4Å. It follows that direct 4f-4f electron overlap is small, so 4f band-widths are generally negligible. The charge densities of the relevant levels in gadolinium are shown in figure 1.1. The effects of perturbations on the 4f level have to be considered according to the

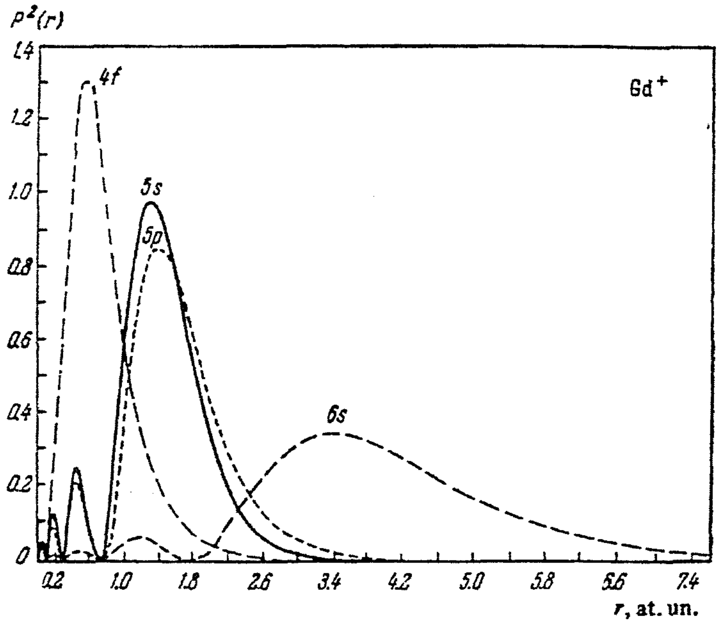

Figure 1.1: Calculated charge densities for outer electron shells in Gd. Reproduced from ref. [2]

strength of each interaction, the strongest first.

1.3.1 Magnetic susceptibility of free ions

The general definition of the magnetisation of a collection of non-interacting ions is

$$M = -\frac{1}{V}\left(\frac{\partial \mathcal{F}}{\partial H}\right)_T, \tag{1.1}$$

where V is the volume occupied by the ions, H is the applied magnetic field and $\mathcal{F}$ is the free energy of the system. A field applied to a material causes a splitting of the energy levels and in thermal equilibrium the equilibrium magnetisation is

$$M(H,T) = \frac{\sum_n M_n \exp(-E_n/k_B T)}{\sum_n \exp(-E_n/k_B T)}, \tag{1.2}$$

where n labels the energy levels E_n and M_n is the magnetisation of energy level E_n given by equation (1.1). The susceptibility is defined as

$$\chi = \left(\frac{\partial M}{\partial H}\right)_T, \tag{1.3}$$

which in the limit of $\mu_B H \ll k_B T$ can be written as $\chi = M/H$. For a collection of N free atoms occupying volume V the susceptibility is given by Curies law,

$$\chi = \frac{C}{T} \tag{1.4}$$

$$\text{where} \quad C = \frac{N}{V}\frac{g^2\mu_B^2 J(J+1)}{3k_B T}. \tag{1.5}$$

J is the total angular momentum quantum number, μ_B is the Bohr magneton and g is the Landé factor for J.

1.4 Spin-orbit coupling

In rare earth compounds the spin orbit interaction is generally much stronger than other interactions such as the crystal field. It acts on the Hunds Rule ground state to combine L and S into a total angular momentum, J, according to two conditions:

i. $J = |L + S|$ if the electron shell is over half full or

ii. $J = |\mathrm{L} - \mathrm{S}|$ if it is less than half full.

The states of different J, produced by this relativistic interaction, are normally split by a large amount so that the lowest lying J level can be considered to be isolated from the others so that the other interactions can be taken to operate only on the groundstate multiplet J [3]. The spin orbit levels of different total J are generally separated by $>$ 0.1eV [4] while overall crystal field splittings are of the order of $\sim$ 30meV.

1.5 The crystal field

If we consider a rare-earth ion in a lattice, the 4f electrons on this ion have certain spatial configurations depending on which sub level, labeled by m_J, of the J ground state multiplet, they are in. In the free atom these levels are all degenerate but when there is a non spherically symmetric external electrostatic potential due to near neighbour ions in a crystal, the degeneracy is removed. The degree of lifting of the degeneracy of the m_J multiplet depends on the symmetry of the rare earth's environment.

The effect on the ground state multiplet of the potential, V_{CF}, due to the arrangement of near neighbour ions, needs to be calculated. It takes the form,

$$V_{\mathrm{CF}}(r_i) = \int \frac{e\rho(R)\mathrm{d}R}{4\pi\epsilon_0|r_i - R|}, \tag{1.6}$$

where r_i is the position of 4f electron i, R labels the electrons on the near neighbour or ligand atoms, $\rho(R)$ is the charge density due to the ligand and the other symbols are the usual physical constants. It is possible to rewrite equation (1.6) as an expansion, in spherical harmonics (or tesseral harmonics) which operate on the coordinates (r, θ, ϕ) of each 4f electron. Stevens [5] showed that the spherical harmonics can be transformed to polynomials in terms of angular momentum operators using the Wigner-Eckart theorem. This is a favourable transformation to make because it is easier to work with angular momentum operators. In terms of this operator-equivalent method the crystal field Hamiltonian is [5],

$$\mathcal{H}_{CF} = \sum_{l,m} A_l^m \langle r^l \rangle O_l^m , \tag{1.7}$$

$\langle r^l \rangle$ is an average over the positions of the 4f electrons and the labels l,m indicate the order of the term. O_l^m are Stevens operators, which may be found in tables [6]. The factors A_l^m are the intrinsic crystal field parameters.

The crystal field parameters contain the information about the magnitudes of different splittings but they are difficult to calculate because the charge distribution $\rho(R)$ in equation (1.6) is unknown.

The Hamiltonian equation (1.7) must have the same symmetry as the crystal and this limits the number of terms. In general only terms for $l < 2J$ (or $l < 6$ whichever is smaller) will be present and many of these may be zero.

As an illustration, the calculation of the crystal field for CePdSb is outlined in section 4.2 of chapter 4.

1.5.1 Magnetic susceptibility including the crystal field

Now we consider the susceptibility of a collection of ions with energy levels, E_n, determined by the crystal field. The susceptibility of the free ion was given previously as equation (1.3). In the presence of a field the crystal field levels are no longer energy eigenstates because the field introduces matrix elements between crystal field eigenstates.

Recall from equation (1.1) that the susceptibility is defined as

$$\chi = \left(\frac{\partial M}{\partial H}\right)_{H\to 0} = -\frac{1}{V}\left(\frac{\partial^2 \mathcal{F}}{\partial H^2}\right)_{H\to 0} \tag{1.8}$$

$$= \frac{N}{V}k_BT\left[\frac{1}{Z}\frac{\partial^2 Z}{\partial H^2} - \frac{1}{Z^2}\left(\frac{\partial Z}{\partial H}\right)^2\right] \tag{1.9}$$

where the free energy $\mathcal{F} = -Nk_BT\ln Z$ and Z is the partition function of an ion. The second term in equation (1.9) is $\propto M^2$ and in the limit of $H \to 0$ we expect $M \to 0$ so we neglect the second term as being small. Essentially we need to evaluate the partition function Z which we can do if we know where the different energy levels are. We can apply perturbation theory to find the energy levels in an applied field. The presence of the field introduces several extra parts to the Hamiltonian [7] but we retain only the terms linear in the field H, hence the perturbation is $\mathcal{H}' \approx g\mu_B J.H$. The perturbation expansion suggests we can write $E_n = E_n^{(0)} + E_n^{(1)}H + E_n^{(2)}H^2 + \ldots$. Where $E_n^{(0)}$ is the zero field unperturbed crystal field level n. The second derivative of Z with respect to H is

$$\frac{\partial^2 Z}{\partial H^2} = \sum_n \frac{1}{(k_BT)^2}\left(\frac{\partial E_n}{\partial H}\right)^2 \exp(-E_n/k_BT) - \frac{1}{k_BT}\frac{\partial^2 E_n}{\partial H^2}\exp(-E_n/k_BT) \tag{1.10}$$

The first and second derivatives of E_n with respect to H in the limit $H \to 0$ are $E_n^{(1)}$ and $E_n^{(2)}$ respectively. So that

$$\chi = \frac{N}{VZ}\sum_n\left[\frac{|\langle n|\mathcal{H}'|n\rangle|^2}{k_BT} - 2\sum_{n\neq n'}\frac{|\langle n|\mathcal{H}'|n'\rangle|^2}{E_n - E_{n'}}\right]\exp(-E_n/k_BT) \tag{1.11}$$

The first term in this equation is the Curie term and the second is the Van Vleck paramagnetic term which only depends on temperature through the Boltzmann population factors. We have not included the Lamor diamagnetic term in equation (1.11) because it is generally much smaller than the Curie term [1].

1.6 The RKKY interaction

Many of the rare-earth metals show magnetic ordering, as do a large number of their compounds. The Heisenberg–Dirac direct exchange mechanism cannot apply in rare-earths since there is no direct overlap of the wave-functions of the magnetic 4f electrons from different ions. Ruderman, Kittel, Kasuya and Yoshida are credited with the formalism of an indirect exchange mechanism between rare-earth ions which can explain the origin of magnetic ordering in the rare-earths and their compounds.

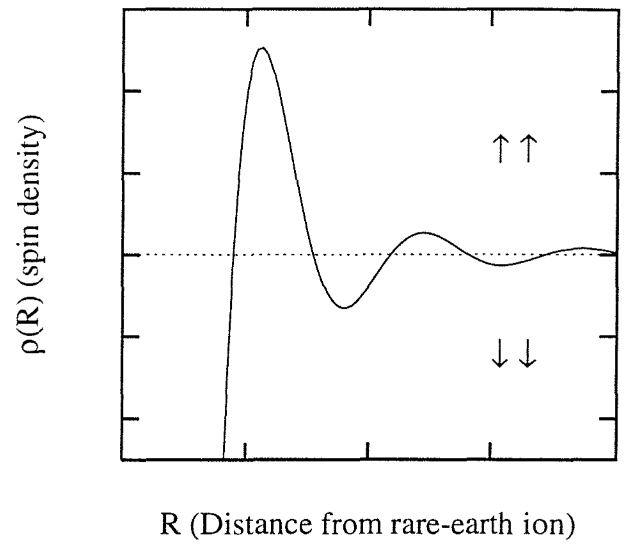

Figure 1.2: The spin density of conduction electrons as a function of distance, r, from a rare-earth.

The basic mechanism involves an effective exchange interaction between the local moments and the conduction electrons with a Hamiltonian of the form

$$\mathcal{H} = -\mathcal{J}_{sf}(g-1)\boldsymbol{J}.\boldsymbol{s}, \tag{1.12}$$

where $\mathcal{J}_{sf}$ is the exchange integral, $\boldsymbol{J}$ is the local moment angular momentum and $\boldsymbol{s}$ is the conduction electron spin.

A perturbation calculation gives the spin density, ρ, of conduction electrons as a function of distance from the rare earth ion. In the limit of free electron behaviour of the conduction electrons the form of this is shown in figure 1.2 and it is given by [8]

$$\rho = \left[-\frac{9\pi n^2 \mathcal{J}_{sf}(g-1)J}{4E_F}\right] F(x) \tag{1.13}$$

with

$$F(x) = \frac{x\cos(x) - sin(x)}{x^4}, \tag{1.14}$$

where n is the number of free electrons, E_F is the Fermi energy and $x = 2k_F R$. The Fermi wave-vector is k_F and the distance from the ion is denoted R. The polarisation of conduction electrons is oscillatory and extends over many lattice spacings. Each rare-earth ion sits in the polarisation cloud due many neighbours and an effective Hamiltonian can be written in the form of an interaction between different rare-earth sites [7, 9],

$$\mathcal{H}_{RKKY} = -\mathcal{J}_{ij}(R)\boldsymbol{J}_i.\boldsymbol{J}_j, \tag{1.15}$$

with

$$\mathcal{J}_{ij}(R) = \frac{3}{2}\pi n D(E_F)(g_J - 1)^2 \mathcal{J}_{sf}^2(0) F(x) \tag{1.16}$$

Where $\mathcal{J}_{ij}(R)$ is the effective exchange between sites i and j separated by R. n is the number of conduction electrons and $\mathcal{J}_{sf}(0)$ is the wave-vector dependent exchange between rare-earth ion and conduction electron, in this case the approximation $\mathcal{J}_{sf}(Q) = \mathcal{J}_{sf}(0)$ is used. $D(E_F)$ is the density of conduction electron states at E_F.

A more realistic model should consider the effect of wave-vector dependent exchange and a more realistic band structure for the conduction electrons. The net coupling between sites can be antiferromagnetic or ferromagnetic and complicated modulated order can result [9].

1.6.1 Magnetic susceptibility including exchange

The susceptibility calculated for the case of ions with crystal field splittings made no account of the fact that there can be interactions between the ions. When the RKKY interaction is present we must modify the uniform susceptibility. We must add the Hamiltonian, given by equation (1.15), to the main Hamiltonian. The appropriate terms are now

$$\mathcal{H} = -\sum_{i \neq j} \mathcal{J}(R_i - R_j)(g_J - 1)^2 \boldsymbol{J}_i.\boldsymbol{J}_j + \sum_i g\mu_B J_i.H\,. \tag{1.17}$$

This is difficult to work with theoretically because every local moment can interact with all the others and it becomes a many body problem. The mean field approximation is a common approach to tackling this problem in which fluctuations of the local moments are neglected. It is convenient to use Fourier transforms when working with intersite interactions. In particular we can define the susceptibility to a spatially varying field with wavevector Q as $\chi(Q) = M(Q)/H(Q)$. We introduce the Fourier transforms of J and $\mathcal{J}$ [7],

$$J(Q) = \sum_i \exp(-iQ.R_i) J_i \tag{1.18}$$

$$\mathcal{J}(Q) = \frac{1}{N} \sum_{i \neq j} \mathcal{J}(R_i - R_j) \exp(-iQ.(R_i - R_j)) \tag{1.19}$$

and now define the exchange Hamiltonian as

$$\mathcal{H} = \mathcal{J}(-Q)J(Q).J(-Q)\,, \tag{1.20}$$

with the approximation that if a spatially varying field $H(Q)$ is applied to our system it responds with a magnetisation with one Fourier component, with wavevector Q, the same as the applied field. This is valid above the ordering temperature [7]. We make the approximation that each Fourier component in equation (1.20) is independent. This constitutes the *random phase approximation* and is equivalent to the mean field approach. From this definition the susceptibility becomes [7]

$$\chi(Q) = \frac{\chi_0}{1 - \chi_0 \frac{(g_J-1)^2 \mathcal{J}(Q) V}{g^2 \mu_B^2}}\,. \tag{1.21}$$

We can use equation (1.4) as the definition of χ_0 in which case,

$$\chi(Q) = \frac{C}{T - \frac{CV(g_J-1)^2 \mathcal{J}(Q)}{g^2 \mu_B^2}}\,. \tag{1.22}$$

where V is the volume of the system. We can see that $\chi(Q)$ will diverge at a critical temperature $T_c = \frac{CV\mathcal{J}(Q)}{g^2\mu_B^2}$ where Q is the wavevector for which $\mathcal{J}(Q)$ is maximum [7]. Equation (1.21) is equivalent to the Curie-Weiss law. We could use equation (1.11) for the definition of χ_0 if appropriate. For a ferromagnet we expect that $\mathcal{J}(Q)$ will be a maximum for $Q = 0$.

The form of the susceptibility above was based on the RKKY model but it does provide a qualitative explanation of the properties of many materials in the temperature range above the ordering temperature.

1.6.2 de Gennes scaling

de Gennes calculated the the ordering temperature for a lattice of interacting ions and found the critical temperature θ, across a family of compounds with different rare-earth ions should scale with $(g-1)^2 J(J+1)$ [3, 8].

In the previous section we derived a result that the ordering temperature $T_c = \frac{CV(g_J-1)^2\mathcal{J}(Q)}{g^2\mu_B^2}$. If we write out the Curie constant, C, in full this leaves

$$T_c \propto \mathcal{J}(Q)(g_J - 1)^2 J(J+1)\,, \tag{1.23}$$

which shows the presence of the de Gennes factor. Generally the family member containing Gd should have the highest ordering temperature since it has the highest value of the de Gennes factor. This behaviour is observed in some series e.g. RE-Pd$_3$ [10] but not in others e.g. RE-PdSb [11]. From equation (1.23) we can see that any discrepancy could arise from either $\mathcal{J}(Q)$ not being constant across the series or the crystal field, which may change the ground state moment.

1.7 The Kondo effect

In this section we briefly examine the Kondo effect which is an important consideration in the study of magnetic materials.

Experiments in the 1930's suggested that the resistivity of pure samples of some metals showed a minimum at low temperatures [12, 13]. It was found that this strange behaviour could be attributed to the presence of a dilute amount of impurities. In particular, alloys of dilute[*] amounts of transition metals in the noble metals and later Ce$\underline{\mathrm{La}}$[†] alloys were found to show a number of physical anomalies which were attributed to a new phenomenon. These anomalies were found in:

i. Resistivity. Historically the most well known anomaly, the resistivity was found to increase logarithmically at low temperatures. When combined with the decreasing phonon contribution this gave a minimum at a characteristic temperature.

ii. Magnetic susceptibility. This was Curie-Weiss like at high temperatures but tended to a temperature independent value at lower temperatures.

iii. Heat capacity. The magnetic heat capacity showed a peak at a characteristic temperature.

iv. Thermopower. This also showed a peak at a characteristic temperature.

The positions of these anomalies roughly defined a characteristic temperature , T_K, now called the Kondo temperature and collectively this behaviour constitutes evidence of the Kondo effect. These anomalies generally indicate a departure from paramagnetic behaviour of the impurities which is observed at higher temperatures.

To understand why this behaviour occurs we begin by examining the Anderson Hamiltonian.

---

[*] Dilute means a few parts per million.

[†] The underlined element indicates the host and the other is the dilute impurity.

1.7.1 The Anderson Hamiltonian

The Anderson Hamiltonian is a model for treating the conditions under which magnetic moments form on impurity atoms in a metallic host. Many theoretical calculations for the effect of impurities in metals start from the Anderson Hamiltonian [13]; the simplest form is [13, 14]

$$\mathcal{H} = \sum_{k\sigma} \epsilon_k n_{k\sigma} + \sum_{f\sigma} E_0 n_{f\sigma} + \sum_{k,f,\sigma} V_{kf\sigma}(c^+_{k\sigma} c_{f\sigma} + c^+_{f\sigma} c_{k\sigma}) + U n_{f\uparrow} n_{f\downarrow} . \qquad (1.24)$$

The first term is the sum of the kinetic energy, ϵ_k of $n_{k\sigma}$ conduction electrons of wavevector k and spin σ. The second term describes the important electrons on the impurity ion, e.g. the 4f electrons for Ce. E_0 is the energy of the 4f level and $n_{f\sigma}$ is the number of 4f electrons with spin σ. The third term models the interaction energy between conduction electrons and the electrons due to the impurity. $c^+_{k\sigma}$ and $c_{k\sigma}$ are creation and annihilation operators for a conduction electron and $c^+_{f\sigma}$ and $c_{f\sigma}$ are creation and annihilation operators for 4f electrons. When this hybridisation term in the Hamiltonian acts on a wavefunction it will destroy a conduction electron and create a 4f electron and vice versa. It is the presence of this term which introduces the possibility of novel behaviour such as the Kondo effect. The fourth term represents the energy associated with coulomb repulsion when more than one unpaired electron is localised at the impurity. This acts only between electrons with opposite spins, because of the Pauli exclusion principle.

The solutions of the Anderson Hamiltonian have several regimes corresponding to the relative strengths of the different terms. The general effect of the hybridisation term is to broaden the localised 4f level. If the broadening is large and the position of the 4f level is close to the Fermi energy then fluctuations in the occupancy of the 4f level would be energetically possible. The 4f electron could transfer back and forth between the conduction band. In the extreme case the 4f level could lie above the Fermi energy. In this situation it would be unoccupied and hence the impurity would be non-magnetic

When the 4f level lies below the Fermi energy and the effects of hybridisation are not so severe the 4f level will resemble a broadened atomic 4f level. This localised level then gives rise to a magnetic moment on the impurity. In this scenario we find that the Kondo effect becomes important. To understand it we should consider the s-d Hamiltonian.

1.7.2 The Schrieffer–Wolff transformation and the s-d Hamiltonian

Schrieffer and Wolff were able to apply a transformation to the above Anderson Hamiltonian and show that it is equivalent to the s-d Hamiltonian, in the limit that U is very large and V_{kf} is weak [15, 16]. These requirements ensure that we are in the magnetic regime of the Anderson Hamiltonian, where there is a well localised f or d electron.

The s-d Hamiltonian is

$$\mathcal{H} = -\mathcal{J} S.s\,, \tag{1.25}$$

where $\mathcal{J}$ is an effective exchange interaction between S, the spin of an impurity ion and s is the spin of a conduction electron. From the Schrieffer-Wolff approach the exchange parameter in the s-d Hamiltonian is

$$\mathcal{J} \propto \frac{|V_{kf}|^2}{E_0 - E_F}\,, \tag{1.26}$$

where $|V_{kf}|$ is the hybridisation parameter from the Anderson Hamiltonian. E_0 is the energy of the 4f level measured from the Fermi energy. This equation is appropriate to a single impurity with only spin degeneracy i.e. in an orbital singlet state. We can see that a large exchange parameter would result from either a large value for $|V_{kf}|^2$ or if the 4f energy level, E_0, was close to the Fermi energy.

1.7.3 Kondo's resistivity calculation

In 1964 Kondo [17] published a calculation of the resistivity of a metal with magnetic impurities, based on the s-d Hamiltonian. Kondo treated the s-d interaction within the framework of perturbation theory, up to third order. He found that for negative $\mathcal{J}_{sd}$, there was an anomalous contribution to the resistivity, ρ_{imp}, due to the impurities which was

$$\rho_{\mathrm{imp}} \propto -\ln T\,. \tag{1.27}$$

This resistivity is due to resonant scattering of conduction electrons by the local moment impurity for conduction electrons near the Fermi surface. The effect can be traced to the hybridisation which results when the localised level lies within the conduction band. When this contribution is combined with a decreasing phonon contribution at low temperature the result is a minimum in the resistivity at a particular temperature. When $\mathcal{J}$ is negative equation (1.25) shows that the lowest energy state is given by opposite i.e. antiferromagnetic coupling of the conduction electron and impurity spin. We can expect that the groundstate is one in which the conduction electrons compensate the impurity moments. This is effectively a singlet state and explains why the susceptibility is independent of temperature in the low temperature limit. Kondo's calculation identified the cause of the anomalous resistivity as due to the interaction of magnetic impurities with the conduction band of the host. The calculation gave a resistivity diverging as $T \to 0$ so the problem at that stage was by no means completely understood.

1.7.4 The Coqblin–Schrieffer model

For rare earth impurities the crystal field does not normally completely remove the orbital degeneracy of the ground state. In this case the s-d spin Hamiltonian is not sufficient. Coqblin and Schrieffer [18] generalised the problem to that of a crystal field split rare earth ion in the presence of the Kondo effect. A calculation of the resistivity on the basis of their solution lead to somewhat different results from the spin $\frac{1}{2}$ impurity case. The resistivity showed a broad maximum at a temperature Δ, which was the overall order of the crystal field splitting. For temperatures well below or above Δ the resistivity showed the usual $-\ln(T)$ behaviour [14]. This behaviour is observed in many Kondo compounds [19].

1.7.5 Summary of single impurity behaviour

In the single impurity case the situation is believed to be well understood. Well above T_K the impurities have a localised moment and behave paramagnetically. Close to T_K the interaction of the localised electrons and conduction electrons begins to dominate. The conduction electrons act to compensate or screen the impurity spin. The groundstate is a singlet formed from a composite of localised and conduction electrons which is of course non-magnetic. The hybridisation between the two electron systems broadens the localised level and leads to a resonance in the density of states at the Fermi energy. This is due to the extra many-body states of the system which result from the conduction electrons screening the local moment. The resonance in the density of states at the Fermi energy is known as the Abrikosov-Suhl resonance.

Noziéres realised that in the low temperature singlet state he could treat the electron system as quasi-particles and could apply Fermi Liquid theory [15, 16, 20].

Wilson was able to tackle the properties of Kondo systems close to T_K using a sophisticated renormalisation group technique [21, 22] which circumvented the problems of logarithmic divergences encountered when using perturbation theory. Wilson's technique has been used to examine the cross over from the magnetic to non-magnetic behaviour. Wilson's work also leads to a definition of the Kondo temperature as

$$T_K \propto (D(E_F)\mathcal{J}_{sf})^{\frac{1}{2}} \exp\left(\frac{1}{|D(E_F)\mathcal{J}_{sf}|}\right) \tag{1.28}$$

where $D(E_F)$ is the density of conduction electron states at the Fermi energy and $\mathcal{J}_{sf}$ is the exchange parameter. Theoretical calculations have been made for the whole temperature range and the single impurity Kondo scenario is well understood for the $S = \frac{1}{2}$ Kondo Hamiltonian [15, 16, 13].

1.7.6 The Kondo lattice

In rare earth compounds for which the rare earths are one of the major constituents the situation is more complicated. We now have a lattice of impurities. A Kondo lattice is any lattice of impurities which show single ion Kondo properties, and the term is used more generally for any concentrated lattice of ions which show some Kondo properties. Physical properties which are dependent on the density of conduction electron states are enhanced below the Kondo temperature because of the formation of the Kondo resonance near the Fermi energy. Enhanced Pauli paramagnetism and large Sommerfeld coefficients are some of these features.

We can expect two things for these Kondo lattice compounds [15, 23]

i. The Kondo effect will compete with the RKKY exchange, which tends to order the magnetic moments. This will suppress the Kondo screening.

ii. The Kondo screening clouds of conduction electrons from different sites might overlap which would lead to interference effects.

In the first case we observe that the Kondo effect and the RKKY interaction both depend on the combined parameter $g = D(E_F)\mathcal{J}$, see equation (1.28) and equation (1.16). Doniach [24] made the first theoretical study of a Kondo lattice using a one dimensional chain of spins. His results are still used as a guide in classifying

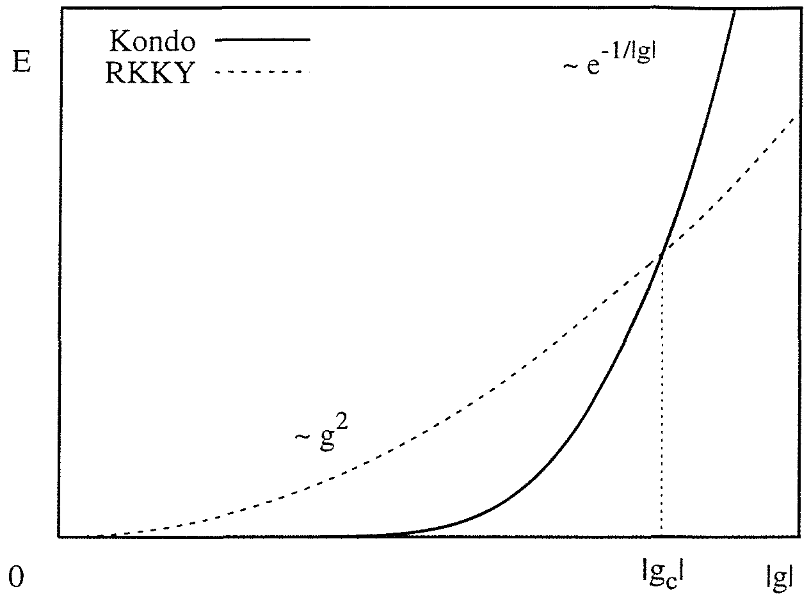

Figure 1.3: Relative strengths of the Kondo and RKKY characteristic energies as a function of the coupling parameter g.

compounds. He found that the groundstate of the Kondo lattice could be non-magnetic (dominated by the Kondo effect) or magnetic (dominated by the RKKY mechanism) according to the strength of $D(E_F)\mathcal{J}$. Figure 1.3 shows the variation of the energy of the two interactions as a function of $g = D(E_F)\mathcal{J}$. Above the critical value g_c the compounds are dominated by the Kondo effect and below they are dominated by the RKKY interaction. Compounds close to g_c are said to be close to a magnetic instability.

As a means of studying the interplay of different effects experimentally, it is possible to control the hybridisation parameter given in equation (1.26) by changing the unit cell volume using pressure. External pressure applied to a material increases the hybridisation and drives the material to the right of figure 1.3. This effect can also be achieved by substituting for one of the components of the material with an element of smaller ionic radius. This 'chemical pressure' can also be made negative by substituting with an ion of larger radius which decreases the hybridisation and pushes the material to the left of figure 1.3.

1.7.7 Heavy Fermions and coherence

When the second condition of section 1.7.6 is true there will be a characteristic temperature for which the lattice of Kondo ions becomes *coherent.* That is, the properties of the system are not well described as a collection of single ion impurities. The composite conduction electron localised electron system can be described as a band of quasi-particles. These quasi-particles are usually observed with effective masses greatly enhanced from that of a bare electron. This phenomenon is related to the formation of the Abrikosov-Suhl resonance in the density of states at the Fermi energy.

The exact nature of this band can lead to a variety of interesting groundstates such as:

i. Heavy Fermion.

ii. Kondo Insulator.

iii. Superconductor.

Heavy Fermions

In the low temperature regime well below T_K some Kondo lattice compounds show coherence. In this state they can be described in terms of Fermi liquid theory. The Fermi liquid state [1] is characterised by its resistivity, ρ,

$$\rho \propto T^2 \tag{1.29}$$

and in addition the heat capacity of a Fermi liquid, C, is

$$C_{\mathrm{p}} = \gamma T \tag{1.30}$$

and the magnetic susceptibility, χ, is a constant. These compounds are called heavy fermions because the quasi-particle fermions have a mass which is greatly enhanced compared to that of a bare electron.

The large effective mass is evident in transport, de Haas van Alphen, and heat capacity measurements. Heavy fermion compounds often show metamagnetic transitions and neutron scattering often reveals magnetic correlations with no ordering. Examples of Heavy Fermions are $CeCu_6$ and $CeRu_2Si_2$ [25].

Kondo Insulator

In Kondo insulators [26] the hybridisation of the localised electrons and the conduction electrons leads to a quasi-particle band with a gap in the density of states at the Fermi energy which forms below a certain temperature. This gap is not likely to open over all the Fermi surface hence we have pseudo gap. The best examples of Kondo insulators are SmB_6, CeNiSn [27], CeRhSb [28] and $Ce_3Pt_3Bi_4$.

At high temperatures these materials behave like paramagnets but at low temperatures coherence develops which leads to semiconductor–like properties and hence the name insulator.

Superconductor

There are a number of heavy fermion rare earth compounds which show superconductivity. The mechanism which causes superconductivity is not well understood but it is thought to be an exotic pairing mechanism involving the heavy fermion quasi-particles. In some cases spin density wave antiferromagnetism appears to coexists with superconductivity in the heavy fermion band.

The main heavy fermion superconductors are $CeCu_2Si_2$, UPt_3 and UBe_{13}. These materials superconduct at very low temperatures under ambient pressure, other materials can be made to superconduct with the application of external pressure [29]. This usually occurs close to the critical pressure for the suppression of magnetic order.

1.8 Valence fluctuation and intermediate valence

In the situation where the hybridisation of 4f and conduction electrons is strong the solution of Anderson Hamiltonian shows that the 4f level is severely broadened such that it does not lie wholly below the Fermi energy. This 4f state need not be occupied and in this case the 4f electrons can be considered to fluctuate between a local and itinerant state. For cerium this means that the valence of the ions is intermediate between Ce^{3+} and Ce^{4+}. Compounds displaying this behaviour can be considered to have a very large Kondo temperature and are termed intermediate valence or valence fluctuating compounds. For a review see ref. [30].

Experimental techniques with a fast enough response, such as XPS, show the presence of two valence signatures for the 4f electrons.

1.9 Generalised magnetic susceptibility

In the previous sections an outline of the definition of the magnetic susceptibility in different cases has been given. The susceptibility of a system to a spatially varying magnetic field has been considered but we could also examine the susceptibility of a system to a field which varies in time with angular frequency ω. This requires a general definition of the susceptibility which has a real and imaginary part. Using perturbation theory we define the frequency dependent single ion susceptibility [31, 32]

$$\begin{aligned}\chi_0^{\alpha\beta}(\omega) = \lim_{\epsilon\to 0^+}\Bigg[&\sum_{\substack{ij\\ E_i\neq E_j}} \frac{\langle i|J^\alpha|j\rangle\langle j|J^\beta|i\rangle}{E_i - E_j - \hbar\omega - i\epsilon}(n_j - n_i) \\ &+ \frac{1}{k_BT}\frac{i\epsilon}{\hbar\omega + i\epsilon}\Bigg\{ \sum_{\substack{ij\\ E_i=E_j}} \langle i|J^\alpha|j\rangle\langle j|J^\beta|i\rangle n_i - \langle J^\alpha\rangle\langle J^\beta\rangle \Bigg\}\Bigg],\end{aligned} \tag{1.31}$$

where $n_i = \exp(\beta E_i)/\sum_l \exp(\beta E_l)$ is a thermal population factor, and the sums are over the crystal field levels E_i

In the presence of exchange interactions the generalised frequency and wavevector dependent susceptibility is written [31, 32, 33],

$$\chi(Q,\omega) = \frac{\chi_0(\omega)}{1 - \mathcal{J}(Q)\chi_0(\omega)}, \tag{1.32}$$

which requires use of the random phase approximation. Note that $\mathcal{J}(Q)$ is the Fourier transform of the exchange interaction. In this approximation the frequency and wavevector dependences are separated, and determined respectively by the single ion characteristics and the two-ion interactions [31]. The poles of equation (1.32) indicate the magnetic excitations of our system [32].

As an example of the use of equation (1.31) and equation (1.32) consider the low temperature limit, where only the groundstate crystal field state is occupied. For Ce^{3+} ions in a uniaxial crystal for example, this would be a doublet state with energy $E_i = E_0$. The quasielastic response (for $\omega \ll E_i - E_0$) due to the groundstate $|0\rangle$ will then be

$$\chi_0^{\alpha\beta}(\omega) = \lim_{\epsilon\to 0^+}\left\{ \frac{1}{k_BT}\frac{i\epsilon}{\omega + i\epsilon}\langle 0|J^\alpha|0\rangle\langle 0|J^\beta|0\rangle n_0 \right\} \tag{1.33}$$

As will be seen in section 2.4 of chapter 2 the inelastic neutron scattering cross-section is proportional to the imaginary part of the dynamical susceptibility.

In Kondo lattice compounds it is common to include the dynamics by making a single pole approximation [33], where instead of taking the limit $\epsilon \to 0^+$ in the above, the imaginary term ϵ is taken to be the relaxation rate Γ of the 4f electrons. It follows that

$$\chi_0^{\alpha\beta}(\omega) = \chi_0(0)^{\alpha\beta}\frac{i\Gamma}{\hbar\omega + i\Gamma}, \tag{1.34}$$

where

$$\chi_0^{\alpha\beta}(0) = \frac{1}{k_BT}\langle 0|J^\alpha|0\rangle\langle 0|J^\beta|0\rangle n_0 . \tag{1.35}$$

We can also see that the imaginary part of $\chi_0^{\alpha\beta}(\omega)$ is given by

$$\mathrm{Im}\chi_0^{\alpha\beta}(\omega) = \chi_0(0)\frac{\hbar\omega}{\hbar^2\omega^2 + \Gamma^2} . \tag{1.36}$$

If we insert equation (1.34) into equation (1.32) this leads to

$$\chi(Q,\omega) = \frac{\chi_0(0)i\Gamma}{\hbar\omega + i\Gamma\left[1 - \chi_0(0)\mathcal{J}(Q)\right]} \tag{1.37}$$

$$= \frac{i\chi(Q)\Gamma(Q)}{\hbar\omega + i\Gamma(Q)} \tag{1.38}$$

where

$$\chi(Q) = \frac{\chi_0(0)}{1 - \mathcal{J}(Q)\chi_0(0)} \tag{1.39}$$

$$\Gamma(Q) = \Gamma_0\left[1 - \mathcal{J}(Q)\chi_0(0)\right] . \tag{1.40}$$

$\Gamma(Q)$ is the wavevector dependent linewidth and both $\Gamma(Q)$ and $\chi(Q)$ will be temperature dependent. Notice that the product $\chi(Q)\Gamma(Q)$ is independent of Q [33].

1.10 Critical behaviour

Materials undergo changes in state as different constraints are altered. These phase transitions such as solid to liquid, superconductor to normal conductor or ferromagnet to paramagnet can be roughly classified as first order or continuous transitions. We can draw a phase diagram which shows what state a material will be in, given certain conditions of temperature, pressure or other constraints.

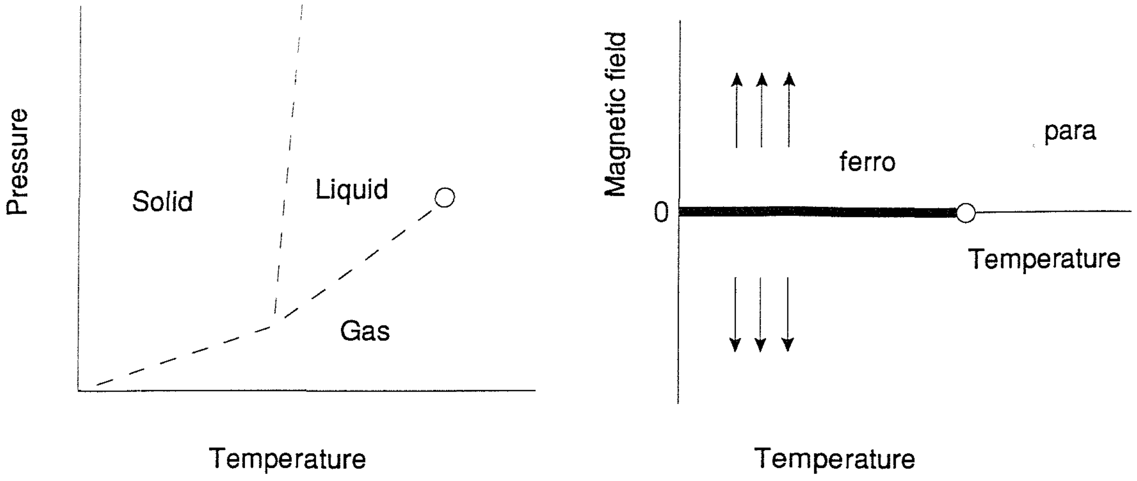

(a) Phase diagram for a material with solid liquid and gas phases.

(b) A phase diagram for a ferromagnet.

Figure 1.4: Two example phase diagrams.

Figure 1.4(a) shows a phase diagram for a material with solid, liquid and gas phases. Taking a piece of this material across any of the phase lines will result in first order phase transitions. If we go through the point at the end of the liquid gas phase line a continuous transition would result. This point on the phase diagram is called the critical point. In figure 1.4(b) the phase diagram for a ferromagnetic material is shown and for this case the critical point lies on the temperature axis. An experiment which takes a ferromagnetic material through the critical point will show critical behaviour in measured properties.

The critical behaviour of continuous transitions is demonstrated by divergences in physical properties which are second order derivatives of the free energy, $\mathcal{F}$. For example, in magnetic systems this means the heat capacity, susceptibility and thermal expansion will diverge near the critical point,

$$\frac{C_H}{T} = \left(\frac{\partial^2 \mathcal{F}}{\partial T^2}\right) \tag{1.41}$$

$$\chi = -\left(\frac{\partial^2 \mathcal{F}}{\partial H^2}\right) \tag{1.42}$$

$$\alpha = \frac{1}{B_T}\left(\frac{\partial^2 \mathcal{F}}{\partial V \partial T}\right) \tag{1.43}$$

where χ is the magnetic susceptibility, C_H is the heat capacity, and α is the coefficient of thermal expansion. B_T is the bulk modulus. For first order transitions discontinuities in physical properties are expected and there will be a latent heat associated with the transition from one phase to another.

Generally magnetic order–disorder transitions are continuous. In ferromagnets the transition is continuous in zero field, as we can see from figure 1.4. When examining continuous phase transitions it is helpful to choose an order parameter. The order parameter tells us which phase we are in. The order parameter should be chosen so that it is zero above the critical point, at the critical point the order parameter should start to increase and below the critical point the order parameter should reflect how far we are into the new phase. For ferromagnets we choose the spontaneous magnetisation as the order parameter and for antiferromagnets we choose the spontaneous sublattice magnetisation.

1.10.1 Correlation functions

In magnetic materials we are interested in the way different moments interact with one another as a function of time. We can measure this by means of a correlation function. For example, at absolute zero in a ferromagnet two neighbouring magnetic moments would be perfectly aligned at all times. The correlation function would be equal to one. At temperatures well above the Curie point the moments would behave completely independently, the correlation function would be zero. Near T$_C$ the correlation between spins would increase and the correlation function should reflect this.

Static correlation functions give an instantaneous picture of a system. They show how correlated different magnetic moments are as a function of distance between them. We define the static magnetic corelation function as

$$C(R) = \langle \boldsymbol{S_0} \cdot \boldsymbol{S_R} \rangle - \langle \boldsymbol{S_0} \rangle \langle \boldsymbol{S_R} \rangle \tag{1.44}$$

where $\boldsymbol{S_0}$ is a moment at the origin and $\boldsymbol{S_R}$ is a moment at a distance R from the origin. The angled brackets indicate a thermal average. The Fourier transform of the previous equation is

$$C(Q) = \sum_R \exp(i\boldsymbol{Q} \cdot \boldsymbol{R}) \left[\langle \boldsymbol{S_0} \cdot \boldsymbol{S_R} \rangle - \langle \boldsymbol{S_0} \rangle \langle \boldsymbol{S_R} \rangle \right] \tag{1.45}$$

This correlation function in reciprocal space can be measured directly by small angle neutron scattering.

For a ferromagnet well above T$_C$ there is no net magnetisation: strong thermal fluctuations prevent any ordering. Closer to T$_C$ the magnetic interactions have the same order of strength as the thermal fluctuations. The motion of individual moments becomes highly correlated which is known as *critical slowing down.* There will be large regions of ordered material which fluctuate in time.

It is possible to observe the transition through these critical fluctuations, for example, the heat capacity shows a sharp peak and the fluctuations give an enhanced neutron scattering cross-section.

1.10.2 Critical exponents and scaling laws

The divergences in physical properties observed at continuous phase transitions can usually be described by power law variations. In the magnetic case this means that close to T_C various physical properties follow power law variations of the form

$$\chi \propto t^{-\gamma} \tag{1.46}$$

$$M \propto t^{-\beta} \tag{1.47}$$

$$C \propto t^{-\alpha} \tag{1.48}$$

$$M \propto H^{1/\delta} \tag{1.49}$$

$$\xi \propto t^{-\nu} \tag{1.50}$$

where $t = (T - T_c)/T_c$. In addition the correlation function follows

$$C(R) \sim R^{2-d-\eta} \tag{1.51}$$

where d is the number of spatial dimensions of the material i.e. 1 for a line, 2 for a plane and so on. The exponents α, β, γ, δ and η are called the critical exponents. It is found that they take the same values in many materials. It appears that things such as lattice type, type of atom or number of electrons do not determine the values of the critical exponents. Only the dimensionality of the material and the dimensionality of the order parameter are of importance [34, 35]. Materials can be put into *universality classes* according to the last two criteria. This means that all the materials in the same universality class will have the same critical exponents. In this way they are said to show universal behaviour [36, 35].

There are laws which relate the values of different critical exponents to one another. These laws are called scaling laws where they link values of critical exponents and they are called hyperscaling laws when they also involve the dimensionality of the system [34].

Any attempts to calculate the properties of a system in the critical region will be difficult because the problem is one of many body physics. However, the mean field approach gives the results $\gamma = 1$, $\beta = \frac{1}{2}$, and $\alpha = 0$. The values do not agree with measured values usually because the mean field approach neglects the all important fluctuations.

Sophisticated renormalisation group calculations allow for predictions of the values of critical exponents and give an understanding of the different types of critical points [36, 37, 38].

Arrot plots

A method of analysing magnetisation data due to Arrot [39] makes use of critical exponents. Arrot's idea was to combine various critical exponents which leads to the equation

$$\left(\frac{H}{M}\right)^{\frac{1}{\gamma}} = M^{\frac{1}{\beta}} + \frac{T - T_C}{T_C} \tag{1.52}$$

which should be valid close to the critical temperature and in low fields. T is the temperature, H is the magnetic field and M is the magnetisation.

If we have some measurements of magnetisation versus field we can use equation (1.52) to plot $\left(\frac{H}{M}\right)^{\frac{1}{\gamma}}$ versus $M^{\frac{1}{\beta}}$ which should yield straight lines. The isotherm at $\mathrm{T_C}$ will intercept at zero. Plots of this type are called Arrot plots and one of their uses is to find $\mathrm{T_C}$ by looking for the isotherm with intercept at the origin. The other use for Arrot plots is in finding values of the critical exponents β and γ.

1.11 Magnetic ordering

At absolute zero the groundstate of a ferromagnet is one in which all the moments are aligned in the same spin state. The total moment would be $g\mu_B NJ$, for N moments. We would like to know what the excitations out of the groundstate are. Changing one spin from J to $(J-1)$ does not constitute a true excited state because this spin flip will move from site to site under the influence of the exchange interaction. The first excited state can be formed by distributing the energy associated with a spin flip over the whole sample. We have to consider the xy components of the spins. A lower energy excited state can be formed by an arrangement of spins with a gradual

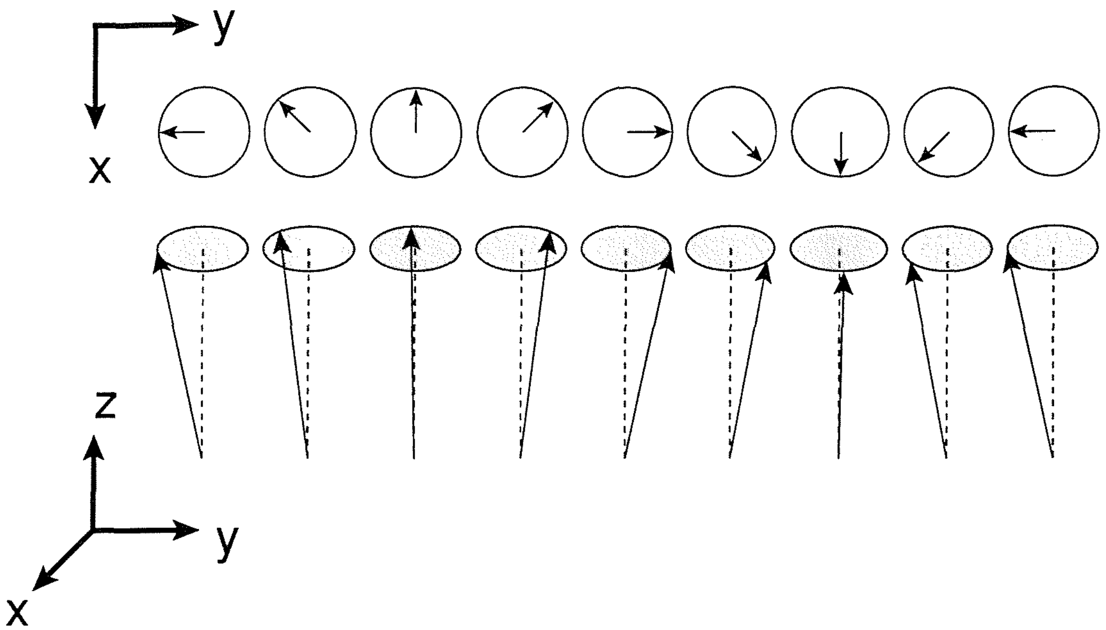

Figure 1.5: A spinwave is a gradual variation of the xy phase between moments. The effect is to reduce the total spin by one.

change of xy phase between successive spins, as shown in figure 4.16. The total spin can be reduced by one, $NJ - 1$, constituting the first excited state. The spin wave state is an eigenstate of the Heisenberg Hamiltonian.

Spin waves can be treated as quantized particles with a definite energy and wavevector. We can think of the reason why the magnetisation drops to zero at the ordering temperature as due to a large thermal population of spinwaves which destroy the magnetisation.

A calculation by Bloch on the basis of the spinwave idea found that at low temperatures the magnetisation should vary as

$$M \propto M_0 \left[1 - T^{\frac{3}{2}}\right] . \tag{1.53}$$

where M_0 is the zero temperature saturation magnetisation and T is the temperature.

The energy of the spin waves depends on the exchange interaction, crystal field anisotropy and other terms in the Hamiltonian. There will be a dispersion relation connecting the energy and wavevector of the spin wave.

1.12 Magnetic models

We can compare the behaviour of a material with what is expected from different theoretical models. The are three classic magnetic models: the Heisenberg model, the Ising model and the XY model. We briefly examine each of these models. In one dimension there is no phase transition to long range order because entropy plays a large role in determining the state of lowest free energy. Some of the models have been examined in two dimensions and show interesting results. In three dimensions there are only partial solutions because the situation is very complex.

1.12.1 The Heisenberg model

The Heisenberg model has three dimensional spins which may point in any direction. It is spatially isotropic. The characteristic Hamiltonian is

$$\mathcal{H}_{\text{Heisenberg}} = \sum_{i,j} \mathcal{J}(r_i - r_j)\boldsymbol{S}_i \cdot \boldsymbol{S}_j = \sum_{i,j} \mathcal{J}(r_i - r_j)(S_i^x S_j^x + S_i^y S_j^y + S_i^z S_j^z) \quad (1.54)$$

In two dimensions this model will not show long range order [7]. In three dimensions this Hamiltonian is expected to show long range order. A mean field solution gives ferromagnetic order with spin wave excitations having energies corresponding to

$$\hbar\omega = S\left[\mathcal{J}(0) - \mathcal{J}(Q)\right] \quad (1.55)$$

where $\mathcal{J}(Q)$ is the Fourier transform of the exchange parameter in the Hamiltonian, equation (1.54).

1.12.2 The Ising model

The Ising model has been solved exactly in two dimensions by Onsager. There is a phase transition at a characteristic temperature. The characteristic Hamiltonian is

$$\mathcal{H}_{\text{Ising}} = \sum_{i,j} \mathcal{J}(r_i - r_j) S_i^z S_j^z \quad (1.56)$$

This model treats the magnetic moments in spin up or spin down states with no xy component. This means that there cannot be any spin waves in the normal sense.

1.12.3 The XY model

The XY model consists of spins which lie in the x-y plane, they have no z component. The model is described by the Hamiltonian

$$\mathcal{H}_{\mathrm{XY}} = \sum_{i,j} \mathcal{J}(r_i - r_j)(S_i^x S_j^x + S_i^y S_j^y) . \tag{1.57}$$

It has analogs in binary alloys and superfluid helium. In two dimensions this model does not show long range order but there is a phase transition into an unusual state. At low temperatures the spins form a set of topological vortices. That means a static arrangement of spins which look like a two dimensional vortex. A phase transition occurs when the vortices become bound together in pairs [34]. This phase is often referred to as the Kosterlitz–Thouless phase.

Approaching the phase transition from above in two dimensions the work of Kosterlitz and Thouless shows that the correlation length should follow

$$\xi \sim \exp\left(b\left(1 - \frac{T}{T_c}\right)^{-\nu}\right) \tag{1.58}$$

where the exponent $\nu = 1/2$ and the susceptibility should be

$$\chi \sim \exp(bt^{\frac{1}{2}(2-\eta)}) \tag{1.59}$$

where the exponent η is temperature dependent but has the value $\eta = \frac{1}{4}$ at $\mathrm{T_C}$.

The XY model does show spinwave excitations in the Kosterlitz–Thouless phase in combination with vortices. A peak in the specific heat is predicted to occur at a temperature slightly above the transition temperature. This peak is related to the onset of vortex binding and has been observed in simulations [40].

A three dimensional XY model is expected to show normal critical behaviour in that the usual powerlaw behaviour of χ and ξ is expected [41].

Chapter 2

Neutron Scattering

2.1 Basic concepts

The first neutron diffraction experiments were performed using bench top beryllium neutron sources in 1936. Todays neutron sources are powerful reactors or spallation sources and the experimental instruments are highly sophisticated. Neutrons from reactor or spallation sources can be produced so that their energies and wavelengths are in the right range to match the static and dynamic processes which occur in all condensed matter.

The theory behind neutron scattering has been throughly constructed and there are many text books on the subject. The experimentally measured quantity in a neutron scattering experiment is the cross-section of the sample and the theory seeks to provide a description of this cross-section. An incident neutron has energy E_i and wavevector $\boldsymbol{k}_i$. After scattering from the sample the neutron has final energy E_i and final wavevector $\boldsymbol{k}_f$. It is useful to define some relevant relations between these quantities,

$$\hbar\omega = E_i - E_f\,, \tag{2.1}$$

$$\boldsymbol{Q} = \boldsymbol{k}_i - \boldsymbol{k}_f\,, \tag{2.2}$$

$$\text{and}\quad Q^2 = k_i^2 + k_f^2 - 2k_ik_f\cos\phi\,, \tag{2.3}$$

where ϕ is the scattering angle.

In order to calculate the cross-section a few assumptions are made. We treat the incident and outgoing neutrons as plane waves and we assume the interaction between the sample and the neutron is weak. Calculating the cross-section involves the first order Born approximation [42]. We use Fermi's golden rule for calculating the probability of a scattering event. Then, the cross section is [43]:

$$\left(\frac{d^2\sigma}{d\Omega d\epsilon}\right)_{\lambda\to\lambda'} = \frac{k_f}{k_i}\left(\frac{m^2}{2\pi\hbar^2}\right)|\langle k_f\lambda'|V|k_i\lambda\rangle|^2\,\delta(E_\lambda - E_{\lambda'} + E_i - E_f)\,. \tag{2.4}$$

The parameter V describes the interaction of the neutron with the sample. λ and λ' are the initial and final states of the sample. The delta function in equation (2.4) ensures we have energy conservation. Equation (2.4) gives the cross-section for a specific transition between states λ and λ' of the sample. To calculate the cross-section in different cases we have to know the form of the interaction, V. Neutrons interact with a sample in two ways, the strong nuclear force, and the magnetic dipole-dipole interaction. We first look at the cross-section for nuclear scattering only.

2.2 Nuclear scattering cross-section

To calculate the nuclear scattering cross-section we have to find the right potential, V, from equation (2.4). The potential we use is called the Fermi pseudo potential, the potential for a single nucleus is

$$V(r) = \frac{2\pi\hbar^2}{m} b\,\delta(r)\,, \tag{2.5}$$

where $\delta(r)$ is the Dirac delta function, m is the mass of the neutron and b is the scattering length.

This potential is not actually like the real nuclear potential (which is generally unknown) but it is chosen because it circumvents the problem of treating a very strong interaction i.e. the nuclear force by perturbation theory and gives the correct result of isotropic scattering [43]. We expect isotropic scattering because the typical nuclear dimension is $\sim 10^{-15}$m and typical neutron wavelengths are $\sim 10^{-10}$m which makes the nucleus look like a point particle as far as the incident neutron is concerned.

The parameter b in equation (2.5) is the important number in characterising a particular nucleus. The scattering length varies with each element and isotope and there are no apparent systematics across the periodic table. In general b can be of either sign and may be a complex number in the presence of absorbtion. For most nuclei absorption of neutrons is small and b can be treated as a real number. This is not true in the case of some strongly absorbing nuclei e.g. Cd and Gd. The scattering length will be different for different isotopes and if the nuclei has spin will depend on the orientation of the nuclear and neutron spin. The scattering lengths of each element can be found in tables in many text books and particularly in ref.[44]. In general we use the bound scattering length, which is the scattering length of a nuclei which is held stationary.

Making use of equation (2.5) in equation (2.4) we find [43]

$$\left(\frac{d^2\sigma}{d\Omega dE}\right)_{\lambda\to\lambda'} = \frac{k'}{k}\left|\sum_j b_j\langle\lambda|\exp(i\boldsymbol{Q}.\boldsymbol{R}_j)|\lambda'\rangle\right|^2 \delta(E_\lambda - E_{\lambda'} + \hbar\omega) \tag{2.6}$$

for the scattering by an array, j, of nuclei with scattering lengths b_j. We have ignored the spin of the neutron in the calculations of the cross-section so far and in fact the cross-section is independent of the neutron spin when the nuclear spins are randomly oriented [42]. In getting to equation (2.6) we have taken the incident and scattered waves to be to be plane waves with wave numbers $\boldsymbol{k}$ and $\boldsymbol{k}'$. To proceed further we assume the array of target atoms are rigidly bound and do not have their quantum states changed so that $|\lambda\rangle = |\lambda'\rangle$ and hence $E_\lambda = E_{\lambda'}$ which means, because of the delta function in equation (2.6), the cross-section is only non-zero when $\hbar\omega = 0$ i.e. the scattering is elastic and also $k = k'$. This now gives us

$$\frac{d\sigma}{d\Omega} = \sum_{jj'} \exp(i\boldsymbol{Q}.(\boldsymbol{R}_j - \boldsymbol{R}_{j'}))b^*_{j'}b_j\,. \tag{2.7}$$

Since we do not know which nuclei sits on which site and there will typically be a very large number of nuclei in any target sample is it sufficient to replace $b^*_{j'}b_j$ by $\overline{b^*_{j'}b_j}$ and this leads to two cases for the sum over the latter quantity [42],

$$\overline{b_{j'}b_j} = \begin{cases} \overline{b_j}\,\overline{b_{j'}} & = |\overline{b}|^2 \quad \text{if } j \neq j', \\ \overline{|b_j|^2} & = \overline{|b|^2} \quad \text{if } j = j'. \end{cases} \tag{2.8}$$

In the above we have dropped the complex conjugate since we are taking b as real. We see now that the sum in equation (2.7) can be rewritten as

$$\begin{aligned} \sum_{jj'} \exp(i\boldsymbol{Q}.(\boldsymbol{R}_j - \boldsymbol{R}_{j'}))b^*_{j'}b_j &= \sum_{j\neq j'} |\overline{b}|^2 \exp(i\boldsymbol{Q}.(\boldsymbol{R}_j - \boldsymbol{R}'_j)) + \sum_j \overline{|b|^2} \\ &= \sum_{jj'} |\overline{b}|^2 \exp(i\boldsymbol{Q}.(\boldsymbol{R}_j - \boldsymbol{R}_{j'})) + \sum_j \overline{|b|^2} - |\overline{b}|^2\,. \end{aligned} \tag{2.9}$$

This makes the cross-section the sum of two parts,

$$\left(\frac{d\sigma}{d\Omega}\right) = \left(\frac{d\sigma}{d\Omega}\right)_{\text{coherent}} + \left(\frac{d\sigma}{d\Omega}\right)_{\text{incoherent}} . \tag{2.10}$$

So now there are two distinct contributions to the cross section of an array of nuclei a so called coherent and incoherent part where the coherent part is,

$$\left(\frac{d\sigma}{d\Omega}\right)_{\text{coherent}} = \sum_{jj'} |\bar{b}|^2 \exp(i\boldsymbol{Q}.(\boldsymbol{R}_j - \boldsymbol{R}_{j'})) \tag{2.11}$$

and the incoherent part is,

$$\left(\frac{d\sigma}{d\Omega}\right)_{\text{incoherent}} = \sum_{j} \overline{|b|^2} - |\bar{b}|^2 , \tag{2.12}$$

where the essential difference is that the coherent cross-section involves a sum over j and j' so there is a possibility of interference between the scattering from different sites while the incoherent cross-section has no interference effects and so measures isotropic scattering.

2.2.1 Nuclear Bragg scattering

If we write $\boldsymbol{l} = \boldsymbol{R}_i - \boldsymbol{R}_j$ then make use of the result

$$\sum_{i} \exp(i\boldsymbol{Q}.\boldsymbol{l}) = N\frac{(2\pi)^3}{v_0} \sum_{\tau} \delta(\boldsymbol{Q} - \boldsymbol{\tau}) . \tag{2.13}$$

for a regular crystal lattice, where v_0 is the unit cell volume and τ is a reciprocal lattice vector. We substitute this result into equation (2.11) and the coherent cross-section becomes [42]

$$\left(\frac{d\sigma}{d\Omega}\right)_{\text{coh}} = N\frac{(2\pi)^3}{v_0} \sum_{\tau} \delta(\boldsymbol{Q} - \boldsymbol{\tau}) |F_N(\tau)|^2 \tag{2.14}$$

where

$$F_N(\tau) = \sum_{d} |\bar{b}_d| \exp(i\boldsymbol{Q}.\boldsymbol{d}) \tag{2.15}$$

which is known as the nuclear unit cell structure factor. We have also generalised to the case of a crystal with more than one atom in the basis. N is the number of unit cells, v_0 is the volume of the unit cell, d is a position vector of an atom in the unit cell, $\boldsymbol{\tau}$ is a reciprocal lattice vector and b_d is the bound scattering length for atom d.

The right hand side of equation (2.14) will be zero except for the case when $\boldsymbol{Q} = \boldsymbol{\tau} = \boldsymbol{k} - \boldsymbol{k}'$. So, according to the cross-section the scattering will be sharply peaked for scattering vectors which match the reciprocal lattice vectors i.e. we get a set of Bragg peaks. The positions of these Bragg peaks in terms of scattering angle θ will conform to Braggs Law

$$2d \sin\theta = n\lambda \,, \tag{2.16}$$

here d is the plane spacing for a given Bragg reflection and λ is the wavelength of the neutron. The structure factor, equation (2.15), acts to modulate the intensity of different Bragg peaks because of the sum over the atoms in the unit cell.

The Debye-Waller factor

In a real crystal it is unrealistic to treat the atoms as bound because thermal excitation causes displacements of the atoms from their mean positions and also permits neutrons to transfer energy to the sample by exciting phonons. So far we have neglected this fact. If this feature is taken into account the result for the coherent cross-section is that there will be both elastic and inelastic terms. If we look at the elastic terms only i.e. the Bragg scattering we find that the cross-section is identical to equation (2.14) but with an additional factor of $\exp(-2W)$. This additional factor is called the Debye-Waller factor and [43]

$$2W = \left\langle (\boldsymbol{Q}.\boldsymbol{u})^2 \right\rangle \approx Q^2 \left\langle u_Q^2 \right\rangle , \tag{2.17}$$

where $\boldsymbol{u}$ is the displacement of a nuclei from its mean position $\left\langle u_Q^2 \right\rangle$ is the mean square displacement of atoms in the direction of Q. Essentially this term will act to reduce the intensity of Bragg peaks at larger Q values. This effect will be most pronounced at higher temperatures because $\left\langle u_Q^2 \right\rangle$ will larger where there is more thermal energy.

2.3 Magnetic scattering

To calculate an expression for the magnetic cross-section we must use the correct form for the interaction potential in equation (2.4). The magnetic interaction between the neutron and sample is written as [45],

$$-\hat{\boldsymbol{\mu}}.\boldsymbol{H} = -\gamma \mu_N \hat{\boldsymbol{\sigma}}.\boldsymbol{H} \,, \tag{2.18}$$

where γ is the gyromagnetic ratio of the neutron, $\hat{\boldsymbol{\sigma}}$ is the Pauli spin matrix of the neutron, μ_N is the nuclear Bohr magneton, and $\boldsymbol{H}$ represents the magnetic field produced by the electrons in the sample. To evaluate the cross-section we substitute equation (2.18) for the potential V in equation (2.4). Now the problem is knowing the form of $\boldsymbol{H}$, which depends on the spin and orbital parts of angular momentum of each electron in the sample. A single electron produces a magnetic field on account of its dipole moment and also a field because of its motion. The total field is the sum of these two contributions.

If we now look at the resulting form of equation (2.4) as result of using the magnetic potential we find [43]

$$\left(\frac{d^2\sigma}{d\Omega E'}\right)_{\sigma\lambda\to\sigma'\lambda'} = (\gamma r_0)^2 \frac{k'}{k} \left|\langle\sigma'\lambda'|\boldsymbol{\sigma}.\boldsymbol{\Omega}_\perp|\sigma\lambda\rangle\right|^2 \delta(E_\lambda - E_{\lambda'} + \hbar\omega)\,, \tag{2.19}$$

where, here, we have σ and σ' as the initial and final spin states of the neutron* respectively.

The quantity $\boldsymbol{\Omega}$ is the magnetic interaction vector and the component of this vector projected onto the plane perpendicular to the scattering vector is $\boldsymbol{\Omega}_\perp$, given by

$$\boldsymbol{\Omega}_\perp = \sum_i \exp(i\boldsymbol{Q}.\boldsymbol{r}_i)\left[\boldsymbol{Q}\times(\boldsymbol{s}_i\times\boldsymbol{Q}) + \frac{i}{\hbar Q}(\boldsymbol{p}_i\times\boldsymbol{Q})\right]\,. \tag{2.20}$$

The sum over i is over all the unpaired electrons in the sample and $\boldsymbol{r}_i$ is the position of the i-th unpaired electron with spin $\mathbf{s}_i$. The vector $\boldsymbol{\Omega}$ is related to the magnetisation density at position r by†

$$2\mu_B\boldsymbol{\Omega} = \boldsymbol{M}(\boldsymbol{Q})\,, \tag{2.21}$$

$$M(Q) = \int M(r)\exp(i\boldsymbol{Q}.\boldsymbol{r})dr\,. \tag{2.22}$$

The first term in equation (2.20) comes from the interaction of the neutron and electron dipole moments and the second term is due to the interaction of the neutron with the magnetic field due to the motion of the electron. They are commonly called the spin and orbital parts respectively. The subscript, $\perp$, in equation (2.19) is important because it tells us that the cross-section only depends on the magnetisation perpendicular to the scattering vector. There is no magnetic scattering if the magnetisation lies along the scattering vector. A geometrical explanation for this feature is given in ref. [46] in terms of dipolar fields.

---

*This notation is not to be confused with $d\sigma$ which is an elemental area of cross section.

†some authors have an additional minus sign in this definition e.g. ref.[43]

To continue we need to work out the form of the squared matrix element in equation (2.19). We also need to sum over all the final spin states of the neutron and the final states of the target and average over the initial neutron spin state and initial target state because we cannot measure a specific scattering event . In doing this we notice that $\boldsymbol{\sigma}$ acts only on the neutron co-ordinates and $\boldsymbol{\mathcal{Q}}_\perp$ acts only on electron co-ordinates. For an unpolarised neutron beam all dependence on the neutron spin factors out to one and so disappears from the cross-section [45]. The matrix element involves terms like $\boldsymbol{\mathcal{Q}}_\perp.\boldsymbol{\mathcal{Q}}_\perp$ and we can write this in terms of Cartesian components as

$$\mathcal{Q}_\perp.\mathcal{Q}_\perp = \sum_{\alpha\beta}(\delta_{\alpha\beta} - \hat{Q}_\alpha\hat{Q}_\beta)\mathcal{Q}^\alpha\mathcal{Q}^\beta\,, \tag{2.23}$$

where $\alpha, \beta = x, y$ or z and $\delta_{\alpha\beta}$ is the Kronecker delta. Now we can write the cross-section in terms of the Cartesian components of $\boldsymbol{\mathcal{Q}}$ so that,

$$\left(\frac{d^2\sigma}{d\Omega dE'}\right) = (\gamma r_0)^2\frac{k'}{k}\sum_{\alpha\beta}(\delta_{\alpha\beta} - \hat{Q}_\alpha\hat{Q}_\beta)\sum_{\lambda\lambda'}p_\lambda\langle\lambda|\mathcal{Q}_\alpha|\lambda'\rangle\langle\lambda'|\mathcal{Q}_\beta|\lambda\rangle\delta(E_\lambda - E_{\lambda'} + \hbar\omega)\,. \tag{2.24}$$

p_λ is the probability that the sample is in state λ.

2.3.1 Cross-section for ions with spin only

If we look at what forms $\boldsymbol{\mathcal{Q}}$ can take, remembering it is related to the magnetisation by equation (2.21), there are a number of forms the cross-section can take. In the case where the magnetic electrons are localized to regular lattice sites (the Heitler-London model) with LS coupling the form of $\boldsymbol{\mathcal{Q}}$ is reasonably simple. The cross-section will be written as

$$\begin{aligned}\left(\frac{d^2\sigma}{d\Omega dE'}\right) = (\gamma r_0)^2\frac{k'}{k}\sum_{\alpha\beta}(\delta_{\alpha\beta} - \hat{Q}_\alpha\hat{Q}_\beta)\sum_{l'd'}\sum_{ld}F^*_{d'}(Q)F_d(Q)\sum_{\lambda\lambda'}p_\lambda \\ \times\langle\lambda|\exp(-i\boldsymbol{Q}.\boldsymbol{R}_{l'd'})S^\alpha_{l'd'}|\lambda'\rangle\langle\lambda'|\exp(-i\boldsymbol{Q}.\boldsymbol{R}_{ld})S^\beta_{ld}|\lambda\rangle \\ \times\delta(E_\lambda - E_{\lambda'} + \hbar\omega)\,,\end{aligned} \tag{2.25}$$

where the labels $l.d$ label the position, l, of the l^{th} unit cell and the position, d, of the d^{th} atom in the cell. S^α_{ld} is the operator which gives the spin for ion ld. The factor $F_d(Q)$ is the form factor, this will be explained in the following section.

Extension to ions with spin and orbital angular momentum

Equation (2.25) is valid only for magnetic ions with spin only. Where the ions have spin *and* orbital angular momentum, which is the case for rare-earth ions in many compounds, the form of $\boldsymbol{\Omega}$ in equation (2.24) is more complicated but the cross-section can be calculated according to the dipole approximation. This assumes $|Q|^{-1}$ is much greater than that the mean radius of the wavefunction of the unpaired electrons[‡]. In this case equation (2.25) has a small modification in that

$$F(Q) = \frac{1}{2} g F(Q) = \frac{1}{2} g_s j_0 + \frac{1}{2} g_l (j_0 + j_2) \tag{2.26}$$

where g is the Landé factor for the ion with $g = g_s + g_l$ and

$$g_s = \frac{1 + S(S+1) - l(l+1)}{J(J+1)}, \tag{2.27}$$

$$g_l = \frac{\frac{1}{2} + L(L+1) - S(S+1)}{2J(J+1)}, \tag{2.28}$$

$$j_n = \int_0^\infty \mathrm{J}_n(Qr) U^2(r) 4\pi r^2 dr, \tag{2.29}$$

with $U(r)$ as the radial wavefunction of the unpaired electrons on the ion and J_n is the n$^{\text{th}}$ order Bessel function. Form factors and the functions j_n have been calculated using Dirac-Foch wavefunctions for the ions [47, 48]. Form factors can also be found from tabulated approximations [49] to the calculations and so the form factor is simple to obtain.

2.3.2 The form factor

The function $F(Q)$ in equation (2.25) is called the form factor. This factor tells us that the scattering from a single magnetic ion will have a dependence on $\boldsymbol{Q}$. If we compare this to what we expect for the scattering from a single nucleus there is clearly a difference. The nucleus is effectively a point particle so the scattering is isotropic. A magnetic ion, however, has a spatial extent comparable to typical neutron wavelengths and so we have to treat the scattered neutron wave as the sum of the scattering from elemental units of the volume. This will lead to interference and at large values of $|Q|$ the scattered wave will be weak. Figure 2.1 shows the variation in the form factor for Ce^{3+} ions. On the IN6 time-of-flight spectrometer at the ILL the measurable elastic wavevector transfers extend up to $Q = 2.2\text{Å}^{-1}$.

[‡] Mean 4f electron radii are $\sim 0.2 - 0.3$ (see section 1.3). On the IN6 spectrometer the largest wavevector transfer is $Q \approx 2\text{Å}^{-1}$ then $|Q|^{-1} = 0.5$ so the approximation seems reasonable.

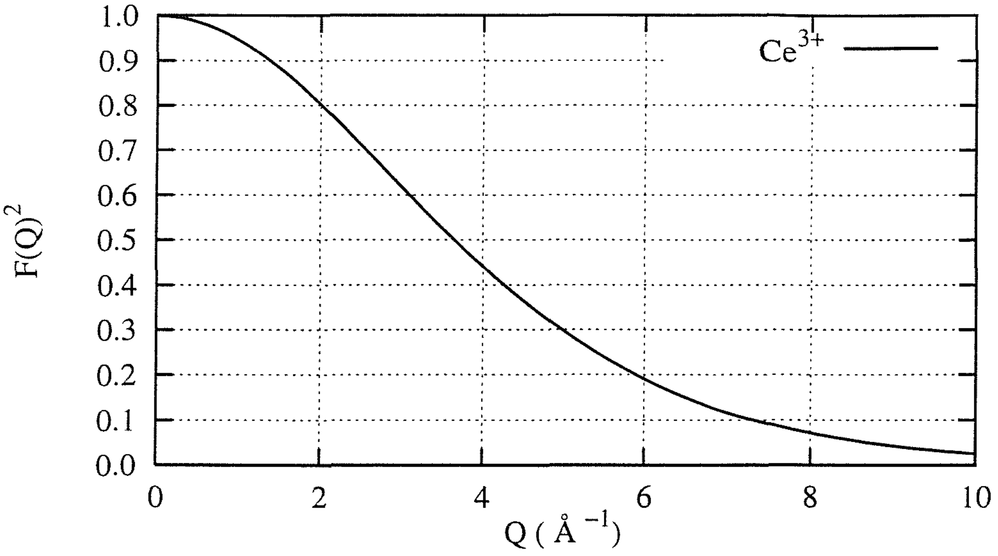

Figure 2.1: Form factor for the Ce^{3+} ion. The form factor reduces the cross-section with increasing wavevector transfer.

2.4 Correlation functions and the cross-section

It is possible to work to a more useful definition of equation (2.25) by introducing time dependent angular momentum operators and by writing the delta function in integral form. In addition we make the assumption that there is no correlation between the electronic spins and the positions of the nuclei so that now,

$$\begin{aligned}\frac{d^2\sigma}{d\Omega dE'} &= \frac{(\gamma r_0)^2}{2\pi\hbar}\left[\frac{1}{2}gF(Q)\right]^2\sum_{\alpha\beta}(\delta_{\alpha\beta}-\hat{Q}_\alpha\hat{Q}_\beta)\sum_l \exp(i\boldsymbol{Q}.\boldsymbol{l}) \\ &\times\int_{\infty}^{\infty}\langle\exp(i\boldsymbol{Q}.\boldsymbol{u}_{\boldsymbol{0}}(0))\exp(i\boldsymbol{Q}.\boldsymbol{u}_l(t))\rangle\langle J_0^\alpha J_l^\beta(t)\rangle\exp(-i\omega t)dt\,.\end{aligned} \tag{2.30}$$

where t is time. This cross-section describes a number of different scattering events including events which are elastic in the spin system but inelastic in the nuclear system (magneto-elastic scattering), magnetic elastic events, magnetic inelastic events and scattering events inelastic in both the spin and nuclear systems. We concern ourselves with scattering which is elastic in the nuclear system so that the correlation function in equation (2.30) which is function of $\boldsymbol{u}$ will eventually become the Debye-Waller factor.

Manipulation of equation (2.30) leads to the final form of the partial differential cross-section for magnetic scattering,

$$\frac{d\sigma^2}{d\Omega dE'} = (\gamma r_0)^2 \frac{k'}{k} \left[\frac{1}{2} g F(Q)\right]^2 \exp(-2W) \sum_{\alpha\beta} (\delta_{\alpha\beta} - \hat{Q}_\alpha \hat{Q}_\beta) S^{\alpha\beta}(Q,\omega)\,, \tag{2.31}$$

$$\text{where} \quad S^{\alpha\beta}(Q,\omega) = \frac{1}{2\pi\hbar} \int_{\infty}^{\infty} \left\langle J_Q^\alpha J_{-Q}^\beta(t) \right\rangle \exp(-i\omega t) dt\,. \tag{2.32}$$

Now we have a very important result. The function $S^{\alpha\beta}(Q,\omega)$ is sometimes called the *scattering law* and it is important because it may be related to the imaginary part of the dynamical susceptibility via the detailed balance factor using the fluctuation dissipation theorem so that,

$$S^{\alpha\beta}(Q,\omega) = [1 + n(\omega)] \frac{1}{g\mu_B} \mathrm{Im}\chi^{\alpha\beta}\,, \tag{2.33}$$

$$\text{and} \quad n(\omega) + 1 = \frac{1}{1 - \exp\left(-\frac{\hbar\omega}{k_B T}\right)}\,. \tag{2.34}$$

$\chi^{\alpha\beta}(Q,\omega)$ is the wavevector and frequency dependent susceptibility of the sample as introduced in section 1.9 and $n(\omega)$ is the detailed balance factor.

2.5 Elastic magnetic scattering

If we look at equation (2.30) the elastic part will be given by the limit of the correlation functions at infinite time,

$$\lim_{t\to\infty} \left\langle J_0^\alpha(0) J_l^\beta(t) \right\rangle = \left\langle J_0^\alpha \right\rangle \left\langle J_l^\beta \right\rangle. \tag{2.35}$$

We must integrate equation (2.30) over energy and if we make the assumption we are dealing with a ferromagnet where we choose the moments to lie along the direction η then equation (2.35) would be equal to $\left\langle J^\eta \right\rangle^2$ since the value of J is the same at each site. Referring to equation (2.30) again we may now write [43, 42]

$$\sum_l \exp(i\boldsymbol{Q}.\boldsymbol{l}) = \frac{(2\pi)^3}{v_0} \sum_\tau \delta(\boldsymbol{Q} - \boldsymbol{\tau}) \sum_d \exp(i\boldsymbol{Q}.\boldsymbol{d})\,, \tag{2.36}$$

where d is the position in the unit cell of the d^{th} magnetic ion , τ is a reciprocal lattice vector and v_0 is the unit cell volume.

The sum over $\alpha\beta$ in equation (2.30) will only have one non-zero value when $\alpha = \beta = \eta$ and in this case the orientation factor will be $(1 - (\kappa_\eta)^2)$ and since equation (2.36) has the delta function only the values $\kappa = \tau$ will give a contribution. This means $\hat{Q}_\eta = \boldsymbol{\tau}.\boldsymbol{\eta}$. Finally, we may write the cross-section for Bragg scattering from a ferromagnet as

$$\begin{aligned}\left(\frac{d^2\sigma}{d\Omega dE'}\right)_{\text{el}} = (\gamma r_0)^2 N \exp(-2W)\frac{(2\pi)^3}{v_0}\langle J^\eta\rangle^2 \left[\frac{1}{2}gF(Q)\right]^2 \\ \times |F_M|^2 \left\{1 - (\hat{Q}.\hat{\tau})^2_{\text{av.}}\right\} \sum_\tau \delta(Q-\tau).\end{aligned} \tag{2.37}$$

2.5.1 Extracting magnetic moment from diffraction data

To extract the magnetic moment from neutron diffraction in a ferromagnet we use the ratio of the cross-sections for nuclear Bragg scattering and magnetic Bragg scattering. If we do this for a ferromagnet, where the magnetic and nuclear Bragg peaks coincide, we find using equation (2.14) and equation (2.37)

$$\frac{I_M}{I_N} = \frac{|F_M|^2 F(Q)^2 (\gamma r_0)^2 \langle \frac{1}{2} g J^\eta \rangle^2 \{1 - \hat{\eta}.\hat{Q}\}}{|F_N|^2}. \tag{2.38}$$

I_M is the intensity of the magnetic and nuclear scattering together, I_N is the nuclear scattering only, F_M is the magnetic cell structure factor, $F(Q)$ is the magnetic form factor, γ is the gyro-magnetic ratio of the neutron, r_0 is the classical electron radius, g is the Landé factor and for the magnetic rare earth ion, J is the angular momentum of the quantum number of the ion, η is a unit vector in the direction of the magnetic moment of the ion and Q is the scattering vector.

2.5.2 Small angle neutron scattering

In equation (2.32) the function $S(Q,\omega)$ is the Fourier transform of the magnetic correlation function. To get information about the static correlations only we want to integrate over energy. This cannot be done analytically because the form of the function $\langle J^\alpha_Q J^\beta_{-Q}(t)\rangle$ is not known. If however we do an experiment in which we make no condition on the energy of the neutrons we detect, we are then measuring the partial cross-section which is in fact the integral we wanted. This experimental method will only be accurate if the neutrons are not scattered much in energy away from their incident value. This is called the quasi-static approximation.

If we do integrate equation (2.31) over energy with the condition that $\hbar\omega \ll E$

we find

$$\frac{d\sigma}{d\Omega} = (\gamma r_0)^2 \left[\frac{1}{2} g F(Q)\right]^2 \sum_{\alpha\beta} (\delta_{\alpha\beta} - \hat{Q}_\alpha \hat{Q}_\beta) \langle J_Q^\alpha J_{-Q}^\beta \rangle \,. \tag{2.39}$$

For ferromagnets the correlation function near $Q = 0$ will be interesting because it provides information on long range correlations. At the critical point for a magnetic phase transition we expect that there will be fluctuations in the magnetisation. The correlation function should represent this and the partial scattering cross-section will be enhanced.

Chapter 3

Muon Spin Rotation and Relaxation

Muon spin rotation relaxation and resonance, or μSR, is the title given to a group of experimental techniques which use muons as a microscopic probe of condensed matter. A positive muon may be regarded as a light proton and it may be used to mimic the behaviour of hydrogen in many materials or, because of its magnetic magnetic moment. it may be used to discern magnetic properties of a material into which it is implanted. Two μSR experiments have been performed on materials studied as part of this thesis and so the focus of the rest of this chapter is on the magnetic aspects of μSR.

3.1 Typical experimental details

The production of muons in large quantities is a task for a large scale facility. The ISIS pulsed proton source, as well as generating neutrons, is used to produce muons. A graphite target placed in the extracted proton beam is used to produce pions which decay into muons. Muons are charged and so they may be directed using electric and magnetic fields. However, the half life of the muon is 2.2μs so experiments have to be performed with this time frame in mind.

Muons are not detected directly: it is their decay products which provide the information. A beam of muons is guided onto a sample and once implanted each muon is sensitive to the local magnetic environment. An important feature of this technique is that the muons thermalise in the sample keeping their spins in the same direction as when they were traveling along their flight path. The initial polarisation

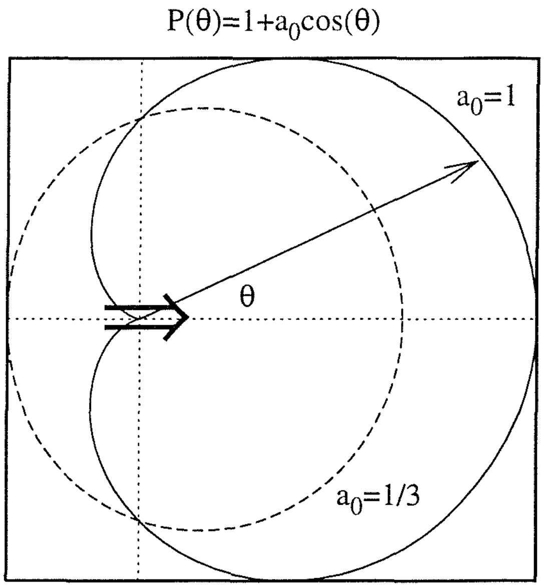

Figure 3.1: Emission probability, P(θ), of the positron as a function of angle to the muon spin. The value of P(θ) is represented by the length of the radius vector in the plot and a_0 is the polarisation factor.

of each muon is typically opposite to the direction of the beam.

When a muon decays it emits a positron preferentially in the direction of its spin. The emitted positron distribution, as a function of time after implantation of the muon, can give information about the time development of the muon polarisation. The decay distribution is shown in figure 3.1. The distribution is a function of the parameter a_0 which is determined from the kinetic energy of the positron. For the range of muon momenta at ISIS, a_0 is one third. In a typical experimental set up there will be two sets of detectors positioned at either end of the sample. The measured polarisation is given by

$$P(t) = \frac{N_F(t) - \alpha N_B(t)}{N_F(t) + \alpha N_B(t)}. \tag{3.1}$$

$N_F(t)$ and $N_B(t)$ are the total count rates as a function of time in the forward and backward groups of detectors respectively and α is an experimentally determined factor to normalise the performance and efficiencies of the two detector groups. The count rate as a function of time, in any detector, will decay exponentially simply because the number of muons remaining shows a radioactive exponential decay. With the definition of the asymmetry in equation (3.1) the radioactive exponential decay cancels out.

3.2 Transverse field μSR.

Muons hit a sample, loose their momentum near the surface, then diffuse slightly deeper before stopping at an interstitial site. In a metallic or intermetallic compound the positively charged muon will be surrounded by a polarisation cloud of conduction electrons. It is also likely that the lattice expands locally to accommodate the muon but these effects are not considered to have a significant effect on the measured properties of the material.

At ISIS, a pulse of muons is implanted with polarisation directed opposite to the beam momentum. The direction of the muon polarisation is the z-direction and if a field is applied transverse to this the muons will be in a coherent super position of quantum spin states and precess about the field with angular frequency

$$\omega_0 = \gamma_\mu B_0 \,, \tag{3.2}$$

where $\gamma_\mu = 0.01355\text{MHz/G}$ is gyromagnetic ratio of the muon and B_0 is the applied field. The asymmetry as a function of time will oscillate, as the muons rotate from pointing forward to backward. If there is a decay envelope to the polarisation there must be fields in the sample with components in the direction of the applied field, nominally called the x- direction. If these local fields are static they increase or decrease the total field a muon sees at any given site so that individual muons will precess at slightly different frequencies, and hence the asymmetry of the ensemble will decay as the individual muons get out of phase. If the local fields are dynamic then fluctuations will flip muons and again the ensemble will dephase.

The decay or damping of the rotation of the muons is described by a relaxation function, $G_x(t)$. In general, if the fields at the muon sites are random, static and have Gaussian distribution the function $G_x(t)$ will also have a Gaussian form,

$$G_x(t) = \exp(-\frac{1}{2}\sigma_x^2 t^2)\,, \tag{3.3}$$

with $\sigma_x = \gamma_\mu \langle B^2 \rangle$. When the muon is mobile, or if the field at the muon site is fluctuating with correlation time ,τ_c, the form of $G_x(t)$ is an exponential,

$$G_x(t) = \exp(-\lambda t)\,, \tag{3.4}$$

with $\lambda = \tau_c \sigma_x$. In the limit between fast and slow fluctuation rates the Abragam form can be found.

$$G_x(t) = \exp\left(-\sigma_x \tau_c \left[\exp\left(\frac{t}{\tau_c}\right) - 1 + \frac{t}{\tau_c}\right]\right)\,. \tag{3.5}$$

Hayano *et al* [50] calculated $G_x(t)$ for a range of fluctuation rates. The work shows that when τ_c is small all the depolarisation curves tend to lie on top of one another. Hence it would be difficult to extract information from transverse field muon spin rotation data in this limit. Zero field μSR is more sensitive for small fluctuation rates. The form of $G_x(t)$ can be more complex than anything outlined here, for example, in type II superconductors the form of $G_x(t)$ can yield the field profile at the muon site in the flux lattice where there is a broad distribution of internal fields in the mixed state.

3.3 Zero field muon spin relaxation.

With no applied field, each muon sees the local field at its site. At each of these sites the fields can have arbitrary direction and strength so each muon will precess about its individual field. The general effect is that the muons precess with different frequencies in different directions and so the ensemble is depolarised.

For the case of static, random fields with a Gaussian distribution we find the Kubo-Toyabe form for the relaxation function, $G_z(t)$,

$$G_z(t) = \frac{1}{3} + \frac{2}{3}(1 - \sigma^2 t^2) \exp\left(-\frac{\sigma^2 t^2}{2}\right) \tag{3.6}$$

In this case $G_z(t)$ shows a recovery to $\frac{1}{3}$, characteristic of this type of behaviour. Initially the muons are fully polarised but they de-phase and after some time the polarisation will be spread evenly over every random direction. What we see at long times is the average polarisation in the measurement direction. For a random distribution the average in any direction is $\frac{1}{3}$ and this is what the measurement shows.

If a longitudinal field is applied equation (3.6) is modified,

$$G_z(t) = 1 - \frac{2\Delta^2}{\omega_0}\left[1 - \exp(-\frac{1}{2}\Delta^2 t^2)\cos\omega_0 t\right] + \frac{2\Delta^4}{\omega_0^3}\int_0^t \exp\left[-\frac{1}{2}\Delta^2\tau^2\right]\sin\omega_0\tau d\tau\,, \tag{3.7}$$

with ω_0 defined by equation (3.2) and $\Delta^2 = \gamma_\mu^2\langle B^2\rangle$.

A Kubo-Toyabe type behaviour has been observed in $\mathrm{CeNi_{0.62}Co_{0.38}Sn}$, shown in figure 3.2. In this compound the behaviour does not follow equation (3.6) in zero field.

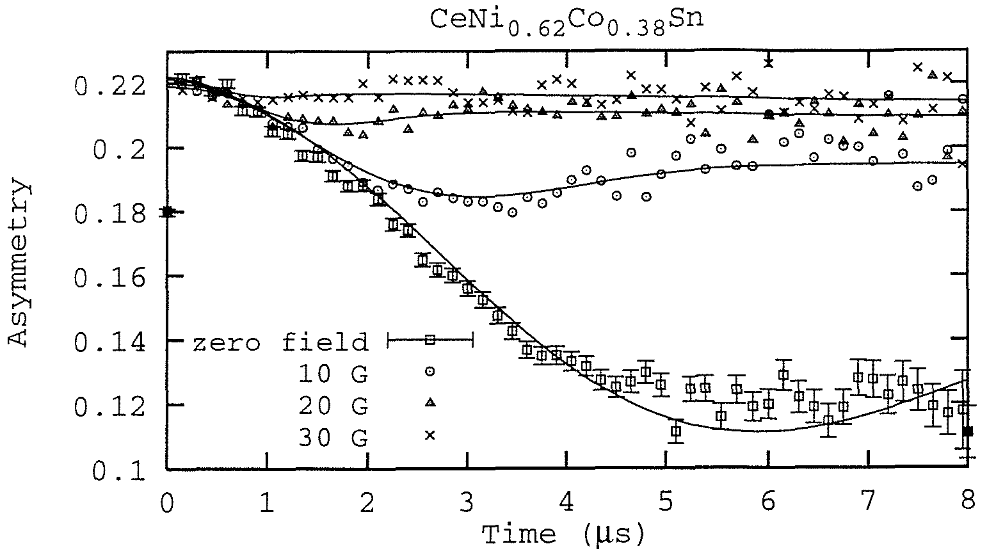

Figure 3.2: Kubo-Toyabe behaviour of polarisation in $CeNi_{0.62}Co_{0.38}Sn$ as a function of applied field. The lines are guides to the eye.

When magnetic order occurs in a material it is possible to observe oscillations in the asymmetry at short times as the muons precess about the internal field. The oscillations are normally only visible in the first few microseconds before they are damped out.

3.4 Longitudinal field muon spin relaxation.

If we have an applied field in the direction of the muon spins each muon starts in a stationary quantum $|+\frac{1}{2}\rangle$ state. If the polarisation changes as a function of time some of the muons must be flipping into a $|-\frac{1}{2}\rangle$ state. This implies that the fields in the sample are supplying the necessary quantum of energy to flip the muons between their two Zeeman states, so the fields must fluctuate with a component at frequency ω, which corresponds to the right energy.

3.4.1 Decoupling nuclear moments

In longitudinal field (LF) muon spin relaxation it is possible to get rid of any relaxation due to nuclear moments. The nuclear fields fluctuate, or relax, on a typically much longer time scale than fields due to unpaired electrons and hence the nuclear magnetic fields do not operate at high enough frequencies to supply a sufficiently large quanta of energy to flip the muons. In this way the nuclear moments are said to be decoupled from the muons, leaving only electronic effects to work on the muons. Typically a longitudinal field of a few milli-tesla is needed to decouple the nuclear moments.

3.4.2 Relaxation functions in LF μSR.

The forms of the relaxation function $G_z(t)$ LF μSR can be quite complicated and there are not a great deal of theoretically calculated functions. However, there are some typical cases. If the fields at the muon site fluctuate rapidly, or if the muon is diffusing rapidly an exponential depolarisation can be observed. For slower fluctuation rates a Gaussian form for $G_z(t)$ may be seen.

In general there may be more than one component to the relaxation and, for example,

$$G_z(t) = \exp(-\lambda_1 t) + \exp(-\lambda_2 t)\,, \tag{3.8}$$

where λ_1 and λ_2 are two different depolarisation rates. In spin glass materials a stretched exponential function can be observed,

$$G_z(t) = e^{(-\lambda t)^{\beta}}\,, \tag{3.9}$$

where the parameter β has been related to a critical exponent.

3.5 Data fitting

In μSR experiments the measured quantity is the count-rate in a set of detectors. Usually the decay of millions muons are counted over an hour. In the first few microseconds of the decay of each pulse of muons the count rate will be high because most of the muons are decaying. The rate can be limited by the "dead-time" of the detection equipment. The dead-time is defined as the minimum separation, in time, between two positrons hitting a detector for which the two positrons will be counted separately. Consider a positron hitting a detector, the finite response time of the detector means that if a second positron arrives too soon it will not register separately. In practice the dead-times of the detection system can be measured and standard programs exist to make a small correction to the data set.

When fitting μSR data a flat background should be considered. The sample holder is typically masked with silver, and silver does not depolarise muons so any muons which stop in the mask will give a time independent contribution to the polarisation.

Typical forms for the asymmetry as a function of time, in an LF experiment, would be,

$$A(t) = A_0 G_z(t) + \text{flat background}\,, \tag{3.10}$$

with A_0 the initial asymmetry at $t = 0$ and $G_z(t)$ is a function which best describes the observed data. For TF data we would fit,

$$A(t) = A_0 G_x(t) \cos(\omega t + \phi)\,, \tag{3.11}$$

where ϕ is a phase and ω is the observed frequency, not necessarily that given by equation (3.2) which implies a Knight shift due the presence of an internal field.

3.5.1 Maximum Entropy method for transverse field data

Maximum entropy is a data analysis technique which can be used to process transverse field μSR data. A μSR experiment reveals measurements of the depolarisation P_i at certain values of time t_i, we expect that the depolarisation is related to the time via

$$P_i \pm e_i = G(t_i; a_1, a_2 \ldots a_k)\,, \tag{3.12}$$

where e_i is a random error and a_k are parameters. To process the data parameters are chosen so that the function G closely represents our data, P_i. The best representation is usually defined to be the one with the particular set of parameters which gives a minimum χ^2, defined by

$$\chi^2 = \sum_i \frac{(P_i - G(t_i; a_1, a_2 \ldots a_k))^2}{e_i^2}\,. \tag{3.13}$$

In transverse field μSR the parameters a_k represent the microscopic fields at the muon sites. We want to know which field strengths are present and this becomes a problem because we anticipate that there will be a range of fields. Our parameter set a_k becomes a continuous distribution $a(k)$.

In effect, the number of parameters has become very large and we cannot determine them all uniquely from our limited data set using a χ^2 test. This is called an inverse problem. We can assume $a(k)$ to be the frequency distribution of the precession of the muons, $a(w)$, because the field strength is related to the precession frequency*.

There is no unique solution to this inverse problem, which means there are multitudes of distributions $a(\omega)$ which will give a reasonable representation of the data. Maximum entropy is a way of picking out one particular solution, which is consistent with the data. We think of the magnitude of $a(w)$ as the probability of having a precession at frequency at ω_i.

The entropy, S, of a solution is given by

$$S = \sum_i a(\omega_i) \log \frac{a(\omega_i)}{b_i}, \tag{3.14}$$

where the interval between ω_i and ω_{i+1} defines the resolution which is better than the experiment could determine and the values b_i are default values which could all be set to unity. When the data has very large error bars and therefore gives no clear information the maximum entropy solution given by maximising equation (3.14) is simply $a(\omega_i) = b_i \mathrm{e}^{-1}$. We can therefore understand the values b_i to be the value the maximum entropy solution will approach for regions of ω_i where there is no information. We can use the b_i's as a default starting point for the maximum entropy search if we already have an idea of the form of $a(\omega_i)$.

Theoretical work [51, 52] shows that the distribution which has the maximum entropy, S, will be a good general solution to the problem. In particular the maximum entropy method produces a distribution which is as uniform as possible and which automatically gives little weight to parts of the distribution which are not well determined from the data.

In practice the a maximum entropy routine finds a distribution with large S and compares this to the data using the χ^2 test. The distribution $a(\omega)$ is the Fourier transform of our depolarisation $G(t)$ and so the maximum entropy routine suitable for μSR has to do this transform to check that the solution is consistent with the data.

The find the most practical solution the maximum entropy routine searches parameter space in order to maximize the quantity $S - \lambda\chi^2$, where λ is a Lagrange

---

*Working with the field distribution is equivalent to working with the frequency spectrum of the precession of the muons because the field and precession frequency are simply related by equation (3.2) multiplier. This technique is used in the analysis of muon spin rotation data for CePdSb in section 4.6 of chapter 4.

Chapter 4

CePdSb

4.1 Introduction

Malik and Adroja [53] initiated the investigation of CePdSb when they made susceptibility, magnetisation and resistivity measurements on a polycrystalline sample. They found the compound to be unusual for a number of reasons:

- It was a ferromagnet. There are only a few Ce based intermetallic ferromagnets but many hundreds of antiferromagnets.
- The Curie temperature (T_C) of 17K was much higher than predicted, according to de Gennes scaling[*] from the ordering temperatures of the other rare-earth R–PdSb compounds.
- The resistivity measurement showed a drop at 17K indicating magnetic ordering. More interestingly, there was a broad maximum at 150K with $-\ln(T)$ behaviour in the high temperature regime. This is a characteristic of a dense Kondo system. The interplay between crystal field effects and the Kondo effect can give rise to this behaviour[†].

They concluded that this compound was an example of a ferromagnetic Kondo compound. These materials are quite rare and there remain only a few examples, e.g. YbNiSn [54], $CePd_2Ga_3$ [55] and $CeRh_3B_2$ [56].

CePdSb has been investigated by zero field NMR, A.C. susceptibility, neutron diffraction and inelastic scattering [57]. Well defined crystal field excitations were

---

[*] de Gennes scaling is discussed in section 1.6.2

[†] see section 1.7.4

found by neutron scattering. NMR and neutron diffraction confirmed the ferromagnetic state below $T_C \approx 17K$ [57]. A.C. susceptibility measurements found that T_C increased under pressure [57].

Following this work Trovarelli *et al* [58] published results for measurements of the heat capacity. They found some extremely interesting behaviour:

- The Sommerfeld coefficient, γ, was quite small and close the value for a normal metal. On the basis of this they suggested that there was no Kondo-type effect involved in this material.
- They found that there was *no cooperative anomaly at T_C in the heat capacity.* However, they saw a rounded maximum centered near 10K which accounted for almost $\frac{1}{2}R\ln 2$ of the entropy. See figure 4.1

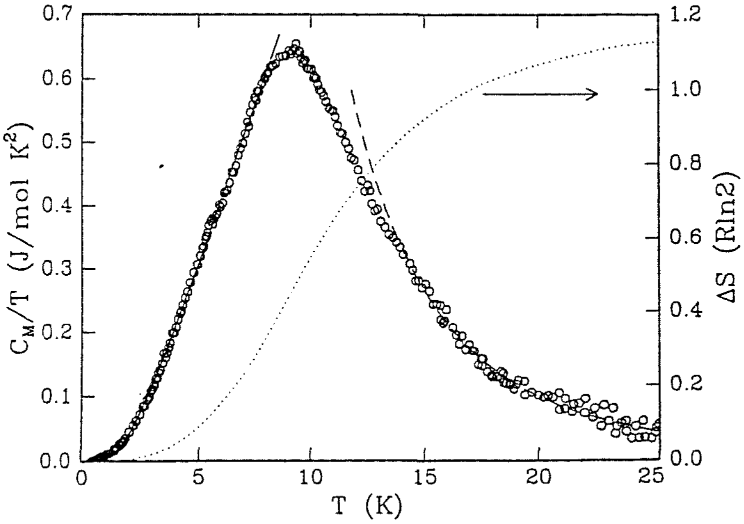

Figure 4.1: Heat capacity data of Trovarelli *et al* [58]. T_C is at 17K. The shape of the anomaly centered near 10K is Shottky–like not a λ–type anomaly.

CePdSb is a planar magnetic with Ce moments lying in the basal plane. Many properties of CePdSb are anisotropic. It is simpler to make measurements using a cartesian co-ordinate system, rather than using hexagonal axes. In the rest of this chapter the directions *a*, *b* and *c* refer to a cartesian axis system. The *a* and *b* axes lie in the basal plane and the *c* axis is perpendicular to the basal plane.

It is important to stress the uniqueness of the heat capacity data. Magnetisation and A.C. susceptibility measurements were made in [58] which quite clearly indicated

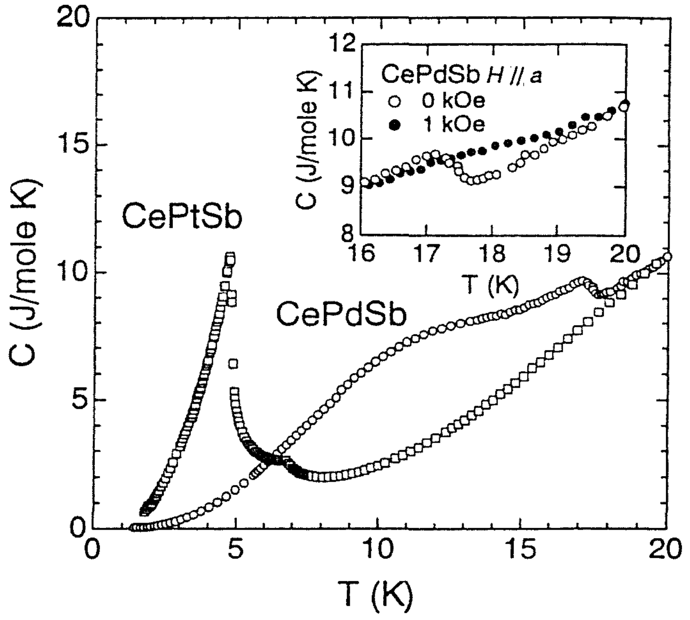

Figure 4.2: Single crystal susceptibility of CePdSb and CePtSb. This data is taken from [59]. The CePdSb data shows a small discontinuity at T_C which is suppressed by an applied field in the c direction.

a ferromagnetic transition at T_C. Since the ferro–to–paramagnetic phase transition is second order there should be a sharp divergence in the heat capacity [34]. A subsequent measurement [59] by another group using a single crystal sample found the same behaviour but with a small discontinuity at T_C. This data is shown in figure 4.2. The discontinuity was suppressed by a 1KOe magnetic field applied in the a direction [59]. Clearly in CePdSb there is a large amount of remaining entropy or disorder below the ordering temperature. This entropy is only removed below 10K.

Thermal expansion measurements [60] on polycrystalline samples indicate a large peak centered near 10K. In an 8T applied field the peak moves upward 3.5K in temperature. This data is shown in figure 4.3. In single crystal measurements [60] the expansion along the c-axis was found to dominate and showed a small anomaly at T_C with a larger rounded peak at 10K. An anisotropy between the expansion along orthogonal a and b axes in the basal plane was also found. See figure 4.4.

Nuclear magnetic resonance (NMR) [61] measurements found a well defined hyperfine splitting at the antimony nuclei sites. The effects of pressure on the effective field at the antimony nuclei showed an increase in effective field under higher pres-

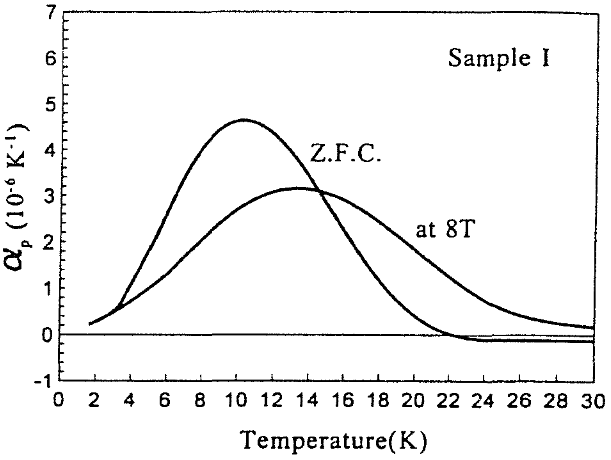

Figure 4.3: The thermal expansion coefficient of a polycrystalline sample of CePdSb in zero field and an 8T magnetic field. Data taken from [60].

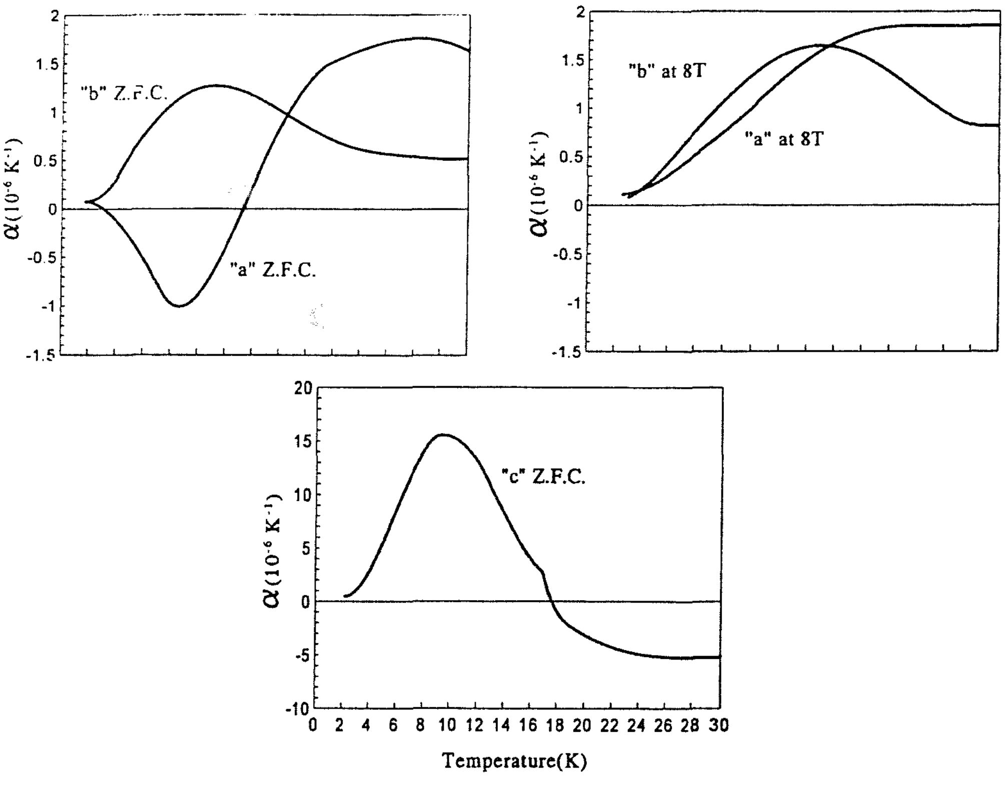

Figure 4.4: Single crystal thermal expansion data, reproduced from [60].

sures [61]. We might expect the transferred hyperfine field at the Sb nuclei to be suppressed with increasing pressure if CePdSb were subject to the Kondo effect.

CePdSb has a hexagonal structure with space group $P6_3mc$. The cerium ions sit on a simple hexagonal lattice with lattice parameters $a = 4.59Å$, $c = 7.89Å$. A unit cell of CePdSb is shown in figure 4.5. There was initially some debate in the literature about this structure because the Pd and Sb ions could be either ordered or disordered on their sublattice, their scattering lengths are too similar to be separated by neutron diffraction. On the basis of crystal field linewidths [62] and NMR splittings [57, 61] the sublattice is thought to be ordered.

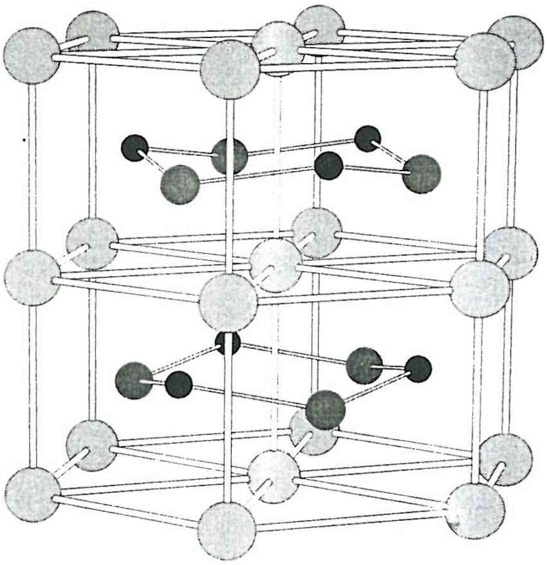

Figure 4.5: GeGaLi type structure. In this figure the Ce ions are the largest with the Pd ions second largest and the Sb ions are the smallest. The relative sizes of the different ions is artificial.

All other work on this alloy has focused on trying to explain the low temperature[‡] behaviour. Presented here are results of several experiments. We have conducted single crystal neutron diffraction, polycrystalline neutron diffraction, small angle neutron scattering, magnetisation, muon spin rotation and relaxation, and low energy neutron scattering measurements.

[‡] here low temperature means less than $\backsim 20K$

atom	position
Ce	(0, 0, 1/4)
Pd	(1/3, 2/3, u)
Sb	(2/3, 1/3, v)

Table 4.1: Positions of ions for the basis of CePdSb. u and v are structural parameters measured by neutron diffraction as [62] u=0.49, v=0.51 respectively.

4.2 Crystal field for CePdSb

Crystal fields were discussed in section 1.5 of chapter 1. An example is given here of the calculation of the crystal field for CePdSb.

The first step in the calculation is to determine the relative positions of the various ions. The unit cell, shown in figure 4.5, shows that the cerium ions lie on a simple hexagonal sublattice. The positions of the three atoms in the basis which when attached to every lattice point gives the correct structure are given in table 4.1. We use hexagonal coordinate axes and lattice parameter units.

It is most convenient to work in spherical polar coordinates. For the crystal field calculation the cerium ion at the center of the middle layer in figure 4.5 is taken to be at the origin and $\phi = 0$ is set so that the first Ce ion in the plane is at $\phi = \frac{\pi}{6}$. The spherical polar co-ordinates of all the nearest neighbours are given in table 4.2.

The radial and polar co-ordinates, $\mathrm{R_{P1}}$, θ_{P1}, of the three palladium ions above the central cerium are given by

$$\mathrm{R_{P1}} = \sqrt{\left(u - \frac{1}{4}\right)^2 c^2 + \frac{a^2}{3}}$$

$$\theta_{\mathrm{P1}} = \tan^{-1}\left(\frac{a}{\sqrt{3}(u - \frac{1}{4})c}\right)$$

and the co-ordinates $\mathrm{R_{S1}}$, θ_{S1} for the three upper Sb ions can be obtained by replacing u by v in the above equations.

Three palladium ions below the central cerium have radial and polar co-ordinates,

Type	co-ordinates		
	R	θ	ϕ
Ce	$c/2$	0	0
Ce	$c/2$	π	0
Ce	a	$\pi/2$	$\pi/6$
Ce	a	$\pi/2$	$\pi/2$
Ce	a	$\pi/2$	$7\pi6$
Ce	a	$\pi/2$	$9\pi/6$
Ce	a	$\pi/2$	$11\pi/6$
Pd	R_{P1}	θ_{P1}	$5\pi/3$
Pd	R_{P1}	θ_{P1}	$\pi/3$
Pd	R_{P1}	θ_{P1}	π
Pd	R_{P2}	θ_{P2}	0
Pd	R_{P2}	θ_{P2}	$4\pi/3$
Pd	R_{P2}	θ_{P2}	$2\pi/3$
Sb	R_{S1}	θ_{S1}	0
Sb	R_{S1}	θ_{S1}	$2\pi/3$
Sb	R_{S1}	θ_{S1}	$4\pi/3$
Sb	R_{S1}	θ_{S2}	$5\pi/3$
Sb	R_{S1}	θ_{S2}	$\pi/3$
Sb	R_{S1}	θ_{S2}	π

Table 4.2: Positions of near neighbours in CePdSb structure with respect to the central Ce ion in figure 4.5. The lattice parameters are a and c and the parameters R_{P1}, R_{P2}, θ_{P1} and θ_{P2} are defined in the text.

R_{P2}, θ_{P2}

$$R_{P2} = \sqrt{\left(u - \frac{3}{4}\right)^2 c^2 + \frac{a^2}{3}}$$

$$\theta_{P2} = \frac{\pi}{2} + \arctan\left(\frac{a}{\sqrt{3}(u - \frac{3}{4})c}\right)$$

and the co-ordinates R_{S2}, θ_{S2} for the three lower Sb ions can be obtained by replacing u by v in the above equations.

At this point we are in a position to consider the crystal field Hamiltonian equation (1.7). It is useful to use part of the superposition theory of crystal fields to ease the determination of the non-zero terms in equation (1.7). The superposition model can be used to separate the geometrical and physical information in the crystal field parameters and make it possible to calculate the parameters. Here we are

$\mathcal{H}_{CF}$	$\|5/2\rangle$	$\|3/2\rangle$	$\|1/2\rangle$	$\|-1/2\rangle$	$\|-3/2\rangle$	$\|-5/2\rangle$
$\langle 5/2\|$	$10B_2^0 + 60B_0^4$	0	0	$3\sqrt{10}B_4^3$	0	0
$\langle 3/2\|$	0	$-2B_2^0 - 180B_4^0$	0	0	0	0
$\langle 1/2\|$	0	0	$-8B_2^0 + 120B_4^0$	0	0	$-3\sqrt{10}B_4^3$
$\langle -1/2\|$	$3\sqrt{10}B_4^3$	0	0	$-8B_2^0 + 120B_4^0$	0	0
$\langle -3/2\|$	0	0	0	0	$-2B_2^0 - 180B_4^0$	0
$\langle -5/2\|$	0	0	$-3\sqrt{10}B_4^3$	0	0	$10B_2^0 + 60B_0^4$

Table 4.3: Matrix elements $\langle\alpha|\mathcal{H}_{CF}|\beta\rangle$ for the crystal field Hamiltonian for CePdSb.

only interested in the form of the Hamiltonian. The superposition model states

$$A_l^m\langle r^l\rangle = \sum_L \bar{A}_l(R_L)K_{lm}(\theta_L,\theta_L)\,, \tag{4.1}$$

where the sum is over the L ligands. The factors $K_{lm}(\theta_L,\theta_L)$ are tabulated functions in terms of the angular co-ordinates of the different ligands defined in a common co-ordinate system. By performing the sum in equation (4.1) we find that some of the A_l^m are zero and hence do not appear in the Hamiltonian.

For CePdSb only the terms A_2^0, A_4^0 and A_4^3 are non-zero which makes the crystal field Hamiltonian

$$\mathcal{H}_{CF} = B_2^0O_2^0 + B_4^0O_4^0 + B_4^3O_4^3\,, \tag{4.2}$$

where the B_l^m are the parameters to be determined from experiment and the O_l^m are Stevens operators introduced in section 1.5

In the free ion the $2J+1$ angular momentum states are defined in terms of spherical harmonics and to calculate the effect of the perturbing crystal field we must find the eigenvalues and eigenstates of the Hamiltonian, equation (4.2). The matrix elements $\langle J;m_J|O_l^m|J;m_{J'}\rangle$ are known and tabulated for most values of J [6], and using these tables we can find the matrix elements $\langle\alpha|\mathcal{H}_{CF}|\beta\rangle$, where for cerium $J=\frac{5}{2}$ so that the $|\alpha\rangle$ and $|\beta\rangle$ states are from the set $|\frac{5}{2}\rangle\,|\frac{3}{2}\rangle\,|\frac{1}{2}\rangle\,|\frac{-1}{2}\rangle\,|\frac{-3}{2}\rangle\,|\frac{-5}{2}\rangle$. Table 4.3 shows the resulting matrix.

By diagonalising this matrix we can find the eigenvalues and the eigenstates. In this case the result is six eigenstates, which are

$$\begin{aligned}\psi_A^{\pm} &= \cos\theta|\pm 5/2\rangle \pm \sin\theta|\mp 1/2\rangle \\ \psi_B^{\pm} &= \cos\theta|\mp 1/2\rangle \mp \sin\theta|\pm 5/2\rangle \\ \psi_C^{\pm} &= |\pm 3/2\rangle\,.\end{aligned} \tag{4.3}$$

We can see that the crystal field has produced three doublets, labeled A, B and C. One of the doublets consists of $\psi_C^{\pm}$ which is simply two of the original states. The other two doublets are admixtures of our original states. The degree of admixture is determined by the parameter θ, the mixing parameter. The eigenvalues for the three doublets are

$$\begin{aligned}\lambda_A &= B_2^0 + 90B_4^0 + \sqrt{(-9B_2^0 + 30B)^2 + 90(B_4^3)^2} \\ \lambda_B &= B_2^0 + 90B_4^0 - \sqrt{(-9B_2^0 + 30B)^2 + 90(B_4^3)^2} \\ \lambda_C &= -B_2^0 - 180B_4^0\,.\end{aligned} \tag{4.4}$$

To determine the parameter θ we know that $\mathcal{H}_{CF}$ is diagonal in the new eigenfunctions so we look at, for example, $\langle\alpha|\mathcal{H}_{CF}|\beta\rangle$ for an off diagonal element and set it equal to zero then solve for θ.

At this point we do not know which of the doublets is the groundstate and we require experimental evidence to tell us which is which. Since equation (4.4) characterises the relevant states for the cerium ions it is possible to calculate the expected neutron scattering cross-section for inelastic transitions between the states. Calculated intensities for all allowed transitions between the different states can be compared with measured intensities to determine the order of the states. In addition, calculating the magnetic moment for each state, given by $g\mu_B\langle\psi^{\pm}|J_z|\psi^{\pm}\rangle$, and comparing with experimental values can determine the groundstate.

Neutron scattering measurements [62] of the crystal field excitations indicates that the level scheme is as shown in figure 4.6. The measured neutron scattering cross-section is shown in figure 4.7. The line in this figure is a fit using the crystal field Hamiltonian with parameters B_2^0 = 1.36meV, B_4^0 = −0.054meV and B_4^3 = 0.857meV [62]. This procedure gives the mixing parameter $\theta \approx \frac{\pi}{8}$ and predicts a moment of $1.2\mu_B$ per Ce lying in the basal plane [62]. The planar nature of the moments suggest that the X-Y model (see section 1.12) is applicable to this material.

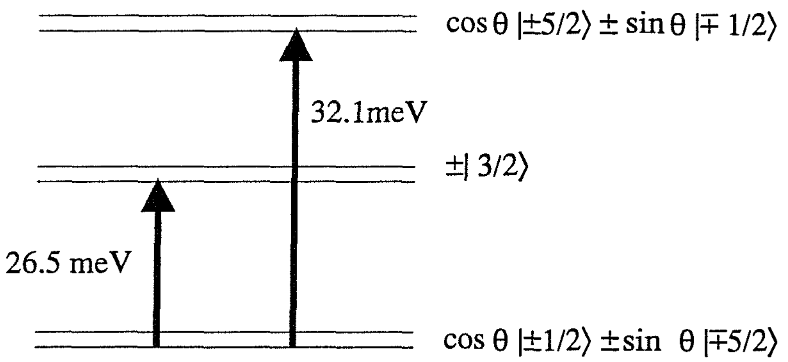

Figure 4.6: Crystal field level scheme for CePdSb, showing three doublets with allowed transitions labelled by arrows.

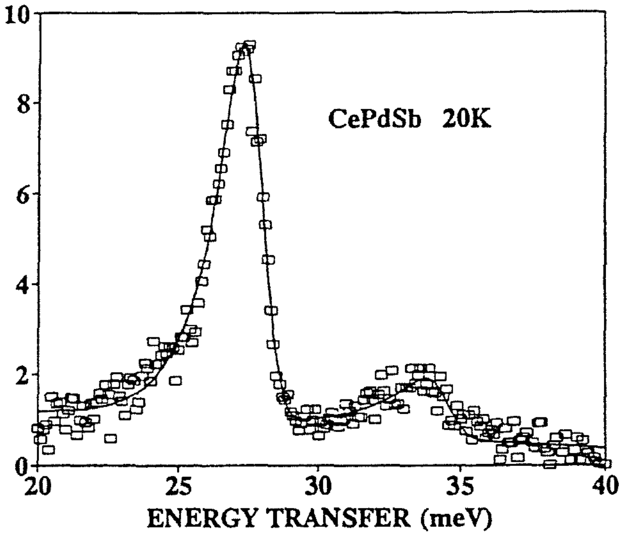

Figure 4.7: Crystal field excitations for CePdSb. Two peaks can be seen which represent the transition between the doublets in figure 4.6. The line represents the fitted neutron scattering cross-section, calculated on the basis of the crystal field Hamiltonian.

4.3 Low field magnetisation and Susceptibility

The magnetisation of a small polycrystalline piece of CePdSb was measured in a small field (100 Oe) using a VSM. The result is shown in figure 4.8. The curve looks like a standard mean field magnetisation curve with T_C clearly around 17K. We note that this data does not show any indication of unusual behaviour below T_C. There are a few scattered points near 12K but they are due to temperature instability in the apparatus when the measurement was made and so are not significant. Some additional measurements were made using a SQUID magnetometer. The measurements were nominally made in zero field but the residual field of the magnetometer is known to be 1G. As a small piece of material was cooled it began to develop a spontaneous magnetisation below ~ 18K. This gives confirmation of a ferromagnetic transition at this temperature.

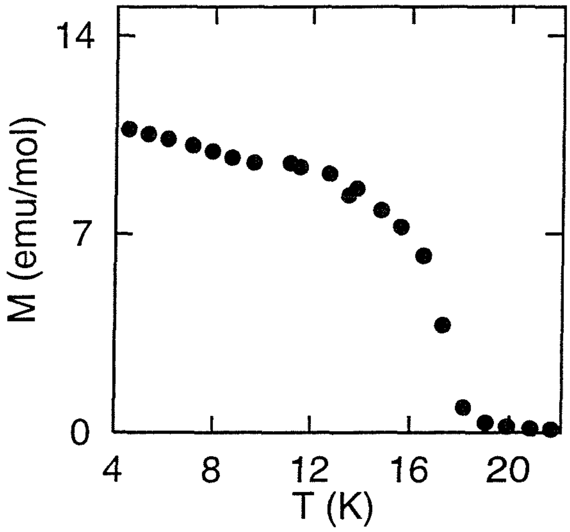

Figure 4.8: Magnetisation of polycrystalline CePdSb in a small field as a function of temperature.

A small fragment of a single crystal was used in a measurement of the susceptibility as a function of temperature. Measurements of the susceptibility were made along the *a*, *b*, and *c*-directions using a VSM. The crystal field model predicts the susceptibility along the *c*-axis to be small and very weakly temperature dependent. The data for the *a* and *b*-directions showed a sharp rise at 18K signalling ferromagnetism. Plots of the reciprocal susceptibility showed that the *a* and *b*-directions had the same susceptibilities while the *c*-direction was clearly different. It was possible to fit this anisotropic behaviour to the susceptibility calculated on the basis of the crystal field model [62]. The sample used was very small and so was difficult to align accurately and this misalignment had to be included in the fit [62]. Katoh *et al* [63] have also made measurements of the susceptibility of a single crystal and it was possible to fit their data to the crystal field model also.

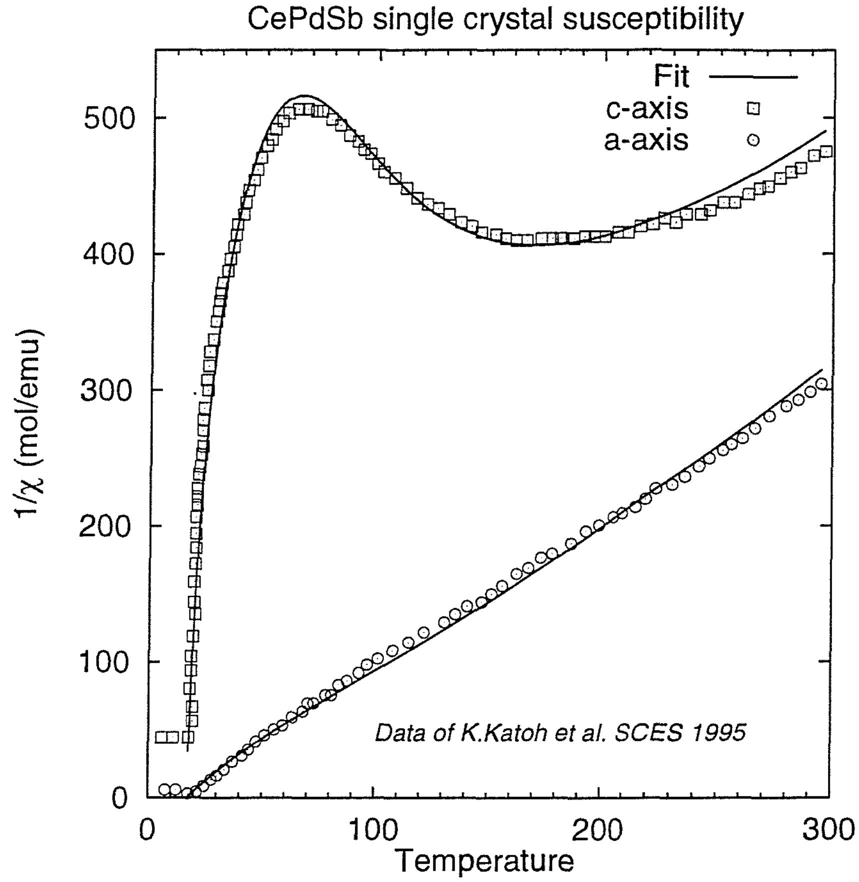

Figure 4.9: Single crystal susceptibility of CePdSb. This data is taken from ref.[63]. Lines are fits using crystal field model.

Recall that the crystal field Hamiltonian is

$$\mathcal{H}_{CF} = B_2^0 O_2^0 + B_4^0 O_4^0 + B_4^3 O_4^3 \,, \tag{4.5}$$

as calculated in section 4.2 where the O_l^m are Stevens operators and the B_l^m are the crystal field coefficients. The single ion susceptibility χ_0 was calculated on the basis of this crystal field Hamiltonian, for the a and c-directions. The single ion susceptibility at a temperature T, is calculated using the Boltzman probabilities of occupation of the different crystal field levels following the procedure outlined in section 1.5.1 of chapter 1.

The effects of exchange were included by a molecular field parameter λ so that the measured susceptibility in a direction ξ is

$$\chi^{\xi} = \frac{\chi_0^{\xi}}{1 - \lambda_{\xi}\chi_0^{\xi}} + \chi_{\text{c.e.}} \tag{4.6}$$

where χ_0 is the single ion susceptibility given in section 1.5.1 by equation (1.11) and $\chi_{\text{c.e.}}$ is a constant contribution due to conduction electrons. Different molecular field parameters were fitted for the a and c directions on the basis that the material is very anisotropic. The fit parameters were λ_a, λ_c, θ the crystal field mixing parameter and $\chi_{\text{c.e.}}$.

The fit indicated that λ_c was about three times as large as λ_a. This means the exchange interactions are much stronger along the c-axis and since the Ce–Ce distance is shortest in this direction it indicates that nearest neighbour exchange is quite dominant. This has been confirmed in recent measurements of the magnon dispersion relations in a single crystal [64]. The fit was improved by including an alignment angle as a fitting parameter which gave the best fit when the c-axis was assumed to be 8.9° away from the vertical.

Figure 4.9 shows the results. This fit gave $\chi_{\text{c.e.}}$ as a small negative contribution and θ, the mixing parameter, to be 0.3292 rad (roughly $\frac{\pi}{10}$) while the crystal field calculation gave $\theta \approx \frac{\pi}{8}$. The fit supports the validity of the crystal field model. Note that because the Ce moments lie in the plane we can examine CePdSb with the XY model in mind, but we should also allow for dominant exchange along the perpendicular c-axis which necessitates the use of a three dimensional model.

4.3.1 Magnetisation

A number of magnetisation isotherms were measured for a small polycrystalline piece again using a Vibrating Sample Magnetometer. Figure 4.10 shows the results in the form of an Arrott plot[§]. The isotherm at 17.5K goes through the origin which is taken to be T_C. Isotherms were measured at temperatures in between those shown on the plot but are not included in an attempt to improve the clarity of the figure. Magnetisation hysteresis loops taken below T_C from zero to positive field and back to zero showed hysteresis of only a few millitesla and a tiny remanent field. The inset to figure 4.10 is an attempt to extract the spontaneous magnetisation from these data using the extrapolation of the linear portion of each isotherm to zero

---

[§] The Arrot plot method is outlined in section 1.10.2 of chapter 1 field. The low field portion of the Arrot plot was used for the extrapolation and there is some uncertainty in the result because the isotherms on the Arrot plot are not linear.

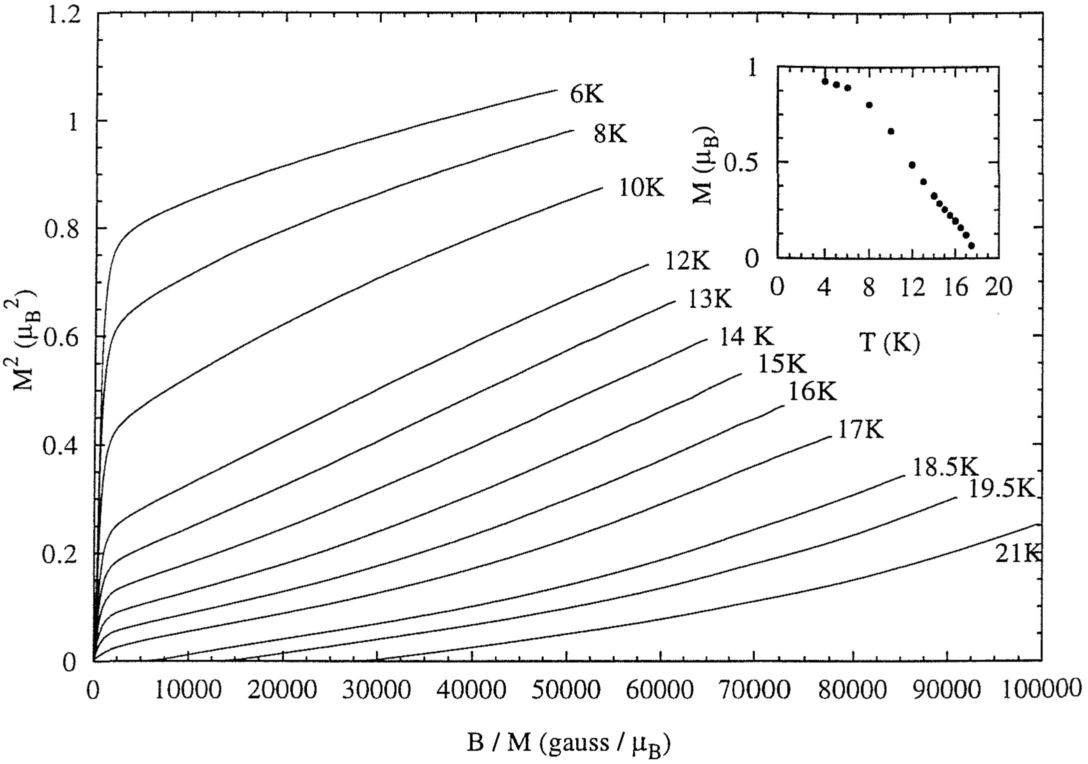

Figure 4.10: Arrot plot of polycrystalline CePdSb magnetisation data. Inset shows the spontaneous magnetisation derived from this data by extrapolating the low field part of the isotherms back to zero field.

Figure 4.11 shows data for the magnetisation along the *b*-axis of a single crystal again in the form of an Arrot plot. These data are very similar to the polycrystalline measurement. The zero temperature limit of the extrapolated spontaneous moment ($\sim 1.2\mu_B$) agrees well with other estimates in this thesis. The polycrystalline value is depressed because the applied field is in different directions in different crystallites, giving an average over the crystallite orientations.

Careful examination of the Arrot plots reveals a change in curvature of the lines around 14K. Below 14K the lines have concave curvature but above this temperature they take on a slight convex curvature. It was not possible to find values of the critical exponents β and γ which made all the isotherms linear and so the mean field values have been used.

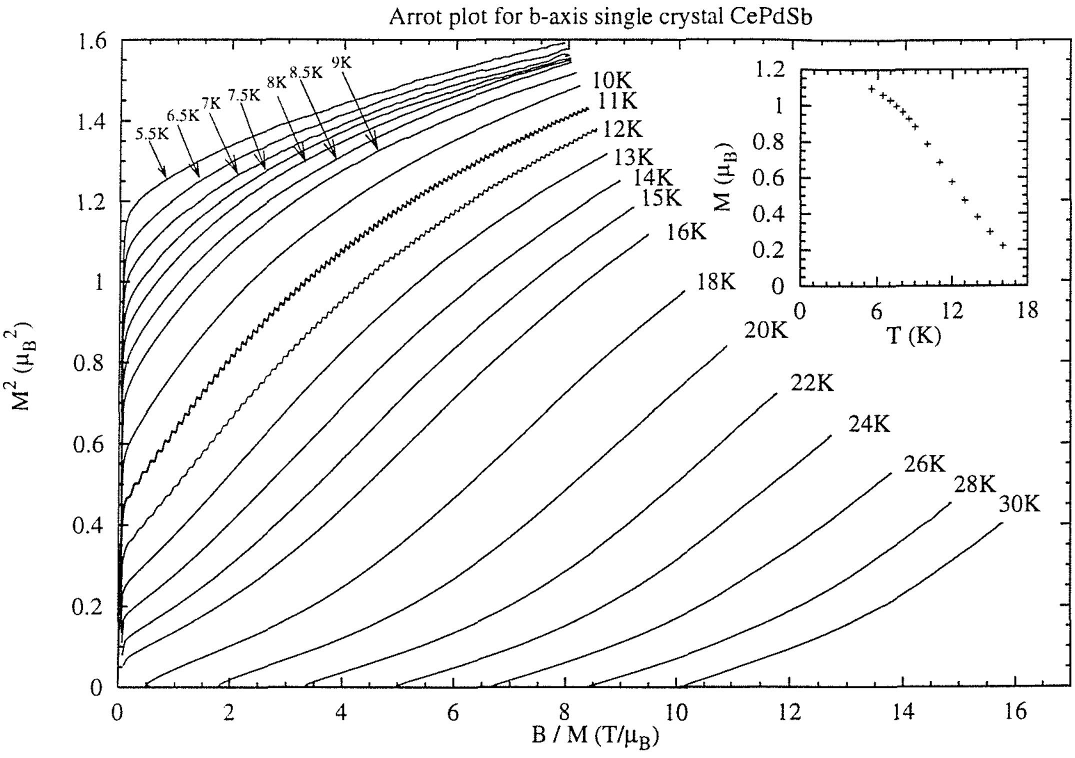

Figure 4.11: Arrot plot of single crystal magnetisation data for field applied along the b-axis in the basal plane. Inset shows the spontaneous magnetisation derived from this data by extrapolating the linear linear low field part of the plot back to zero field.

4.4 Neutron Diffraction

A neutron diffraction experiment was performed using the D1B neutron diffractometer at ILL, Grenoble. The D1B spectrometer has a detector bank covering an angle of ~ 80°. A crushed polycrystalline sample was used and was placed in a cylindrical vanadium can. Neutrons with incident wavelength $\lambda = 2.52$Å were used for this study.

Figure 4.12 shows the pattern obtained at 21K. This temperature is above T_C and so there will be no magnetic Bragg peaks corresponding to long range order. All the major peaks could be indexed on the basis of the hexagonal structure. The lattice parameters found using a simple refinement program were $a = 4.591(14)$, $c = 7.921(27)$. These values are in good agreement with previous reports [53]. There were a few low intensity peaks which could not be attributed to the hexagonal lattice of CePdSb which indicate a small amount of impurity in the sample.

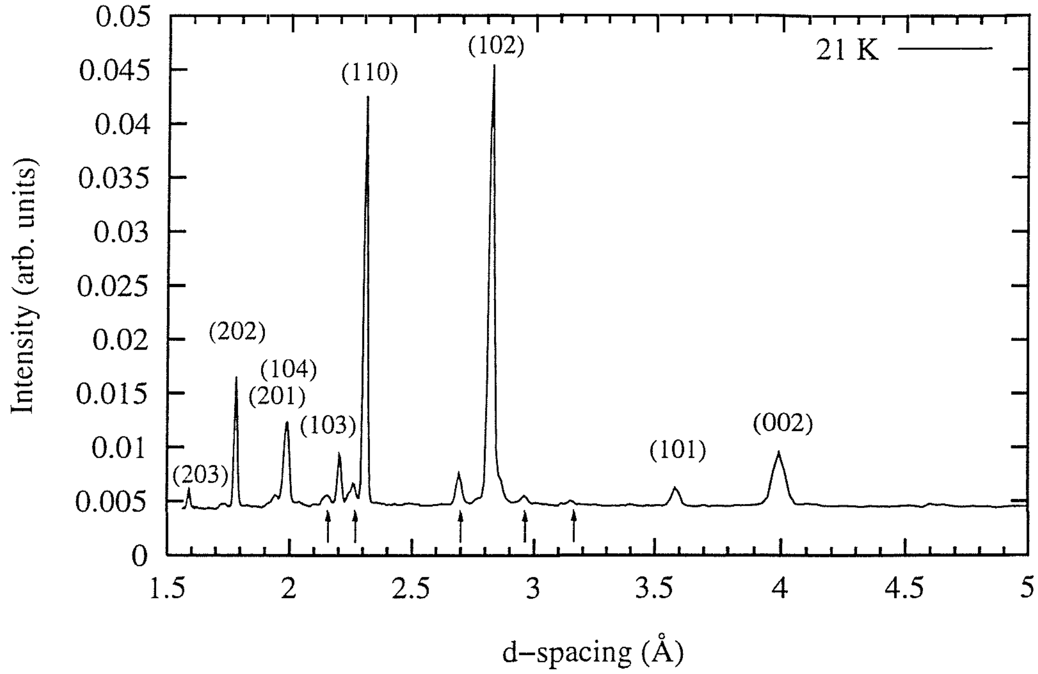

Figure 4.12: The nuclear Bragg pattern at 21K, this was used to subtract from lower temperature data. Note that the intensity of these Bragg peaks is far greater than those of figure 4.13. The arrows indicate unidentified peaks due to impurity phases.

Measurements of the diffraction pattern were made at a number of temperatures below T_C. To facilitate analysis of these patterns the intensity due to nuclear Bragg scattering was removed by subtracting the 22K pattern from all the other data, leaving only the magnetic part. Figure 4.13 shows magnetic Bragg patterns at four temperatures below T_C. At each of these temperatures the pattern can be indexed assuming the hexagonal structure. There are no additional peaks at any temperature which shows that we have purely ferromagnetic ordering. However, it is to be remembered that we are working with a powder diffraction pattern so that, for example, very long range helical order would not be resolved by this experiment.

It is clear from figure 4.13 that the intensity of the magnetic peaks increases steadily as the temperature is lowered. We have used the intensity of the 002 magnetic Bragg peak to extract a value for the spontaneous magnetic moment as a function of temperature following the prescription of section 2.5.1 and this is shown figure 4.14 in combination with other data. The intensity of the 002 Bragg reflection at different temperatures was determined by fitting a Gaussian function to the data. This gave good fits and the area of the Gaussian was used as the intensity of the reflection. We have assumed that the moment lies wholly in the basal plane and any magnetic domains have their magnetisation confined to the basal plane. The 002 reciprocal lattice vector is then perpendicular to the magnetic moment so that the orientation factor in the cross-section for this peak is equal to one for all domains.

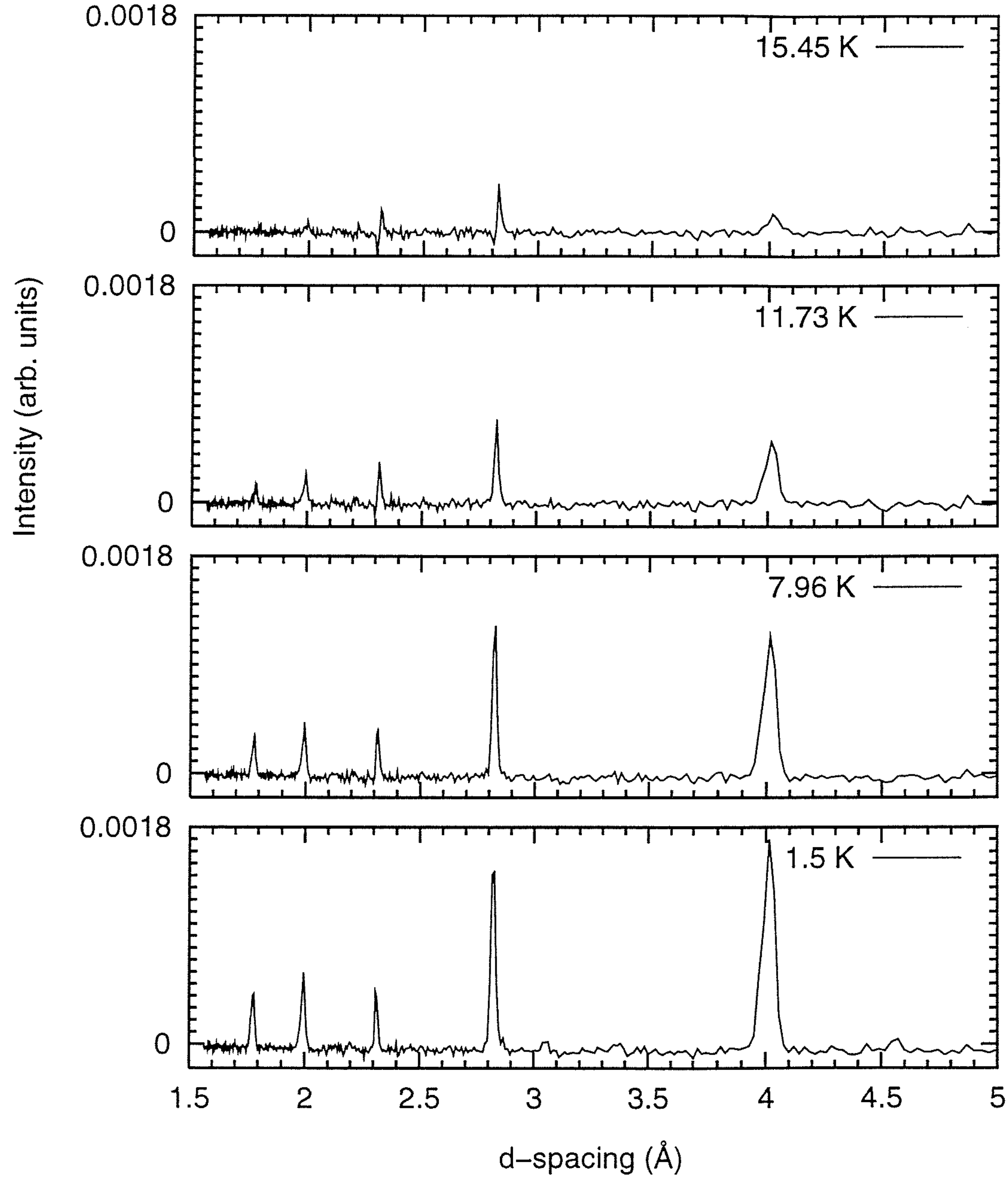

Figure 4.13: The magnetic Bragg pattern of a poly crystalline sample at a number of temperatures. The nuclear Bragg intensity has been subtracted.

4.4.1 Single crystal diffraction

Prior to the powder diffraction experiment we made measurements of three Bragg peaks as a function of temperature in a single crystal, using the TAS7 triple axis spectrometer at Risø, Denmark. The single crystal was large but had a very poor mosaic, which precluded any experiments other than diffraction. We were able to measure the temperature dependence of the (110), (112) and (002) Bragg peaks. The temperature dependence of the intensity of the (002) peak was used to determine the temperature dependence of the magnetic moment, in the same manner as the powder diffraction data. The result is shown in figure 4.14 which includes the data from the powder diffraction work and the spontaneous moment taken from the Arrot plot (figure 4.10). Figure 4.14 shows good agreement between the three data sets. By comparing with figure 4.8 we see that the spontaneous moment shows a somewhat unusual behaviour. The spontaneous moment approaches zero relatively slowly. The magnetisation in a small field (figure 4.8) indicates a much sharper drop off close to T_C. The derived spontaneous moment shows a linear drop with a small 'foot' just below T_C where the magnetisation drops to zero.

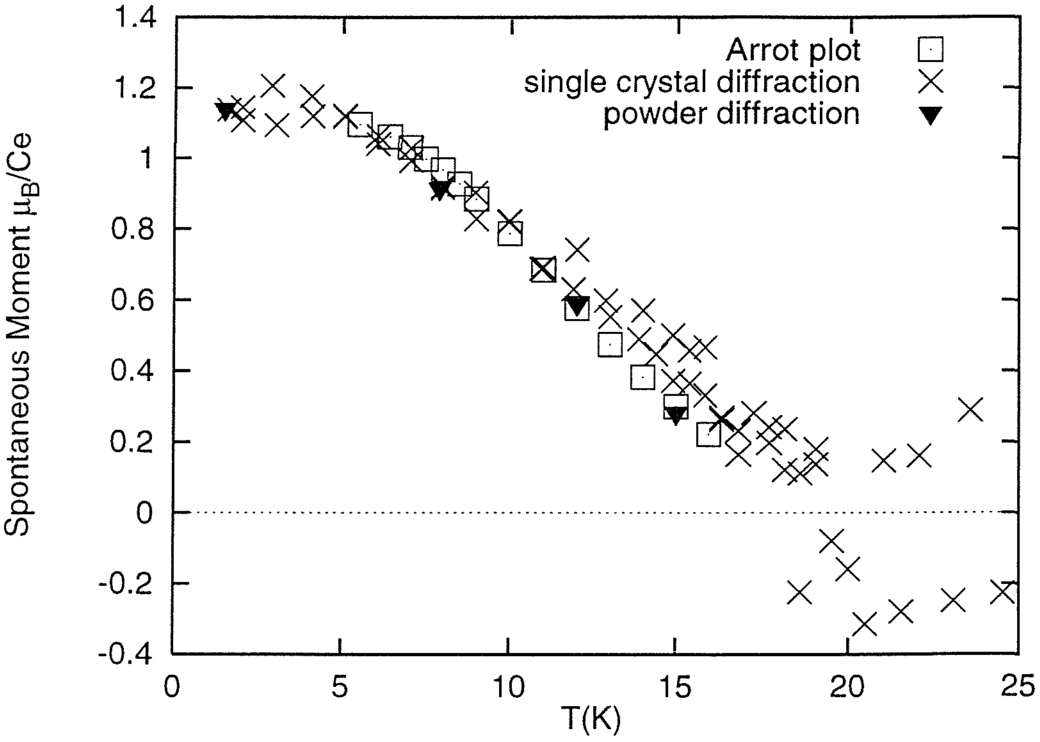

Figure 4.14: Spontaneous moment in CePdSb as measured by different techniques.

In a small applied field the magnetisation below T_C develops much more rapidly than the spontaneous moment shown in figure 4.14.

4.5 Low energy neutron scattering

The IN6 spectrometer at I.L.L. was used to measure the low energy response in a polycrystalline sample. Temperatures in the range 1.5–100K were studied and the data was merged into 19 detector groups with elastic wavevectors ranging from 0.26 to 2.05 Å^{-1}. The data was corrected for background scattering, sample absorbtion and self shielding, and was normalized to the scattering from a vanadium plate. No corrections were made for phonon scattering because we are working in an energy window close to zero, at small wavevectors and at low enough temperatures for there to be only minimal phonon scattering.

At temperatures of 17K and above the scattering response is well described by a quasi-elastic Lorentzian lineshape and an elastic line representing the incoherent elastic scattering. Figure 4.15 shows the scattering for a number of detector groups at 100K. Quasielastic scattering can be seen in the figure and the elastic scattering is also indicated.

Figure 4.17 shows the variation of the quasielastic linewidth as a function of wavevector transfer for different temperatures. At these temperatures we are in the paramagnetic regime and the linewidth is clearly wave-vector dependent implying spin-spin interactions between Ce ions, as expected for a localised ferromagnet. The response remains quasielastic down to 10K, well below T_C but below this temperature inelastic features begin to appear. At 6K and 4K we observed inelastic scattering from spinwaves which is most intense in the lowest angle detector groups.

4.5.1 Low temperature response

As the sample was cooled through T_C the quasielastic scattering persisted, with no evidence of inelastic scattering. However, at 10K, the response in the low angle detectors was not a simple quasi-elastic Lorentzian. There was some evidence of inelastic scattering.

At 6K and 4K there is pronounced inelastic scattering in the low angle detectors only. Figure 4.16 shows contour plots of the scattering as a function of energy

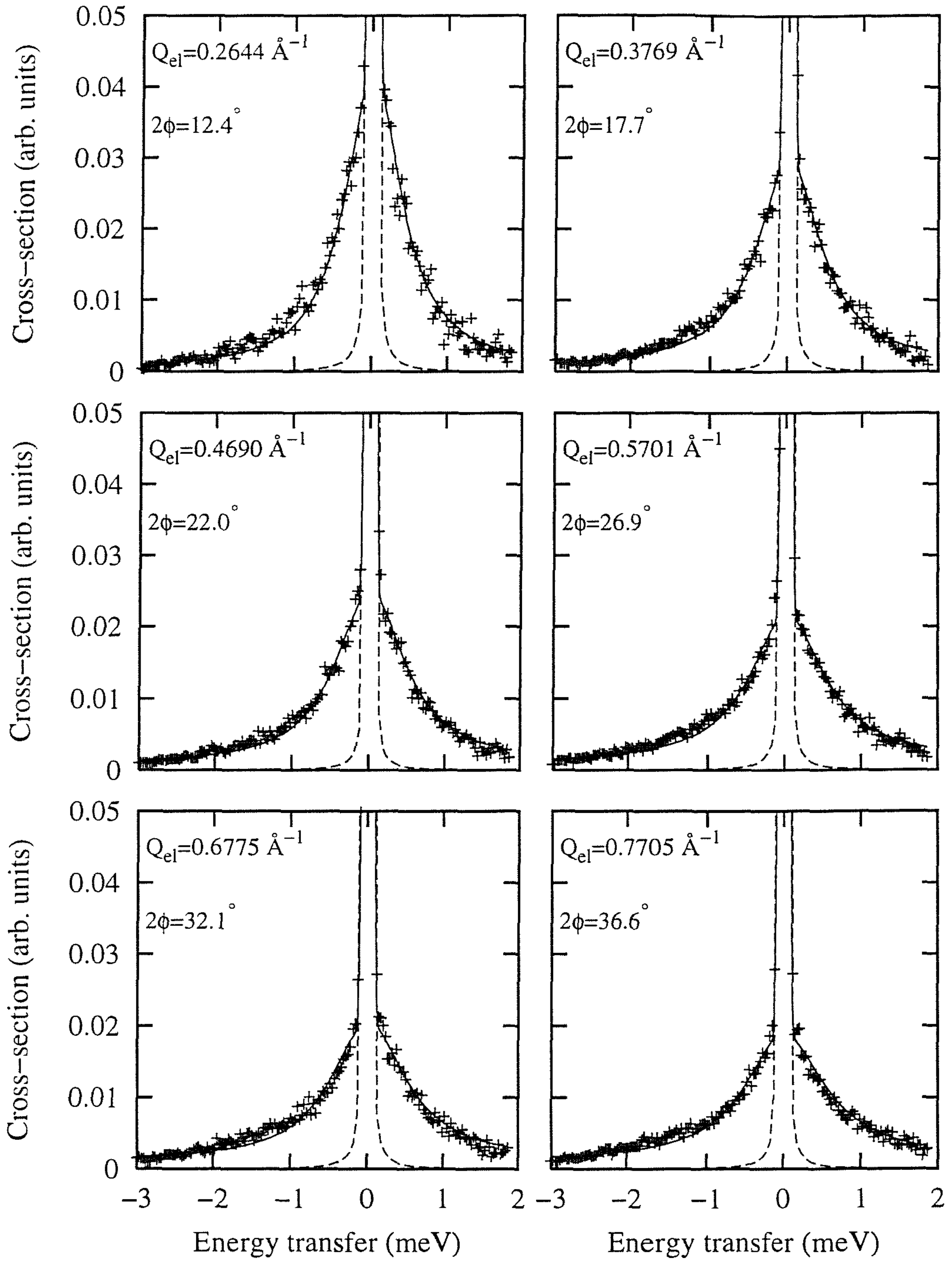

Figure 4.15: This figure shows the measured scattering in detector groups one to six for CePdSb at 100K. The data was fitted using a Lorentzian lineshape for the quasielastic part. The fitted elastic scattering is indicated by the dashed line.

transfer and wavevector transfer. The plots show the region of Q and ω space which is accessible with the detector bank on the IN6 spectrometer.

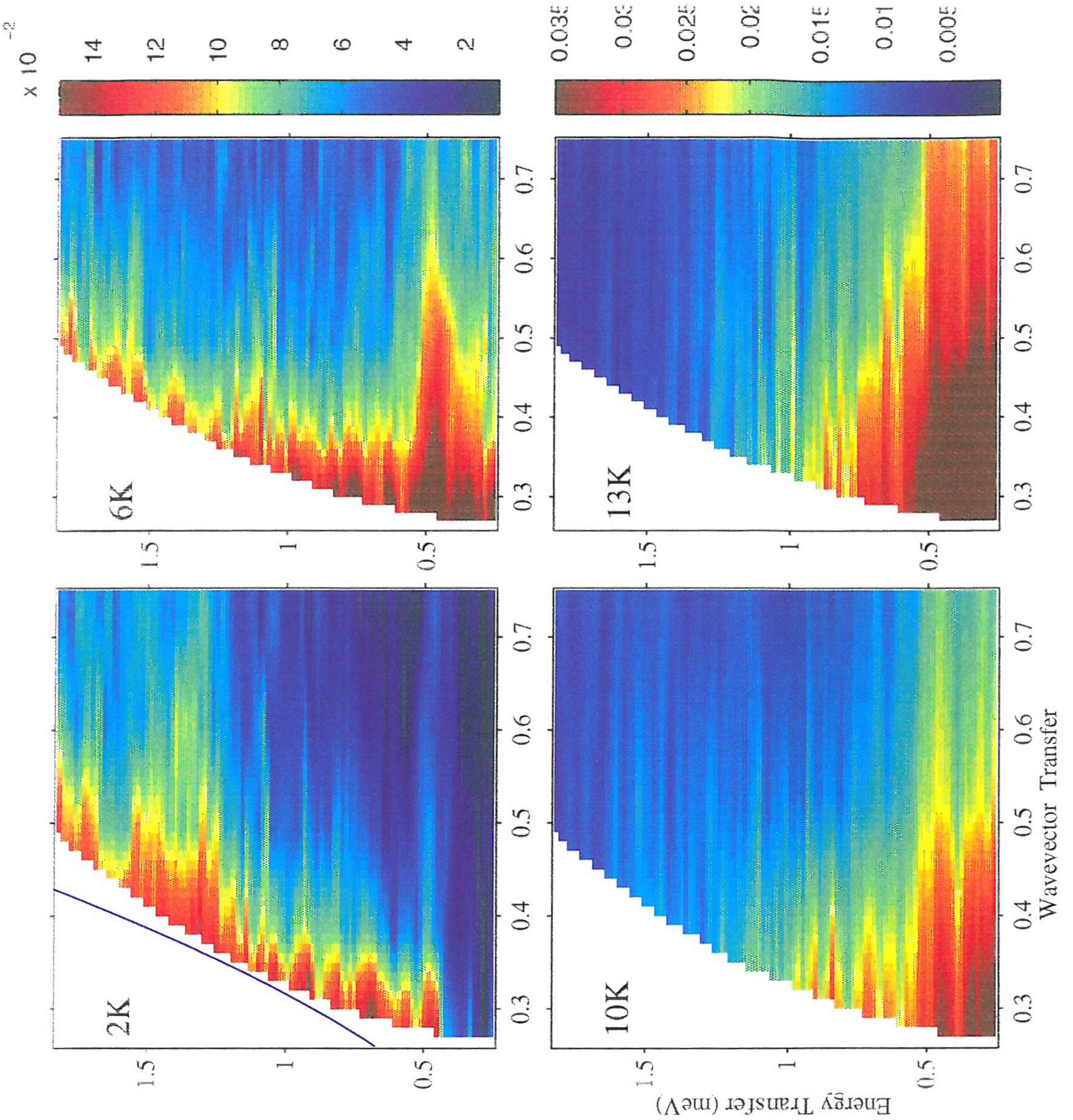

Figure 4.16: Spinwave scattering in CePdSb. The 10K and 13K figures show only a quasielastic response. Note that the plots do not include the origin, simply to exclude the intense elastic scattering. The line in the 2K plot indicates a spinwave dispersion curve as discussed in the text.

Below 10K it appears that the lowest angle detector is just grazing a spinwave dispersion curve. At small wavevectors the Heisenberg model gives a quadratic spinwave dispersion, $\hbar\omega = DQ^2$, where D is the spinwave stiffness constant. We can use this as a guide and the line on the 2K plot of figure 4.16 shows the dispersion curve corresponding to $D = 10$ meVÅ^2. This dispersion curve lies close to the edge of the detector range and it would appear that the scattering we see is due to the edge of some spinwave scattering. This means that the spinwaves should have stiffness of at least $D = 10$meVÅ^2. However we note that this is based on data from a polycrystalline sample.

At 10K and 13K we can see from figure 4.16 that there appears to be only quasielastic scattering with no spinwave scattering. However, a recently performed triple axis neutron scattering experiment [64] has confirmed that there are spinwave excitations at these temperatures. The triple axis data shows that the spinwaves soften as the temperature approaches T_C and additionally that an anomalous quasielastic component develops above ~ 6K. The IN6 data shown in figure 4.16 is dominated by this quasielastic central peak component above 6K.

In the following chapter we show data for isostructural CePtSb which is ferromagnetic at ~ 4.5K. The measurements show that in contrast to CePdSb spinwave excitations can be seen right up to T_C.

4.5.2 Analysis of intersite interactions

The quasielastic scattering for $T \geq T_c$ can be analysed to give information on the strength of intersite interactions, however it is difficult to calculate an analytical form for the response function in an exchange coupled paramagnet. Two approaches can be used: the method of moments or the random phase approximation (RPA) approach.

The method of moments due to de Gennes [65] is appropriate for a localised magnetic system with Heisenberg-like exchange. It describes the form of the response function in terms of ratios of its moments, in the limit of infinite temperature. The moments of the scattering response function are defined as [7],

$$M_n = \int_{-\infty}^{\infty} \omega^n F(\omega) d\omega \quad , \tag{4.7}$$

where $F(\omega)$ is the response function. The method of moments uses a ratio of two moments, M_2 and M_4. The ratio used is $M_4/(M_2)^2$, which will have different values depending on the form of function $F(\omega)$. Calculations indicate that the ratio will be close to one if $F(\omega)$ is Lorentzian-like and equal to three if $F(\omega)$ is Gaussian-like [7, 65].

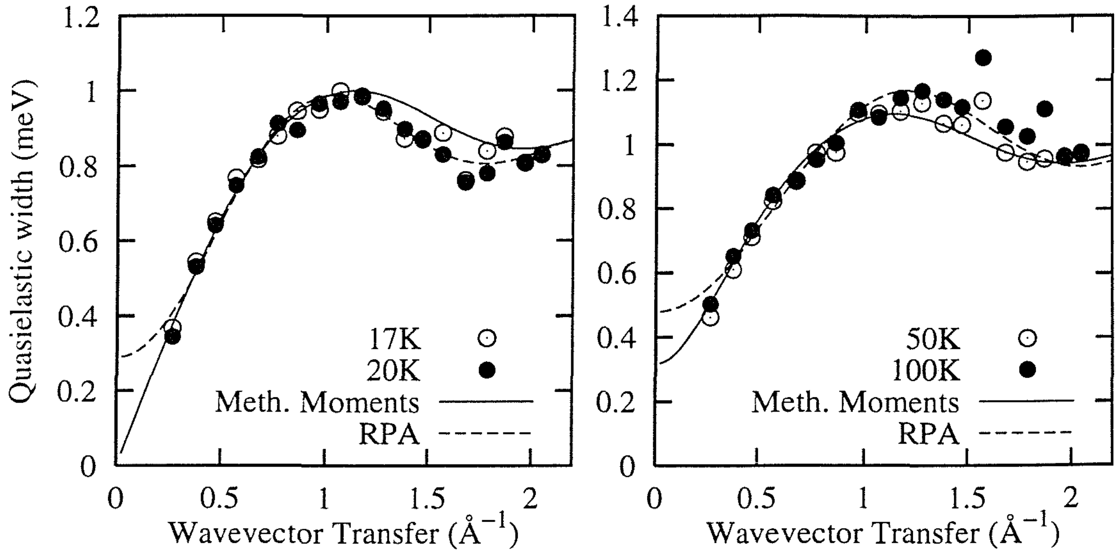

Figure 4.17: Quasielastic linewidth in CePdSb.

Following ref. [65] the second moment of the scattering in the limit of infinite temperature is ,

$$M_2 = \frac{2}{3}J(J+1)\sum_i \nu_i \left(\frac{\mathcal{J}_i}{\hbar}\right)^2 \left(1 - \frac{sin(Qr_i)}{Qr_i}\right) , \tag{4.8}$$

where the ν_i is the number of neighbours at distance r_i with exchange interaction $\mathcal{J}_i$. The fourth moment, M_4, can also be calculated and has a much more complex form [65]

In ref. [65] a general prediction suggests that the response function should be Lorentzian like at small wavevector transfer and Gaussian like at large wavevector transfer. The parameter which determines where this cross over should take place is the product of the wavevector, Q, and the lattice parameter, for which we use the nearest neighbour distance, r_i. For $Qr_i \leq 4$ we expect Lorentzian lineshapes and for $Qr_i \geq 4$ we expect Gaussian lineshapes. For $r_1 = 3.945$Å the cut off is $Q \approx 1$Å. In this case our lineshape appears to be always Lorentzian, though we only consider the data up to $Q \approx 1$Å for fitting purposes.

The Lorentzian function actually has infinite moments, so it must be used in a cut off form. We use an approximation by taking the squared width of the fitted

Lorentzian to be the second moment of the scattering. Using equation (4.8) the form of the width which has been used to fit the data is

$$\Gamma(Q) = \left(\frac{2}{3}J(J+1)\nu_1\mathcal{J}_1^2\left(\frac{1-\sin(Qr_1)}{Qr_1}\right)+d\right)^{\frac{1}{2}}, \tag{4.9}$$

where $\Gamma(Q)$ is the width of the fitted Lorentzian. Only the nearest neighbour interaction has been used and d is a constant to account for single ion anisotropy. The fits to equation (4.9) are shown in figure 4.17.

At 100K and 50K the data are not significantly different so both sets were fitted with a common set of parameters. The same approach was used to fit the 20K and 17K data. The fitting procedure indicated that it was sufficient to consider only the nearest neighbour interactions at all temperatures. At 100K and 50K it was necessary to use a non-zero value for d in equation (4.9) which gives a non-zero intercept of the linewidth at $Q = 0$. At 100K and 50K the exchange constant for the nearest neighbours was $\sim$ 0.26meV and the fits are reasonably good. The spinwave energy dispersion relation given is section 1.12.1 of chapter 1 was

$$\hbar\omega = J\left[\mathcal{J}(0) - \mathcal{J}(Q)\right]. \tag{4.10}$$

For nearest neighbours only, in a hexagonal lattice, $\mathcal{J}(0)$ and $\mathcal{J}(Q)$ are $2\mathcal{J}_1$ and $2\mathcal{J}_1\cos(Qr_1)$ respectively. At small Q, using the approximation for the cosine we find that the dispersion relation is

$$\hbar\omega = J\mathcal{J}_1 r_1^2 Q^2, \tag{4.11}$$

where $J\mathcal{J}_1 r_1^2 = D$ is the spinwave stiffness. If $J = \frac{5}{2}$, $\mathcal{J}_1 = 0.26$meV and $r_1 = 3.945$Å then $D \approx 10$meVÅ^2, which is the line shown in figure 4.16 indicating the fits to the quasielastic linewidth are consistent with the spinwaves.

The alternative approach is to use the RPA theory which correctly gives the Lorentzian lineshape (refer to section 1.9 of chapter 1). The RPA fits give a non-zero linewidth at $Q = 0$ and it was necessary to include second nearest neighbour exchange to improve the fits.

Since it is not clear whether the method of moments or the RPA approach is the correct way to treat this data table 4.4 outlines a comparison of the two methods. It shows that neither gives full agreement with the results. Our measured linewidth shows Q dependence and the lineshape is Lorentzian out to large Q, all in agreement with the RPA approach. The similarity of the 100K and 50K linewidths suggests

Feature	Results	Predictions	
		Method of moments	RPA
Lineshape.	Lineshape is always Lorentzian.	Lorentzian at small Q only. Gaussian at large Q.	Always Lorentzian.
Width	The width is Q dependent. At 100K and 50K the linewidth is not very different implying T independence.	Q dependent but T independent (valid at T = ∞).	Q dependent and T dependent.

Table 4.4: Comparison of two approaches for examining the quasielastic neutron scattering data.

that there is little temperature dependence which is in agreement with the method of moments predictions in the infinite temperature limit.

A proper treatment of the spin dynamics in the paramagnetic phase of CePdSb would have to take account of the XY nature of the magnetism. We are not aware of any theoretical predictions for the form of the scattering law for a three dimensional XY model.

4.6 μSR

Two series of experiments were carried out on the longitudinal geometry EMU spectrometer at ISIS. For both experiments the sample was in the form of a crushed polycrystalline button mounted on a flat aluminium plate. The edges of the aluminium plate were masked with silver. The data were corrected for detector deadtimes using a standard ISIS program.

In the first experiment Muon Spin Relaxation measurements both in zero field and with applied longitudinal fields (LF) were made using a closed cycle refrigerator (CCR) temperature environment. The CCR gives a minimum temperature of ~10K. In addition to the LF measurements we were able to apply a transverse field (TF) of 100G using the small transverse field coils and TF measurements were made using the longitudinal geometry.

In the second experiment the zero field and LF measurements were made using a helium flow cryostat environment which gave a minimum temperature of ~2K.

4.6.1 Longitudinal field measurements

In CePdSb the antimony nuclei have a non zero spin which contribute to the muon depolarisation. To eliminate the effects of this a longitudinal field was applied (see section 3.4.1). At 50K the polarisation had an exponential decay and the application of a 50G LF field reduced the damping rate but 100G had no additional effect. We attribute this reduction to the decoupling of the Sb nuclei. All the measurement were made with either a 50 or 100G LF field applied.

From 50K to 11.5K the longitudinal field spectra were fitted to,

$$G_z(t) = a_0 \exp(-\lambda t) + b\,, \tag{4.12}$$

with a_0 the initial asymmetry, λ the damping rate and b a flat background to account for muons which stopped in the silver mask.

The background, b, was determined from the fit to the lowest temperature data and was then held constant.

For temperatures between 50K and 11.5K the depolarisation was well represented by equation (4.12), but at 10K it was qualitatively different. At this temperature there is a two component depolarisation and there is drop in the initial asymmetry. Figure 4.18 shows the data for 50K and 10K. It is clear that there is a big difference.

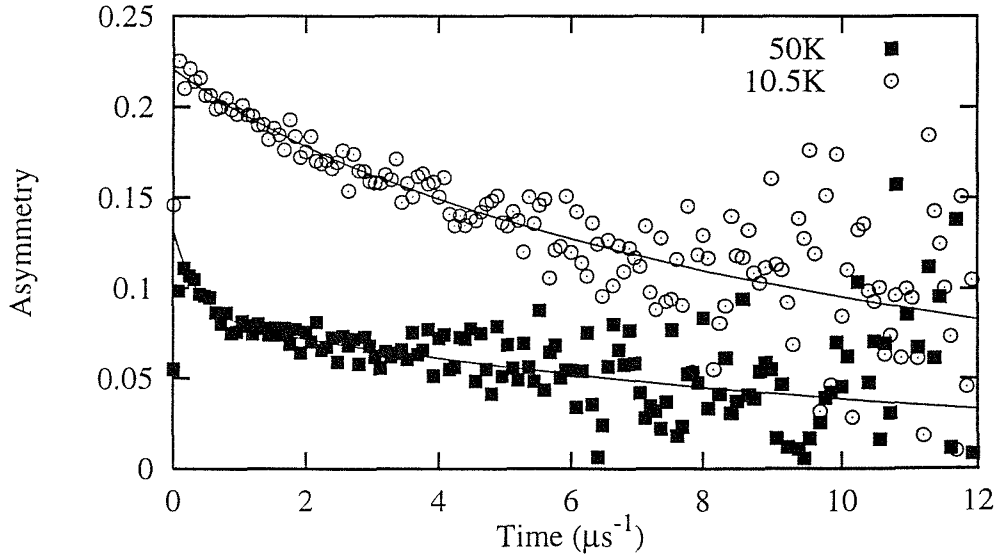

Figure 4.18: Depolarisation at 10.5K and 50K, in 50G LF. The lines are fits to a simple exponential for 50K and the sum of two exponentials at 10.5K.

Figure 4.19 shows the damping rate parameter, λ, as a function of temperature. Since these measurements were made using a CCR the data does not extend below 10K. The damping rate shows a weak peak at 15.5K followed by a drop. The data at 10K was fitted to the sum of two exponentials and the point on figure 4.19, for 10K, is for the component with the smallest damping rate. The initial asymmetry begins to drop near 19K, shown in figure 4.20, as the damping rate begins to increase.

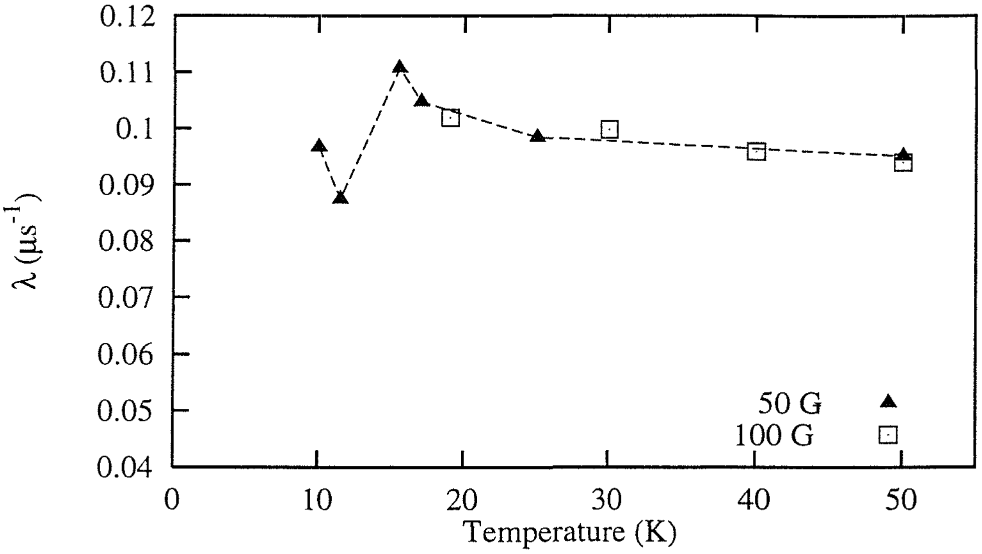

Figure 4.19: Damping rate as a function of temperature, for two different longitudinal fields.

In these measurements the onset of slower dynamic behaviour is seen, roughly at T_C but there is no *strong* enhancement of the depolarisation at T_C as we might expect at a ferromagnetic phase transition. We also note that at 10K there is a two component damping. Two component behaviour in μSR data is sometimes explained in terms of two muon sites where the local fields are different. The muon site is not known in this case, but we might expect two components if magnetic fluctuations in CePdSb were different in different directions, in particular it is possible that the fluctuations along the *c*-axis have a different character to those in the basal plane.

Measurements in different strength longitudinal fields

The application of longitudinal fields of increasing strength at 10K removed the second rapidly decaying component. Figure 4.21 shows the measured depolarisation, at 10K, with increasing applied field. A 300G field is sufficient to suppress the rapidly

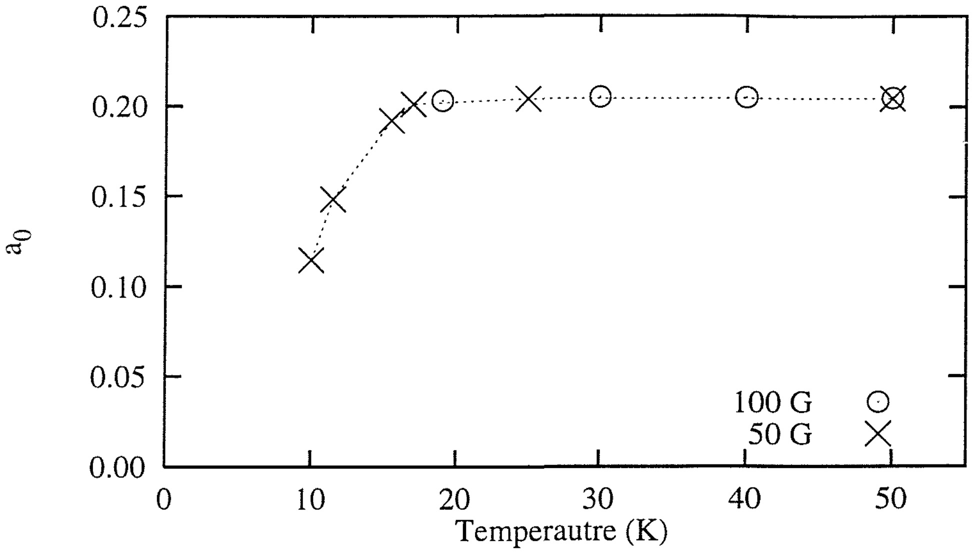

Figure 4.20: Total initial asymmetry, sum of all the fitted components. The initial asymmetry begins to drop below T_C.

damped component and to recover some of the initial asymmetry. With 4KG the initial asymmetry is recovered to the 50K level but a significant relaxation still exists.

From this data appears that there are two types of relaxation. There is clearly a rapidly damped component, responsible for the loss of initial asymmetry, that is suppressed by the application of the field. There is also a slower relaxation which is not affected by the field. Fitting an exponential decay to the 300–4KG field data shows that the relaxation rate is not affected by the field, but the initial asymmetry is recovered. This relaxation must result from highly dynamic processes since it is not suppressed by an applied field up to 4KG.

4.6.2 Transverse field measurements

In the first experiment transverse field measurements were made. The experimental conditions were identical to those for the LF measurements. Measurements were made between 100K and 10K with one additional point at 250K.

The applied transverse field causes all the muons to precess and the result is an oscillating signal, as described in section 3.2. Figure 4.22 shows a summary of the data. The oscillating signal was described by

$$G_x(t) = a_0 \cos\left(2\pi f' t + \phi\right) e^{-\lambda t} , \tag{4.13}$$

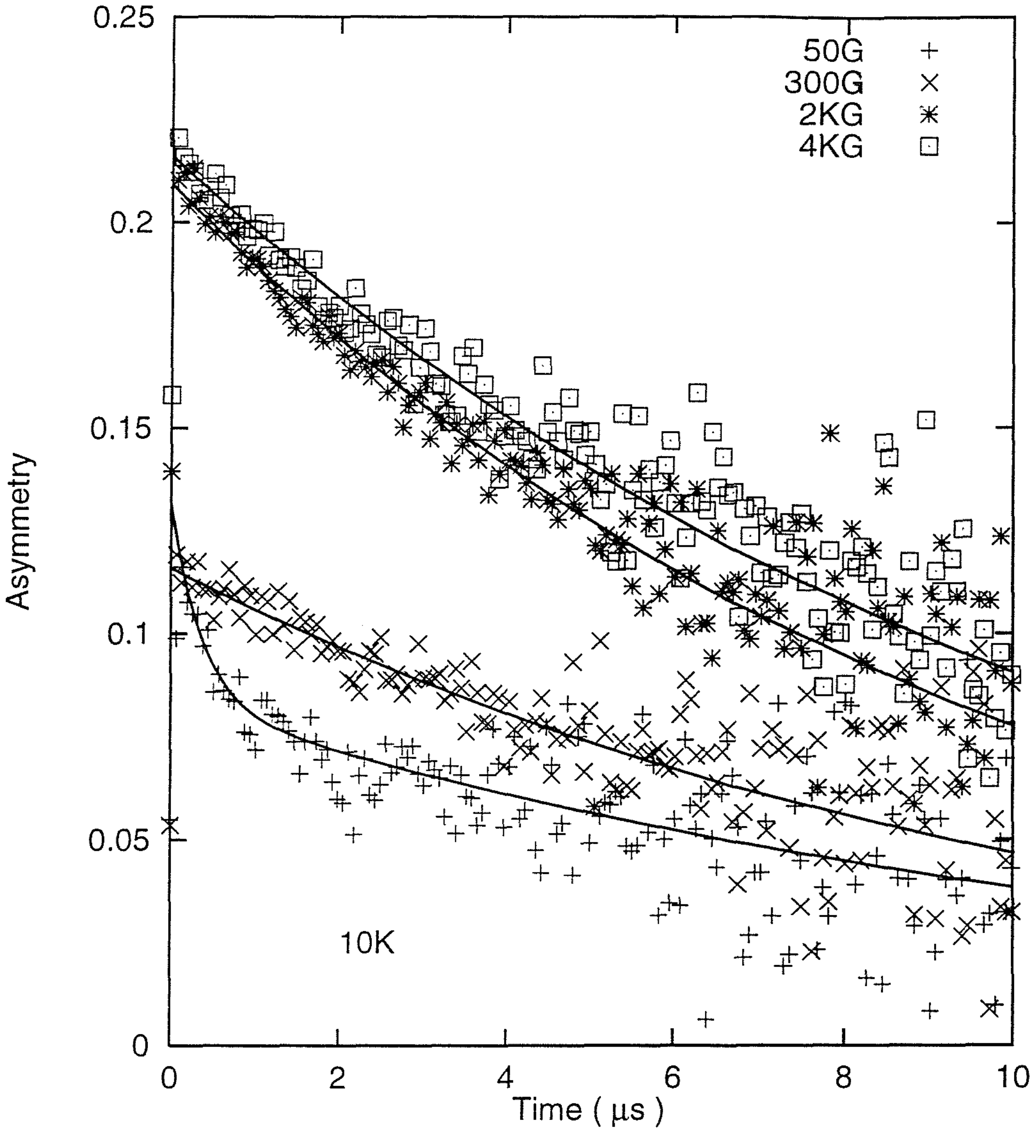

Figure 4.21: Depolarisation at 10K with increasing applied field.

where a_0 is the initial asymmetry, f' is the precession frequency, ϕ is the initial phase of the oscillation and λ describes the damping rate of an envelope function which is taken to be an exponential in this case. Fits of equation (4.13) are shown as solid lines in figure 4.22. We can determine the transverse field strength from a given oscillation frequency using equation (3.2). At 250K the frequency was 1.374MHz so that the field is 101.4G – in good agreement with the strength of the external applied field.

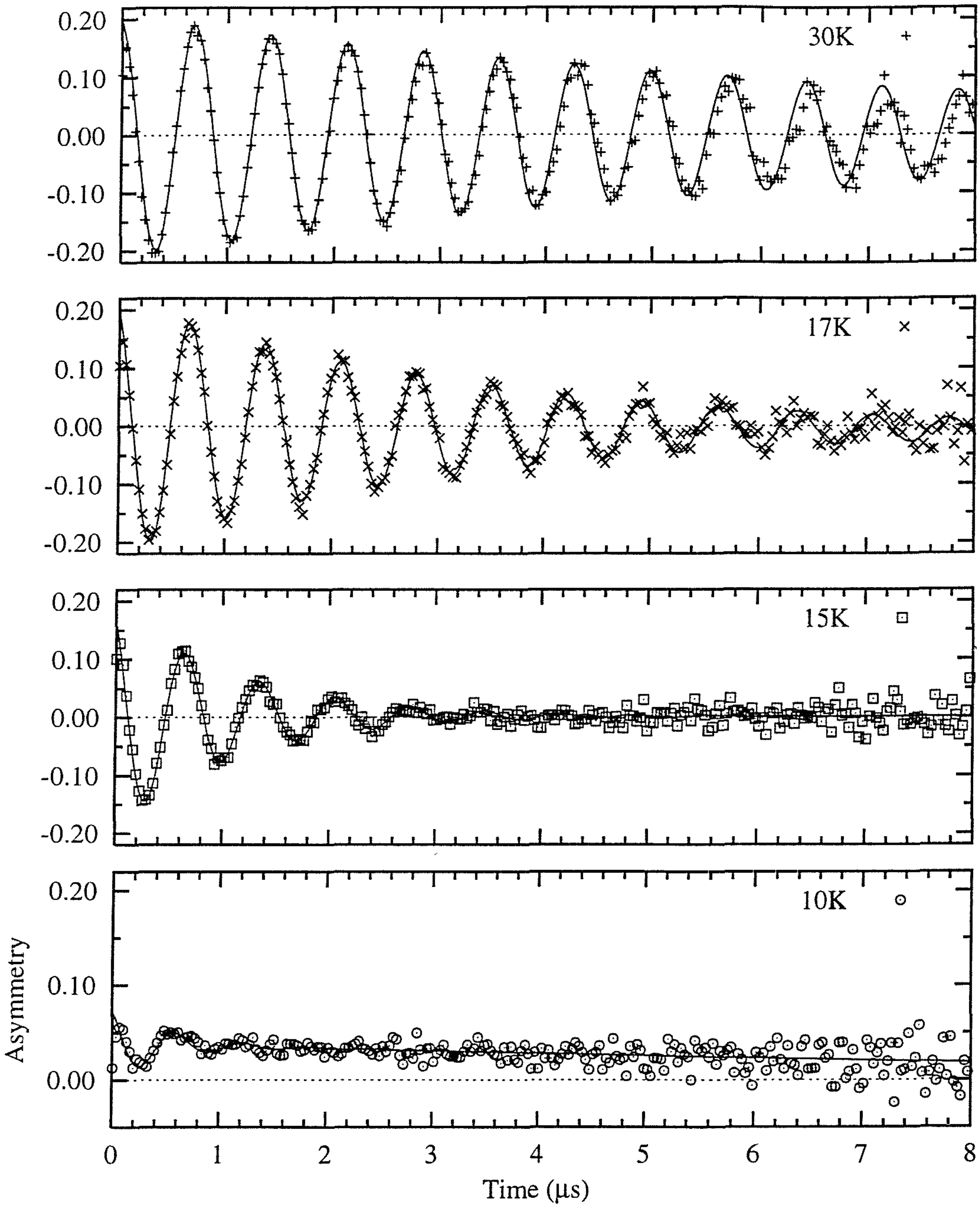

Figure 4.22: Transverse field data at several temperatures. Solid lines are fits to equation (4.13).

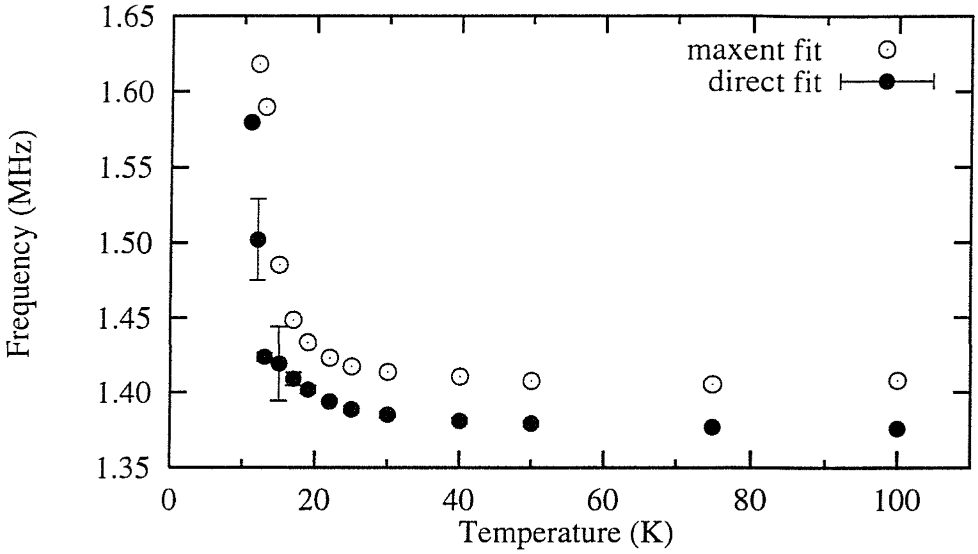

Figure 4.23: Oscillation frequencies from direct fitting and using maximum entropy. The maximum entropy value is the centroid of the frequency spectrum.

Equation (4.13) gives a reasonable description of the data for temperatures down to 17K. For temperatures below 17K the signal starts to oscillate about a non-zero value and to fit these data it was necessary to add an additional component to equation (4.13). The data below 17K were fitted to

$$G_x(t) = a_1 \cos\left(2\pi f' t + \phi\right) e^{-\lambda_1 t} + a_2 e^{-\lambda_2 t}, \tag{4.14}$$

where a_2 and λ_2 are the asymmetry and damping rate of the additional exponential component. This component arises from muons in crystallites where the internal field of increasing strength is not in a transverse direction. The polarisation of these muons decays as for a longitudinal field measurement. The damping rate of this component could be held constant at $0.1\mu s^{-1}$ and the asymmetry associated with it increased as the temperature decreased.

The frequency of the oscillation determined by fitting equations (4.13) – (4.14) showed only a very small increase between 100K and 30K and then rose more rapidly down to 10K, as shown in figure 4.23. This figure also shows the frequency derived from maximum entropy data processing, which is discussed in the next section. The data in this figure indicate that the muons do not experience a critical slowing down of the magnetic moments on the Ce ions at T_C.

The Knight shift of the frequency away from the high temperature value is equivalent to ~16.6G at 10K.

The damping rate, λ, showed the same properties as the frequency: increasing slowly from 100K down to 30K and then more rapidly as the temperature was lowered towards 10K. Magnetic transitions in other materials tend to show a sharp increase in the damping rate at the transition temperature but that is not the case here. The transition temperature is not apparent from either the muon Larmor frequency or the damping rate but there is an indication of some change from the extra component which appears below 17K.

As mentioned previously the damping rate of the new component is not temperature dependent but its asymmetry is. At 10K the asymmetry is roughly 17% of the full high temperature initial asymmetry. This part of the signal may be due to muons precessing around local internal fields, not aligned with the applied field.

Maximum entropy analysis

Maximum entropy analysis of the transverse field data reveals the frequency distribution or equivalently the field distribution in the sample. The centroid of the distribution was found according to

$$\text{centroid} = \sum_{\text{channels}} \frac{(\text{channel} - 1) \times \text{weight}}{\sum \text{weight}}, \tag{4.15}$$

where only channels which have a weight above the default are considered. At 250K the centroid of the frequency distribution was found to be at a frequency corresponding to an applied field of 103.3G which is consistent with the 100G applied field and the value found from directly fitting the data. Note that the two methods of obtaining the frequency give values which differ by a few tenths of a MHz. In figure 4.23 this looks quite significant but the difference only translates to a few gauss in field strength. The larger value from the maximum entropy analysis is probably due to the tail of the frequency distribution.

At 250K the maximum entropy distribution is not symmetrical and this remains the case down to 17K. The distribution is quite sharp on the low frequency side but with an extended tail on the high frequency side. This may be due to an intrinsic feature of the applied field. For this experiment the TF20 coils on EMU were used; these do not have a high degree of homogeneity. As the temperature is lowered the centroid of the distribution shifts upward as shown in figure 4.23. Below T_C where the oscillation starts to be heavily damped, the maximum entropy distributions start to have extra weight at low frequencies. The main line shifts

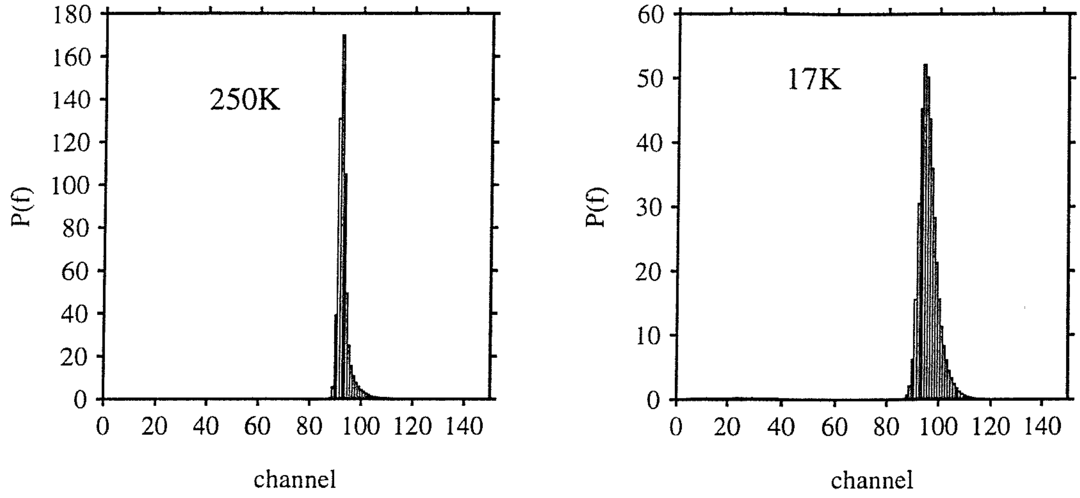

(a) Distribution at 250K.

(b) Distribution at 17K.

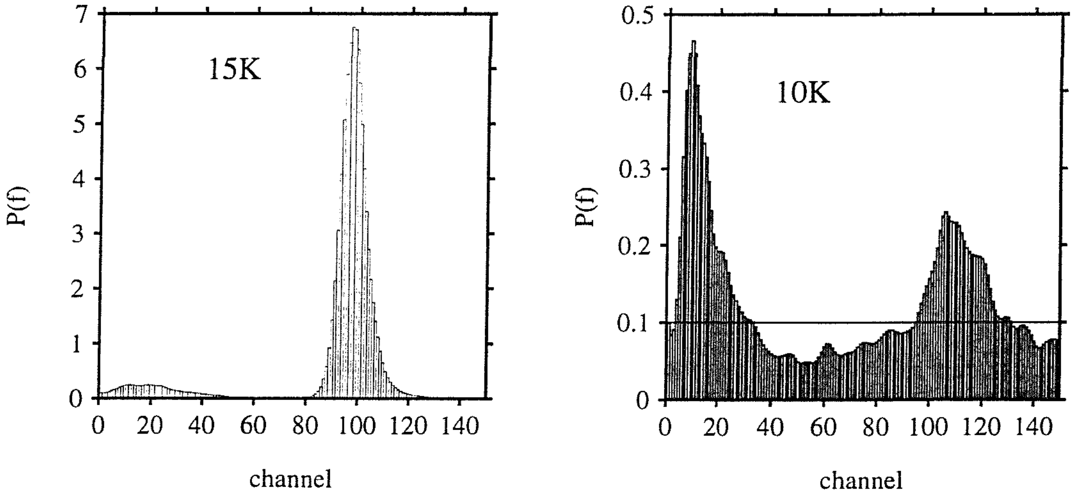

(c) Distribution at 15K.

(d) Distribution at 10K. The line shows the default level.

Figure 4.24: Maximum entropy spectra for different temperatures. P(f) is the weight for each frequency channel. Fig. 4.24(d) shows the default level used in accordance with equation (3.14). Note that the vertical scale changes dramatically over the four figures.

to higher frequencies at lower temperatures corresponding to an increasing internal field. At 10K the oscillation is barely recognizable so the maximum entropy routine produces a distribution with weight close to zero frequency to try to reproduce the d-c component.

4.6.3 Second μSR experiment

The second μSR experiment was also conducted on EMU, but with a helium flow cryostat so that measurements could be extended down to lower temperatures. A complete set of zero field measurements were obtained and some additional LF measurements were made.

Longitudinal field measurements

Measurements made with a 50G longitudinal field at 30K and between 11.5K and 4.5K confirmed the previous results. At 11.5K the depolarisation could be fitted by the sum of two exponential decays. One decay component was much more rapid than the other. The faster component had a damping rate $\lambda \approx 2.5\mu s^{-1}$ compared to $\lambda \approx 0.1\mu s^{-1}$ for the slower component. At lower temperatures the asymmetry associated with the rapid component decreased until it was only possible to distinguish a single component. The smallest damping rate was observed at 4.5K. At this temperature the dynamics of the Ce moments should be increasingly frozen by the ferromagnetic molecular field, although at this temperature there is considerably less initial asymmetry than at 30K. Increasing the strength of the applied field recovered the initial asymmetry. At 30K even in 4KG field a significant amount of damping remains, and the same is true at 14.5K.

Zero field measurements

The zero field data between 30K and 4.5K were fitted to a stretched exponential of the form,

$$G(t) = a_0 e^{(-\lambda t)^{\beta}} + b\,, \tag{4.16}$$

where a_0 is the initial asymmetry, λ is the damping rate and β is a temperature dependent exponent and b is the fixed flat background. There is no specific reason *a priori* for using this form other than that it gives a reasonable description of the

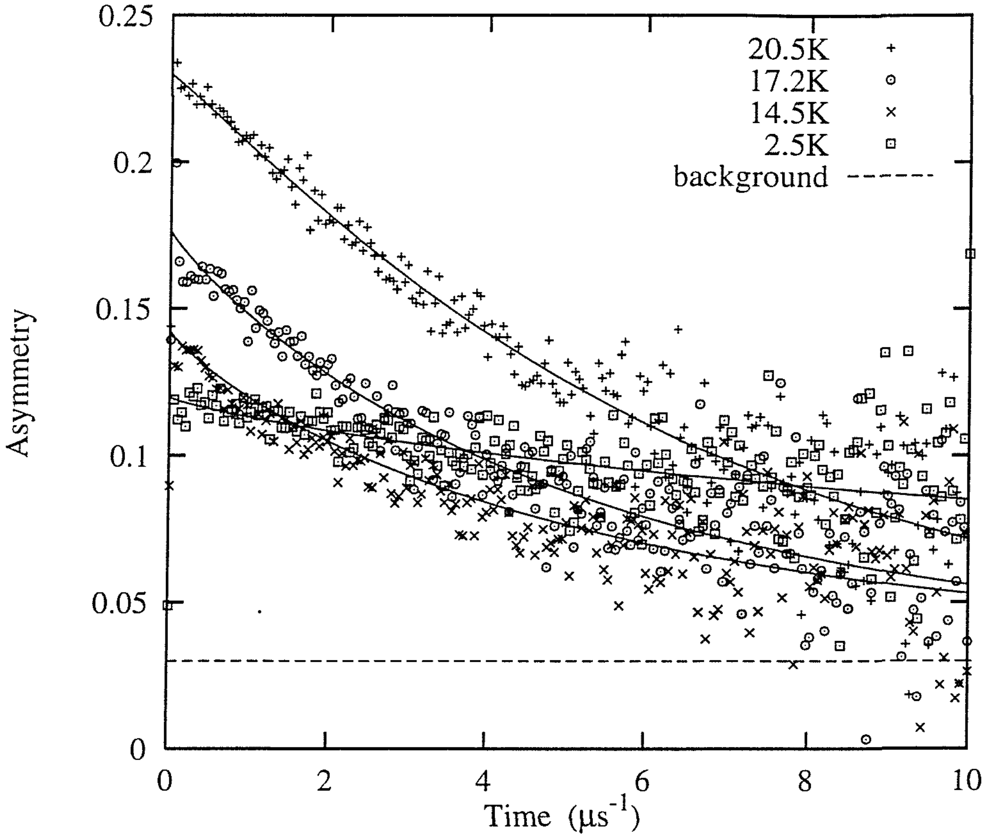

Figure 4.25: Zero field μSR data for CePdSb at three different temperatures. The lines are fits using equation (4.16).

data and therefore a means to parameterise it. Some data is shown in figure 4.25 where the lines indicate fits using equation (4.16). Attempts to use a two component Lorentzian decay, as for the longitudinal field data below 10K, did not give as good fits as the stretched exponential.

T_C is quite apparent in the zero field data. The initial asymmetry drops rapidly at T_C and the damping rate shows a step. The exponent β shows that the depolarisation is an exponential from 30K to T_C but below T_C the depolarisation changes form. The values for the fitted parameters are shown in figure 4.26.

We would expect to be able to see a sharp increase in the value of the parameter λ on the approach to T_C. This would indicate rapid fluctuations in the internal fields acting on the muons at the ferromagnetic critical point. This is not the case but the transition is clearly seen from the rapid drop of the initial asymmetry. This loss of asymmetry is a typical feature of magnetic phase transitions.

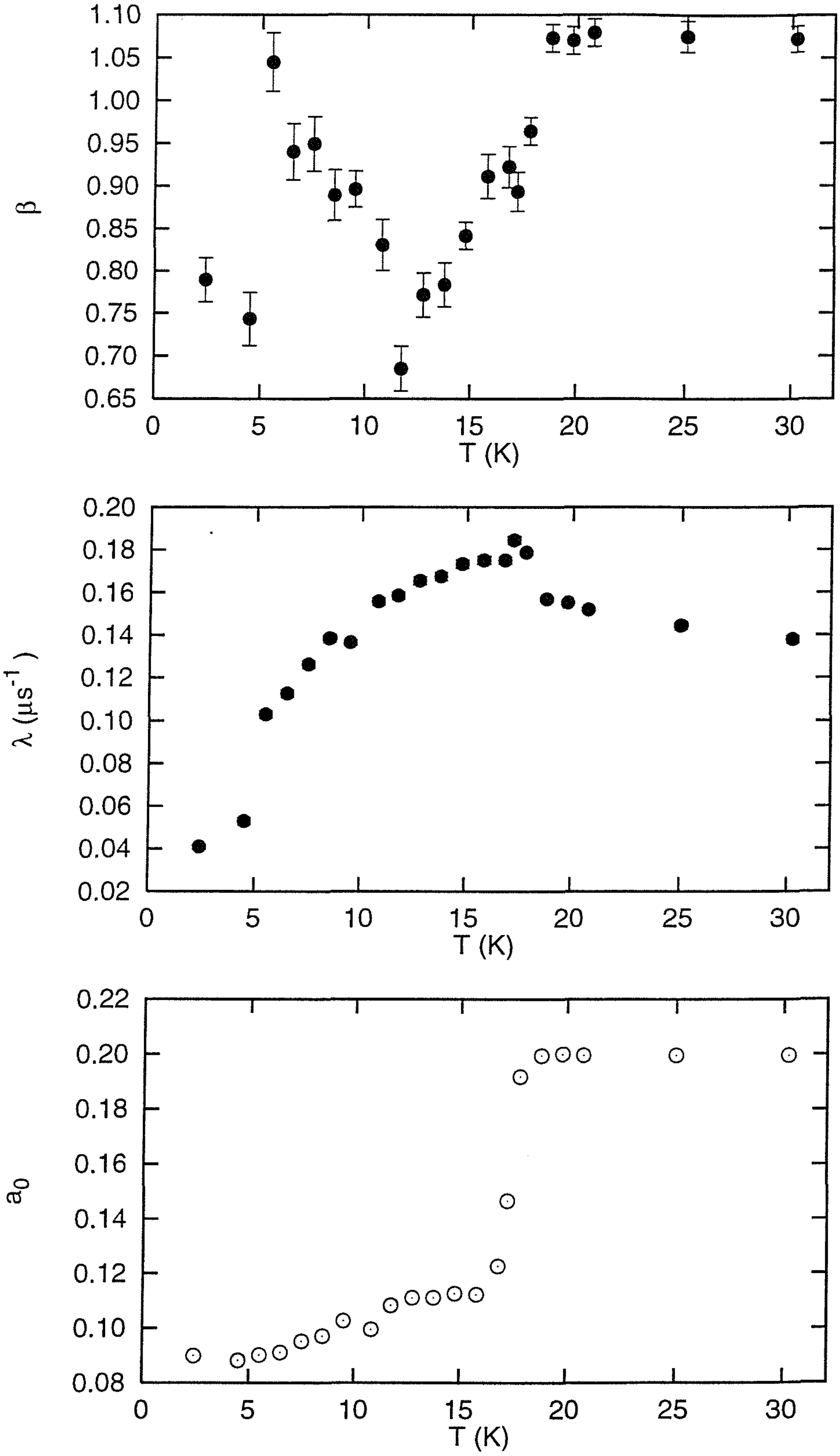

Figure 4.26: Parameters for stretched exponential fitted to zero field data.

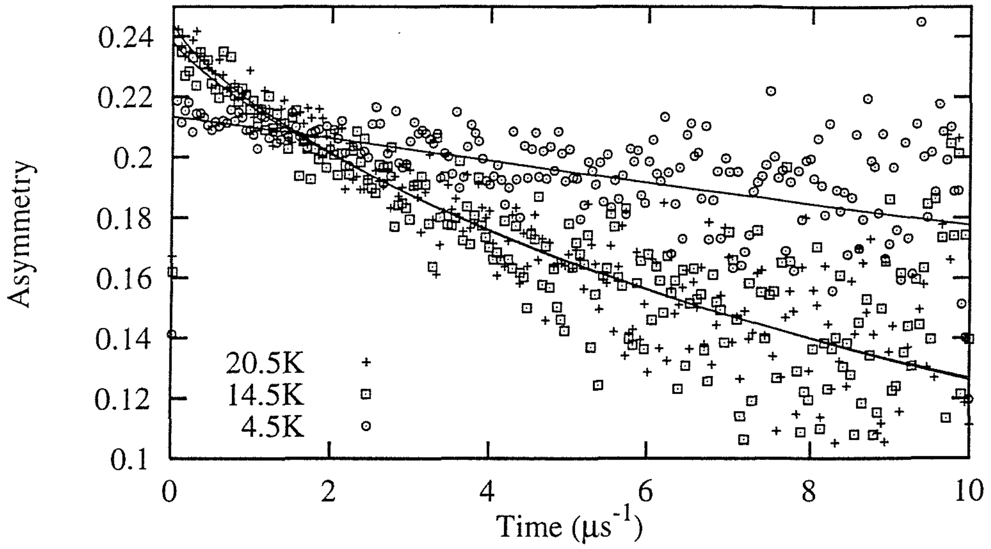

Figure 4.27: μSR data for CePdSb in a 2KG longitudinal field. There is only a weak loss of asymmetry below T$_C$.

The background parameter, b, was held fixed at 0.03 for all of the fits. If we take this background into account it would appear that roughly two thirds of the true initial asymmetry are rapidly lost below T$_C$.

The temperature dependence of the parameter β is unusual. The data was also fitted using a simple exponential function. This requires only two parameters, a damping rate and the intial asymmetry. The temperature variation of these two parameters was very similar to the corresponding parameters for the stretched exponential. The stretched exponential fits were marginally better, according to the least squares minimisation test (χ^2). It is not clear what the variation of the parameter β indicates, it may be an artefact.

Data for strong longitudinal field

In the second experiment a sequence of measurements were made with a 2KG applied longitudinal field. The data was treated in the same way as the zero field measurements and the stretched exponential form was used to parameterise the data. Figure 4.27 shows some example data. There is only a very slight change in initial asymmetry below T$_C$ and hence these data lie very close together.

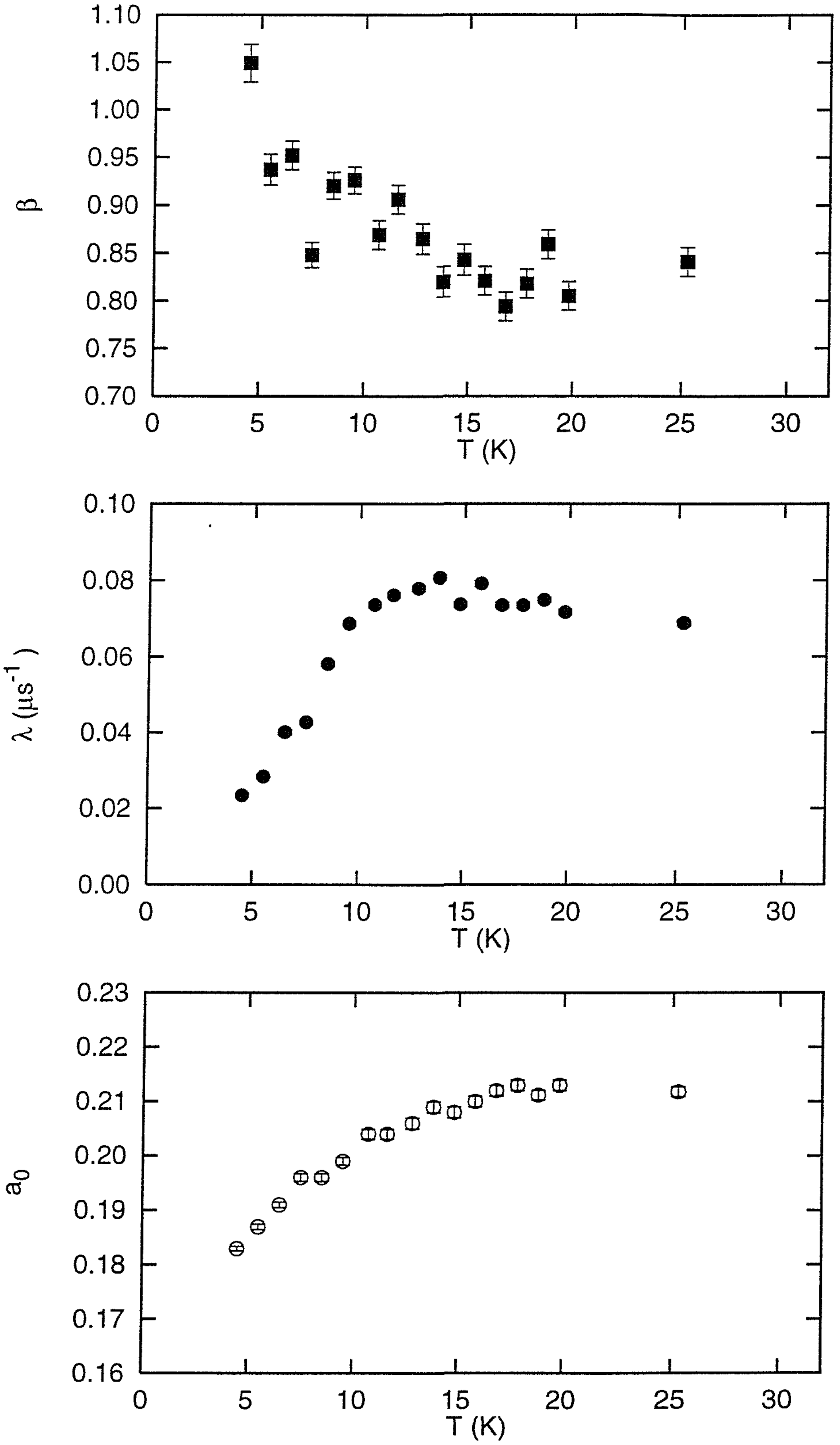

Figure 4.28: Fit parameters for stretched exponential fit to μSR data in an applied magnetic field.

Figure 4.28 shows the temperature variation of the three parameters, a_0, λ, β. The fitted damping rates are smaller than in zero field but the overall behaviour is similar to that observed in zero field. The initial asymmetry does not show a sharp drop at T_C with only a weak decrease at lower temperatures and the exponent β tends to one as the temperature is lowered from T_C.

Other measurements in an applied field show that anomalies at 10K move to higher temperatures under the influence of the field. Here the field smears out the details seen in zero field, but there is a steady drop in the damping rate below T_C. This indicates either more rapid magnetic fluctuations in the sample or an increase in the field width of the fluctuations.

4.7 Small Angle Scattering

A single crystal of CePdSb was used for a small angle neutron scattering (SANS) experiment using the D17 instrument at ILL, Grenoble. The crystal, approximately 1cm^3 in volume, was mounted in a helium flow cryostat with quartz windows. The crystal was mounted with the *c*-axis approximately vertical and a *b*-axis along the beam. This gave scattering vectors in the *a*-*c* plane. An incident wavelength of 12Å was used for most of the study and the scattering was measured on a 2-D multi-detector. The detector was normalised using a standard water run.

It is important to remember the effect of the orientation factor in the magnetic cross-section. Neutron scattering measures components of magnetic fluctuations and correlations perpendicular to the scattering vector. Referring back to equation (2.31) in chapter 2 we can write the sum in this equation as

$$\sum_{\alpha\beta}(\delta_{\alpha\beta} - \hat{Q}_\alpha \hat{Q}_\beta)S^{\alpha\beta}(Q,\omega) = (1 - Q_x^2)S^{xx} + (1 - Q_y^2)S^{yy} + (1 - Q_z^2)S^{zz}$$

so that when Q lies along one of the cartesian directions x, y or z the magnetic correlations and fluctuations in that direction do not scatter neutrons. In the following we analyse data for Q_z and Q_x directions. In each case the cross-section is

$$\frac{d\sigma}{d\Omega} \propto \begin{cases} S^{xx}(Q) + S^{yy}(Q) & \text{for } \; Q_z \\ S^{yy}(Q) + S^{zz}(Q) & \text{for } \; Q_x \end{cases} \tag{4.17}$$

where the $S(Q)$ is $S(Q,\omega)$ integrated over energy. The function $S(Q)$ only gives information on instantaneous static correlations. For example, correlations in the *a*-*b* plane of CePdSb would give a response for wavevectors with a component along Q_z.

Measurements were made between 1.6K and 30K with two points at 60K. The majority of the measurement were made warming the sample. A small electromagnet was used to apply fields up to 0.4T in the *b*-direction.

4.7.1 SANS response

An overview of the small angle scattering data is given in figure 4.29, in the form of contour plots. The contours are on an arbitrary vertical scale but the individual levels are the same in every plot. Above T_C the scattering is very slightly anisotropic, as we can see from the slight oval shape of the contours for 24K in figure 4.29. Below T_C a very anisotropic response builds up to a maximum at around 8K. Figure 4.29 shows that the form of this anisotropic response has an X-shape in the *a*-*c* plane. Below 8K the response changes again and the X-shape disappears. In figure 4.29 the plot at 1.6K shows the largest response to be along the *c*-direction, as we would expect if the fluctuations were confined to the *a*-*b* plane.

The total scattering summed over all the detector is shown in figure 4.30. The peak scattering is close to 8K with no sign of critical scattering actually at T_C. The position of this peak compares well with the heat capacity anomaly [58]. In an applied field the peak in the scattering moves upward in temperature as does the heat capacity peak [58]. The peak in the scattering coincides with the temperature showing the largest X-shape response. In the case where the magnetic field is applied the peak total scattering is reduced in size and it is the same on either side of the peak. In the the zero field case there is more scattering at low temperatures.

At 8K the crystal was rotated about the *c*-axis ~15° clockwise and anti-clockwise with no affect on the measured response. This suggests that the scattering is cylindrically symmetric about the *c*-axis. Also at 8K measurements were made with 8.5Å and 20Å neutrons, which gave different Q ranges, and there was no difference in the observed scattering.

The existence of the arms of this pattern suggest moment fluctuations are occurring with a small component out of the basal plane. However, the moments would appear to be locked into the basal plane because of the strong crystal field anisotropy so there must be another effect competing with the crystal field.

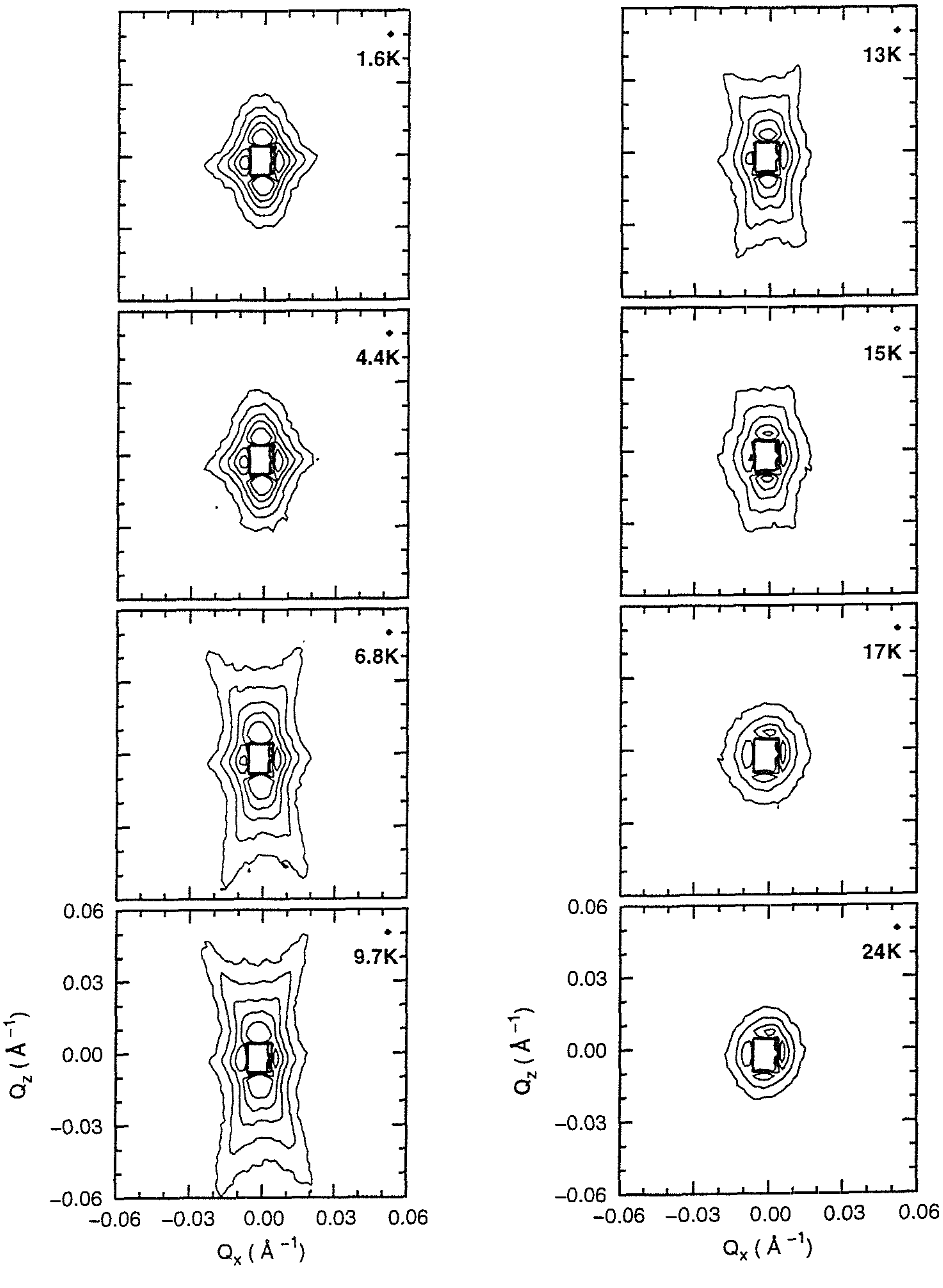

(a)

(b)

Figure 4.29: Contour plots of SANS data at different temperatures in zero applied field. The contours for each temperature are at the same levels and are plotted on an arbitrary scale.

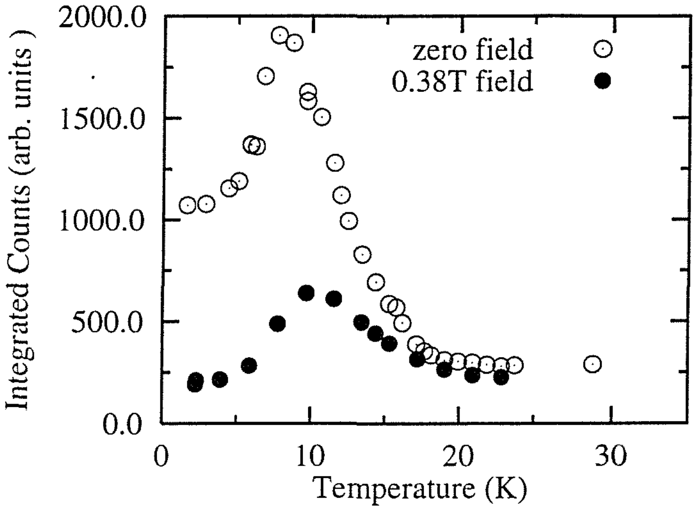

Figure 4.30: Total counts summed over the whole detector. Data for zero field and in a 0.38T field applied in the *a*-direction.

4.7.2 Correlation lengths

Correlation lengths can be measured from the variation of the small angle scattering with increasing wave-vector transfer. It is reasonable to assume that for any ferromagnet the correlation length will be very small in the paramagnetic phase and should increase as T$_C$ is approached from above. In the ordered phase the correlation length should be immeasurably large. Since the small angle scattering measured here is highly anisotropic it is clear that the correlations between magnetic moments in different directions is highly anisotropic also.

In order to try to analyse the response we have examined slices through the data. The data for six central rows and six central columns of detector pixels were averaged so that we have slices, through the centre of the detector, along the Q_x and Q_z directions respectively. The two dimensional slices, intensity *vs.* Q, can be visualised more readily than the three dimensional data.

Q_z direction, Q parallel to $c^\star$

Attempts to fit the data for slices in the Q_z direction showed that a Lorentzian was not a good description for a significant number of temperatures. It was found that the squared Lorentzian was more widely applicable. The squared Lorentzian takes the form

$$I(Q) = I_0 \frac{2\kappa^3}{\pi} \left(\frac{1}{(\kappa^2 + (Q - \Delta_Q)^2)} \right)^2 + b , \tag{4.18}$$

where $I(Q)$ is the measured intensity at wave-vector Q, I_0 is an area parameter, Δ_Q is a small offset from zero, b is a flat background and κ is the inverse correlation length of magnetic fluctuations.

Initial fitting showed that centre of the Q_z data, given by Δ_Q, shifted below T$_C$, by an amount corresponding to roughly one pixel on the detector. The background showed signs of a small peak at T$_C$ suggesting that there is a component of critical scattering underlying the data which appears as a flat background because it is associated with a small correlation length. The background parameter was held fixed in subsequent fits to remove this degree of freedom.

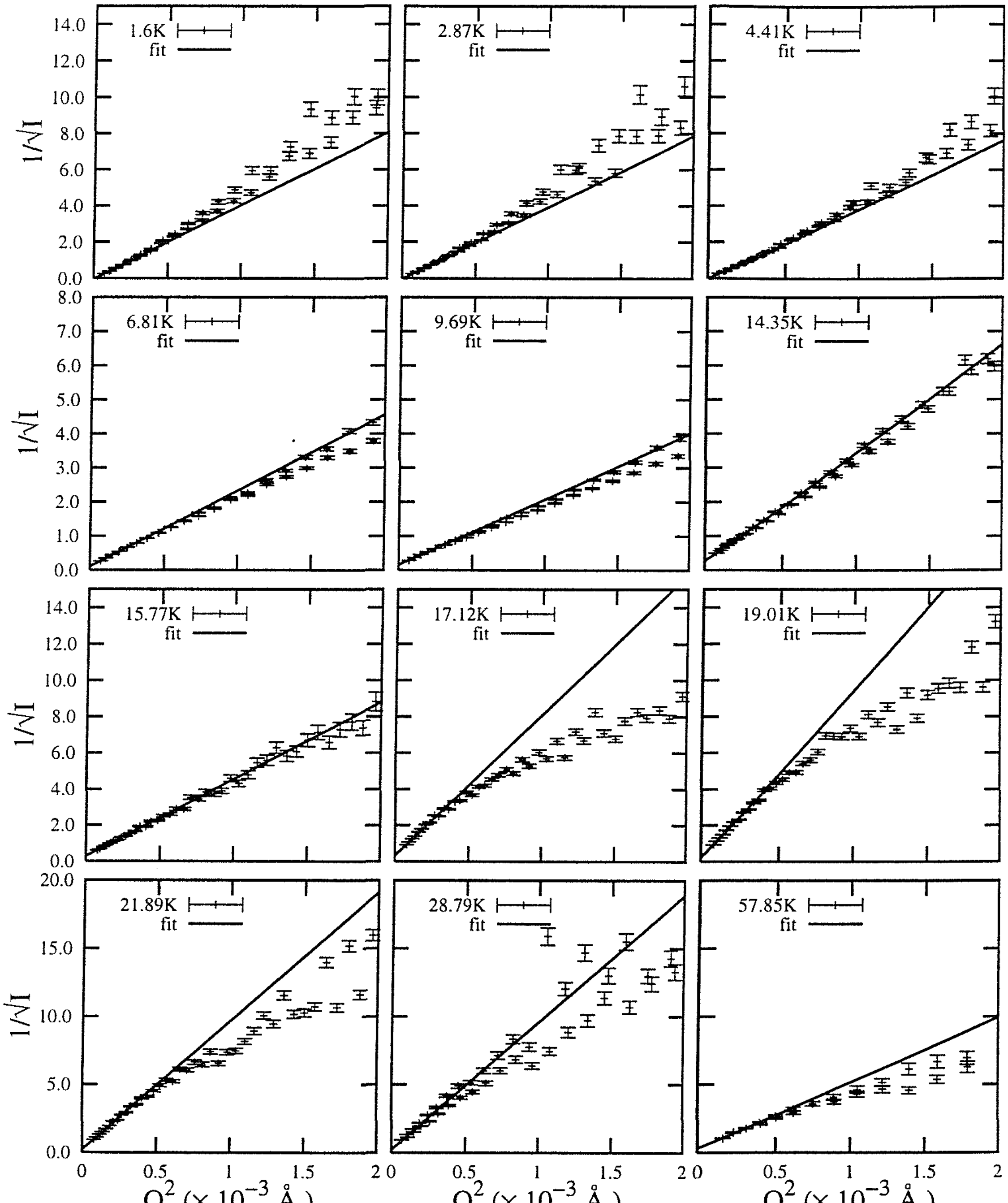

Figure 4.31: Squared Lorentzian behaviour of SANS in the Q_z direction data. Near T_C the behaviour is different.

The best method to use for fitting the squared Lorentzian function is to rearrange equation (4.18)

$$\frac{1}{\sqrt{I(Q)-b}} = \sqrt{\frac{\pi}{2\kappa^3 I_0}}(Q-\delta_Q)^2 + \kappa^2\sqrt{\frac{\pi}{2\kappa^3 I_0}}, \qquad (4.19)$$

and then plot the data as $\frac{1}{\sqrt{I(Q)-b}}$ *vs.* Q^2. The data will lie on a straight lines if the squared Lorentzian is the correct model. The square root of the ratio of the intercept and gradient of the straight line yields κ. Fitting straight lines in this way gives a more sensitive measure of the viability of the squared Lorentzian.

Figure 4.31 shows the data plotted as $\frac{1}{\sqrt{I(Q)-b}}$ *vs.* Q^2 and also shows fits using equation (4.19). For the data outside $|Q| = 0.022\text{Å}^{-1}$ the background level is a significant percentage of the scattering and the choice of the level adjusts the data on the plot considerably so this region was not included in the fit. Only the region for Q^2 between 0 and $0.5 \times 10^{-3}\text{Å}^{-2}$ has been fitted.

There appear to be three regimes in the data. Between 30K and ~ 23K the squared Lorentzian appears to be a good description, shown by the straight lines in figure 4.31. In the range 23–16K the data does not lie on straight lines so the squared Lorentzian is not the correct form in this range. Below 16K the data lies on straight lines indicating that the squared Lorentzian is a good fit, the data below 5K bends slightly above the straight line indicating a small departure from the squared Lorentzian again.

The data in the range 20–17K appears to be a function intermediate between a Lorentzian and a squared Lorentzian. However the limiting form in the small Q regime appears to be well described by a squared Lorentzian so we can examine the temperature dependence of the correlation length determined in this way over the whole temperature range.

The area of the squared Lorentzian function for the Q_z slices showed the same behaviour as the total scattering in figure 4.30. The inverse correlation length, κ, found by fitting is shown in figure 4.32. From figure 4.32 the correlation length appears to diverge in the *a*-*b* plane below ~ $5K$. This can be contrasted with what is found from the data in the x direction.

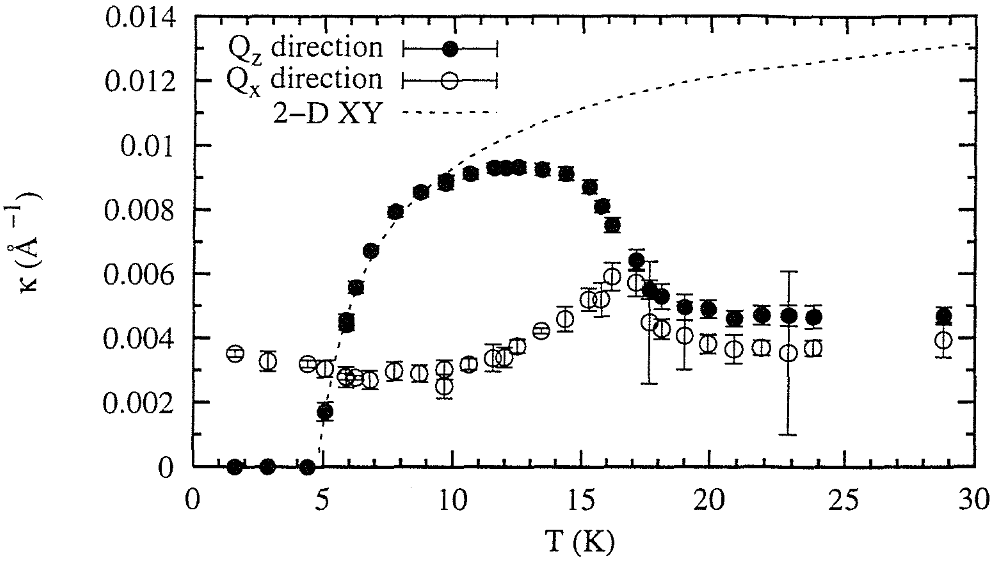

Figure 4.32: Inverse magnetic correlation length in CePdSb as a function of temperature. The inverse correlation length for Q_z goes to zero at roughly 5K which signifies a divergence of the correlation length in the *a*-*b* plane. The line is a fit to the expected behaviour of the 2D XY model, see text. Note that above 10K the fits are quite poor and therefore data above 10K is unreliable.

Q_x direction, Q parallel to $a^\star$

Data for slices through the measured response in the Q_x direction were analysed in the same manner as the Q_z data. The background was held fixed at an appropriate average value and straight line fits were applied to the data.

Figure 4.33 shows the data and fits. In the temperature region around $\mathrm{T_C}$ the squared Lorentzian form is not well suited to the data as figure 4.33 shows. However at 9.7K and lower temperatures the fits are much better showing that the squared Lorentzian is a good description.

The variation of the centre parameter was not significant and the area parameter showed a small increase below $\mathrm{T_C}$˙

Attempts to fit a simple Lorentzian over the whole temperature regime did not give good fits but the derived variation of κ with temperature was qualitatively the same as found by using the squared Lorentzian. The temperature dependence of κ for the Q_x data is shown in figure 4.32.

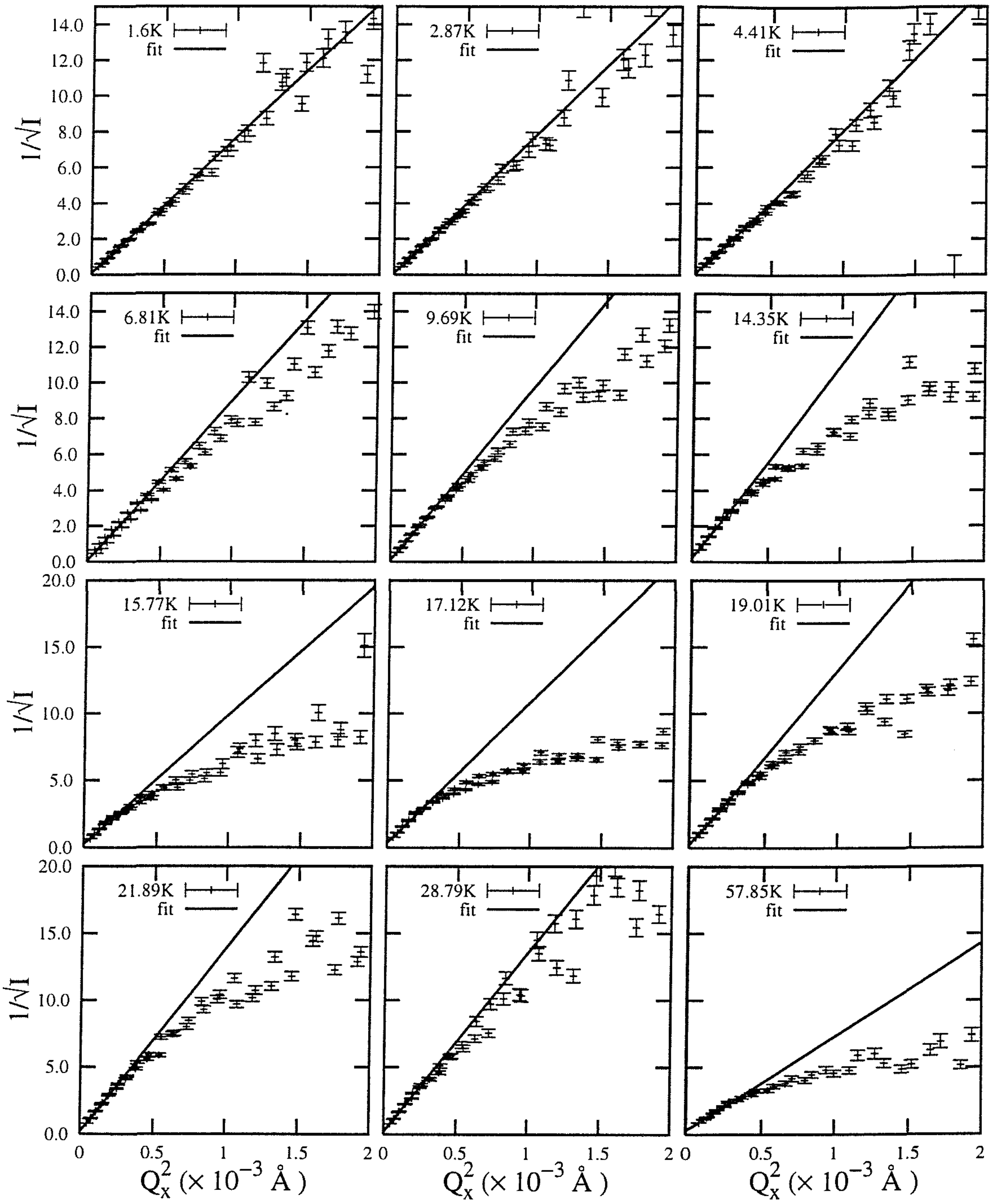

Figure 4.33: Squared Lorentzian behaviour of SANS in the Q_x direction data.

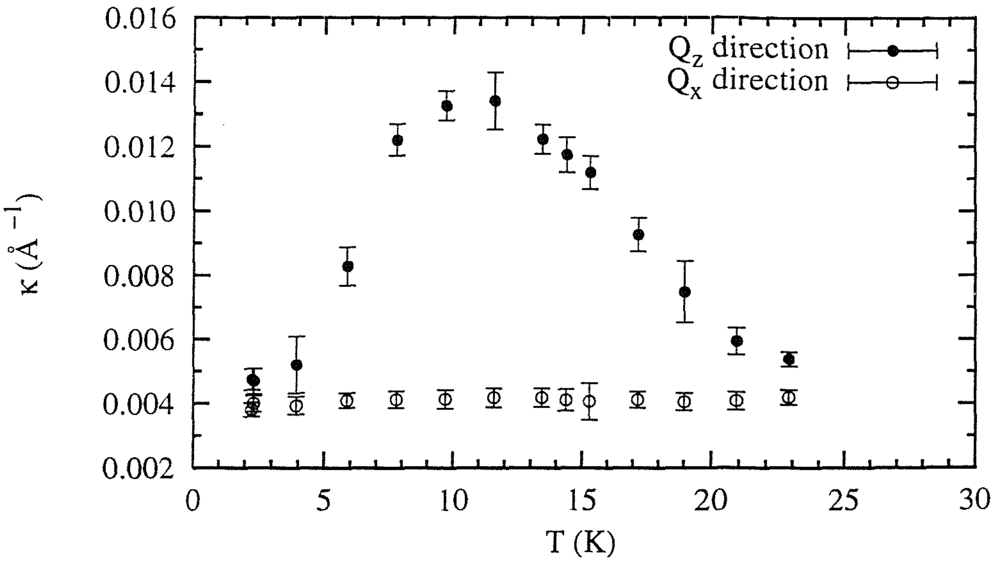

Figure 4.34: Inverse correlation length with a field applied along a-direction. The fits which produced this data were quite poor above 10K, hence that region of the figure is not reliable.

4.7.3 Magnetic Field Measurements

A field was applied in the a-direction and measurements were made at several temperatures and at different fields. We would expect that fluctuations in the direction of the field to be suppressed.

One effect of the field was to reduce the overall intensity of the scattering. Figure 4.30 shows the reduction in intensity compared to zero field. The peak scattering is shifted slightly upwards in temperature with the applied field. The heat capacity [58, 59] and the thermal expansion [60] peaks also shift upwards in an applied field. The strongest applied field was $\sim$ 0.38T and contour plots of the data taken in this field were the same as those of figure 4.29.

The data was analysed by taking Q_x and Q_z slices, the small Q limit of which was fitted to the squared Lorentzian formalism as described previously. The variation of the inverse correlation length in the two directions as a function of temperature is shown in figure 4.34.

With a field applied the scattering in the z direction revealed that the inverse correlation length in this direction showed similar behaviour to that in zero field. However, the maxima in figure 4.34 is at a higher temperature than in figure 4.32 and there is no clear indication of the inverse correlation length going to zero. The inverse correlation lengths are larger with the field applied implying a smaller correlation length than in zero field.

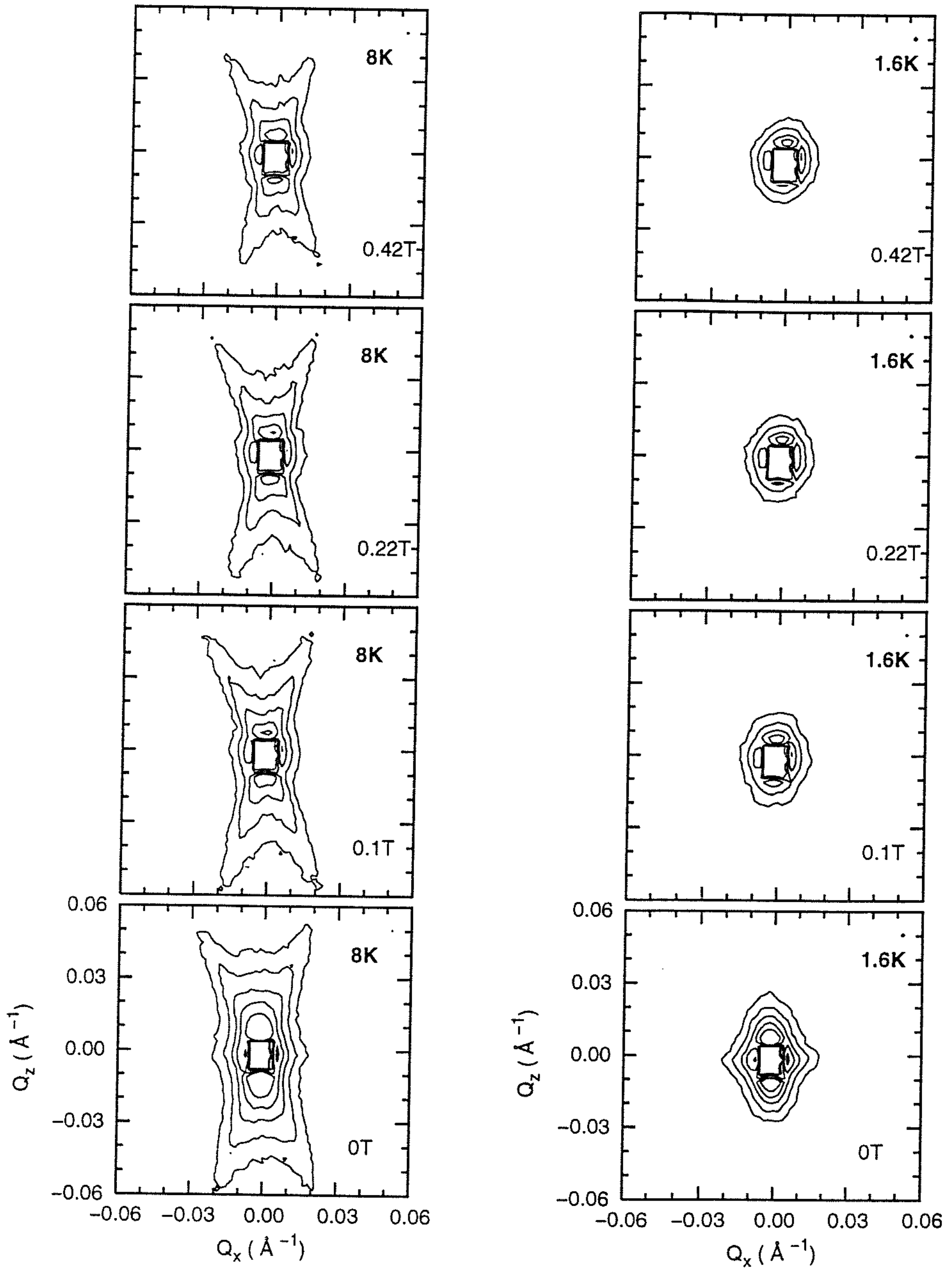

(a) SANS at 8K in different applied fields.

(b) SANS at 1.6K in different applied fields.

Figure 4.35: Contour plots of SANS data in different applied fields. The field reduces the total intensity. At 1.6K the field makes the scattering isotropic.

In the x direction the field suppressed any temperature dependence of κ. The inverse correlation length remained constant through T_C and down to the lowest measured temperature.

In zero field the maximum scattering is at 8K and at this temperature the applied field tends to reduce the total scattering. The X–shape pattern remains up to the largest field measured. Figure 4.35(a) shows contour plots of the scattering at 8K in different fields up to 0.42T.

Figure 4.35(b) shows the effect of an applied field of increasing strength at 1.6K. The pattern becomes more isotropic with increasing field. If we refer back to equation (4.17) it is possible to understand this effect. If S^{zz} were negligible and the applied field in the a-direction suppressed the fluctuations in this direction i.e. S^{xx} then only a response due to S^{yy} would remain and this would correspond to correlations which were always perpendicular to any scattering vector on the detector. Hence, an isotropic pattern. This scenario only holds for the temperatures below 4K the next available data set is at 6K and the applied field does not have such a dramatic effect at this or any higher temperature. If this analysis is correct it suggests that CePdSb is displaying two dimensional behaviour below $\sim$ 6K, whereas we would expect that at lower temperatures full three dimensional ordering should take place.

4.7.4 Discussion of SANS data

The SANS data is highly anisotropic and this makes analysis difficult. Attempts to analyse the data have shown that it is difficult to find a model which fits adequately over the full temperature regime studied.

Some features of the data are clear. The total scattering does not show any signs of critical scattering at T_C in agreement with other data. As an additional test of this the data for 25K was subtracted from the lower temperature data and this showed that there was almost no additional scattering until below T_C.

At low temperatures, roughly < 5K, the data suggests that CePdSb is two dimensional. The values of κ derived from fitting data in different directions suggest that correlations in the basal plane are very long ranged, while those along the c-axis are finite. The effect of an applied field on the SANS patterns at low temperatures can be interpreted by assuming only two dimensional planar correlations are present.

However, the magnetic susceptibility data presented in section 4.3 appear to indicate that exchange interactions are strongest along the c-axis which would invoke three dimensional correlations.

In the temperature range between 5K and T_C the implications of the small angle scattering data are less clear. The values of κ in different directions as found from fitting seem to show that at T_C the correlation length along the c-axis is a *minimum* and the in the basal plane the correlation length actually decreases below T_C leveling off at 14K. The analysis of the data is complicated by the anisotropy in its shape.

Since CePdSb has planar moments it may be possible to describe its behaviour in terms of the XY model. The theoretical behaviour of the XY model in two dimensions (2D) has been widely studied both analytically and in simulations. In three dimensions (3D) the XY model is less well studied so far. Theoretical predictions show that the 3D XY model will display a phase transition with normal critical behaviour and an associated set of critical exponents. However planar vortices as predicted in 2D are not expected to be observed in 3D.

The line in figure 4.32 is a fit to the expected behaviour of the 2D XY model. Equation (1.58) from chapter 1 has been used. Only data in the range 4.5–10K was used in the fit and we can see that the fit does not work outside of the chosen range. The transition temperature was used as a parameter and the best fit gave $T_{KT} = 4.6$K. The same range of data could be equally well fitted by a powerlaw with exponent $\nu = 0.4$ and a slightly larger T_{KT}. Powerlaw behaviour is expected in the 3D XY model, although $\nu = 0.67$ is expected [41].

In the 2D XY model vortex diffusion above T_{KT} is predicted to lead to quasielastic dynamics [66, 67]. This behaviour has been bourne out experimentally in some model systems [68]. In CePdSb we do see that the spin waves apparently give way to a quasielastic response at ~ 5–6K in the IN6 data. If the quasielastic response were due to diffusing vortices then the SANS pattern might be showing some details of this. Gouvêa *et al* [67] have examined the anisotropic Heisenberg model in 2D. In this model planar vortices are allowed to have an out of plane spin component which can be stabilized when vortices are in motion. This could could give rise to the diagonal arms in the SANS patterns, though detailed calculations are required to verify this speculation.

Finally we should note that small angle neutron scattering is sensitive to fluctuations and static correlations. It is not a simple matter to separate critical scattering from small angle scattering from other sources. Figure 4.30 shows a peak centred at 8K but it still unclear if this is true critical scattering associated with a phase transition. There is certainly no sign of critical scattering at T_C but details of the behaviour at lower temperatures are still not well understood. The precise origins of the observed anisotropic pattern still remain undetermined.

4.8 Summary and conclusions

This section gives a brief summary and some further discussion on the data presented in this chapter.

The interest in CePdSb stems from a missing anomaly in the heat capacity. CePdSb shows many signatures consistent with ferromagnetism at 17K but the heat capacity is not dominated by the normal lambda type anomaly at the Curie temperature. The main feature of the heat capacity is a large rounded anomaly centered at 10K. The implications are that the ground state entropy is not removed at the ferromagnetic ordering temperature so that some sort of disorder remains. The work in this chapter has been motivated by the desire for an understanding of this unusual material.

Our magnetisation measurements show that the Curie temperature in CePdSb is marked by an increase in susceptibility. Below T_C the magnetisation as a function of field behaves like that of a ferromagnet. Neutron diffraction reveals magnetic Bragg peaks which begin to appear at the Curie temperature. The magnetic Bragg pattern contains only ferromagnetic peaks.

An extrapolation from magnetisation data plotted as an Arrot plot reveals a spontaneous magnetisation curve for the basal plane which agrees with that produced from single crystal and polycrystalline neutron diffraction. The spontaneous magnetisation curve for the basal plane is in fact somewhat unusual, the magnetisation increases fairly slowly below T_C. In contrast the magnetisation measured in a small field for a polycrystal is quite rapid below T_C.

Magnetic susceptibility data can be well fitted by a crystal field model which shows that the groundstate of this material is a doublet in which both states are admixtures of $|5/2\rangle$ and $|3/2\rangle$. The crystal field has been shown [62] to lead to a considerable anisotropy which makes CePdSb an easy plane system.

Low energy neutron scattering measurements find that the quasielastic scattering above the ordering temperature is well described by a Lorentzian lineshape. The fitted linewidth is wavevector dependent implying spin-spin relaxations. The temperature and wavevector dependence of the linewidth does not fit completely within either a RPA or de Gennes approach. However, an analysis based on the de Gennes approach reveals some interesting information about the wavevector dependence of the linewidth. The fit indicates that nearest neighbour exchange is dominant. This is confirmed by fits to the single crystal susceptibility data which demonstrates that the molecular field is strongest along the c-axis.

We should examine any parallels between the XY model and CePdSb because of the planar nature of CePdSb. Strong exchange along the c-direction means that CePdSb is a true 3D XY system.

The 3D XY model has not been extensively studied yet and the literature is lacking detailed theoretical studies. It is clear that CePdSb is a strongly 3D XY system but there appear to be several features of the magnetic correlations which are reminiscent of the 2D XY model.

Theoretical predictions and numerical work [68, 67, 66] suggest that in the Kosterlitz–Thouless phase of the 2D XY model there will be spin wave excitations and above this phase there will be some correlated diffusive motion of topological vortices. This diffusive motion should lead to quasielastic neutron scattering of the type seen above 6K in the IN6 data.

A recent neutron scattering study [64] on a single crystal of CePdSb found that in addition to spin wave scattering, above $\sim$ 6K a quasielastic component of scattering began to develop. In the 2D XY model the spin wave energy is predicted to drop discontinuously to zero at the KT phase transition but only a smooth renormalisation in the energy was observed in the neutron scattering study [64]. The small angle scattering data shows that the correlation length in the basal plane is large below $\sim$ 5 K but it decreases above this. In the region between 5–10K the inverse correlation length can be described by the 2D XY model, although this region of the data can be fitted equally well by a power law.

We can interpret the small angle scattering data below $\sim$ 6K by assuming that the magnetisation is confined to the basal plane and the application of a magnetic field in the a-direction makes the scattering isotropic.

The small angle scattering data has a squared Lorentzian profile in the basal plane below T_C and this has been predicted theoretically for vortex motion in the 2D XY model.

It is possible that in CePdSb, despite the strong interplanar interactions that there is some cross over between 3D and 2D character. Aspects of this have been examined in simulations [41] but we are not aware of any predictions which we could compare with our data.

Muon spin relaxation experiments in zero field show that T_C is marked by a drop in initial asymmetry. Fits to a stretched exponential model show that the damping rate has only a weak peak at T_C where we might expect to see a sharp divergence. The exponent of the stretched exponential starts at ~ 1.05 above T_C and falls between T_C and ~ 12K. Below 12K the exponent increases once more and at ~ 5K it appears to drop rapidly. This parameter indicates that there is some anomalous change taking place below T_C. At 10K the damping rate shows two component behaviour but there is no spontaneous precession of the muons below the ordering temperature. A transverse field measurement down to 10K shows that the precession frequency of the muons does not show any features at T_C but it increases sharply down to 10K.

4.8.1 Further Work

The anomalous phase transition in CePdSb is still not understood. It appears that 17K is clearly fixed as a transition to ferromagnetism yet there is only a very small or minor indication of this in the specific heat. It is not clear what maintains the entropy below T_C we would expect that the doublet groundstate should be split by the exchange field therefore removing disorder from the system.

So far it is not clear if there is any anisotropy in the basal plane, magnetisation measurements suggest not but thermal expansion finds a clear anisotropy. Magnetisation measurements using a torque magnetometer on single crystals would help resolve this.

μSR experiments using single crystals would be more useful than poly crystalline data. In general any further work should use single crystals because of the anisotropic properties of CePdSb. Using a μSR spectrometer with better resolution on the sub microsecond time scale might test if there is in fact any spontaneous precession of the muons in zero field below the ordering temperature.

In the next chapter on CePtSb we suggest that alloys the form $\mathrm{CePd}_{1-x}\mathrm{Pt}_x\mathrm{Sb}$ would be interesting to study also. Pt and Pd are isoelectronic and the structure of the two parent compounds is the same also. Compounds such as CeRhSb and CePdSn which have one different element from CePdSb have a different structure and very different properties.

Since the properties of the exchange interactions between different Ce ions is one of the main devices that controls CePdSb it may be worthwhile to examine these more closely. In particular a measurement of the form factor in a single crystal might help to determine the role of the antimony or palladium ions in superexchange with neighbouring ceriums. A comparison with the same data for CePtSb might be useful also.

A number of effects exist which might be contributing to the anomalous behaviour in CePdSb. Magneto-elastic effects might be important. Since the Ce-Ce ions are closest in the *c*- direction these chains might show low dimensional properties. The planar nature of the magnetic moments might make this material a candidate for an example of the three dimensional X-Y model. An energy gap of 0.4meV in the magnetic excitation spectrum has been suggested from the heat capacity data, but very recent single crystal measurements of the dispersion relations find only a much smaller gap, 0.1meV.

Chapter 5

CePtSb

CePtSb has the same crystal structure as CePdSb [69] with very similar lattice parameters. The hexagonal lattice parameters are a = 4.5327, c = 8.0580 [19]. Some experimental work on CePtSb is presented here to be used to make some comparisons with the behaviour of that of CePdSb.

CePtSb is a ferromagnet with a T_C of 4.5K. It has a normal metallic resistivity and shows a standard λ-type anomaly in the heat capacity at T_C [70, 59], see figure 4.2. CePtSb has the same crystal field Hamiltonian as CePdSb and the fitted crystal field parameters are comparable to those of CePdSb [69]. The crystal field model predicts a low temperature moment of $\sim 1\mu_B$, slightly smaller than that of CePdSb.

Experiments on single crystal samples have found that the resistivity is highly anisotropic [59]. The resistivity along the c-axis is larger than in the basal plane. The same result was found for the isostructural compounds CePdSb, LaPdSb and LaPtSb which indicates that the anisotropic resistivity is probably due to the conduction band structure. The resistivities are relatively large which indicates low carrier concentrations.

Optical conductivity measurements find that there is a larger carrier density in the a-c plane which accounts for the resistivity behaviour [71].

There have been no reports of Kondo lattice behaviour in CePtSb and while it shows the same structural features as CePdSb the transition to ferromagnetism appears to be quite normal. The next sections contain descriptions of neutron scattering and magnetisation measurements on CePtSb which can be compared with the results of the previous chapter.

5.1 Magnetisation

Magnetisation experiments were carried out on a small polycrystalline piece of CePtSb using a Vibrating Sample Magnetometer. Magnetisation isotherms are shown in figure 5.1. The lowest temperature isotherm shows a sharp increase from zero, clearly indicating a ferromagnetic state. It also shows a saturation value of $\sim 0.9\mu_B$ per Ce at 5T. Magnetisation loops from zero to positive field and back to zero showed that there was a small hysteresis with a small remnant field, as for CePdSb.

Fitting the data for the critical isotherm, at 5K, using $H \propto |M|^\delta$ gives a reasonable fit in the field region above 10000G. For H< 10000G the fit did not have the right curvature. The critical exponent δ was found to be ~ 4.9.

The same magnetisation data is shown in the form of an Arrot plot in figure 5.2. The arrot plot shows the 5K data goes through zero which indicates T_C. The lines on this Arrot plot are curved, but the difference from CePdSb is that the curvature is concave throughout. This is suggestive that the normal case is to have the same type of curvature for each line of the Arrot plot*, data for the ferromagnets CeAgGa and $CeRu_2Ge_2$ support this fact. Consequently, the change of curvature in the Arrot plot for CePdSb would seem to be anomalous.

It is possible to get reasonable fits to the magnetisation data using an Arrot plot with the critical exponents $\beta = 0.3$ and $\gamma = 1.5$. The extrapolated spontaneous magnetisation is consistent with power law behaviour with critical exponent $\beta = 0.3$. This indicates that the ferromagnetic transition in CePtSb can be described by normal critical behaviour. The modified Arrot plot is shown in figure 5.3. The effect of the demagnetising field can be seen as the apparent shift of the data away from the origin. The inset to the figure shows the derived spontaneous magnetisation. This line on this inset corresponds to a powerlaw with critical exponent $\beta = 0.3$. The good agreement indicates that the derived spontaneous magnetisation is consistent with the exponent used for the Arrot plot.

---

*the curvature comes from using the mean field critical exponents

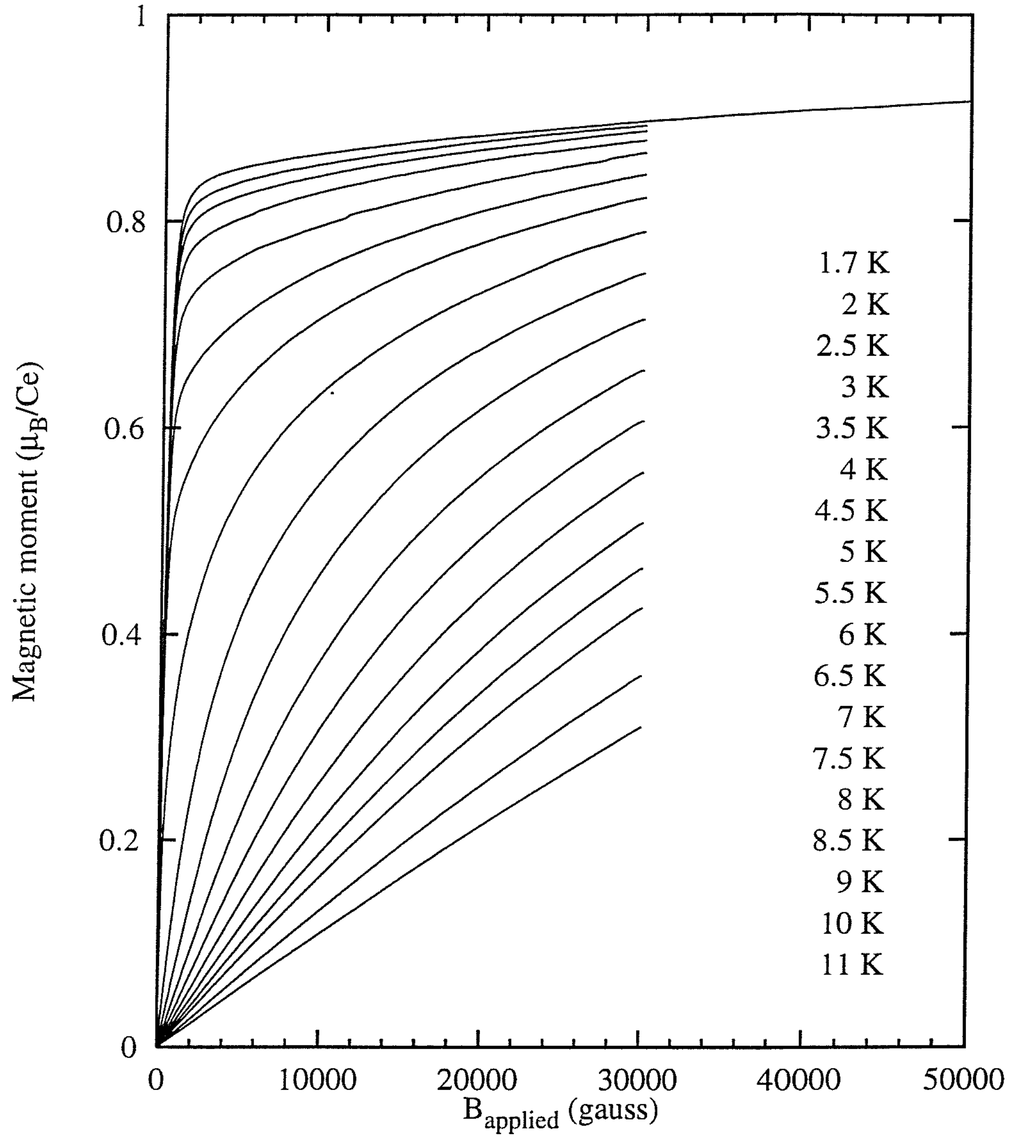

Figure 5.1: Magnetisation isotherms in CePtSb. The bottom data line corresponds the the last temperature in the list and so on. The data has not been corrected for demagnetising factor effects.

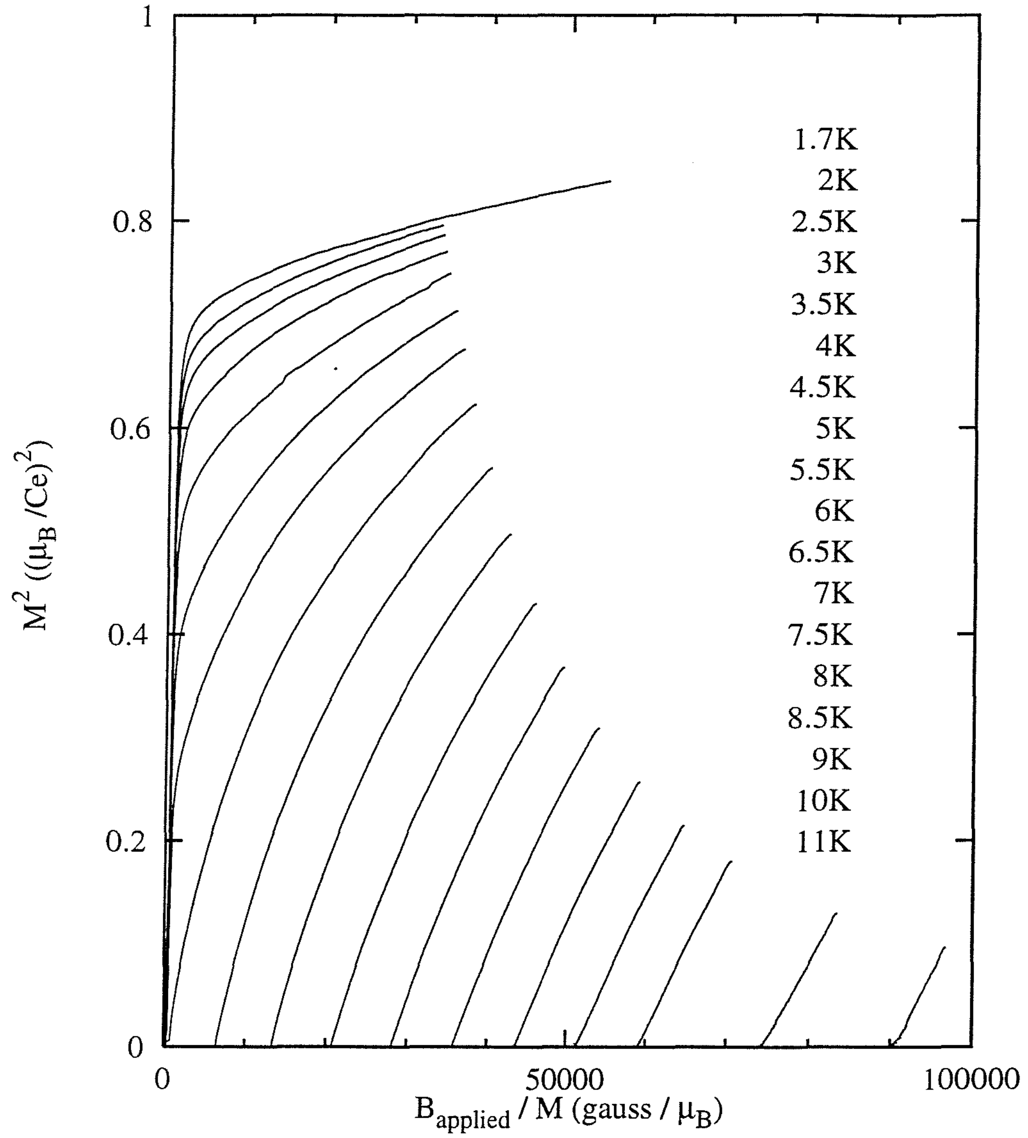

Figure 5.2: Arrot plot of CePtSb magnetisation data.

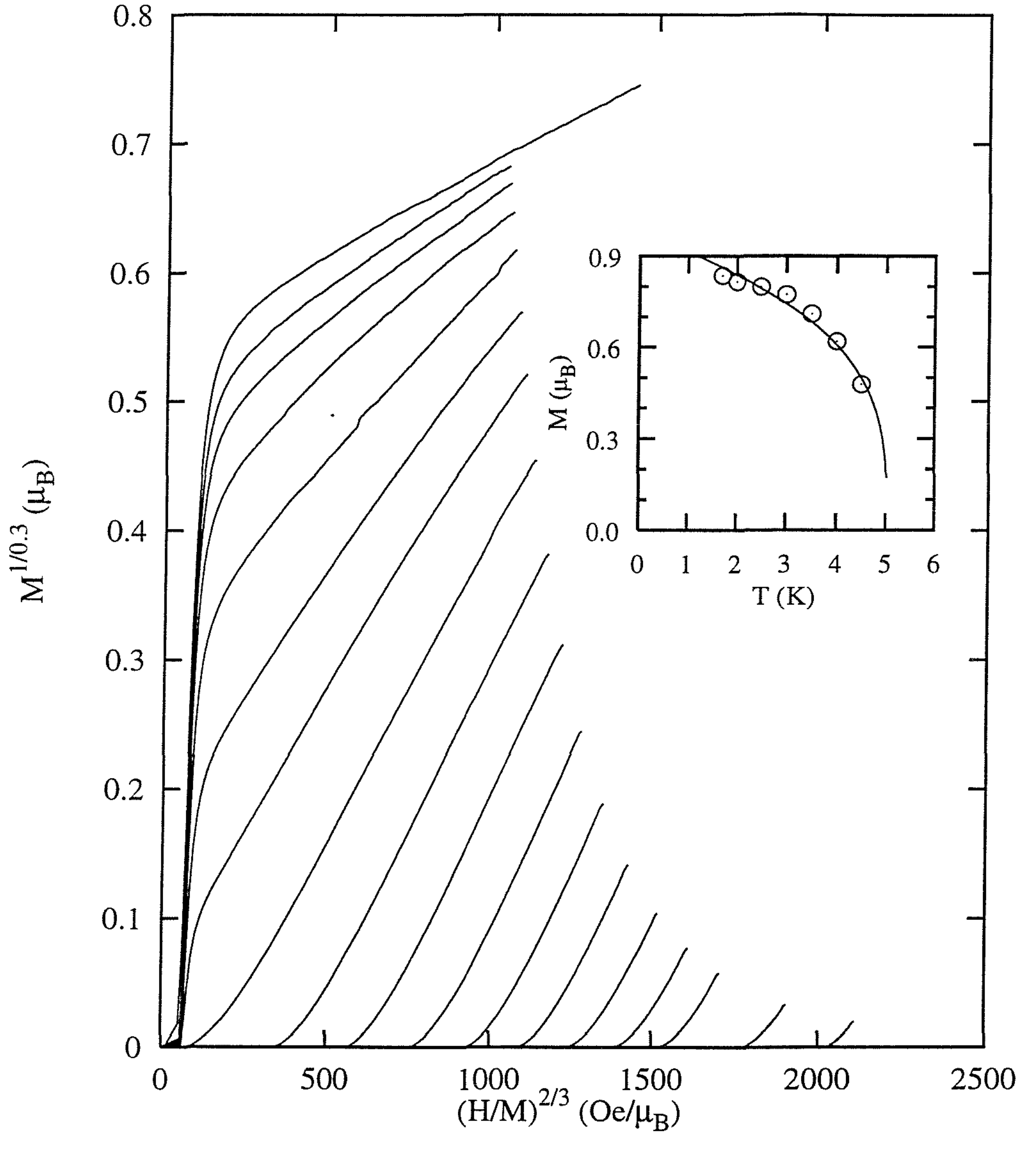

Figure 5.3: Arrot plot of CePtSb magnetisation data. Plotting $\left(\frac{H}{M}\right)^{1/\gamma}$ *vs.* $M^{1/\beta}$ with $\gamma = 1.5$ and $\beta = 0.3$. The inset shows the spontaneous magnetisation found by fitting straight lines to the data below T_C, the line is a power law fit $M \propto (T_C - T)^{\beta}$ with $\beta = 0.3$ and $T_C = 5.03$K.

5.2 Neutron scattering

Low energy neutron scattering from a polycrystalline sample was measured on the IN6 spectrometer at I.L.L. Measurements were made using 3.12meV incident energy neutrons. The sample was mounted in a helium flow cryostat and measurements were made at 50, 20, 4.5 and 1.5K. The data was corrected for various effects as described in the previous chapter.

5.2.1 Quasielastic scattering

At 50K and 20K wave-vector dependent quasielastic scattering was observed in all detector groups. The quasielastic scattering appeared to be intermediate between a Lorentzian and a Gaussian. The fitting procedure showed that the Lorentzian gave marginally better results and so the data was fitted to a Lorentzian. The fits indicated that the width of the quasi-elastic line was wavevector dependent.

The modulation of the width with wave-vector indicates spin-spin interactions in the paramagnetic phase as we expect for a material with exchange interactions. Figure 5.4 shows the variation of the half-width of the quasielastic Lorentzian at 20K and 50K. It was possible to fit the wave-vector dependence according to the method of moments [65, 45] as used in section 4.5 using only the interaction between nearest neighbours. The linewidth of CePtSb is smaller than that of CePdSb. The value of the exchange constant between nearest neighbours found from the fits was $\mathcal{J} = 0.11$meV.

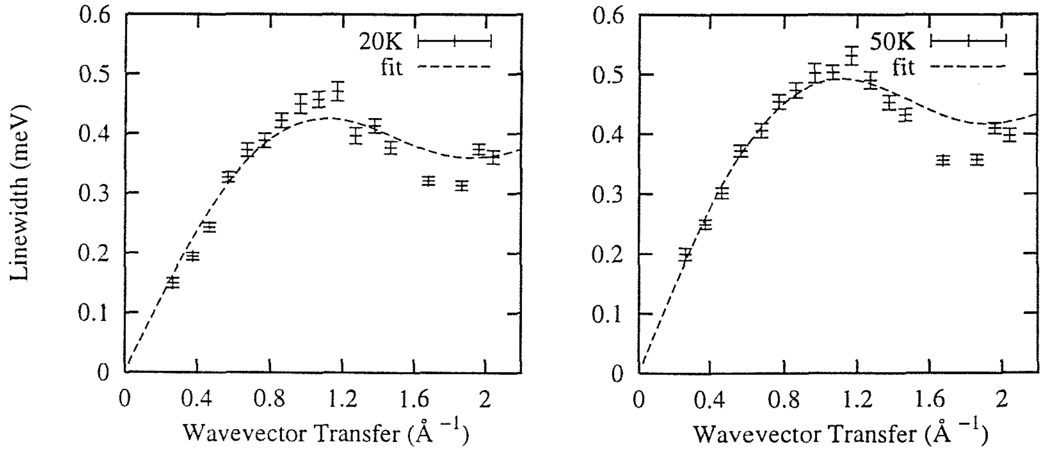

Figure 5.4: Quasi-elastic linewidth in CePtSb. Lines are fits using equation (4.9).

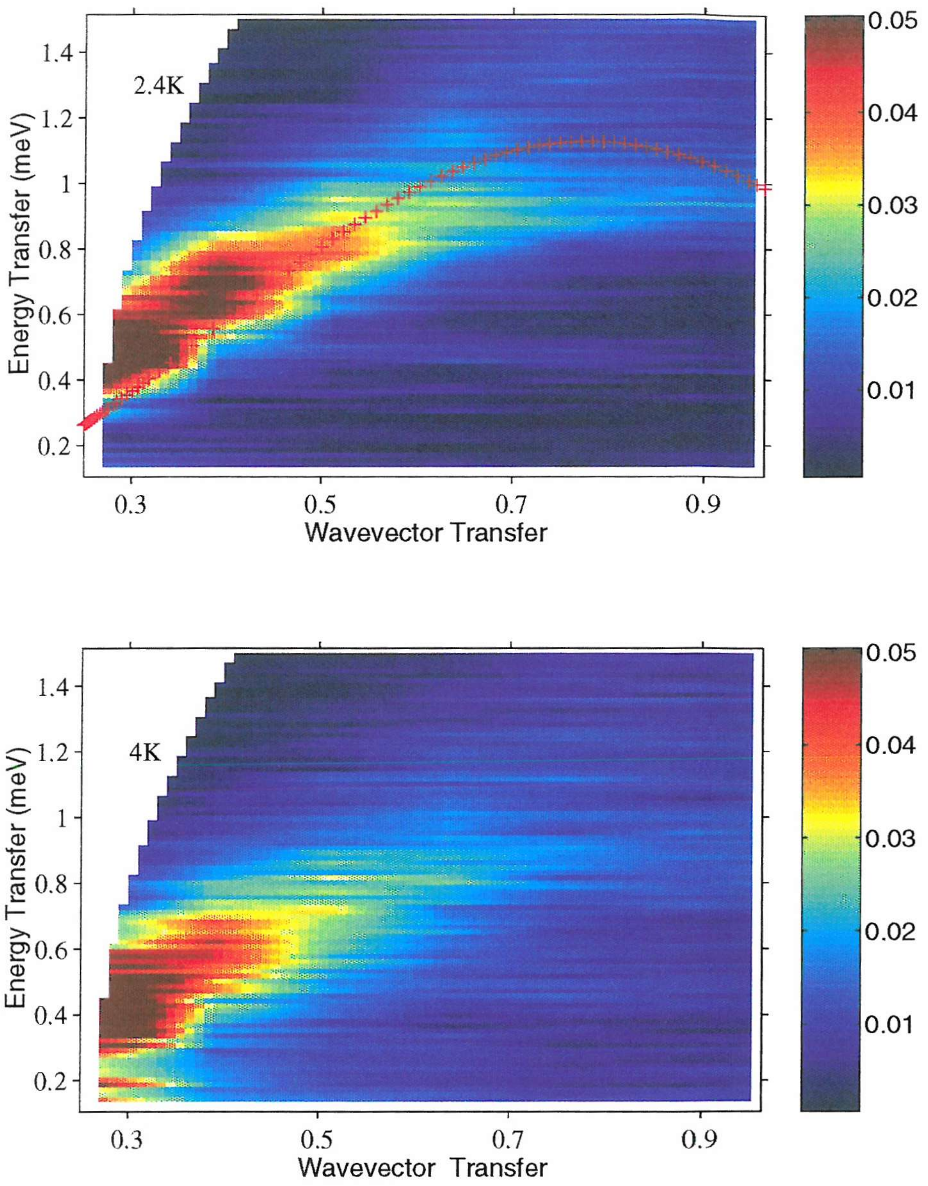

Figure 5.5: Spin waves in CePtSb.

5.2.2 Low temperature scattering

At the lowest temperature we observe a clear inelastic distribution indicative of spin waves. Contour plots over the whole energy transfer wave-vector transfer grid are shown in figure 5.5. The spin wave dispersion relation shows up clearly and at the larger wave-vector transfer values it is even possible to see the dispersion relation splitting into two branches. However, this is a polycrystalline measurement so for wave-vectors outside the first Brillouin zone we a seeing an average over something which is not necessarily isotropic.

Figure 5.5 has a line on the diagram for 2K corresponding to a simple dispersion curve. The dispersion curve is given by

$$\hbar\omega = J\left(\nu_1 \mathcal{J}_1 - \nu_1 \mathcal{J}_1 \cos(Qr_1)\right) , \tag{5.1}$$

with $\nu_1 = 2$, $\mathcal{J}_1 = 0.11$meV and $r_1 = 4.03$Å. $\mathcal{J}_1$ has been taken from the quasielastic line fits. Equation (5.1) is over simplified but figure 5.5 shows a rough agreement with the data. Bearing in mind that the data is for a polycrystalline sample the dispersion curve shows that the quasielastic linewidth fits are roughly correct.

The dispersion relation is visible right up to T_C which is what we might expect in a normal ferromagnet and in contrast to what we have observed in CePdSb.

5.3 Comparison

CePtSb has the same structure as CePdSb and there is only a slight difference between their lattice parameters.The crystal field Hamiltonian is the same for both and the parameters are quite similar.

Neutron scattering shows that in the paramagnetic state the two materials are similar in that they both have wavevector dependent quasielastic scattering. This indicates spin-spin relaxations which is what we expect knowing that there must be exchange interactions which will lead to magnetic ordering at lower temperatures.

Both are ferromagnets but CePtSb has a much lower ordering temperature. It seems to be possible to describe the behaviour of magnetic properties of CePtSb by critical exponents. The crude estimates of the critical exponents are consistent with those expected for the three dimensional Heisenberg and XY models [34]. CePtSb also has a typical anomaly in the heat capacity at T_C.

The difference in ordering temperatures suggests much stronger exchange in CePdSb. It would appear that one of the main differences between the two compounds is in fact the strength of the exchange interactions. One interesting fact from NMR data [61] for CePdSb showed that the effective field at the Sb site increased under pressure implying that the Curie point should increase under pressure too. The unit cell volume of CePtSb is only around 1Å^{-3} smaller, almost identical, to that of CePdSb. The lattice parameters for the two compounds show that the unit cell of CePtSb is expanded along the c-axis by a few tenths of an Å and contracted along the a-axis by a few hundredths of an Å. Pressure dependent studies of single crystals of the two compounds might reveal interesting results. A study of alloys of the form $\mathrm{CePd}_{1-x}\mathrm{Pt}_x\mathrm{Sb}$ might produce useful information also.

If we compare the crystal field groundstates of CePdSb and CePtSb there is an interesting difference. The anisotropy of the magnetisation of the groundstate can be described by two effective Landé factors, $g_{||}$ and $g_{\perp}$ for the c-axis and basal plane respectively. This is done by equating the moments $\langle\mu_x\rangle$ and $\langle\mu_z\rangle$ to the values expected for a spin half groundstate using the two effective g factors.

The ground state for CePdSb is $\cos\theta|\pm 1/2\rangle \pm \sin\theta|\mp 5/2\rangle$ with $\theta \approx \pi/8$. This leads to $g_{||} = 0.104$ and $g_{\perp} = 2.194$ so that

$$\langle\mu_z\rangle = 0.052\mu_B \tag{5.2}$$

$$\langle\mu_x\rangle = 1.097\mu_B \tag{5.3}$$

where the ratio of the two effective Landé factors is 21.1, which shows considerable anisotropy.

For CePtSb the groundstate is the same except that $\theta = 0.49$ rad [69, 72]. This gives $g_{||} = 0.2876$ and $g_{\perp} = 2.549$ which leads to

$$\langle\mu_z\rangle = 0.1438\mu_B \tag{5.4}$$

$$\langle\mu_x\rangle = 1.2746\mu_B \tag{5.5}$$

with the ratio of the Landé factors equal to 8.86. This raises two interesting comparisons, firstly CePtSb is anisotropic but less so that CePdSb and CePtSb has a relatively larger value for $\langle\mu_z\rangle$. This suggest that CePtSb is less XY–like than CePdSb.

Chapter 6

$CeRu_2Si_{2-x}Ge_x$ alloys

6.1 Introduction

The family of $CeRu_2Si_{2-x}Ge_x$ alloys are part of the vast number of compounds which have the $ThCr_2Si_2$ type structure; the so-called rare earth ternary silicides. The characteristic structure is shown in figure 6.1. Many different compounds of the form CeT_2X_2 (T=transition metal, X=Group III or IV element) have this body

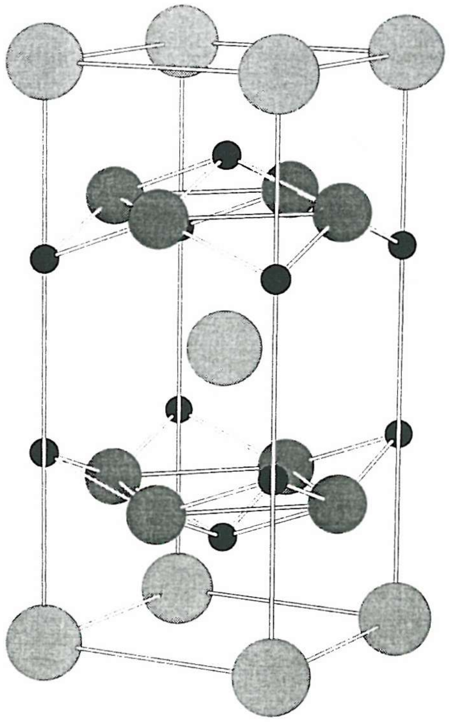

Figure 6.1: The $ThCr_2Si_2$ type tetragonal structure

centred tetragonal structure (space group I4/mmm) with two formula units per unit cell*. One compound in particular, $CeCu_2Si_2$, was responsible for generating huge interest in compounds of this type when it was shown to be the first 'heavy fermion superconductor'[74]. Of the Ce compounds discovered so far with this structure there is a rich variety of properties from intermediate valence to heavy fermion behaviour and long range order. In the following paragraphs we briefly review the properties of $CeRu_2Ge_2$, $CeRu_2Si_2$ alloys of the $CeRu_2Si_{2-x}Ge_x$ series and other related alloys.

$CeRu_2Ge_2$ lies at one end of the composition range and it displays quite distinct character to $CeRu_2Si_2$. Measurements of the heat capacity [75, 76] show a prominent λ-type anomaly at $\sim$ 8K, with a Shottky anomaly at higher temperature consistent with ferromagnetic ordering at 8K and a large crystal field splitting. The first excited crystal field levels lies at $\sim$ 35meV and the second at $\sim$ 42meV [77]. The value of the Sommerfeld coefficient, $\gamma = 20$mJ/mol K^2, is only slightly enhanced compared to a normal metal. Magnetisation and neutron diffraction [75] give a moment of $\sim 2\mu_B$ per Ce which has been determined to lie along the tetragonal c-axis. The crystal field groundstate makes $CeRu_2Ge_2$ an Ising-like magnet. The quasielastic linewidth, as measured by neutron scattering, shows linear temperature dependence (Korringa-like [78]) over a wide temperature range with a small low temperature intercept [79]. This and the low value of γ suggest hybridisation effects are not very important in this compound. $CeRu_2Ge_2$ is a good local moment ferromagnet with a Curie temperature reported to lie around 7.5K [80, 81].

$CeRu_2Si_2$ is a good example of a heavy fermion compound. It has been widely studied by many experimental techniques. It shows no magnetic ordering or superconductivity down to milli-Kelvin temperatures [82] but does show a large linear term in the low temperature heat capacity, $\gamma = 350$ mJ/mol K^2, characterising a Fermi liquid state of heavy quasi-particles [82]. The susceptibility follows the Curie-Weiss law at high temperatures with an effective moment close to the Ce^{3+} free ion value [83]. The effects of a large crystal field splitting can be seen in the heat capacity [83]. Neutron scattering has shown that antiferromagnetic spin fluctuations exist at low temperatures, saturating below $\sim$ 15K [84]. μSR measurements suggest that there may be ultra small Ce moments of order $0.003\mu_B$ [85, 86]. $CeRu_2Si_2$ is very anisotropic and magnetisation measurements show a meta-magnetic step at a field of 8T applied parallel to the c-axis [83, 87]. de Haas–van Alphen mea-

---

*Structural parameters of over 500 compounds are given in ref.[73]

surements show a change in character of the Fermi surface above and below the metamagnetic transition. This difference can be ascribed to the behaviour of the 4f electrons. Below the transition the observed frequency branches can be related to itinerant 4f electrons but above the assumption of localised 4f states is required [88]. The metamagnetic transition appears to be associated with the collapse of the antiferromagnetic correlations with increasing field [89].

Many studies of the effects of alloying on $CeRu_2Si_2$ have been made. Substitution at the Ce site with La drives the system to magnetic order, while substitution with Y has the opposite effect and increases the Kondo temperature [90, 87]. Studies of the effects of replacing Ru by Rh, Au, Fe[81], Os[80] and Mo are also reported in the literature. In general increasing the unit cell volume by alloying, even by a small amount, induces magnetic order confirming that $CeRu_2Si_2$ is very close to an antiferromagnetic instability.

In $Ce_{1-x}La_xRu_2Si_2$ with small amounts of La doping ($0.08 < x < 0.13$) magnetisation measurements show that the same metamagnetic transition is observed in the paramagnetic state, but at lower fields. In fact these alloys show a coexistence of static order and fluctuations [91]. Y doping decreases the unit cell volume and no ordering is induced, a metamagnetic transition occurs as for $CeRu_2Si_2$ but it is at higher fields [87]. Neutron diffraction studies on $Ce_{1-x}La_xRu_2Si_2$ reveal a complex phase diagram with at least three different regions of commensurate and incommensurate magnetic ordering [92]. An interesting point is that the zero field antiferromagnetic ordering wavevector is the same as the wavevector of the antiferromagnetic fluctuations in $CeRu_2Si_2$. In $Ce_{0.8}La_{0.2}Ru_2Si_2$ an additional transition to another phase has been found by transport and heat capacity measurements [93]. This phase boundary does not show up in neutron diffraction measurements [94].

$CeRu(Ru_{1-x}Rh_x)_2Si$ alloys have been studied by several experimental techniques. The substitution of Rh into the lattice causes expansion which results in magnetic order as for La substitution. μSR measurements indicate that short range magnetic correlations are present. An alloy with $x = 0.15$ showed a drop in the initial asymmetry at 5.5 K and the presence of a highly inhomogeneous field at the muon site indicating antiferromagnetism.

The $CeRu_2Si_{2-x}Ge_x$ alloys is an attractive series to study because the two parent compounds lie at opposite extremes of the physical properties scale. Ge and Si are isoelectronic, with Ge having the larger atomic radius. The lattice parameters vary linearly across the series and it is considered that the main effect of substitution of

Si by Ge is to change the hybridisation of 4f electrons with conduction electrons, through the increase in the unit cell volume. This is sometimes called 'negative chemical pressure'. We may study the change in magnetic properties in this system as the nature of the 4f electrons changes across the series. It has been shown [77, 95] that for $x = 0.1$ magnetic order is induced. Neutron diffraction in zero field has shown that alloys with $x \leq 1.0$ show sinusoidally modulated antiferromagnetic order with modulation wavevector $q \approx (0.3, 0, 0)$ [95]. The magnetic moment on the Ce ion increases sharply as x increases and begins to saturates around $x = 1.0$. Magnetisation measurements on the Si rich compounds show metamagnetic steps [95, 77] which have been related to changes in the magnetic order [96], in parallel with the behaviour in the La substituted alloys [92]. The ground state in these alloys is a virtually pure $|\pm\frac{5}{2}\rangle$ doublet [97] with strong crystal field anisotropy aligning the moment in the tetragonal c-direction. This $|\pm\frac{5}{2}\rangle$ groundstate coupled with the large crystal field splitting forces the system to be Ising-like. An unusual consequence of the Ising-like groundstate in these alloys is that the transverse susceptibility is negligible, only χ^{zz} is important.

Neutron scattering experiments on some alloys with $x < 1.0$ found a quasielastic line in all the compounds. The lineshape was Lorentzian at all temperatures and was found to be highly modulated as a function of wavevector transfer. Analysis of the linewidths showed the single ion linewidth was largest in the compositions with smallest x, with an unusual temperature dependence. The low temperature intercept of the single ion linewidth, used as a measure of the hybridisation, showed a decrease with increasing x and roughly exhibited scaling behaviour. An inelastic excitation was observed in the alloys for one temperature below ~ 3K. This excitation was not a spinwave because of the Ising groundstate. Instead, it was thought to be a novel longitudinal spin fluctuation in the sinusoidally modulated groundstate [97].

While the Si rich end of this family has received a lot of attention the Ge rich end has received comparatively less. Presented here is a study of some properties of the Ge rich alloys with $x = 1.0$, 1.25, 1.5, 1.75 and 2.0. The change from a ferromagnetic to antiferromagnetic groundstate is studied using magnetisation measurements and μSR and we examine the novel low temperature magnetic excitation in this end of the series using neutron scattering.

Table 6.1: Lattice parameters for $CeRu_2Si_{2-x}Ge_x$ alloys as a function of Ge composition, x.

x	a (Å)	c (Å)	reference
0.1	4.19(5)	9.78(7)	[77]
0.2	4.2(1)	9.80(2)	[77]
0.35	4.2(6)	9.82(0)	[77]
0.5	4.2(9)	9.83(5)	[77]
1.0	4.22(8)	9.90(9)	[77]
1.25	4.228(3)	9.947(7)	this work
1.5	4.236(20)	9.96(52)	this work
1.5	4.245	9.968	[80]
1.75	4.238(20)	9.973(54)	this work
2.0	4.26(7)	10.0(3)	[77]

6.2 Synthesis.

Some samples were already available from previous work but polycrystalline buttons of the alloys with $x = 1.25$, 1.5 and 1.75 were made by arc melting stoichiometric amounts of the elements on a water cooled Cu hearth in an argon atmosphere. Xray diffraction confirmed the samples were single phase. The Xray patterns were indexed on the basis of the tetragonal unit cell and the lattice parameters found using a simple refinement program are shown in table 6.1 in conjunction with other values taken from the literature. Xray microprobe measurements at ten spots on a small piece of the $CeRu_2Si_{0.75}Ge_{1.25}$ alloy showed that there were fluctuations in the composition of germanium and silicon from spot to spot. The variation from spot to spot is shown in table 6.2. The composition of cerium and ruthenium was close to stoichiometric.

6.3 Magnetisation Data

When the polycrystalline buttons were crushed many small shiny platelets were seen along with other granular fragments. We were able to remove some of the small platelets which were taken to be small single crystals with c-axes normal to the plane face. These platelets had masses of around 1mg and after examination under a microscope the flattest ones were chosen for magnetisation measurements.

For each sample magnetisation versus field isotherms were measured at several temperatures between 1.7K and 20K. A measurement of magnetisation in a small

Percentages by mass			
Ce	Ru	Si	Ge
21.16	42.05	20.48	16.31
21.59	41.53	7.20	29.68
22.09	43.40	17.61	16.91
19.94	42.03	18.72	19.31
21.76	42.03	15.77	20.44
20.53	42.02	17.03	20.41
20.64	40.87	17.33	21.16
22.43	43.41	13.93	20.22
23.31	39.20	12.35	25.14
20.27	43.65	9.04	27.04
20.94	41.16	12.72	25.18

Table 6.2: The results of microprobe of analysis at ten random spots on a piece of $CeRu_2Si_{0.75}Ge_{1.25}$. The percentages by mass for the exact composition would be Ce 20%, Ru 40%, Si 15% and Ge 25%.

field as a function of temperature was also made for each sample. All the measurements were made with a vibrating sample magnetometer (VSM). Since the experiments used flat samples we expect that demagnetising effects would be considerable.

6.3.1 Low field magnetisation

The magnetisation of a small platelet of each alloy was measured. The platelets were aligned with the plane face parallel to the field. This orientation gave a measurement in the c-axis direction. A 100 Oe applied field was used for most of the measurements. The data are shown in figures 6.6—6.2. The y-axis of each plot shows the magnetisation divided by the applied field, in units of emu/mol. This quantity is referred to as the susceptibility.

The $CeRu_2Ge_2$ sample clearly shows a sharp upturn in the susceptibility at around 8K, indicating a ferromagnetic transition, with a slight residual increase at lower temperatures, see figure 6.2. In the $CeRu_2Si_{0.25}Ge_{1.75}$ alloy there is a maximum in the susceptibility at around 9K which is followed by a sharp increase where, again, the susceptibility saturates, see figure 6.3. We may take this as evidence of an, initially, antiferromagnetic phase which quickly becomes ferromagnetic. Figure 6.3 also shows the measured susceptibility perpendicular to the c-axis. A 5000 Oe field was used for this measurement and the susceptibility is seen to be very small giving confirmation that the magnetic moments lie in the c-direction and that the sample

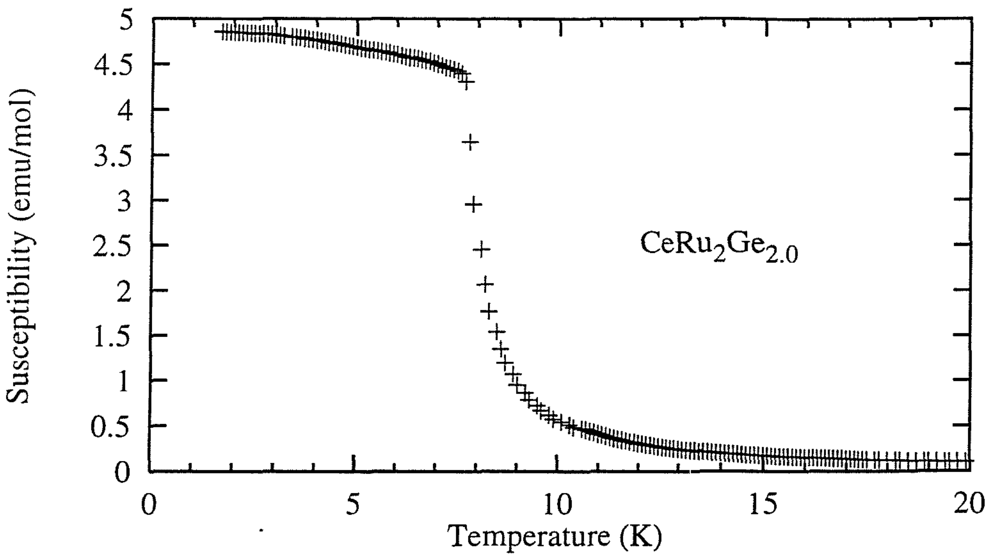

Figure 6.2: Molar susceptibility for $CeRu_2Ge_2$.

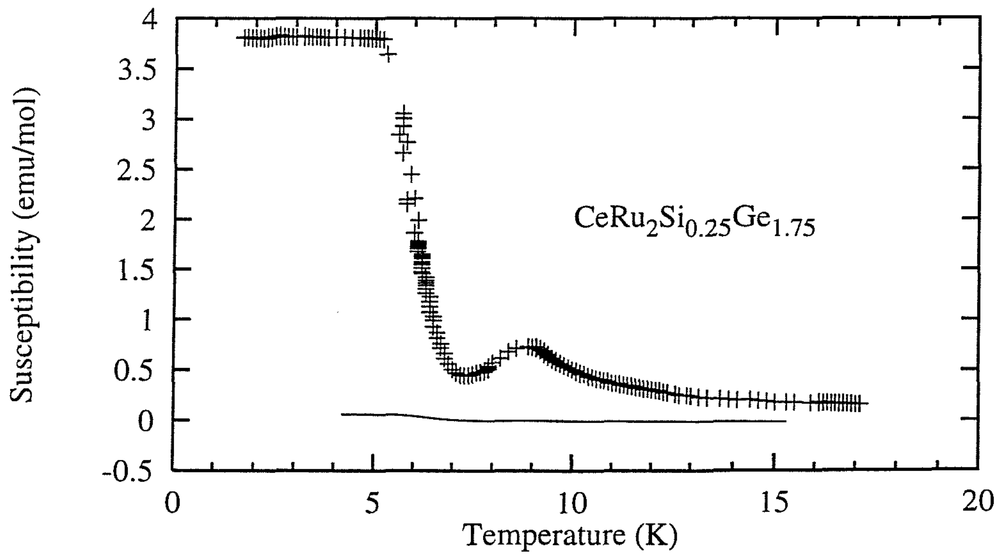

Figure 6.3: Molar susceptibility for $CeRu_2Si_{0.25}Ge_{1.75}$. Points show result for B$||c$ and the line shows B$||a$. The negligible susceptibility for B$||a$ is evidence that the sample is a well aligned single crystal.

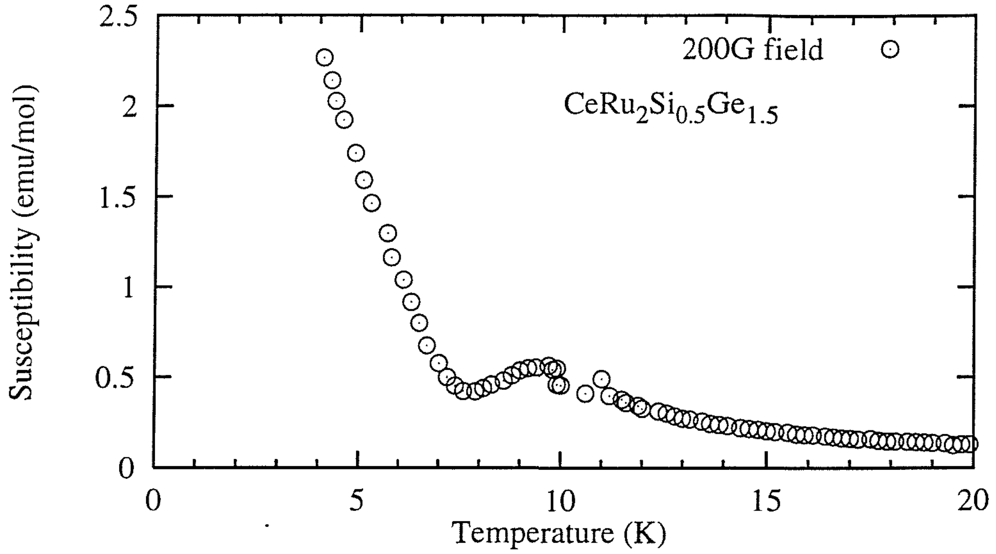

Figure 6.4: Molar susceptibility for $CeRu_2Si_{0.5}Ge_{1.5}$. The break in the data near 10K is not significant, temperature control during the experiment was poor in this small region.

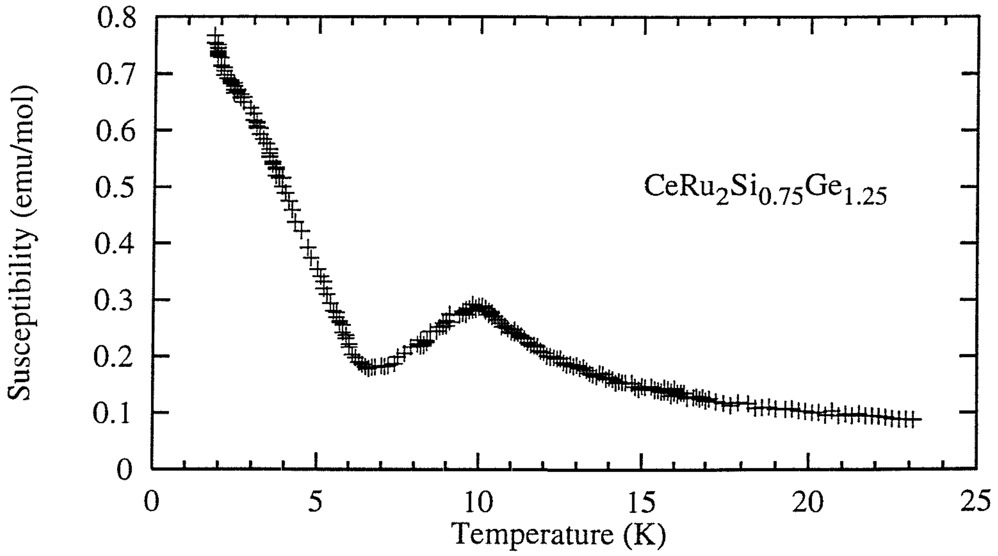

Figure 6.5: Molar susceptibility for $CeRu_2Si_{0.75}Ge_{1.25}$.

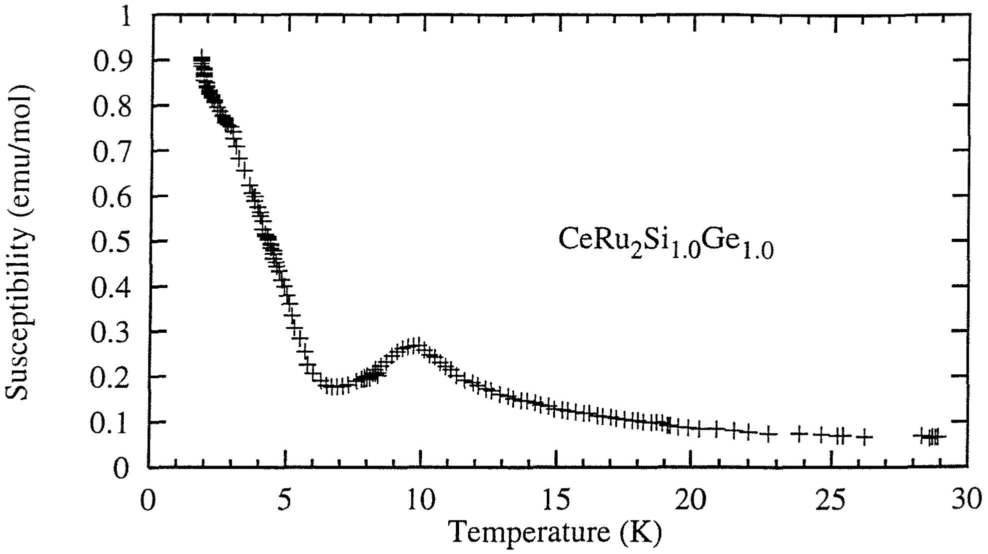

Figure 6.6: Molar susceptibility for $CeRu_2Si_{1.0}Ge_{1.0}$.

is well aligned.

In the other alloys (x = 1.0, 1.25, 1.5) a peak is observed near 10K followed by a steady rise at lower temperatures. Ref. [80] reported the susceptibility of $CeRu_2Si_{1.0}Ge_{1.0}$ and $CeRu_2Si_{0.25}Ge_{1.75}$. Their data for $CeRu_2Si_{1.0}Ge_{1.0}$ is very similar to that presented here but for $CeRu_2Si_{0.25}Ge_{1.75}$ their data does not show the initial antiferromagnetic transition found here.

From these measurements it clear that $CeRu_2Ge_2$ is a ferromagnet. The $x = 1.75$ alloy shows two transitions, and from heat capacity measurements the authors in [98] infer that an alloy with $x = 1.6$ shows the same behaviour. The significance of the rising susceptibility at low temperature for the $x = 1.0$, $x = 1.25$ and $x = 1.5$ alloys is not clear. Additionally, for $x = 1.0$ and $x = 1.25$ there is a change in slope around 3K. In a recent publication the authors in [99] consider that fluctuations in the local concentration of Si and Ge in polycrystalline samples can give rise to spurious effects. In particular the low temperature rise in the susceptibility could be due to a ferromagnetic contribution from clusters of Ge. Their work shows that single crystals show much sharper heat capacity anomalies and metamagnetic steps. A single crystal of $CeRu_2Si_{1.0}Ge_{1.0}$ does not show the low temperature rise in susceptibility found here. Microprobe analysis of our samples with $x = 1.0$ and $x = 1.25$ did show fluctuations in concentration but there is no indication of portions of the sample which have excessive concentrations of Ge.

There is much speculation about the existence of an unknown low temperature phase in these alloys. Heat capacity and resistivity measurements on alloys with concentrations up to $x = 1.2$ show anomalies at $\sim$ 2K [98, 99]. Neutron diffraction studies have not found a change in magnetic structure except for a very small anomaly in the third harmonic of the modulation wavevector. A similar picture has emerged from studies on the $Ce_{1-x}La_xRu_2Si_2$ alloys.

At present it is uncertain at which composition the double transition behaviour disappears. $CeRu_2Si_{0.25}Ge_{1.75}$ has an antiferromagnetic transition followed by a ferromagnetic transition but the question remains whether the lower composition alloys do also.

The data of figures 6.6—6.3 show the initial transition at T_N, represented by the maximum in the susceptibility, is remarkably composition independent. We would expect T_N to move down in temperature as the hybridisation increases but in fact T_N shows a slight increase with decreasing x in the compositions studied here. The ordering temperatures including the ferromagnetic transition in $CeRu_2Si_{0.25}Ge_{1.75}$ are in good agreement with the data of ref. [99].

6.3.2 High field magnetisation

Magnetisation isotherms were measured for each alloy at several temperatures up to high fields. The data is plotted in figures 6.7—6.11 where for the alloys $x = 1.5$, 1.75 and 2.0 a correction for the demagnetising factor has been made by estimating a value from fitting the initial slope of the lowest temperature data. For the alloys $x = 1.0$ and 1.25 it is not easy to estimate the demagnetising factor because there is no clear region of the data which appears to be limited by the demagnetising factor. The average of the values for the other samples was used on the basis that the samples were similar sizes and shapes.

The magnetisation saturates at $\sim 2.1\mu_B$ in all the compositions measured which is a little higher than previously reported. If the groundstate were a pure $|\frac{5}{2}\rangle$ state then we would expect the magnetic moment to be $g_J\mu_B J_z = \frac{6}{7}\frac{5}{2}\mu_B = 2.14\mu_B$. The data reveals meta-magnetic steps in all but the $x = 2.0$ alloy. de Haas van Alphen measurements have shown the meta-magnetic step in $CeRu_2Si_2$ is associated with a large change in the character of the 4f electrons and neutron scattering has shown that antiferromagnetic correlations which are present below the metamagnetic step are not found above. It is thought that the 4f electrons in $CeRu_2Si_2$ become more localised above the (pseudo) metamagnetic step.

In this data the metamagnetic steps are due to a spontaneous change in the antiferromagnetic order. In ref. [96] a phase diagram for an $x = 0.2$ single crystal was reported, where the phase diagram was produced from neutron diffraction in an applied field. The zero field phase was found to correspond to a modulated structure with $Q = (0.309, 0, 0)$ and two other regimes were found, at different temperatures and fields, with mixtures of new incommensurate and commensurate modulated structures. Zero field neutron diffraction on $x = 1.0$ found only one antiferromagnetic transition and for $x = 1.6$ there was an antiferromagnetic transition followed by a crossover to ferromagnetic ordering [99].

To make this magnetisation data more clear the derivative, $(\frac{\mathrm{dM}}{\mathrm{dB}})$, was taken for every isotherm of each sample. This technique makes the data much more revealing and a novel representation of $\frac{\mathrm{dM}}{\mathrm{dB}}$ as a function of field and temperature for $CeRu_2Si_{1.0}Ge_{1.0}$ is presented in figure 6.12. This can be compared with the original data in figure 6.7 which shows that the lowest temperature isotherm has a kink at low field and a metamagnetic-like step near 1T. Figure 6.12 shows the kink as a sharp step and the other feature as a relatively broad peak. The peak quickly separates into two as the temperature increases slightly and the peak at higher field moves in a broad arc as the temperature is raised while the original lower field peak stays at a roughly constant position but begins to bend to lower fields near T_N.

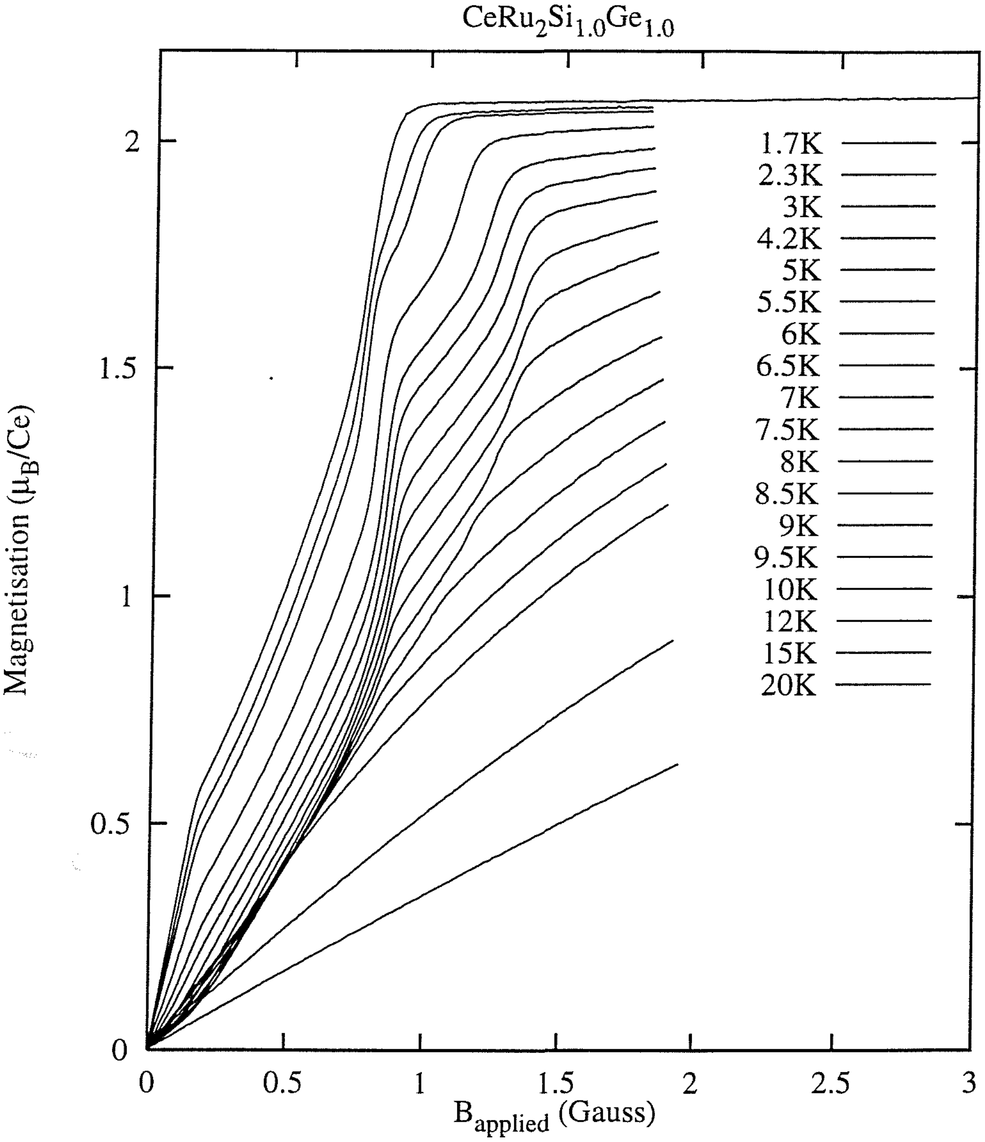

Figure 6.7: Magnetisation in an applied field up to 2T. There are possibly three metamagnetic steps in this data.

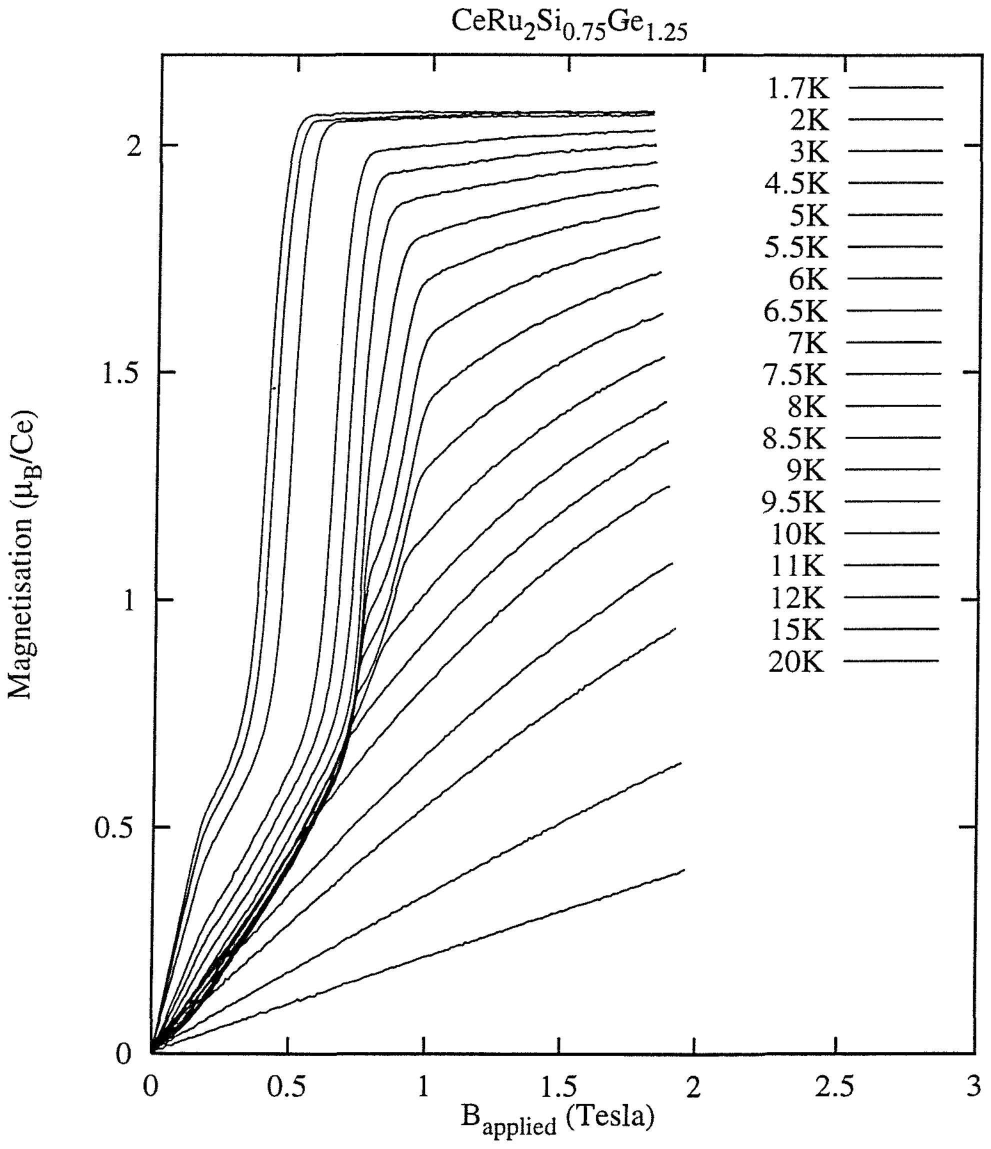

Figure 6.8: Magnetisation in an applied field up to 2T. There are three metamagnetic steps in this data with no evidence of a ferromagnetic phase at the lowest temperature.

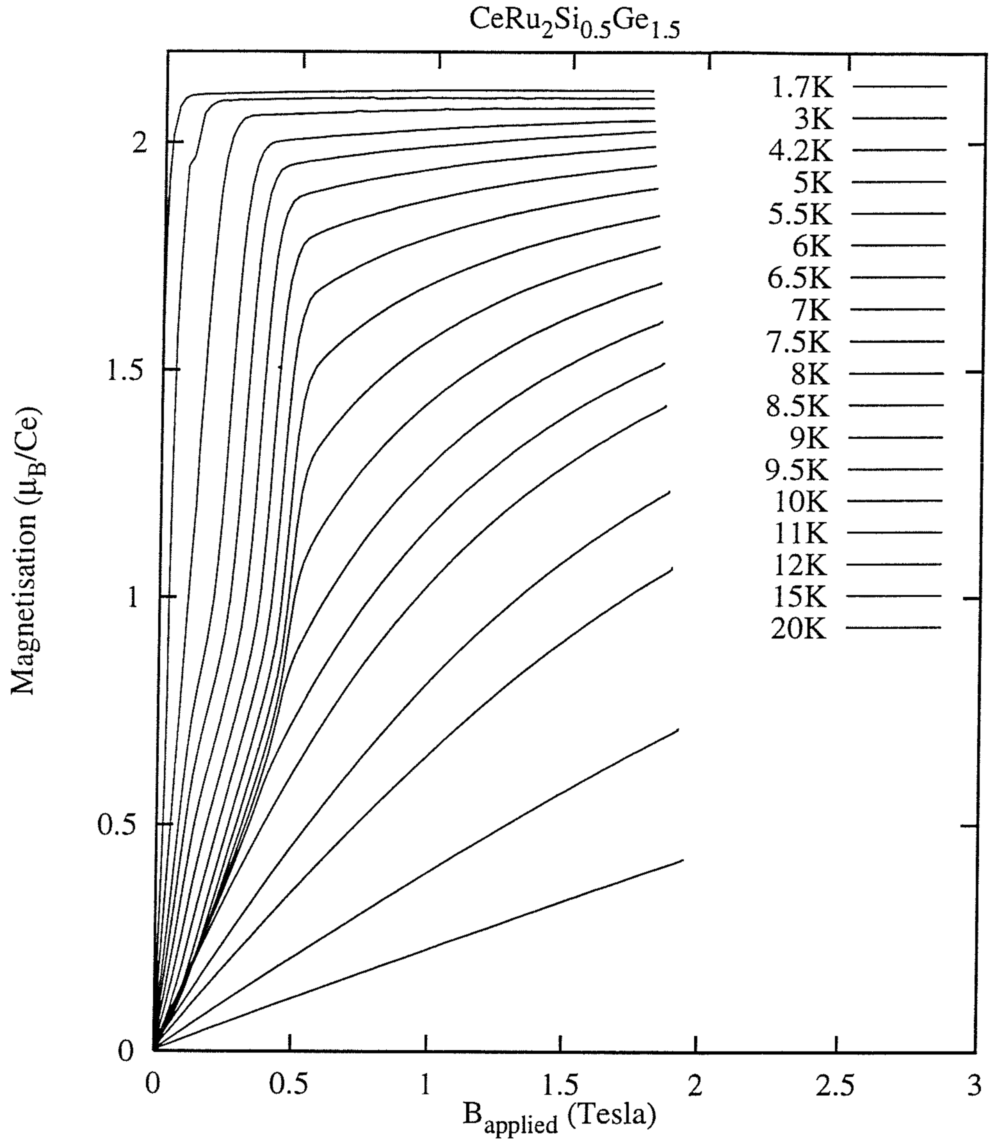

Figure 6.9: Magnetisation for $CeRu_2Si_{0.5}Ge_{1.5}$ in an applied field up to 2T.

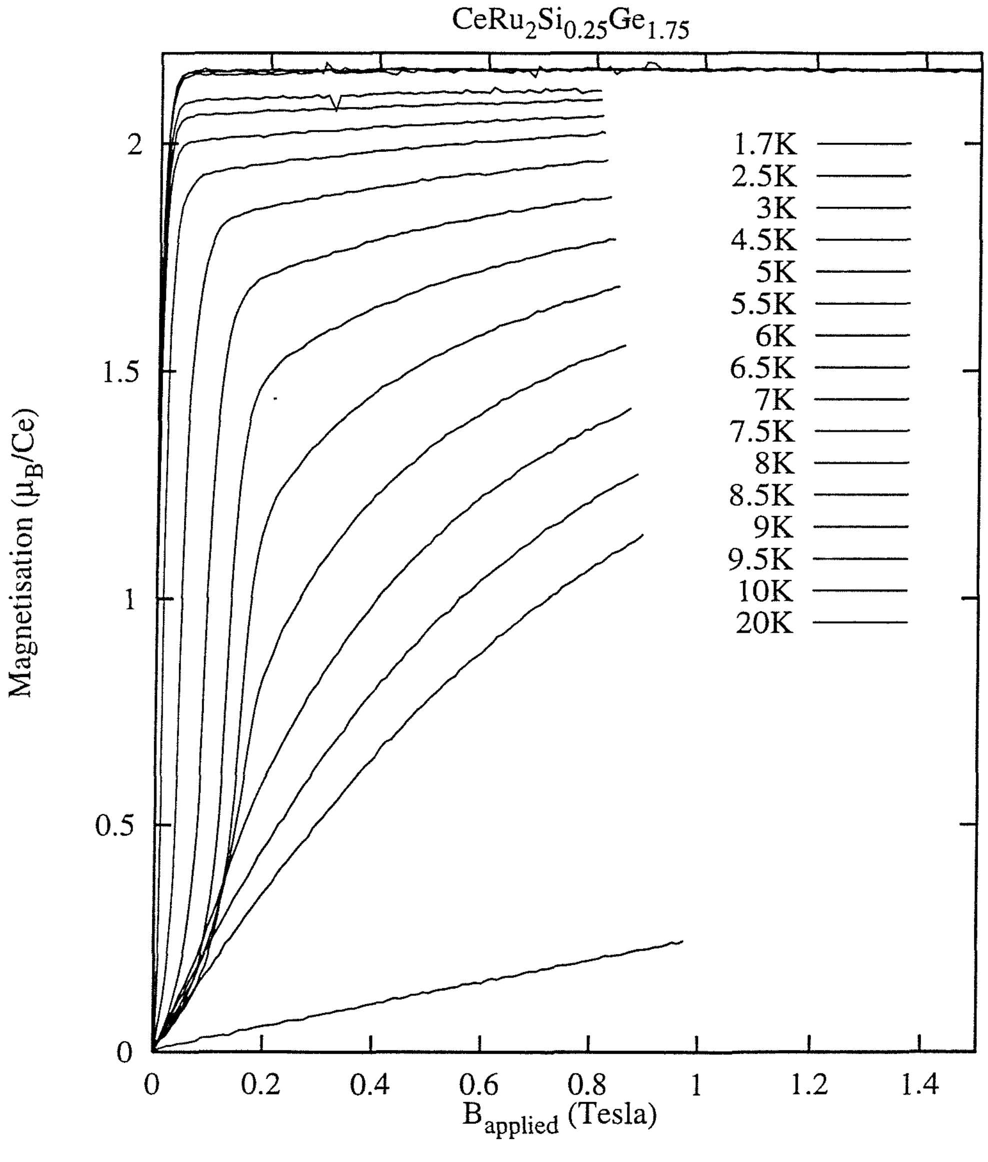

Figure 6.10: Magnetisation in an applied field up to 2T. There is just one metamagnetic step in this data which corresponds to a jump into the a ferromagnetic state.

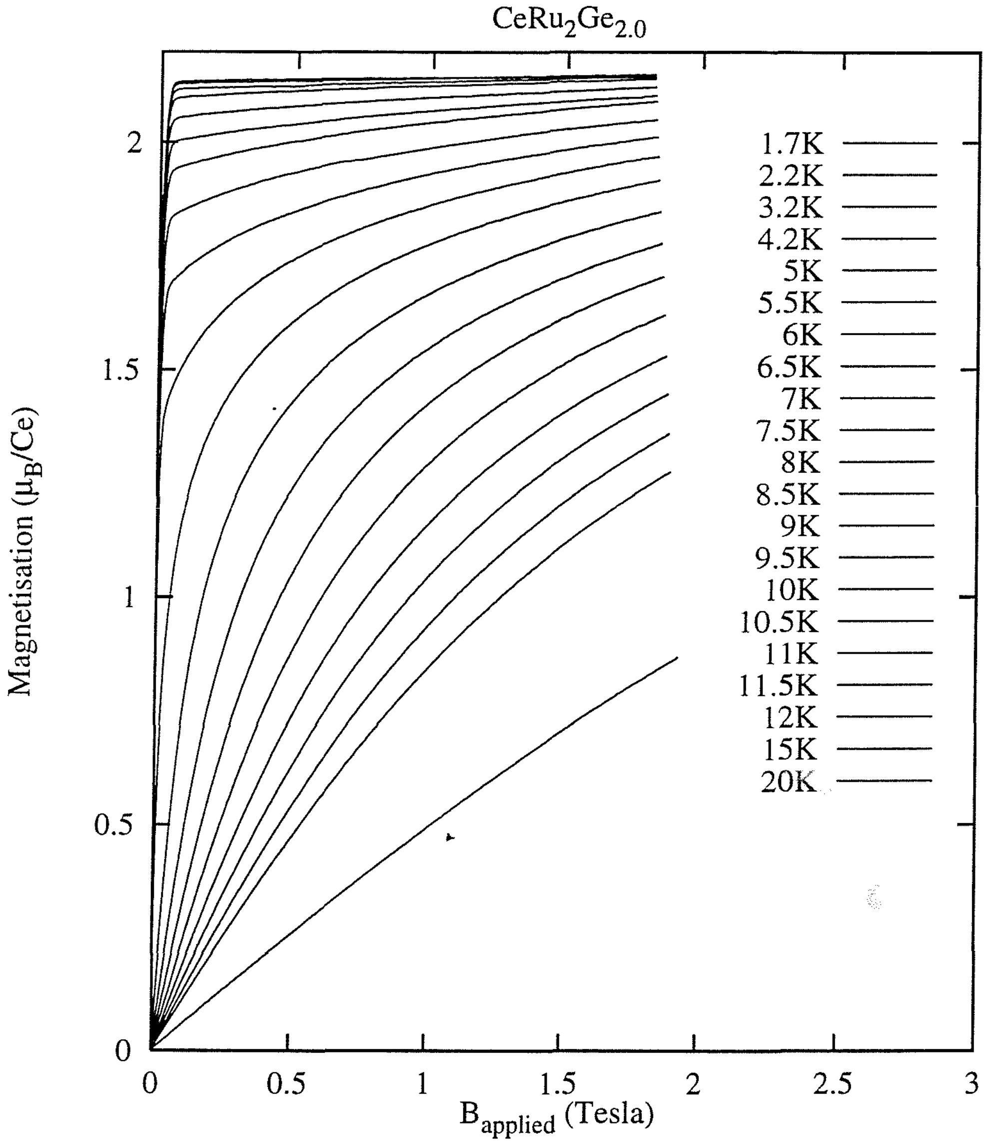

Figure 6.11: Magnetisation isotherms of the ferromagnet $CeRu_2Ge_2$. This data shows no metamagnetic steps. T_C is estimated to be 8K. The 8K critical isotherm roughly follows the scaling law $H \propto M^\delta$, with $\delta \sim 7.5$ whereas the Ising model with a 3-D order parameter gives $\delta = 4.78$ [34].

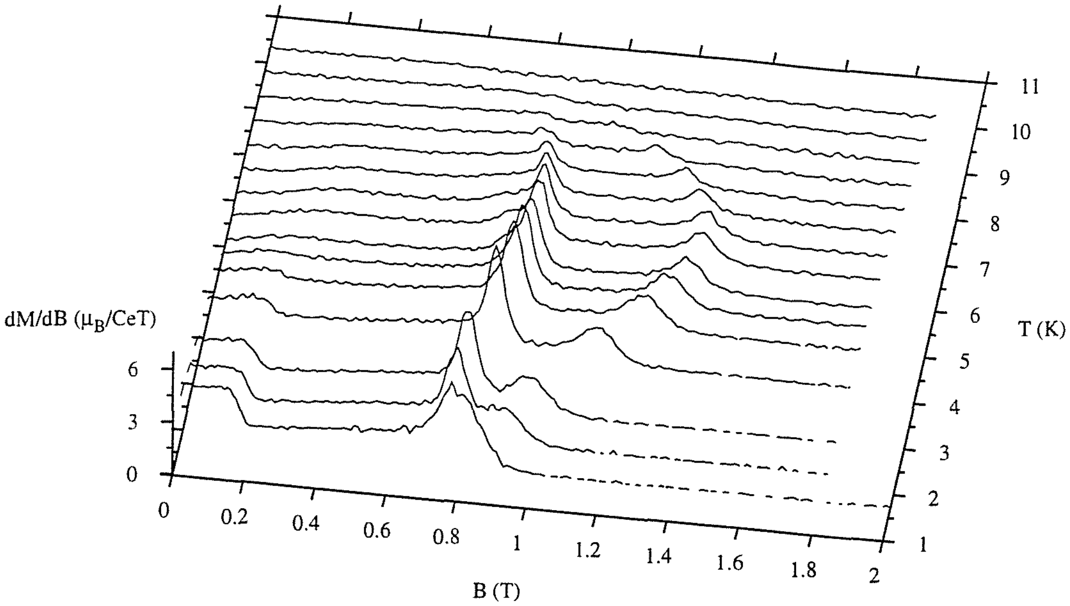

Figure 6.12: The data of figure 6.7 are plotted here on a three dimensional grid. The vertical axis is the derivative of the figure 6.7 data. The ridges are where there are meta-magnetic steps in the magnetisation and hence separate different regions of the phase diagram.

By taking the centre of the peaks and steps in $\frac{dM}{dB}$ as the boundary between different phases we can plot a rough phase diagram from the magnetisation data. For $x = 1.0$ and $x = 1.25$ phase diagrams are shown in figure 6.13 and the phase diagrams of the $x = 1.5$ and $x = 1.75$ alloys are shown in figure 6.14. The ends of the lines indicate where it becomes impossible to determine any features from the magnetisation and its derivative. It is not possible to determine from the magnetisation data exactly what changes take place in these systems as we go through the various phase boundaries, however, looking at the diagrams, figs. 6.13(a) and 6.13(b), we note that the line H_a corresponds to a kink in the magnetisation but the lines H_b and H_c correspond to metamagnetic steps. The kink at H_a was also found in an magnetisation measurement on a polycrystalline alloy with $x = 1.2$ but did not appear in measurements on a piece of a Czochralski grown single crystal with $x = 1.0$ [99]. It is not clear how this kink can be explained by concentration fluctuations in polycrystalline samples but it may be related to this problem.

We expect that the line H_c corresponds to the transition into a polarized ferromagnetic state since the magnetisation saturates above this. So far there have not been any neutron diffraction experiments in an applied field on alloys with these compositions. Work on lower Ge compositions and the La substituted alloys show

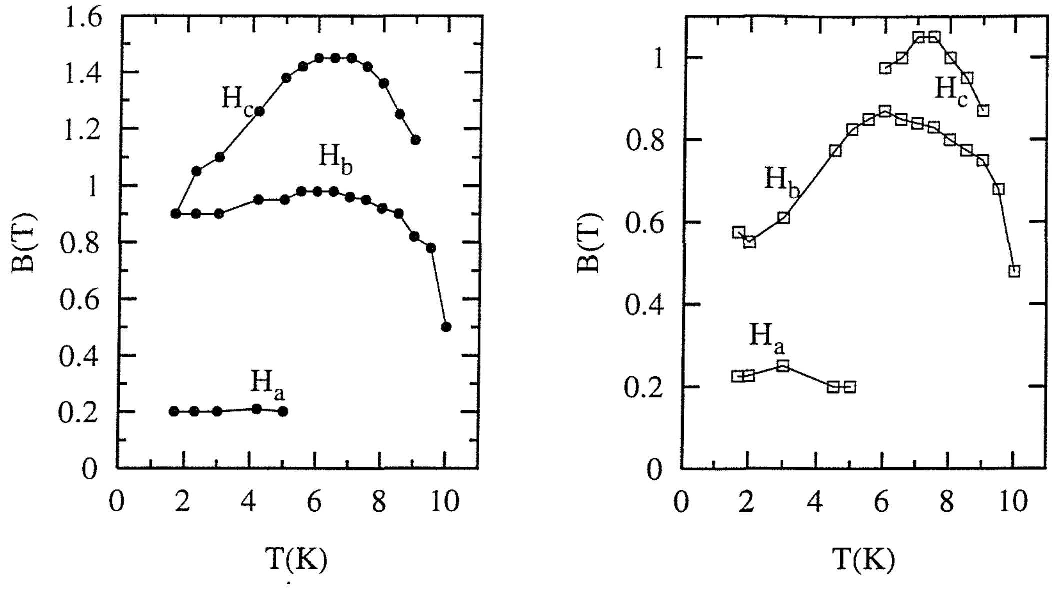

(a) Phase diagram of $CeRu_2Si_{1.0}Ge_{1.0}$ derived from magnetisation data. Several phase boundaries are seen.

(b) Phase diagram of $CeRu_2Si_{0.75}Ge_{1.25}$ derived from magnetisation data. Phase lines are shifted slightly compared to figure 6.13(a).

Figure 6.13: Two approximate phase diagrams derived from magnetisation data. Three regions can be identified in each and the dividing lines are labeled H_a, H_b and H_c. Figure 6.13(b) shows that the region between H_b and H_c is squeezed out as x increases.

modulated order in zero field with wavevector $Q \approx (0.309, 0, 0)$ and it is likely that the same occurs in these alloys. This means that the lines H_a and H_b most likely divide phases with different types of modulated order. It interesting that the line H_a does not continue up to T_N implying that it goes to zero field near 6K, approximately where the low field susceptibility starts to increase. In figure 6.14(a) we see that the effect, on the phase diagram, of adding Ge is to squeeze out the region between H_b and H_c so that the line H_b is the boundary to the polarized ferromagnetic state. On increasing the Ge content to $x = 1.75$ the majority of the phase diagram is ferromagnetic. Figure 6.14(b) shows a small region bounded by the line H_b which must be the only region with antiferromagnetic order. This diagram ties in nicely with the low field susceptibility if we consider what happens as we decrease the temperature in zero field – near T_N we enter an antiferromagnetic phase then at $\sim$ 6K we cross into a new regime. Figure 6.3 shows that H_b bounds an antiferromagnetic phase which quickly goes over to a ferromagnetic one at $\sim$ 6K.

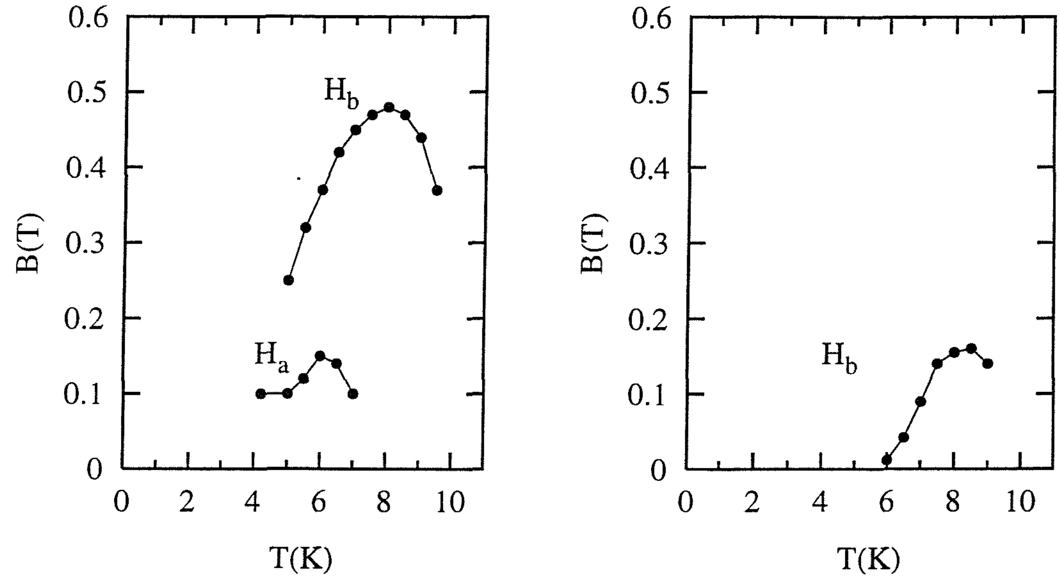

(a) Phase diagram of $CeRu_2Si_{0.5}Ge_{1.5}$ derived from magnetisation data.

(b) Phase diagram of $CeRu_2Si_{0.25}Ge_{1.75}$ derived from magnetisation data.

Figure 6.14: Two approximate phase diagrams derived from magnetisation data. Three regions can be identified in each and the dividing lines are labeled H_a, H_b and H_c. Figure 6.14(b) shows that the region between H_b and H_c is squeezed out as x increases.

6.4 Neutron scattering measurements.

Neutron scattering measurements were carried out on the IN6 time of flight spectrometer at ILL, France, with an incident energy of 3.1meV. Crushed polycrystalline alloys $x = 1.25$, 1.5 and 1.75 were studied in detail over the temperature range 150 - 1.6K and the response in the $x = 1.0$ alloy for temperatures T< 10K was closely examined also. The raw time of flight spectra were corrected for sample absorbtion, self shielding and background scattering and converted to energy transfer. The spectra were normalised to the scattering from a vanadium plate, which also corrected for different detector efficiencies.

The data from the bank of detectors on IN6 were grouped so that 19 effective detectors were analysed with elastic Q's from 0.264–2.046 $Å^{-1}$, at roughly $0.1Å^{-1}$ intervals. The elastic scattering from the vanadium plate was fitted for each detector group. A Gaussian lineshape plus a small Lorentzian was used to represent the resolution function of the instrument and hence the elastic scattering. The widths of the Gaussian and Lorentzian and the ratio of their areas for each detector group were used as a constant parameters when fitting the elastic line in all the other data.

Detector groups 11, 14, and 15, at $Q = 1.27$, 1.57, 1.68 $Å^{-1}$ respectively, contained Bragg peaks. The positions of these peaks were consistent with the (103), (112) and (004) nuclear Bragg reflections of the tetragonal structure.

Dakin *et al* [62, 77] studied alloys with concentrations up to $x = 1.0$ previously. They found a Lorentzian quasielastic line in all the alloys. The linewidth of the quasielastic scattering was modulated with wavevector transfer indicating the presence of intersite interactions. They also saw an inelastic excitation in one low temperature measurement. This excitation was unexpected because these alloys are Ising–like and no spinwave excitations are allowed in this case. The experiments carried out here have investigated the nature of this excitation in more detail, in order to determine how it changes with composition and to look at its energy and wavevector dependence.

For temperatures, T, such that 10K<T<150K we find quasielastic scattering in all the alloys. Each of the spectra were fitted to the sum of the resolution function described above, representing the elastic scattering and a Lorentzian, convoluted with the resolution function. The Lorentzian was also multiplied by the detailed balance factor. This formalism gave excellent fits for the first 12 detector groups but became more unreliable for the larger Q groups, because the parameters for the resolution function fitted from the vanadium data appeared to be too large. It is worth noting that all the data have been treated as constant Q data when in fact it is constant scattering angle, ϕ, data. If the scattering varies smoothly with Q this will not introduce significant errors.

In section 1.9 an expression for the generalised susceptibility was given. The imaginary part of the generalised susceptibility is what we measure with neutron scattering and we see that equation (1.36) in section 1.9 describes a quasielastic Lorentzian which is what obtains here. The linewidth was largest in the alloys closest to $CeRu_2Si_2$ and decreases with an increase in Ge content x. This is consistent with the hybridisation decreasing with increasing x.

In all the alloys the half width, Γ, of the quasielastic Lorentzian was both temperature and wavevector dependent. This was previously observed in alloys at the other end of the composition range [97]. Figure 6.15 shows an example of the fits for the first six detector groups with data for $CeRu_2Si_{0.75}Ge_{1.25}$. Labels in the figure indicate the average elastic wavevector and average scattering angle, 2ϕ, for each group.

It was possible to fit the wavevector dependence by assuming a form for the wavevector dependent linewidth as

$$\Gamma(Q) = \Gamma_0 \left[1 - \chi_0 \mathcal{J}(Q)\right] , \tag{6.1}$$

$$\text{with} \qquad \mathcal{J}(Q) = \sum_n \mathcal{J}_n \exp(i\boldsymbol{Q}.\boldsymbol{r}_n) , \tag{6.2}$$

as defined in section 1.9, where n labels near neighbours in the lattice at a distance r_n corresponding to exchange parameter $\mathcal{J}_n$. Equation (6.2) needs to be spherically averaged because we are dealing with a polycrystalline sample and this leads to,

$$\mathcal{J}(Q) = \sum_n \mathcal{J}_n \frac{\sin(Qr_n)}{Qr_n} \tag{6.3}$$

so that $\Gamma(Q)$ is now,

$$\Gamma(Q) = \Gamma_0 \left[1 - \sum_n \chi_0 \mathcal{J}_n \frac{\sin(Qr_n)}{Qr_n}\right] . \tag{6.4}$$

We may fit the form of $\Gamma(Q)$ using Γ_0 and $\chi_0\mathcal{J}_n$[†] as parameters. Within RPA, as shown in section 1.9, the product $\Gamma(Q)\chi(Q) = \Gamma_0\chi_0$ is independent of Q.

[†] The value of $\chi\mathcal{J}_n$ must be fitted as one parameter because since only the value of the product will be unique and not the individual values of χ and $\mathcal{J}_n$.

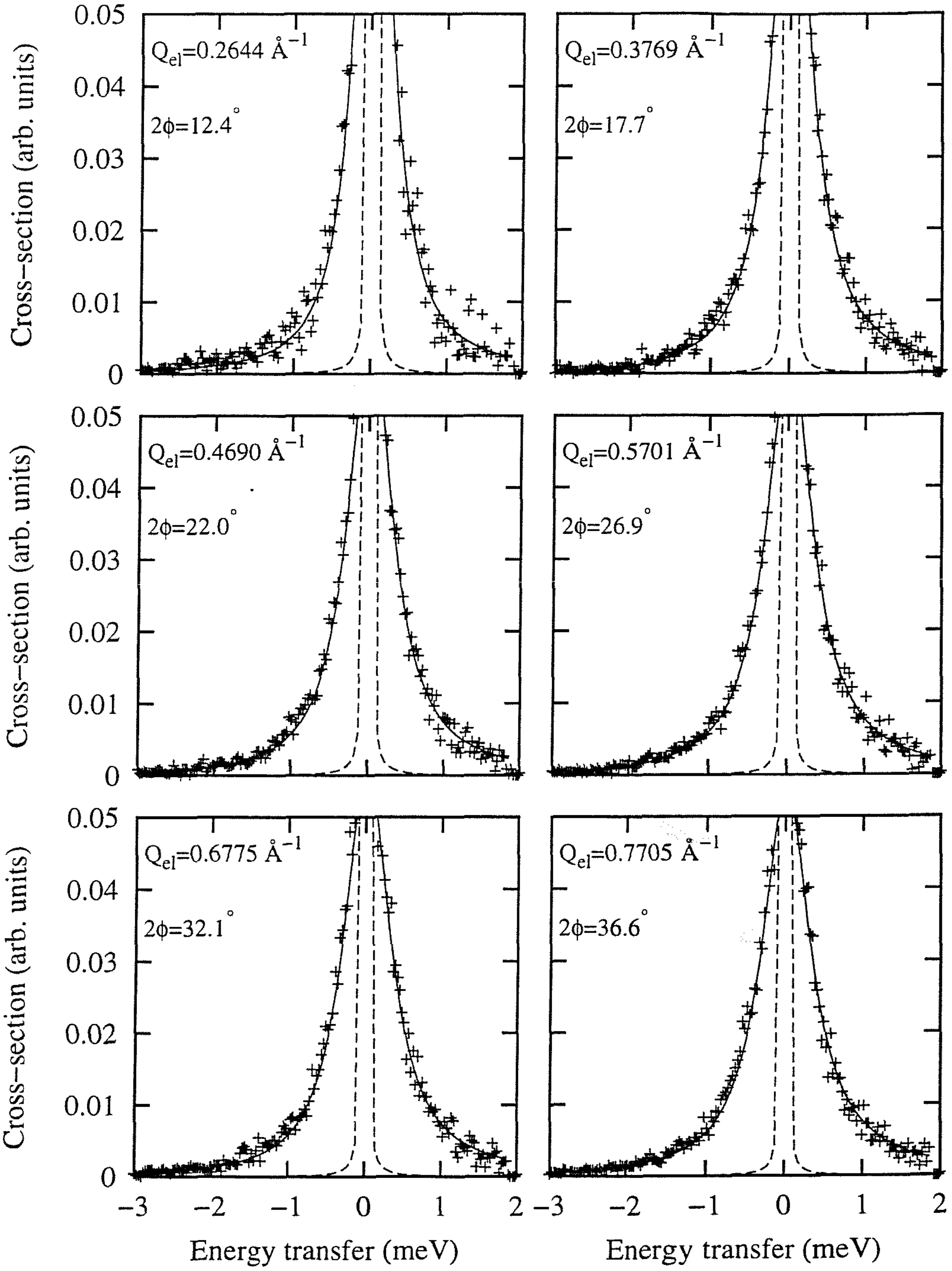

Figure 6.15: Neutron scattering in $\mathrm{CeRu_2Si_{0.75}Ge_{1.25}}$ in different detector groups. The solid lines show total fits using a Lorentzian quasielastic line and the dashed line shows the elastic line used as part of the fit.

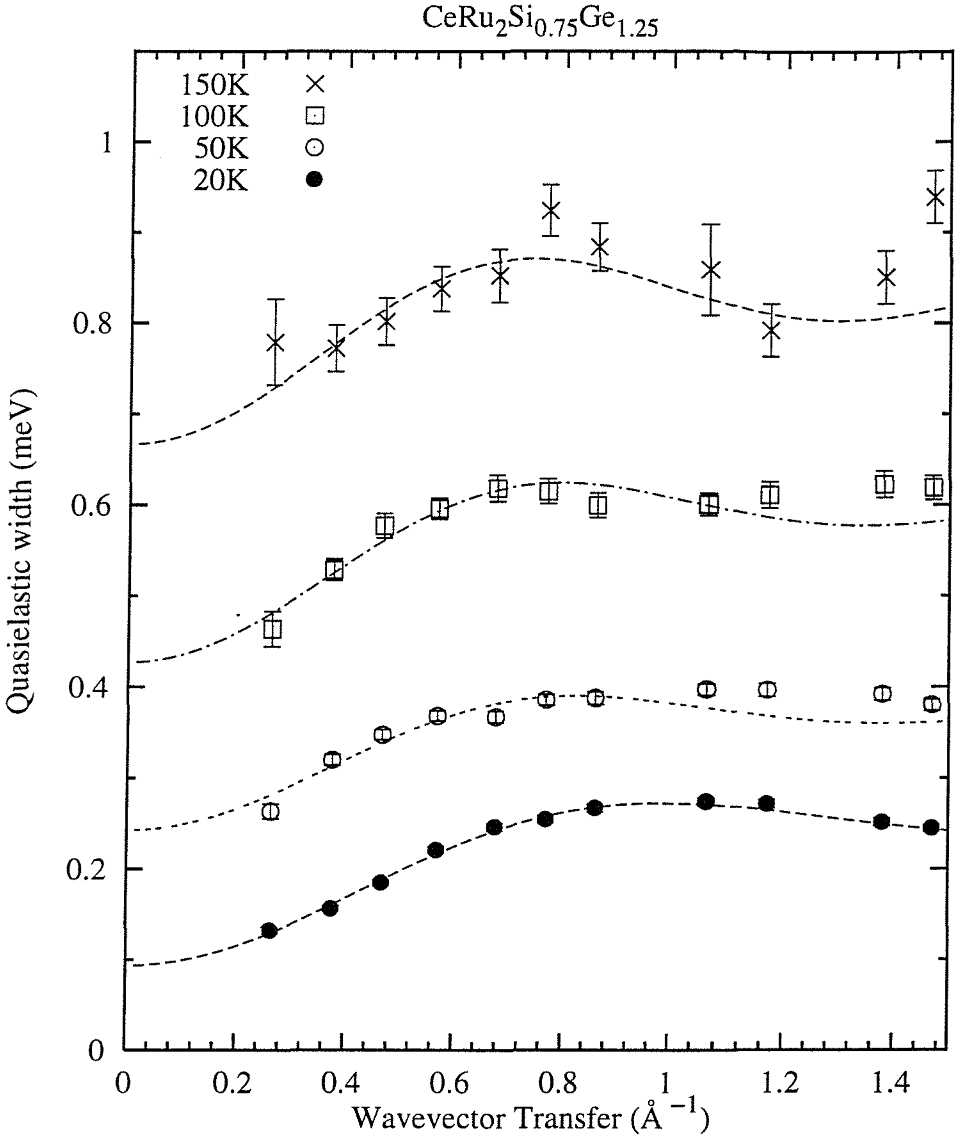

Figure 6.16: Quasielastic linewidth in $CeRu_2Si_{0.75}Ge_{1.25}$. The lines show fits to equation (6.4) using three parameters. Only the data up to $Q = 1.0$Å^{-1} was used in the fit.

The data was fitted up to $Q \approx 1$Å^{-1} corresponding to the edge of the Brillouin zone. Two parameters $\chi_0\mathcal{J}_1$ and $\chi_0\mathcal{J}_2$ were used. It was possible to include many more parameters, $\chi_0\mathcal{J}_n$, to fit a line through every data point but that was not considered sensible since there was no unique combination. Because only $\chi_0\mathcal{J}_1$ and $\chi_0\mathcal{J}_2$ were used there is considerable uncertainty in the value of $\sum_n \mathcal{J}_n$ but this cannot be avoided. An example of some of the fits are given in figure 6.16, which shows the variation of the quasielastic linewidth in $CeRu_2Si_{0.75}Ge_{1.25}$ as a function of wavevector and temperature. The lines are fits to equation (6.4). The fits give values of Γ_0 at different temperatures and the values of $\chi_0\mathcal{J}_1$ and $\chi_0\mathcal{J}_2$. If, from the original fits of the Lorentzian quasielastic line, we plot the value of $\Gamma(Q)$ and $\chi(Q)$ as a product this should be independent of Q. This has been done in figure 6.19. Where $\chi(Q)$ was given by the area of the fitted Lorentzian. We can find the value of $\Gamma_0\chi_0$ and since Γ_0 has been found separately we can also obtain χ_0.

6.4.1 Single ion behaviour

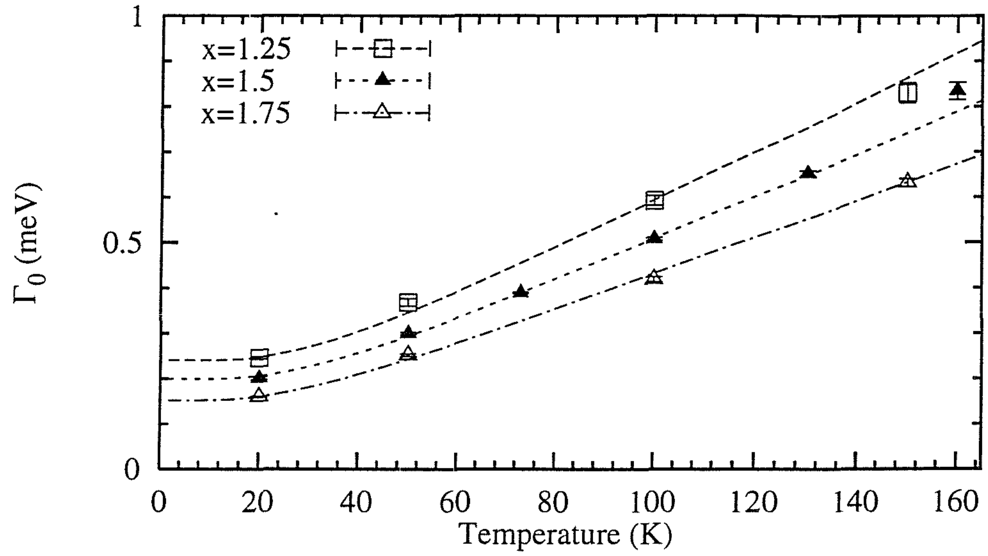

Figure 6.17: Behaviour of single ion linewidth as a function of temperature. The straight lines are fits using equation (6.6). The $T = 0$K intercept gives a measure of the Kondo energy.

The single ion behaviour is revealed by the parameters Γ_0 and χ_0. The single ion linewidth for $x = 1.25$, $x = 1.5$, and $x = 1.75$ as a function of temperature is shown in figure 6.17. Kondo lattice compounds are often found to have a linewidth which goes as [32]

$$\Gamma_0 \propto T^{\frac{1}{2}}\,. \tag{6.5}$$

The alloys studied by Dakin *et al* were found to have a temperature dependence of the form

$$\Gamma_0(T) = I\coth\left(\frac{1}{Gk_BT}\right)\,, \tag{6.6}$$

with I as the $T = 0$ intercept and G as the gradient. It was found that equation (6.6) gave good fits to the data for $x = 1.75$ and $x = 1.5$, however, a simple straight line fit was superior for the $x = 1.25$ alloy. In order to compare this work with that of ref. [77] the form of equation (6.6) has been used for all the data. The fits are shown as lines in figure 6.17. The figure shows the intercept decreasing with an increase in Ge content.

The Kondo temperature, T_K may be taken to be the zero temperature intercept of $\Gamma_0 = k_B T_K$. Dakin et al [77, 97] found the Kondo temperature to scale reasonably well with the change in coupling parameter $\rho \mathcal{J}_{sf}$ as derived from the high temperature slope of Γ_0 vs. T. For compositions between $x = 1.0$ and $x = 2.0$ this scaling does not appear to be followed, the Kondo temperature measured by the quasielastic linewidth is only weakly dependent on the concentration of Ge. Figure 6.18 shows how the Kondo temperature changes across the series.

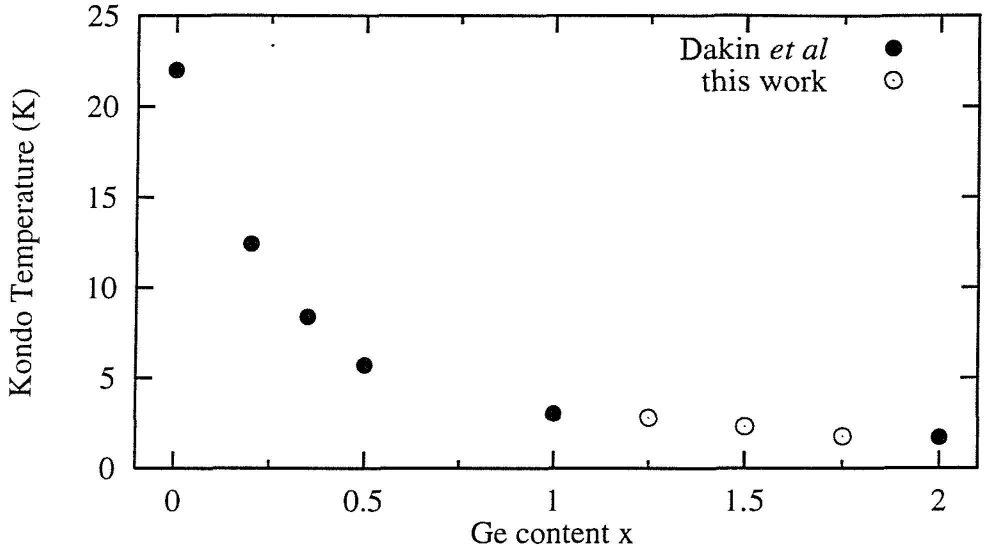

Figure 6.18: The Kondo temperature as a function of Ge content in the alloy. The Kondo temperature does not change much beyond the composition $x = 1.0$.

Figure 6.19 shows the product $\chi(Q)\Gamma(Q)$ as a function of Q for $CeRu_2Si_{0.75}Ge_{1.25}$, the product does appear to be independent of Q as indicated by the lines. The single ion susceptibility at a given temperature is found by dividing the value of $\chi_0\Gamma_0$ by Γ_0. The single ion susceptibility closely follows the Curie law for the three alloys studied, the data is presented in figure 6.20. The same Curie law behaviour was observed at the lower Ge composition range [77].

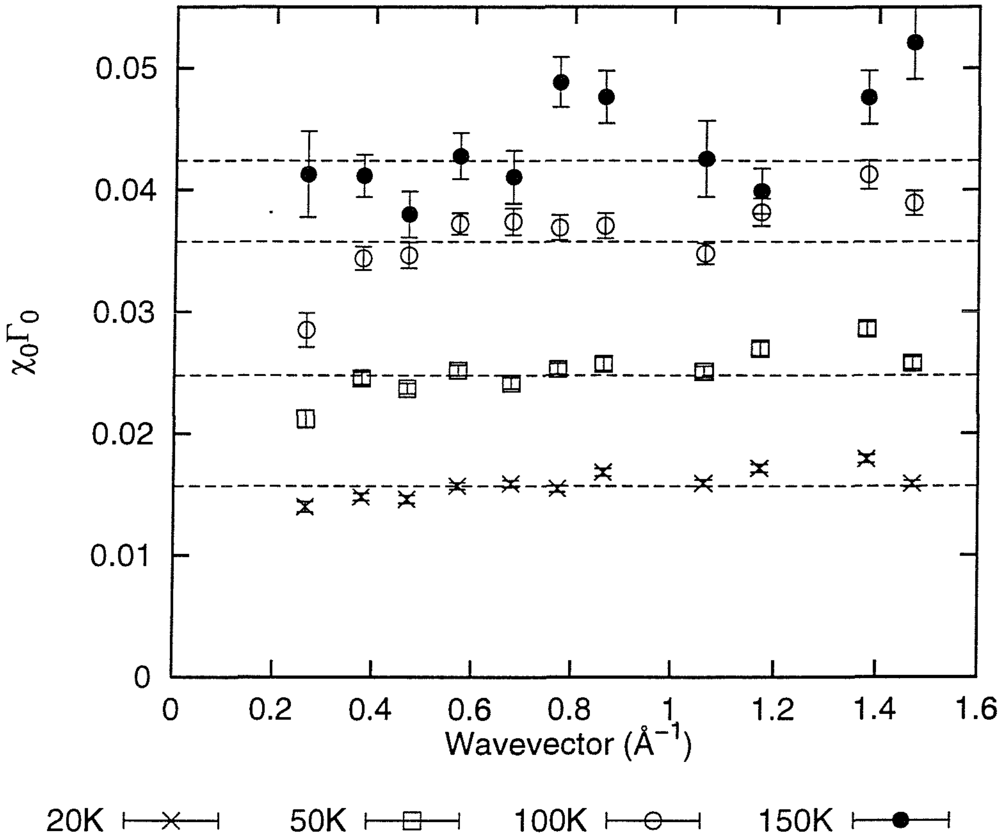

Figure 6.19: Variation of $\chi(Q)\Gamma(Q)$ in $CeRu_2Si_{0.75}Ge_{1.25}$. The value is independent of Q at any temperature.

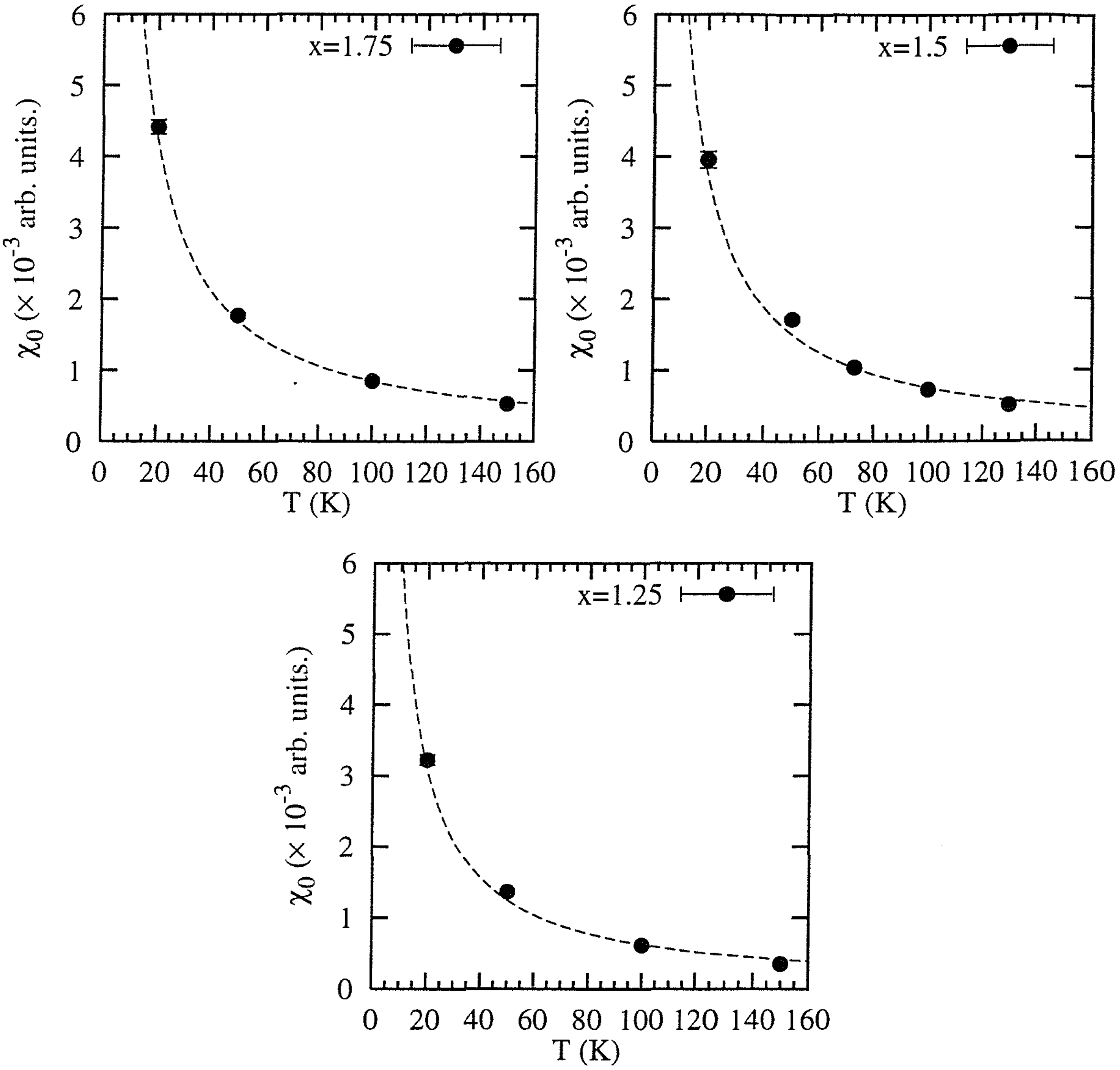

Figure 6.20: χ_0 as a function of temperature for x = 1.75, 1.5, 1.25 alloys. The dashed lines show Curies law. The magnitude of the Curie constant, $C = \frac{N}{3Vk_B}(g\mu_B)^2 J(J+1)$, was treated as the only adjustable parameter.

6.4.2 Intersite interactions.

In the preceeding sections the analysis of the neutron scattering data has yielded information on single site properties but we can also get information on intersite properties. In particular we can determine the uniform susceptibility, that is $\chi(Q = 0)$, and also the $Q = 0$ linewidth. We expect that these quantities should behave like those of typical magnets.

Uniform Susceptibility

The uniform susceptibility, $\chi(Q = 0)$, should follow the susceptibility measured in, for example, a VSM. For these alloys, which order magnetically, we would expect $\chi(Q = 0)$ to follow the Curie-Weiss law. $\chi(Q)$ is defined as

$$\chi(Q) = \frac{\chi_0}{1 - \chi_0 \mathcal{J}(Q)} \tag{6.7}$$

$$= \frac{\chi_0}{1 - \sum_n \chi_0 \mathcal{J}_n} \quad \text{when } Q = 0\,. \tag{6.8}$$

where the value $\sum_n \chi_0 \mathcal{J}_n$ is extracted by summing the parameters used in equation (6.4).

In practice this gave reasonable fits to the data but the Curie temperatures were very small, typically between −1K and zero. The Curie temperatures should be ~ -10K. This is most likely due to the considerable error in $\sum_n \chi_0 Jn$. However we can see from equation (6.8) that the ordering temperature is determined by the condition that $1 - \chi_0 \mathcal{J}(Q_{\mathrm{max}}) = 0$ where Q_{max} is the wavevector for which $\mathcal{J}$ is a maximum. These alloys order at an incommensurate value of Q so the uniform susceptibility will not necessarily diverge at the correct $\mathrm{T_C}$.

Linewidth $\Gamma(Q = 0)$.

The $Q = 0$ linewidth was found to be linear with temperature. Figure 6.21 shows the measured behaviour in the $x = 1.25$, 1.5 and 1.75 alloys. The intercept for the $x = 1.75$ and 1.5 alloys is not zero. There will be some uncertainty in the values of $\Gamma(Q)$ because of the ambiguity of $\sum_n \chi_0 \mathcal{J}_n$. As for $\chi(Q)$ we are probing the linewidth at $Q = 0$ which is not at the ordering wavevector, this might make $\Gamma(Q)$ intercept at a non zero temperature.

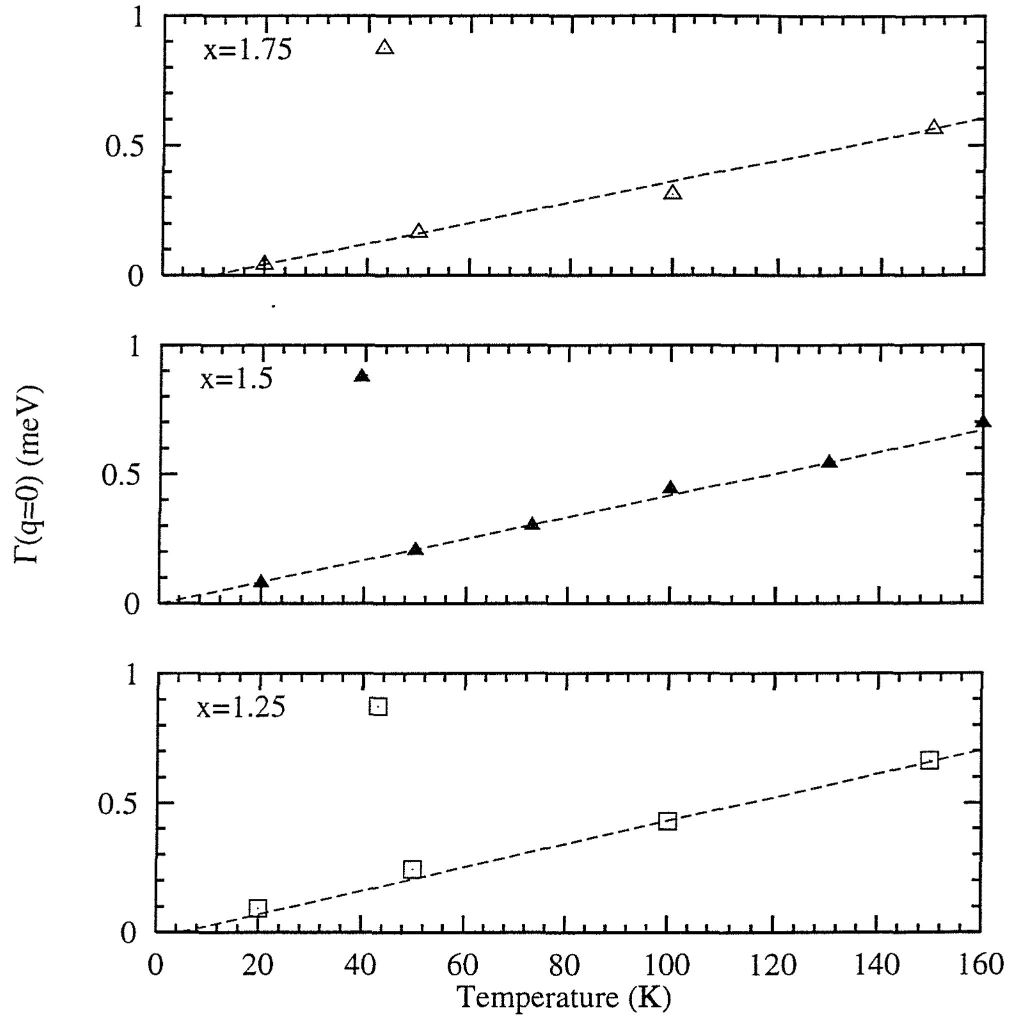

Figure 6.21: Korringa like behaviour of the $Q = 0$ linewidth. The intercept on the temperature axis is indication of the uncertainty in the measurements.

6.4.3 Low Temperature response.

Dakin *et al* observed an inelastic response in the $x = 1.0$ alloy for one measurement below $\sim$ 3K. The Ising nature of these systems means that there should be no transverse component to each magnetic spin and hence there can be no transverse spin-waves. The inelastic peak observed in the neutron cross-section must be due to a *longitudinal* spin fluctuation. In the alloys studied here only the $x = 1.0$ and 1.25 alloys show this excitation, and only at temperatures below approximately 2K.

All the alloys showed a large increase in the intensity of the elastic scattering for detector group number three below their ordering temperatures. The average wavevector for group number three is $Q = 0.469\text{Å}^{-1}$. We can assume that this additional elastic intensity is due to Bragg scattering from the sinusoidally modulated magnetic structure. Work on other alloys has shown that the ordering wavevector is $Q \approx 0.3$ and therefore we would expect that the same should be true here. It is not clear why there is a difference.

In the $x = 1.5$ and $x = 1.75$ alloys the intensity of the elastic scattering in detector group three showed a decrease at lower temperatures indicating that the magnetic structure was changing. None of the other detector groups indicated any increase. This suggests that the modulation wavevector was not changing to represent another antiferromagnetic state but was changing to $Q = 0$. This is in agreement with our magnetisation data in which there is an apparent crossover to ferromagnetism at lower temperatures.

The following sections outlines a brief summary of the neutron scattering results for temperatures below the ordering temperature of each alloy.

$CeRu_2Si_{0.25}Ge_{1.75}$

For $CeRu_2Si_{0.25}Ge_{1.75}$ figure 6.22 shows the quasielastic scattering collapsing below T_C. At the lowest temperatures the scattering was well described by the elastic line with no other peaks present. This is consistent with the low temperature phase of the Ising system, for which there should be no dynamics and hence no inelastic scattering. The width and area of the quasielastic peak collapse below the ordering temperature.

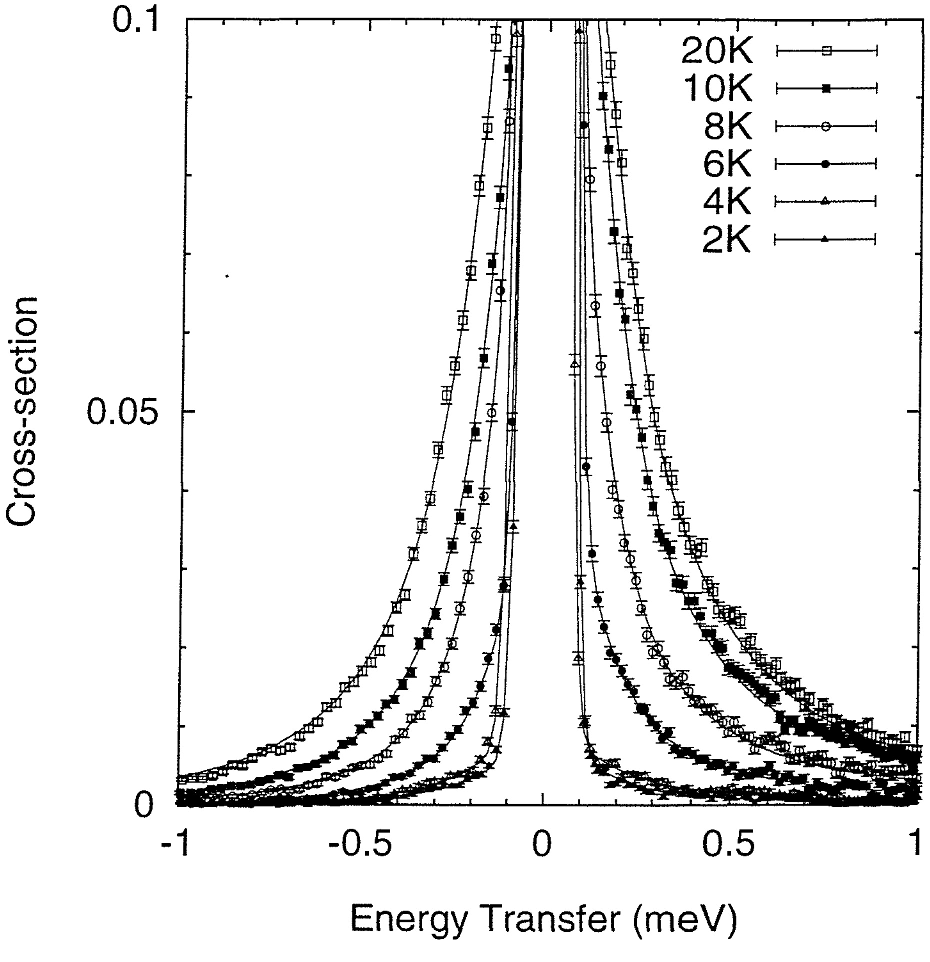

Figure 6.22: Temperature dependence of the quasielastic line for $x = 1.75$ alloy. The intensity collapses below T_c. Solid lines are fits to a Lorentzian lineshape

$CeRu_2Si_{0.5}Ge_{1.5}$

In the lowest temperature regime for $CeRu_2Si_{0.5}Ge_{1.5}$ the data can be fitted acceptably well with a single elastic line, in a similar manner to the behaviour of $CeRu_2Si_{0.25}Ge_{1.75}$. This again suggests an Ising groundstate with no dynamics. However, if we refer forward to figure 6.24 which shows grouped data, covering a large angle of the available detector, there is some evidence of inelastic scattering. This scattering was too weak to be fitted in any individual detector group. In the next paragraph $CeRu_2Si_{0.75}Ge_{1.25}$ is discussed, this alloy does show inelastic scattering therefore the concentration range between $x = 1.25$ and $x = 1.5$ is the cutoff for the novel low temperature behaviour.

$CeRu_2Si_{0.75}Ge_{1.25}$

In $CeRu_2Si_{0.75}Ge_{1.25}$ an inelastic peak was observed below ~ 2K. The peak was centered around 0.5meV energy transfer with a width of ~ 0.26 meV.

An attempt was made to fit the data by including a symmetrised Lorentzian lineshape to account for scattering in energy loss and energy gain. The fits showed that the position, width and intensity of the excitation was only weakly wavevector dependent. Contour plots of the scattering over the whole wavevector transfer energy transfer grid did not show any clear dispersion. This is a result of the spherical average from the polycrystalline sample: we have measured the average over all possible crystallite orientations which conceals the true behaviour of a wavevector dependent excitation. However the observation of a well defined peak in this circumstance must mean that any dispersion is weak.

The excitation is extremely sensitive to temperature. At 3K there is no sign of any inelastic scattering but at 2.1K the excitation becomes visible. At 1.9K and 1.7K the excitation is clearly present.

$CeRu_2Si_{1.0}Ge_{1.0}$

A clear inelastic peak was observed in $CeRu_2Si_{1.0}Ge_{1.0}$ also. Measurements were made at several temperatures and at 2.5K the peak is just visible. At slightly lower temperatures it becomes more prominent. The evolution of the peak with temperature is shown in figure 6.23.

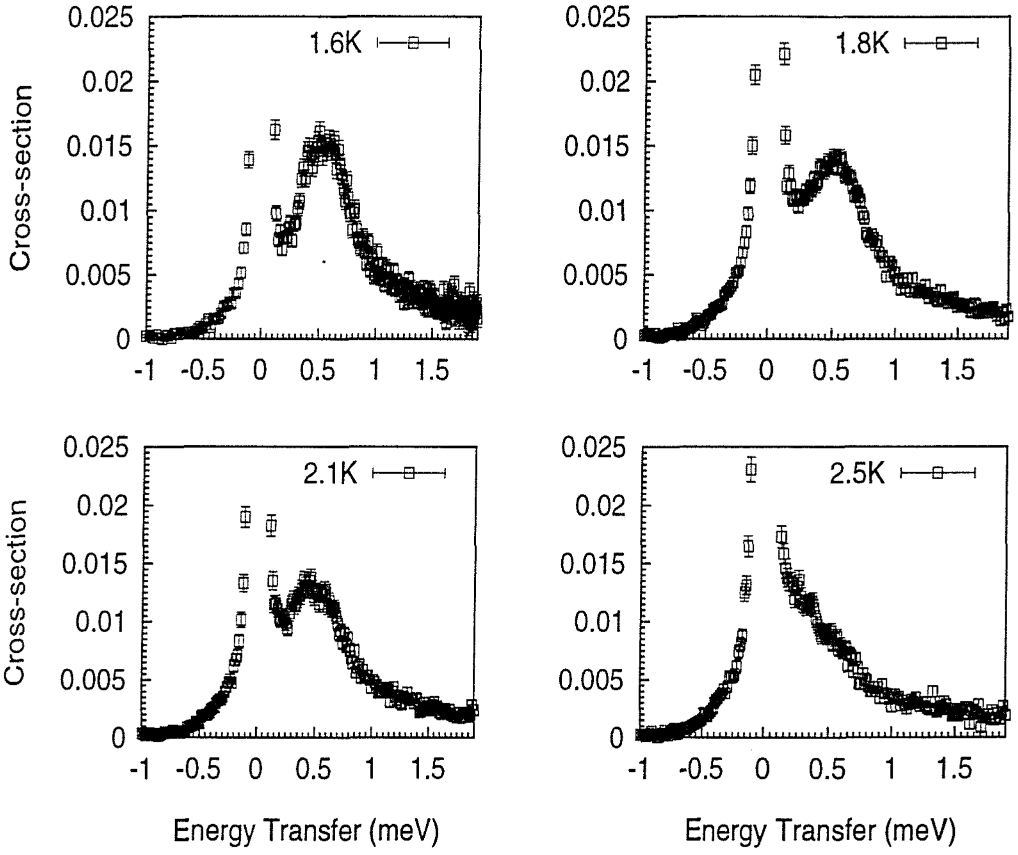

Figure 6.23: Neutron spectrum for the $x = 1.0$ alloy as a function of temperature, showing the collapse of the inelastic excitation. This figure shows grouped data averaged from several detector groups.

At the lowest temperature the peak is well defined, it moves closer to the elastic line as the temperature increases until it merges into a quasielastic response. As for $CeRu_2Si_{0.75}Ge_{1.25}$ attempts to fit this peak showed it to be independent of wavevector which is taken to be a sign that the polycrystalline sample has averaged out any information. Recent work [100] using a single crystal sample of $CeRu_2Si_{1.0}Ge_{1.0}$ has shown that this excitation is indeed wavevector dependent. The excitation has different intensity for different wavevectors in the basal plane and its position shows dispersion, with a wavevector dependent width also. The excitation was measured at several points in the Q=(1,1,0) direction and along the (1,0,0) direction also. The peak was less intense in the (1,0,0) direction [100].

6.4.4 Comparison and model

Figure 6.24 shows a comparison between three of the alloys where the data has been grouped to improve the statistics. This figure shows clearly that the excitation is most prominent for the alloy with the lowest Ge concentration. The temperature scale for the excitation to appear is $\sim$ 2K. We also recall that there are anomalies in the heat capacity and resistivity at $\sim$ 2K for this alloy with which have been used to question the existence of an unknown low temperature phase [99].

The occurrence of the excitation in some of these alloys is unexpected. The temperature at which the excitation occurs is well below the magnetic ordering temperature, therefore, we anticipate the presence of an exchange field which should split the crystal field doublet ground state. As remarked above the excitation cannot be a spin wave, because of the Ising nature of the ground state. Neutrons cannot induce transitions between the split ground state since the magnetic dipole selection rules do not allow transitions between the $|\pm5/2\rangle$ states. Hence this splitting will not produce an observable excitation. This corresponds to the situation for $CeRu_2Ge_2$ with its ferromagnetic groundstate.

To shed more light on this excitation we need to consider the possibility that the two components of the ground state are hybridised together, by the Kondo effect, with the conduction electrons. This conjecture is supported by mean field solutions to the slave–boson treatment of the Anderson Model [101]. For the present purpose we can imagine that the Kondo effect is represented by an off diagonal matrix element between the $|+5/2\rangle$ and $|-5/2\rangle$ states. This results in two basis states which have singlet character.

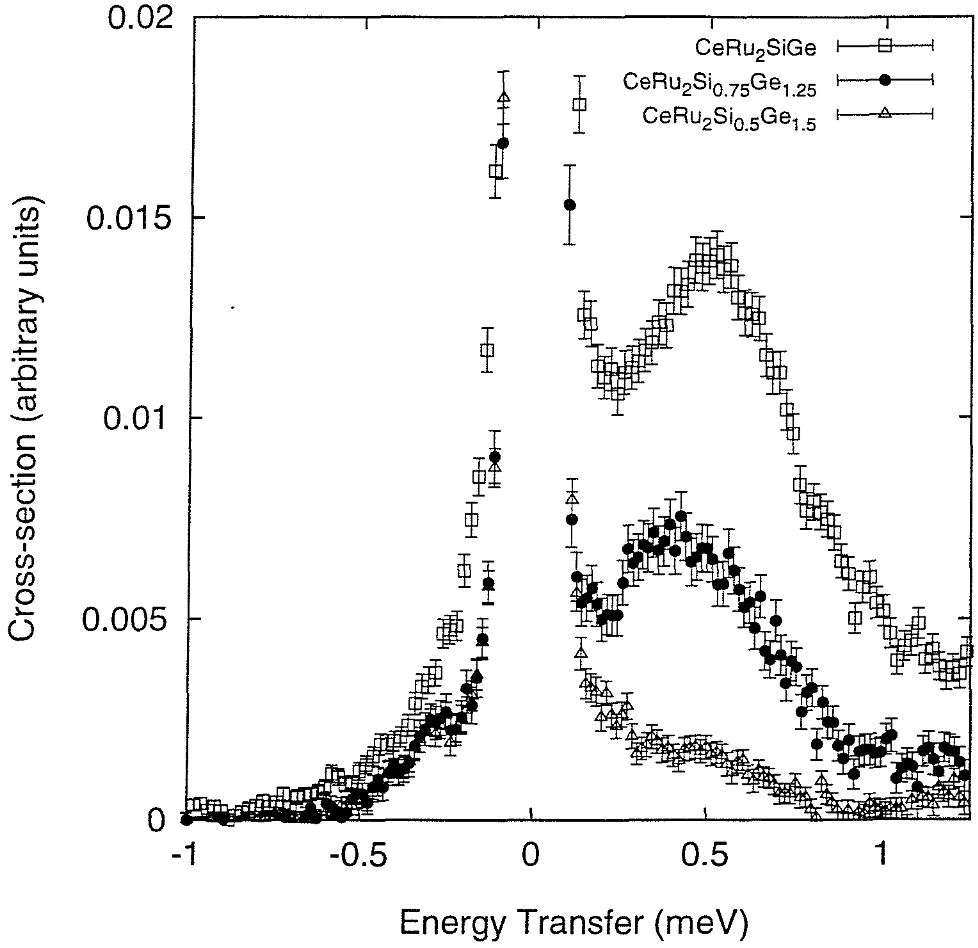

Figure 6.24: Inelastic neutron scattering spectrum for alloys with $x = 1.0, 1.25, 1.5$ at 1.7K. Peak intensity decreases with as x increases.

In $\mathrm{CeRu_2Si_2}$ for example the situation would be two states

$$\psi_a = \frac{1}{\sqrt{2}}\left(|{+5/2}\rangle - |{-5/2}\rangle\right) \tag{6.9}$$

$$\psi_s = \frac{1}{\sqrt{2}}\left(|{+5/2}\rangle + |{-5/2}\rangle\right) \tag{6.10}$$

which are symmetric and antisymmetric combinations of $|\pm 5/2\rangle$ separated by an energy Δ, which is a measure of the strength of the off diagonal matrix element.

We now consider the effects of an applied field (or internal field due to magnetic order). A magnetic field, B, gives rise to diagonal matrix elements in the $|\pm 5/2\rangle$ basis, which are $\pm 5/2 g\mu_B B$. This introduces a Zeeman splitting, and changes the degree of hybridisation between the $|\pm 5/2\rangle$ states.The new basis states are

$$|\psi_1\rangle = \cos\theta|\psi_s\rangle + \sin\theta|\psi_a\rangle \tag{6.11}$$

$$|\psi_2\rangle = \cos\theta|\psi_a\rangle - \sin\theta|\psi_s\rangle \tag{6.12}$$

where $\tan 2\theta = \alpha g\mu_B B/\Delta$, and $\alpha = \langle\psi_a|J_z|\psi_s\rangle$.

In the limit where $\alpha g\mu_B B \gg \Delta$, that is the applied field or exchange field is large compared to the Kondo effect, the wavefunctions revert to the $|\pm 5/2\rangle$ basis. This would be the case for $\mathrm{CeRu_2Ge_2}$.

Within this simple model it is straight forward to calculate the neutron scattering cross-section using RPA as in section 1.9. The result is

$$\begin{aligned}\mathrm{Im}\chi^{zz}(\omega) \propto \cos^2(2\theta)\tanh\left(\frac{\epsilon}{2k_BT}\right) \times \left[\frac{\Gamma}{(\omega-\varepsilon)^2+\Gamma^2} - \frac{\Gamma}{(\omega+\varepsilon)^2+\Gamma^2}\right] \\ + \sin^2(2\theta)\mathrm{sech}^2\left(\frac{\varepsilon}{2k_BT}\right)\frac{\omega}{k_BT} \times \left[\frac{\Gamma}{\omega^2+\Gamma^2}\right]\end{aligned} \tag{6.13}$$

where ε is the exchange spitting of the two states. The main features of this equation are

i. the first term on the right hand side represents inelastic excitations centred at $\pm\varepsilon$, the exchange splitting of the two hybridised states. The weight of this term is a maximum for zero exchange field and its temperature dependence has the normal form expected for a crystal field excitation: $\tanh(\varepsilon/2k_BT)$.

ii. the second term on the right is a quasielastic response (as found in $\mathrm{CeRu_2Ge_2}$). This term is a maximum when $\sin 2\theta = 1$, corresponding to $\Delta = 0$ or the limit $\alpha g\mu_B B \ll \Delta$. The temperature dependence in this case is $\propto \mathrm{sech}^2(\varepsilon/2k_BT)$.

This function falls rapidly to zero at low temperature, and gives the correct qualitative behaviour for the inelastic response in $CeRu_2Ge_2$ and $CeRu_2Si_{0.25}Ge_{1.75}$.

This simple mean field approach can be extended to the case of the saturation magnetisation and the ordering temperature, as a function of the relative strength of the Kondo effect to the exchange field. The predictions are in good qualitative agreement with the experimental results for $CeRu_2Si_{2-x}Ge_x$ alloys.

The identification of this mode as a new type of excitation in a Kondo lattice depends crucially on the Ising nature of the ground state.

6.5 Muon spin relaxation measurements.

Muon spin relaxation measurements were carried out on the MuSR spectrometer at ISIS. A helium flow cryostat was used to reach temperatures down to ~ 1.5K. Crushed polycrystalline samples were mounted on an aluminium plate masked with silver. The MuSR spectrometer was used in longitudinal mode so that longitudinal fields could be applied. Samples with $x = 1.0$, 1.5, 1.75 and 2.0 were measured in the temperature range 1.5K – 20K. Aspects of μSR experiments are discussed in chapter 3.

The aim of these experiments was to examine the behaviour of the low temperature phases of these alloys. Our magnetisation measurements suggest the presence of two low temperature phases. The results of these experiments help us to study this more closely.

The general behaviour for each of the alloys was similar. Above the ordering temperature each alloy showed a weak Lorentzian depolarisation of the muon asymmetry over long times. The total initial asymmetry showed a sharp decrease from the very high value of ~ 0.35 to ~ 0.24 over the first 0.1μs. This initial value is too large, a value of 0.25 is more common for the MuSR spectrometer, and it it likely to be due to some noise at the start of the muon pulse. As a result of this the first $0.1\mu s$ have been ignored in all the data.

All the alloys showed similar features in that above the ordering temperature we see an exponential decay of the polarisation with a damping rate that increases on approaching the magnetic ordering temperature. The initial asymmetry associated with the exponential component dropped sharply at the ordering temperature. Below the ordering temperature the polarisation showed a spontaneously precessing component indicating a coherent internal field. This is unusual because the groundstate is sinusoidally modulated which we would expect to produce a broad field distribution at the muon site.

Some previous attempts have been made to locate the muon stopping site in the I4/MMM tetragonal structure. A μSR study on URu_2Si_2 [102], which has the same structure, found it difficult to determine unambiguously any specific stopping site. Comparisons of the measured and calculated depolarisation due to dipolar fields in $CeRu_2Si_2$ [85] concluded that the muon site was (1/2,1/2,0).

The following sections describe the data for each of the alloys and a comparison is made at the end.

6.5.1 $CeRu_2Ge_2$.

At temperatures above T_C the decay of the asymmetry can be fitted with a Lorentzian depolarisation. The damping rate increases to a peak value at 8K, which gives a rough measure of T_C, in agreement with our magnetisation data. The approach to T_C is clearly indicated by the critical slowing down of magnetic fluctuations which enhances the depolarisation of the muons and $CeRu_2Ge_2$ shows typical ferromagnetic behaviour in this respect. The initial asymmetry drops rapidly at 8K also indicating the magnetic transition. Below the ordering temperature the decay of the asymmetry is more complicated. A clearly defined oscillation is observed, see figure 6.25, which is damped out leaving an almost flat level.

The approach to T_C from above is indicated by the damping rate of the single exponential component, shown in figure 6.26. The line on figure 6.26 is a fit to

$$\lambda(T) = c_0 \left(\frac{T - T_c}{T_c}\right)^\gamma , \tag{6.14}$$

where $c_0 = 0.05$, $\gamma = -0.69$ and $T_c = 7.8$K. The fit indicates critical behaviour in the damping rate parameter λ.

Below T_C the data has been fitted to the form

$$P(t) = a_1 \cos(2\pi\nu t + \phi)e^{-\lambda_1 t} + a_2 e^{-\lambda_2 t} + bck\,, \tag{6.15}$$

with a_1 and a_2 asymmetries, λ_1 and λ_2 damping rates, ν the frequency of the oscillation (in MHz) with a phase shift ϕ and bck is a background.

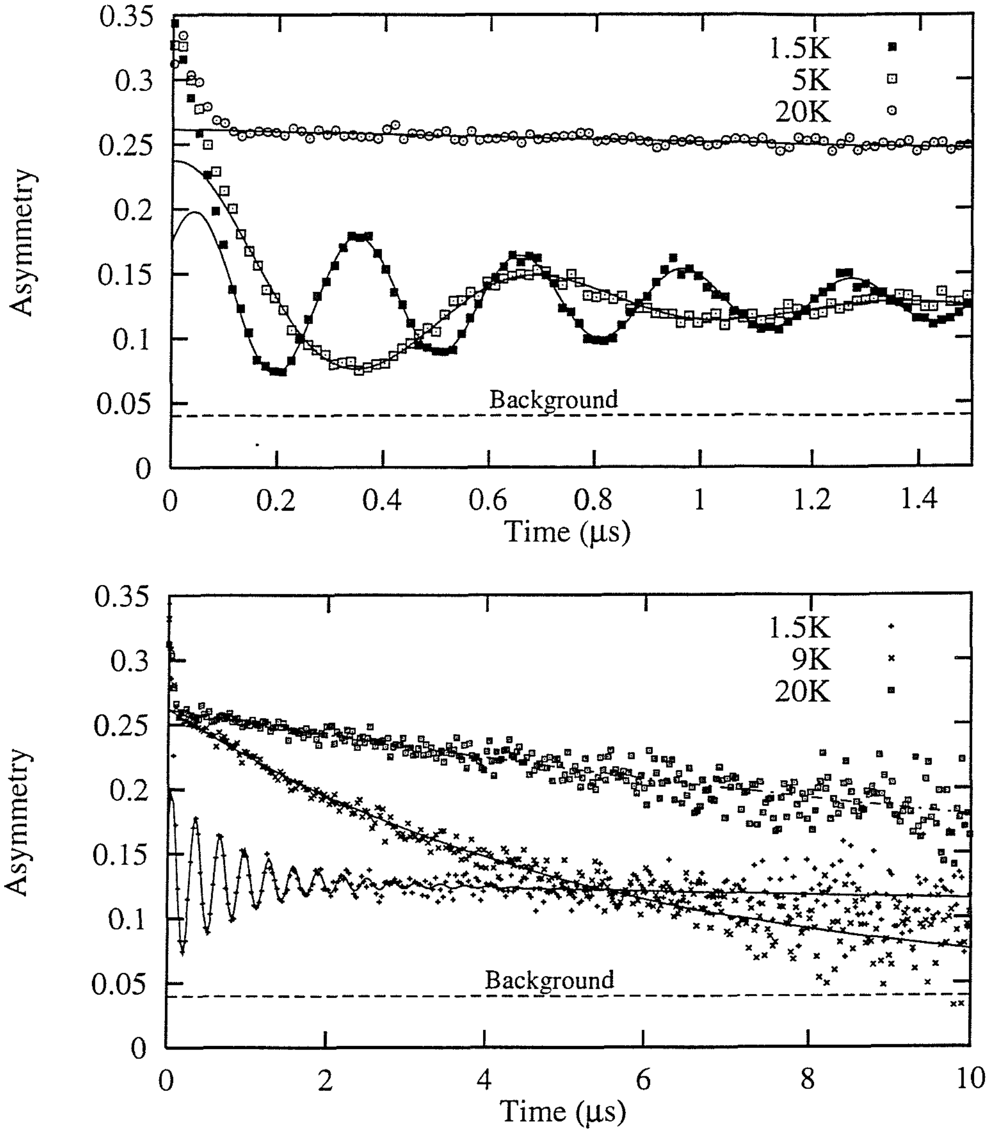

Figure 6.25: An overview of the μSR data for $CeRu_2Ge_2$. Note the different x-axis scales in the two figures. A simple exponential depolarisation is observed above T_C. Below T_C a spontaneous precession of the muons occurs indicating a coherent internal field. The frequency of the oscillation increases as the temperature is lowered. The solid lines are fits, see text. Note that at times $< 0.1\mu s$ the data is ignored because of the precipitous drop of the depolarisation.

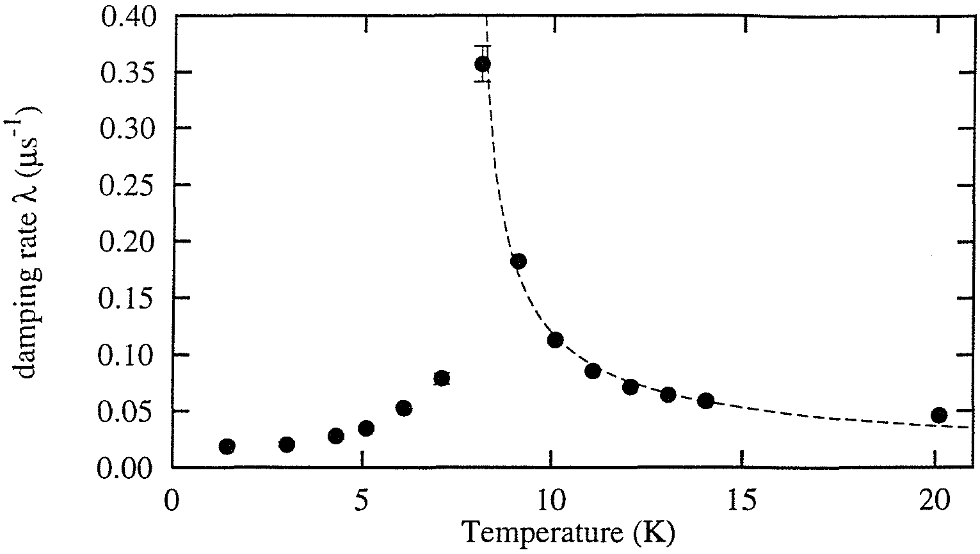

Figure 6.26: Damping rate of simple exponential term in $CeRu_2Ge_2$.

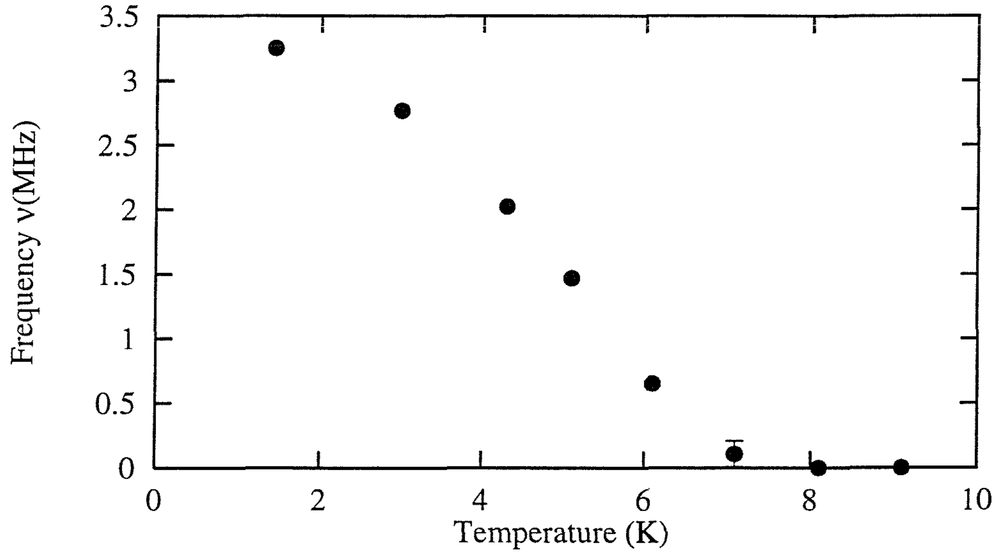

Figure 6.27: Frequency of oscillating part of asymmetry for $CeRu_2Ge_2$.

Equation (6.15) gave good fits, some of which are indicated as lines in figure 6.25. The frequency of the oscillation as a function of temperature is plotted in figure 6.27. The frequency of the oscillation can be converted into an estimate of the average field at the muon site using equation (3.2). This gives a maximum internal field of $\sim$ 250G at the muon site. The frequency decreases smoothly as the temperature is increased consistent with a reduction in the ordered moment.

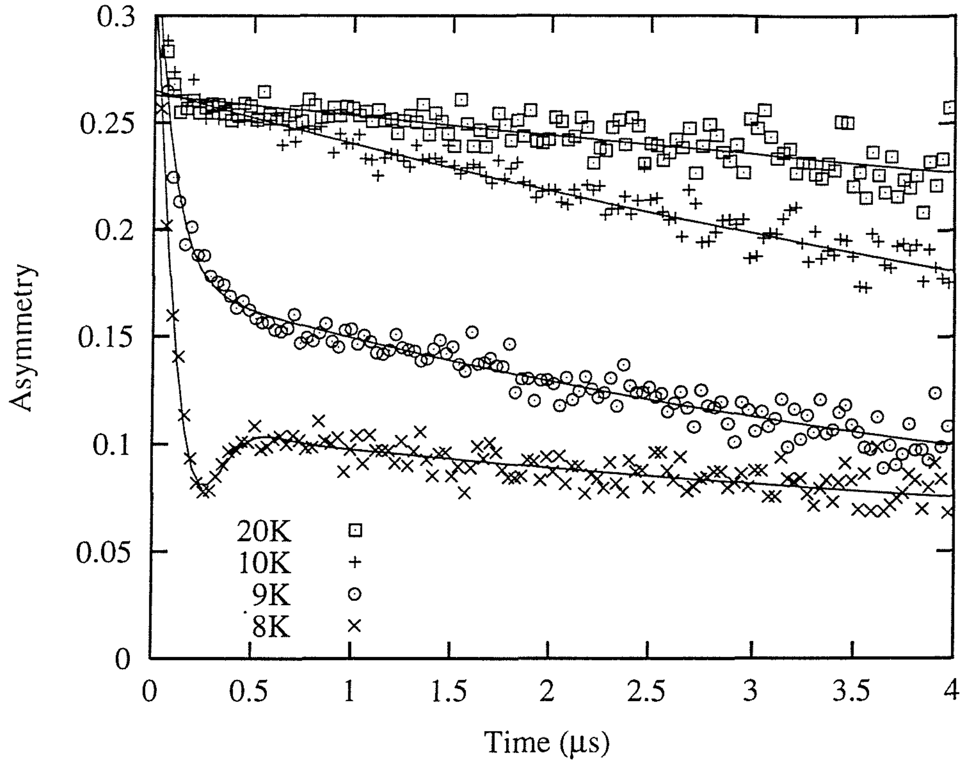

Figure 6.28: Increase in damping of muon polarisation near 9K in $CeRu_2Si_{0.25}Ge_{1.75}$. A partial period of one oscillation is visible at 8K. The lines are fits, see text.

6.5.2 $CeRu_2Si_{0.25}Ge_{1.75}$ alloy

Measurements on this alloy show a Lorentzian depolarisation of muons at higher temperatures with a highly damped spontaneous oscillation appearing below the ordering temperature. A general overview of the data is given in figure 6.28 which shows the change in the depolarisation on approaching 8K. The exponential damping rate increases to a maximum at 8K although figure 6.28 shows that at 9K the damping rate is changing dramatically.

The damping rate in the paramagnetic phase shows a divergence as was found in $CeRu_2Ge_2$ but it did not fit a powerlaw behaviour as well as the data for $CeRu_2Ge_2$. The damping rate is shown in figure 6.29

At 9K and below equation (6.15) was used to fit the data. At 9K the fit required two exponential components which corresponds to equation (6.15) with zero frequency and phase shift. For temperatures below this the data could be fitted with the full equation. Since we are entering a modulated antiferromagnetic state in $CeRu_2Si_{0.25}Ge_{1.75}$ below the ordering temperature we would expect the muon to

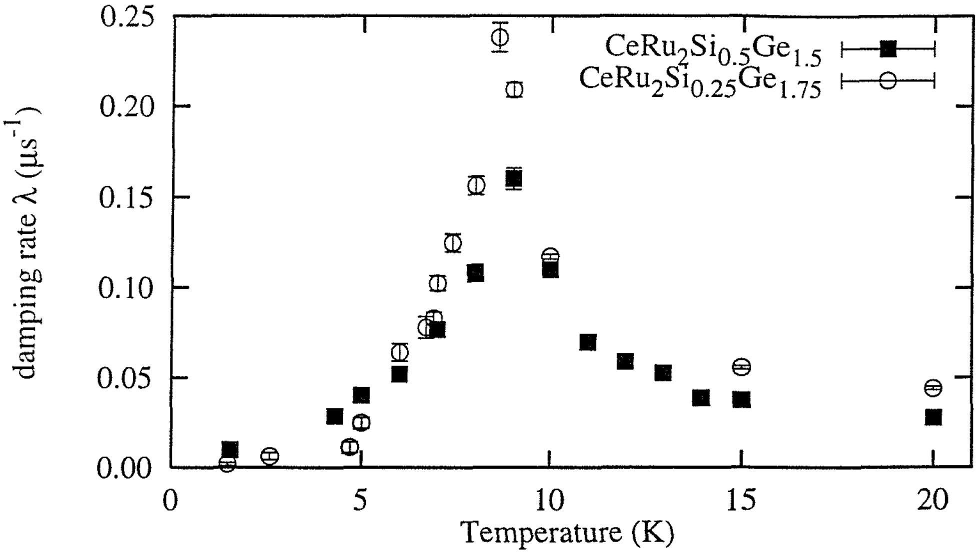

Figure 6.29: Increase in damping rate of muon polarisation near 9K in $CeRu_2Si_{0.25}Ge_{1.75}$ and $CeRu_2Si_{0.5}Ge_{1.5}$.

experience a distribution of fields. Given that $CeRu_2Ge_2$ shows clear oscillations the fact that the oscillation in this composition is not well defined can be taken as evidence of a wide field distribution at the muon site. The frequency found from fitting equation (6.15) must correspond to an average value.

Figure 6.30 shows the polarisation at short times for the lower temperatures. The oscillation reaches a peak frequency before dropping close to zero and then increasing once more. In order to get equation (6.15) to fit some of these data it was necessary to add an extra exponential component with an extremely large damping rate, ($\lambda \approx 30\mu s^{-1}$), to fit the decay of the polarisation for times $< 0.1\mu s$. This extra component improved the fit outside that range. The variation of the fitted frequency parameter for $CeRu_2Si_{0.25}Ge_{1.75}$ is shown in figure 6.31. The very large error bar on the point at 6.7K indicates the the oscillation was not really resolved in the fitting procedure. This indicates severe damping of the spontaneous precession of the muons, which is likely to be due to highly dynamic fluctuations on the phase boundary between the ferro and antiferromagnetic states. Comparison with figure 6.14(b) in section 6.3.2 shows a phase boundary at 6K consistent with the sharp change in the frequency of the oscillation found here. It is not clear why the frequency should drop to zero at the transition between the ferro and antiferromagnetic phases.

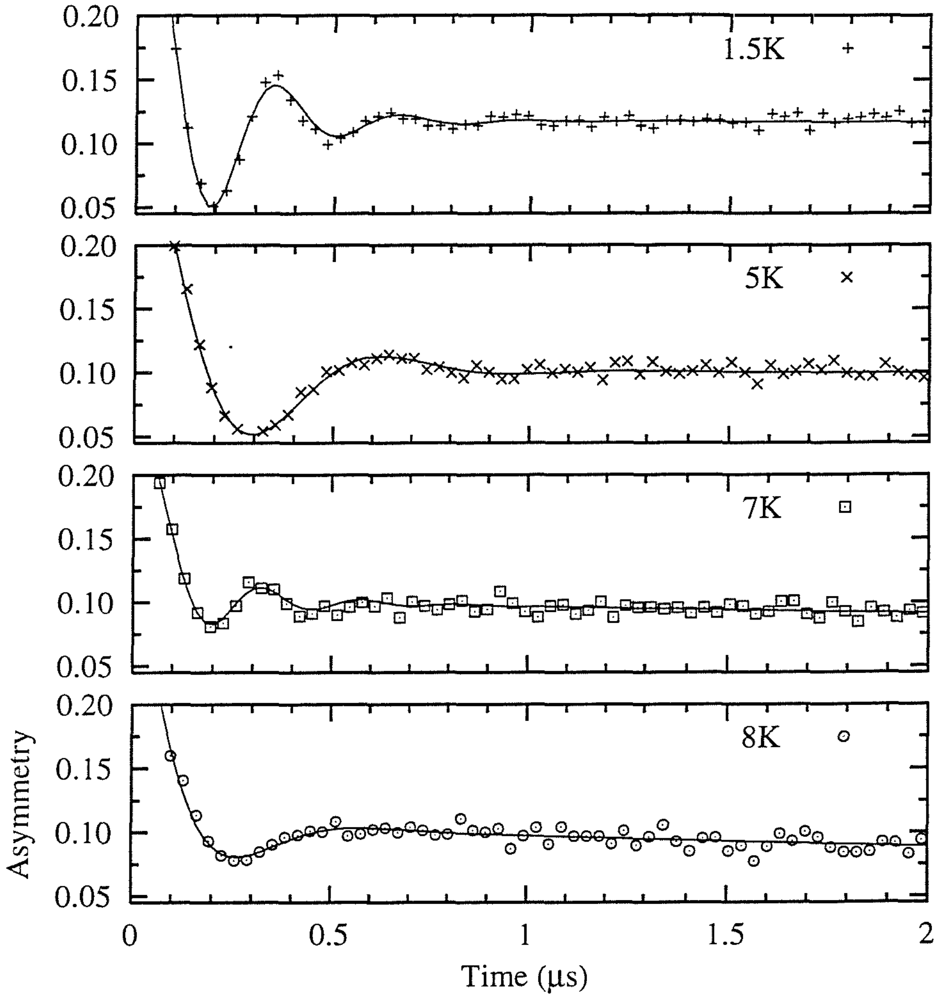

Figure 6.30: Highly damped oscillation in the asymmetry for CeRu$_2$Si$_{0.25}$Ge$_{1.75}$ as a function of temperature. At around 8K it is just possible to determine the oscillation. The frequency increases to a maximum at 7K then rapidly drops before increasing again as the temperature is lowered to 1.5K. Solid lines are fits.

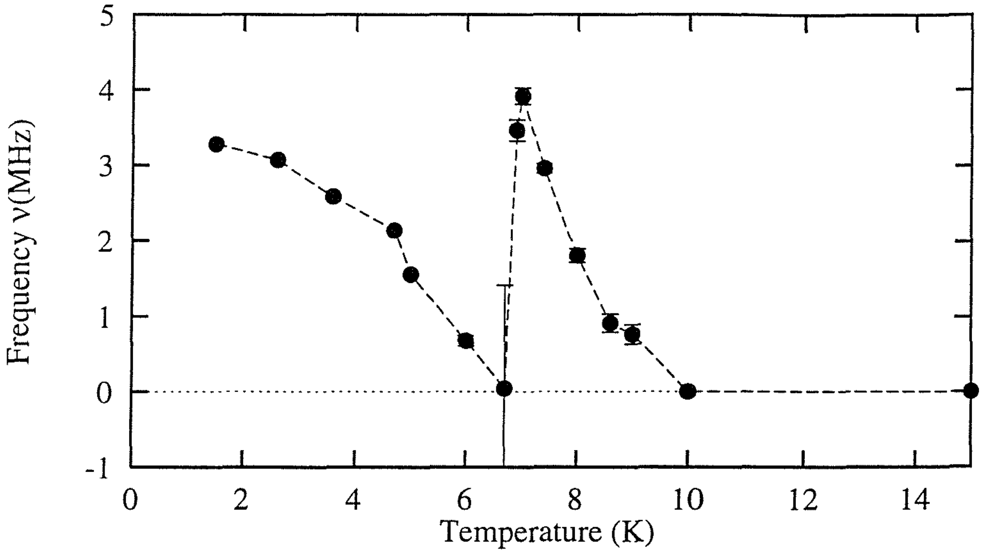

Figure 6.31: Frequency of oscillating part of asymmetry in $CeRu_2Si_{0.25}Ge_{1.75}$.

6.5.3 $CeRu_2Si_{0.5}Ge_{1.5}$ alloy

$CeRu_2Si_{0.5}Ge_{1.5}$ shows many features in common with $CeRu_2Si_{0.25}Ge_{1.75}$. A single exponential is sufficient to fit the data for temperatures above T_C but below the ordering temperature equation (6.15) was needed to describe the data. The damping rate in the paramagnetic phase showed similar behaviour to $CeRu_2Si_{0.25}Ge_{1.75}$, see figure 6.29.

The damping rate of the single exponential showed an increase towards 10K and the asymmetry of this component dropped rapidly at 10K indicating magnetic order. At lower temperatures there was a spontaneous oscillation in the polarisation. As in $CeRu_2Si_{0.25}Ge_{1.75}$ this oscillation was highly damped but it was possible to perform fits to equation (6.15) to get an average value of the frequency. The spontaneous oscillation of a component of the polarisation increased in frequency initially before dropping rapidly to a value near zero at roughly 6K before increasing once more, in the same manor as figure 6.31.

Our magnetisation measurements presented earlier (see section 6.3) found features in the magnetisation and susceptibility which suggested that ferromagnetism occurs at some temperature below the Neel temperature of this alloy. Figure 6.32 shows the variation of the frequency of the oscillation in the muon polarisation. We can compare this with the behaviour for $CeRu_2Si_{0.25}Ge_{1.75}$ and find that they are very similar.

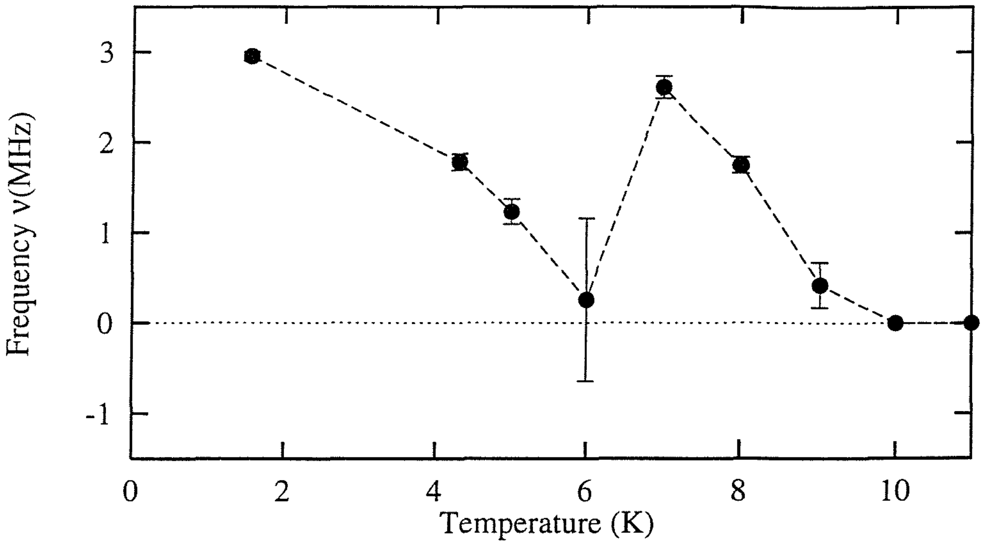

Figure 6.32: Frequency of oscillating part of polarisation in $CeRu_2Si_{0.5}Ge_{1.5}$. This figure is very similar to figure 6.31.

The oscillations in the polarisation are highly damped in $CeRu_2Si_{0.5}Ge_{1.5}$, even at the lowest temperatures measured. There are no convincing oscillations like those in $CeRu_2Ge_2$ or $CeRu_2Si_{0.25}Ge_{1.75}$ so it is difficult to say that ferromagnetism does develop. Figure 6.32 show the fitted frequency. This figure does indicate that there is some significant change in the fields acting on the muons. Since the muons are a microscopic probe it does suggest that there are two transitions.

The data presented in the next section shows that in $CeRu_2Si_{1.0}Ge_{1.0}$ the muons do not experience the two transition behaviour at the microscopic level.

It is not clear whether the lowest temperature phase is ferromagnetic in this alloy. The low field susceptibility data did not show as sharp a rise as for $CeRu_2Ge_2$ and $CeRu_2Si_{0.25}Ge_{1.75}$at the ferromagnetic transition temperature, but this data seems to be very similar to that of $CeRu_2Si_{0.25}Ge_{1.75}$ which is a ferromagnet at the lowest temperatures.

6.5.4 $CeRu_2Si_{1.0}Ge_{1.0}$ alloy

For temperatures above T_C the muons show an exponential depolarisation as do all the other alloys. At 21K a 200G LF field reduces the damping rate but higher fields have no additional effect. At 10K there is a rapid loss of initial asymmetry and a more complex depolarisation appears. The damping rate of the exponential is shown

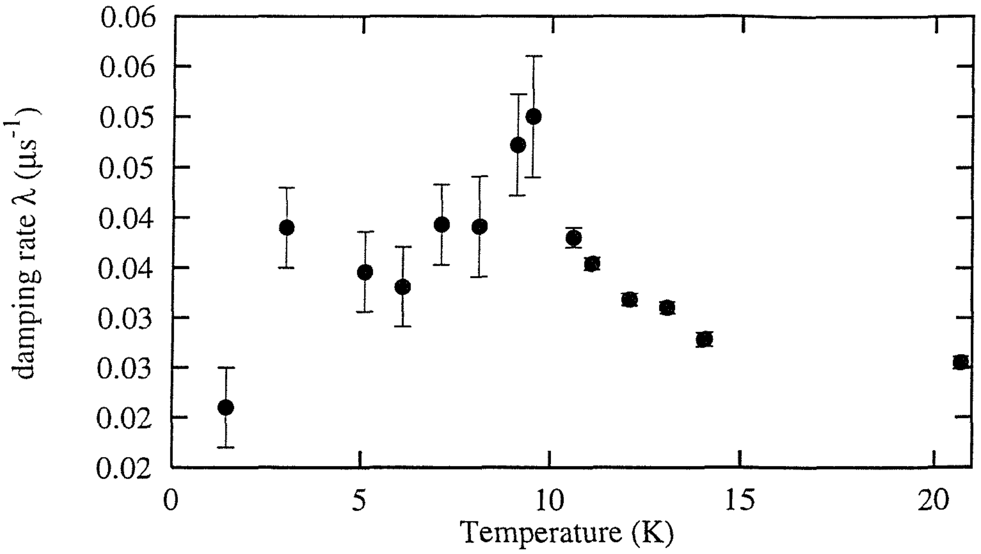

Figure 6.33: Damping rate of exponential component in $CeRu_2Si_{1.0}Ge_{1.0}$.

in figure 6.33. It does not show a clear divergence at the ordering temperature and the points below T_C correspond to the damping rate of the second component in equation (6.15).

As with the other alloys the form of equation (6.15) was used to fit the data below the ordering temperature. The polarisation indicated a heavily overdamped oscillation. As with $CeRu_2Si_{0.25}Ge_{1.75}$ and $CeRu_2Si_{0.5}Ge_{1.5}$ the oscillation results because the muons sit in the magnetic field due to antiferromagnetically ordered moments, which cause the muons to precess. The heavily damped oscillation demonstrates a broad field distribution. The frequency found from fitting equation (6.15) is plotted as a function of temperature in figure 6.34.

Figure 6.34 shows an increase in frequency up to a roughly constant value of $\sim$ 0.27, there is no indication in this figure of a drop in the frequency after the initial increase. This shows evidence that there is only one phase transition. It also suggests that $CeRu_2Si_{0.5}Ge_{1.5}$ does exhibit two transitions.

At the lowest temperature the modulated magnetic structure should begin to "square up" to remove entropy. The data for $CeRu_2Si_{1.0}Ge_{1.0}$ does not show any features of this. The lowest temperature reached was 1.5K and the signal from the muons is almost at background level so it is difficult to see any effects associated with the development of the inelastic excitation in this alloy.

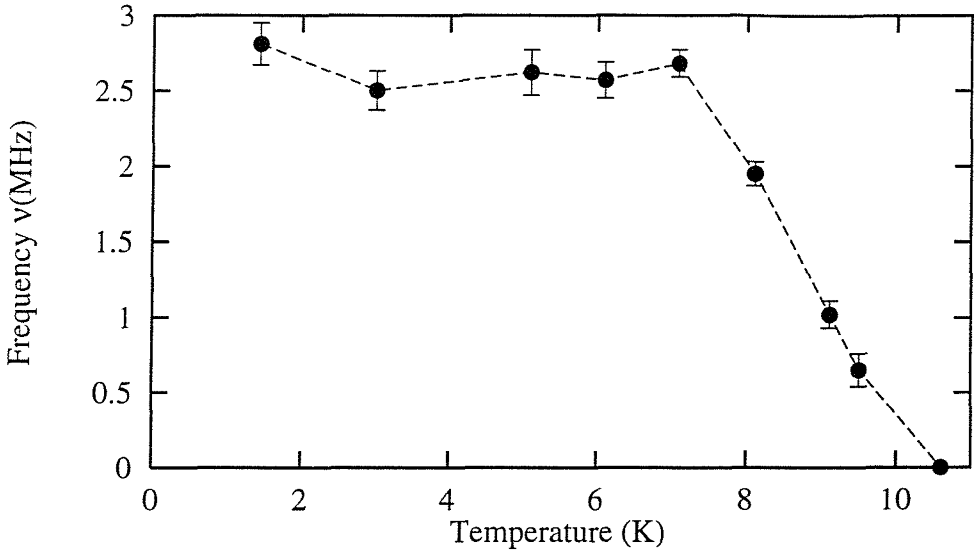

Figure 6.34: Oscillation frequency in $CeRu_2Si_{1.0}Ge_{1.0}$.

6.6 Summary and Further work

The $CeRu_2Si_{2-x}Ge_x$ family of alloys are interesting and challenging to study because they exhibit a wide variety of properties. $CeRu_2Si_2$ is dominated by the Kondo effect and is a heavy fermion, $CeRu_2Ge_2$ on the other hand is dominated by the RKKY interaction and is a normal ferromagnet. In the intermediate alloys the competition between the two effects produces novel behaviour. Any expansion of the unit cell of $CeRu_2Si_2$ reduces the hybridisation between 4f and conduction electrons and results in magnetic ordering of reduced moments at low temperatures. A contraction of the unit cell volume of $CeRu_2Ge_2$ induces an additional antiferromagnetic state which is stable at a higher temperature than the ferromagnetism. All the alloys have an Ising like groundstate due to the action of the crystal field on individual moments.

The magnetisation measurements presented in this chapter have confirmed that for alloys with Ge content of $x = 1.5$ or above have a ferromagnetic groundstate at the lowest temperatures measured. The antiferromagnetic state, a few degrees Kelvin higher in temperature, is unstable in a magnetic field and many metamagnetic steps are seen in data measured in different field strengths. The positions of the various features in the magnetisation data were use to mark phase boundaries on field temperature phase diagrams. A neutron diffraction study in different applied fields would give more detailed information on the particulars of the various antiferromagnetic phases.

Neutron scattering has found that there is quasielastic scattering in all of these alloys above the ordering temperature. Using a RPA approach the data has be fitted and analysed. The analysis has shown that wavevector dependent width of the quasielastic scattering and the derived zero wavevector susceptibility conform to normal behaviour for materials which order magnetically.

The single ion linewidth does not follow a $T^{1/2}$ form, which is common for materials where the Kondo effect is at work. It is linear at high temperatures with a low temperature intercept, as for equation (6.6). The Kondo temperature for $CeRu_2Si_2$ is of the order of 22K and it has been shown to decrease with an increase in Ge doping. From the analysis of the quasielastic linewidth we have shown that the Kondo temperature is small, and does not change appreciably in the alloys with compositions $x = 1.25$,$x = 1.5$ and $x = 1.75$.

The neutron scattering experiments have also revealed that an inelastic excitation occurs in some of these alloys. $CeRu_2Si_{1.0}Ge_{1.0}$ was found to have the most intense peak and in $CeRu_2Si_{0.5}Ge_{1.5}$ the excitation disappeared. This excitation cannot correspond to a spinwave mode since the groundstate in all the alloys is Ising like. A simple mean field model explains various features of this excitation. It disappears when the exchange field is larger than the effects of the Kondo screening, as in $CeRu_2Ge_2$and $CeRu_2Si_{0.25}Ge_{1.75}$. This novel excitation warrants more detailed investigation and a neutron scattering experiment on $CeRu_2Si_{1.0}Ge_{1.0}$ has recently been performed. The dependence of the excitation on the composition of the alloys reflects the underlying role of hybridisation between 4f and conduction electrons in its formation. It would be interesting to find out more about the formation of the state which produces this excitation. There are other anomalies which occur in the resistivity [93] and heat capacity [98] at roughly the same temperature and hence the suggestion is that there is a new novel low temperature phase in some of these alloys.

Chapter 7

Summary and Conclusions

This thesis contains the results of experimental work on CePdSb, CePtSb and alloys from the $CeRu_2Si_{2-x}Ge_x$ series. A brief summary of the work on each of these materials is given here.

7.1 Summary of CePdSb experiments

The most striking feature of this ferromagnetic compound is the lack of a co-operative anomaly in the heat capacity at the ordering temperature. This work has attempted to gain some insight into this phenomenon. The main results and conclusions are:

- The crystal field, determined from inelastic neutron scattering, produces an X-Y groundstate with cerium moments confined to the basal plane.
- Magnetisation measurements on small polycrystalline pieces of CePdSb show that the compoud is clearly ferromagnetic with a Curie temperature of $\sim$ 17K. Similar measurements on a sample cut from a single crystal also confirm this. The spontaneous magnetisation extracted from Arrot plots shows an anomalous temperature dependence.
- Neutron diffraction measurements confirmed the simple ferromagnetic structure. The temperature dependence of the spontaneous moment derived from the magnetic Bragg peaks was in agreement with the magnetisation measurements.

- Inelastic neutron scattering on CePdSb showed quasi-elastic scattering above the Curie temperature, as expected for an exchange coupled paramagnet. This is strong evidence that CePdSb is not a Kondo lattice compound. Spinwave excitations were only observed below 10K.

- Small angle neutron scattering produced some interesting results. Below the ordering temperature the scattering developed into a diagonal cross pattern in the $a^{\star}$-$c^{\star}$ plane. The highly anisotropic pattern was difficult to analyse but the correlation length in the basal plane, derived from fitting the data to a squared Lorentzian profile, appears to diverge at around 5K. Above 10 - 15K fits were much poorer and so the analysis produced confusing results.

- Muon spin relaxation measurements showed a considerable loss of asymmetry at the ordering temperature but the muons were apparently not severely damped until a much lower temperature. This is surprising since a ferromagnet with a $1\mu_B$ moment should produce strong damping of the muon polarisation.

When CePdSb was first discoverd it was thought that it might be a ferromagnetic Kondo lattice compound, this does not appear to be the case since there are no indications of Kondo behaviour in any of this work. The strange behaviour of CePdSb is still not well understood. Further investigation of high quality single crystals using a range of experimental techniques will be very worthwhile.

7.2 Summary of CePtSb experiments

CePtSb, like CePdSb, is a ferromagnet with a Curie temperature of 5K. This compound has the same structure as CePdSb and similar lattice parameters but it behaves like an ordinary local moment ferromagnet. CePtSb has been investigated here to provide a standard against which the unusual properties of CePdSb can be compared. The main results of the experiments are listed below.

- Magnetisation work shows the Curie temperature of CePtSb to be 5K. Arrot plots of the data do not show the same anomalies found in CePdSb.

- Neutron scattering found that spinwave excitations can be seen just below the ordering temperature, in contrast to CePdSb.

CePtSb appears to be a normal ferromagnet. Further work on this compound would be useful, in particular an interesting comparison could be made if small angle neutron scattering data was available for CePtSb.

7.3 Sumary of work on $CeRu_2Si_{2-x}Ge_x$ alloys

The $CeRu_2Si_{2-x}Ge_x$ alloys show a range of properties across the series. The alloy with the composition $x = 1.0$ is one of the most interesting since inelastic neutron scattering shows it has an anomalous longitudinal excitation at low temperatures. A number of alloys from the Ge rich end of the series were investigated with a view to discovering more details of the changes which take place across the series. The main experimental results are listed below.

- Magnetisation measurements on alloys $CeRu_2Si_{0.75}Ge_{1.25}$ and $CeRu_2Si_{0.5}Ge_{1.5}$ showed several metamagnetic features. In $CeRu_2Si_{0.25}Ge_{1.75}$ there was only one apparent feature, in zero field this alloy orders antiferromagnetically at 10K then becomes ferromagnetic at $\sim$ 6K. Phase diagrams have been derived for all three alloys..

- In inelastic neutron scattering measurements all the alloys showed quasielastic scattering at higher temperatures, with a Lorentzian lineshape. The low temperature intercept of the linewidth was used as an estimate of the Kondo temperature. This was around 2K for all the alloys studied.

- In $CeRu_2Si_{1.0}Ge_{1.0}$ and $CeRu_2Si_{0.75}Ge_{1.25}$ an inelastic excitation developed below $\sim$ 2K. The excitation was composition dependent because it was not observed in the alloys with higher Ge content.

- A simple mean field model can account for the qualitative behaviour of this series of alloys. The action of an internal field combined with the effects of Kondo mixing of the two components of the Ising doublet groundstate is believed to be a possible cause of the excitation in some alloys.

Single crystals were not available for the studies in this thesis but great benefits could be derived from having crystals, suitable for neutron scattering, in compositions around $CeRu_2Si_{1.0}Ge_{1.0}$. Inelastic studies on single crystals would allow the dispersion and strucutre factor of the longitudinal excitation to be studied across the Brillouin zone. The model outlined in this thesis predicts that a magnetic field applied parallel to the *c*-axis should destroy the excitation. Experiments to test this would give an excellent indication of the validity of the model.

Appendix A

Neutron scattering time-of-flight data

Time of flight measurements are a routinely used method for conducting inelastic neutron scattering experiments. The time-of-flight of neutrons between the sample and detector is measured. The time-of-flight of neutrons is $\tau = \frac{t}{L}$ where t is the flight time and L is the flight path. τ is actually the reciprocal velocity.

For neutrons with fixed incident energy the time-of-flight between sample and detector characterises the scattered energy. The raw data in a time-of-flight experiment is a histogram of neutron counts in time of flight bins or channels. A example histogram for one of the detectors on the IN6 instrument is shown in figure A.1.

Chapter 2 introduced various ways of writing the partial differential cross-section. In time-of-flight experiments we measure

$$\frac{d^2\sigma}{d\Omega d\tau} = \frac{\text{No. of neutrons scattered into } d\Omega \text{ per unit time with t-of-f between } \tau \text{ and } \tau + d\tau}{d\Omega d\tau \times \text{incident flux}}, \tag{A.1}$$

note that the cross-section per unit energy transfer and this cross-section are related by

$$\frac{d^2\sigma}{d\Omega d\tau}\Delta\tau = \frac{d^2\sigma}{d\Omega d\varepsilon}\Delta\varepsilon \tag{A.2}$$

In terms of the number of counts C_j in channel j, the cross-section per formula unit is

$$\left(\frac{d^2\sigma}{d\Omega d\tau}\right)_j = \frac{1}{M_s}\frac{C_j}{\Delta\tau\Delta\Omega N_s} \tag{A.3}$$

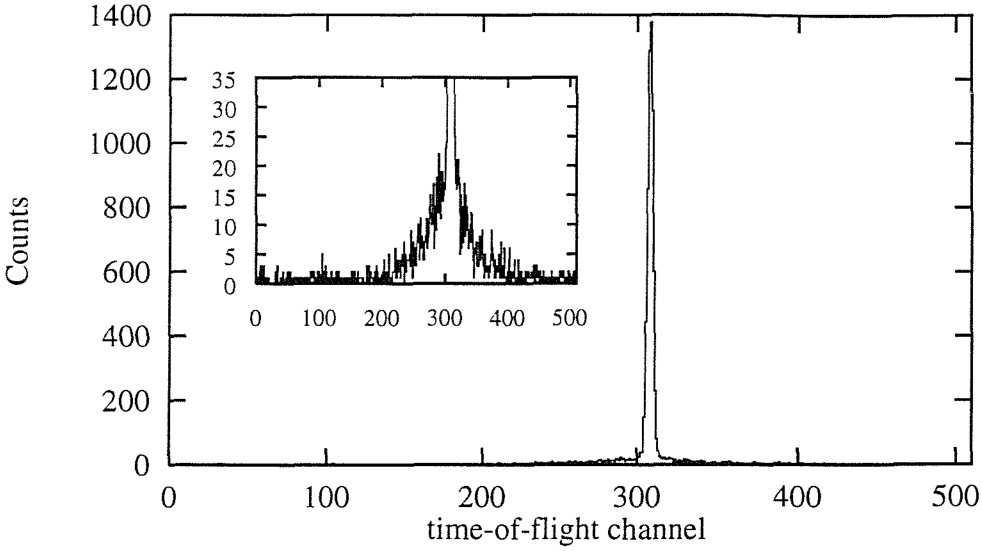

Figure A.1: Typical time of flight histogram for IN6. The inset shows quasielastic scattering on a much reduced scale.

where M_s is the monitor counts for the run, N_s is the number of formula units in the mass of sample used, $\Delta\tau$ is the time-of-flight width of one of the channels in figure A.1 and $\Delta\Omega$ is the solid angle defined by the detector, which we do not necessarily know. Equation (A.3) is actually the cross-section per incident monitor count. Using equation (A.2)

$$\left(\frac{d^2\sigma}{d\Omega d\varepsilon}\right)_j = \frac{1}{M_s}\frac{C_j}{\Delta\varepsilon\Delta\Omega N_s} \tag{A.4}$$

with

$$\varepsilon = E_i - \frac{m}{2\tau^2} \tag{A.5}$$

then

$$\Delta\varepsilon_j = \Delta\tau\frac{m}{\tau_j^3}\,. \tag{A.6}$$

Note that the width of our channels in time-of-flight is a constant but from equation (A.6) the width in energy transfer of the channels depends on $\frac{1}{\tau^3}$ which will make the channels at short time of flight very much wider in ε than the later channels.

We can get the cross-section on an absolute scale using the scattering from a vanadium plate. The total scattering integrated over all time of flight for a given

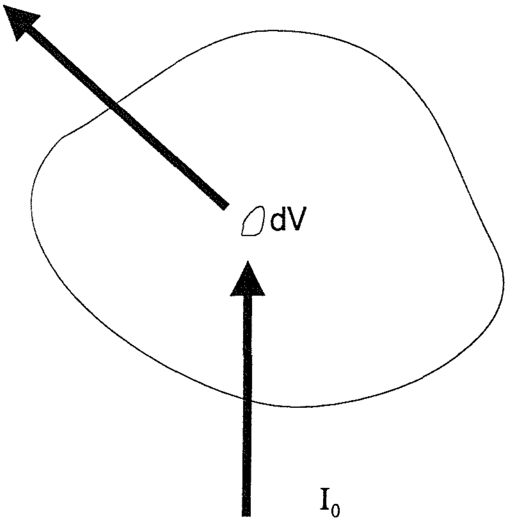

Figure A.2: Scattering from an elemental volume of sample, dV.

detector is V_{el}. And the differential cross-section for vanadium will be

$$\left(\frac{d\sigma}{d\Omega}\right)_{\Omega_d} = \frac{V_{\mathrm{int}}}{\alpha M_v \Delta\Omega N_v} = \frac{\sigma_{\mathrm{inco}}}{4\pi} \tag{A.7}$$

since the scattering from vanadium is dominated by the isotropic incoherent cross-section, σ_{inco}. Rearranging the above equation gives an expression for $1/\Delta\Omega$, which can be substituted into equation (A.4) to give

$$\left(\frac{d^2\sigma}{d\Omega d\varepsilon}\right)_{\varepsilon_i} = \frac{C_i}{\Delta\varepsilon V_{\mathrm{int}}} \times \frac{\sigma_{\mathrm{inco}}}{4\pi}\frac{N_v}{N_s}\frac{M_v}{M_s} \tag{A.8}$$

A.1 correcting data

Generally at the time of the experiment we must make additional measurements: scattering from the empty sample holder, a measurement of the scattering from the empty sample holder with an absorbing cadmium mask in place of the sample and a measurement of the scattering from a vanadium plate in place of the sample. These will be used to get the true scattering from the sample.

To get the best measurement of the cross-section we need to know the ratio of the intensity of the scattered beam to that of the incident beam. Consider figure A.2, with a beam of incident intensity I_0. We want to know the ratio of the incident and scattered intensity. We could work this out for an elemental volume dV then sum dV over all the sample. However, the incident intensity at dV is not I_0 because any scattering or absorbtion processes which occur before reaching dV reduce the beam

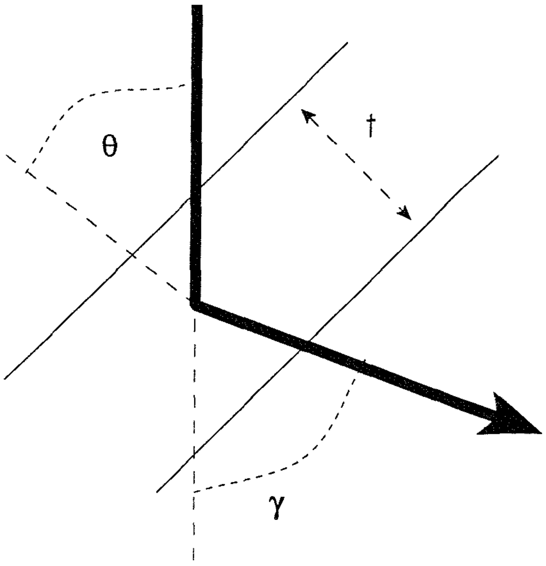

Figure A.3: Scattering picture.

intensity. This is called self shielding. The measured scattered intensity is not the true scattered intensity because any second scattering process or absorbtion on the path out of the sample will again reduce the intensity of the scattered beam.

We can in principle correct for this effect because we know the scattering and absorbtion cross-sections. The correction for an arbitrary shaped sample however is not easy and so exact analytical forms only exist for planar samples, numerical techniques should be used in other circumstances.

For a plate sample at angle γ to the incident beam the attenuation coefficient is given by [103]

$$A(\gamma, \phi) = \frac{\exp(-N\sigma t \sec\gamma) - \exp\left[-N\sigma' t \sec(\phi - \gamma)\right]}{N\sigma' t \sec(\phi - \gamma) - N\sigma t \sec\gamma} \tag{A.9}$$

where N is the number of formula units per unit volume, σ is the cross-section of a formula unit at the incident energy, σ' is the attenuation at the scattered energy. The angle γ is the angle of the plate defined in figure A.3 and ϕ is the scattering angle. There are two terms one for attenuation at the incident energy and one for attenuation at the scattered energy. For the reduction in the intensity of the incident and scattered beams we can replace σ and σ' by $\sigma_{\text{total}} = \sigma_{\text{inco}} + \sigma_{\text{coh}}$, which is the total scattering cross-section.

The true scattered counts will be given by

$$C_{\text{True}} = \frac{C_{\text{total}}}{A_{ss}A_a} - \frac{B_1}{A_{ss}A_a} - B_2 \tag{A.10}$$

where C_{total} is the total measured counts, B_1 is the background counts for neutrons which have passed through the sample position and B_2 is the counts from neutrons which reach the detector without passing through the sample position.

The number B_2 is given by the run with a cadmium mask in the sample position and B_1 is given by the difference between the run with the empty sample can and the run with the sample masked with cadmium. B_2 will typically be very small and B_1 will only have counts near the elastic line.

A.2 Absolute time-of-flight

We need not measure the absolute time-of-flight of our scattered neutrons. We must now the width of our time-of-flight bins $\Delta\tau = \Delta t/L$. Neutrons with infinite final energy will arrive at $\tau = 0$ and for elastically scattered neutrons we find from equation (A.5) that

$$\tau_{\text{el}} = \sqrt{\frac{m}{2E_i}} \tag{A.11}$$

so that the elastic channel number should be $\tau_{\text{el}}/\Delta\tau$. For the IN6 spectrometer $E_i = 3.12\text{mev}$, $L = 2.48\text{m}$ and $\Delta t = 9.625\mu\text{s}$ which gives the elastic channel as number 333.5 whereas the data in figure A.1 show that the elastic channel is number 309. The difference is -24.5, infinite energy neutrons would arrive in channel -24.5 and this defines $\tau = 0$. We write the shift due to the infinite energy channel as Δ_∞. Our conversion from time-of-flight to energy transfer is now

$$\tau_j = (j - \Delta_\infty)\,\Delta\tau\varepsilon = E_i - \frac{m(\Delta\tau)^2}{2(j - \Delta_\infty)^2} \tag{A.12}$$

A.3 Absorbtion cross-section

We work out the cross-section per unit cell. There are tables which give the absorbtion cross-section for the specific 2200m/s neutrons. We should convert to our energy by assuming that the cross-section is directly proportional to the velocity.

$$\sigma = \sigma_{2200m/s} \times \frac{v}{2200} \tag{A.13}$$

where v is the velocity of our neutrons. The unit cell cross-section is the sum of all atoms in the unit cell. There may be more than one formula unit per unit cell so we should remember this. The number of unit cells per unit volume is the reciprocal of the unit cell volume. We are left with

$$N\sigma = \frac{1}{V}\sum_{n}\sigma_n \tag{A.14}$$

for n atoms in the unit cell. The units of equation (A.14) should be cm^{-1} and the value is ~ 0.5 for most compounds studied in this thesis.

Bibliography

[1] N. W. Ashcroft and N. D. Mermin, *Solid State Physics* (Saunders College, Philadelphia. 1976).

[2] V. I. Vonsovskii, *Magnetism* (John Wiley and sons, New York, 1974), Vol. 2.

[3] K. N. R. Taylor and M. I. Darby, *Physics of Rare-Earth solids* (Chapman & Hall, London. 1972).

[4] R. J. Elliott. in *Magnetism*, edited by G. T. Rado and H. Suhl (Academic press, New York, 1965), Vol. IIa.

[5] J. Jensen and A. R. Macintosh, *Rare Earth Magnetism: Structures and Excitations* (Oxford University Press, Oxford, 1991).

[6] M. T. Hutchings. in *Solid State Physics*, edited by F. Seitz and B. Turnbull (Academic Press, New York, 1964), Vol. 16.

[7] R. M. White. *Quantum Theory of Magnetism* (Springer-Verlag, Berlin, 1983).

[8] W. E. Wallace. *Rare earth intermetallics* (Academic Press, New York, 1973).

[9] D. H. Martin. *Magnetism in Solids* (Iliffe Books, London, YEAR).

[10] O. Elsenhans *et al.*, Zeitshrift fur Physik B – Condensed Matter **82**, 61 (1991).

[11] S. Malik and D. T. Adroja, J. Mag. Mag. Mat. **102**, 42 (1991).

[12] C. Kittel, *Introduction to solid state physics* (Wiley, New York, 1986).

[13] A. C. Hewson. *The Kondo problem to heavy fermions* (Cambridge University Press, Cambridge. 1993).

[14] B. Coqblin, in *Magnetism of metals and alloys*, edited by M. Cyrot (North-Holland, Amsterdam, 1980).

[15] N. B. Brandt and V. V. Moshchalkov, Adv. Phys. **83**, 373 (1984).

[16] A. M. Tsvelick and P. B. Wiegmann, Adv. Phys. **32**, 453 (1983).

[17] J. Kondo, Rep. Theor. Phys. **32**, 37 (1964).

[18] B. Coqblin and J. R. Schrieffer, Phys. Rev. **185**, 847 (1969).

[19] D. T. Adroja, B. D. Rainford, and S. K. Malik, Physica B **194–196**, 169 (1994).

[20] G. Zwicknagl, Adv. Phys. **41**, 203 (1992).

[21] R. G. Wilson, Rev. Mod. Phys. **47**, 773 (1975).

[22] H. R. Krishna-Murthy, J. W. Wilkins, and K. G. Wilson, Phys. Rev. B **21**, 1003 (1980).

[23] C. Lacroix, J. Mag. Mag. Mat. **100**, 90 (1991).

[24] S. Doniach, Physica B **91**, 231 (1977).

[25] G. R. Stewart, Rev. Mod. Phys. **56**, 755 (1984).

[26] G. Appeli and Z. Fisk, Comments Cond. Mat. Phys. **16**, 155 (1992).

[27] T. E. Mason *et al.*, Phys. Rev. Lett. **69**, 490 (1992).

[28] D. T. Adroja and B. D. Rainford, J. Mag. Mag. Mat. **135**, 333 (1994).

[29] R. Movshovich *et al.*, Phys. Rev. B **53**, 8241 (1996).

[30] J. M. Lawrence, P. S. Riseborough, and R. D. Parks, Rep. Prog. Phys. **44**, 1 (1981).

[31] A. R. Mackintosh, in *The Neutron and its applications* (Institute of Physics, London, 1983).

[32] P. Fulde and M. Loewenhaupt, Adv. Phys. **34**, 589 (1985).

[33] Y. Kuramoto, Physica B **146**, 789 (1989).

[34] M. F. Collins, *Magnetic critical scattering* (Oxford University Press, Oxford, 1989).

[35] J. M. Yeomans, *Statistical mechanics of phase tranisitions* (Oxford University Press, Oxford, 1992).

[36] M. E. Fisher, in *Critical Phenomena*, edited by F. J. W. Hahne (Springer-Verlag, Berlin, 1983), Chap. 1.

[37] P. Pfeuty and G. Toulouse, *Introduction to the Renormalisation Group and to Critical Phenomena* (John Wiley & Sons, London, 1977).

[38] S.-K. Ma, Rev. Mod. Phys. **45**, 589 (1973).

[39] A. Arrot and J. E. Noakes, Phys. Rev. Lett. **19**, 786 (1967).

[40] C. Bowen, D. L. Hunter, and N. Jan, J. Stat. Phys. **69**, 1097 (1992).

[41] W. Janke and K. Nather, Phys. Rev. B **48**, 15807 (1993).

[42] S. W. Lovesey, *Theory of Neutron Scattering from condensed matter* (Oxford University Press, Oxford, 1984), Vol. 1.

[43] G. L. Squires, *Introduction to the Theory of Thermal Neutron Scattering* (Cambridge University Press, Cambridge, 1978).

[44] V. F. Sears, Neutron News **3**, 26 (1992).

[45] S. W. Lovesey, *Theory of Neutron Scattering from condensed matter* (Oxford University Press, Oxford, 1984), Vol. 2.

[46] *Neutron Diffraction*, edited by H. Dachs (Springer-Verlag, Berlin, 1978).

[47] A. J. Freeman and J. P. Desclaux, JMMM **12**, 11 (1979).

[48] J. P. Desclaux and A. J. Freeman, J. Mag. Mag. Mat. **8**, 119 (1978).

[49] P. J. Brown, in International Tables for Crystallography.

[50] R. S. Hayano *et al.*, Phys. Rev. B **20**, 850 (1979).

[51] G. J. Daniell, in *Neutron Scattering at a Pulsed Source*, edited by Newport, Rainford, and Cwyinski (Adam Hilger, London, 1988), Chap. 9.

[52] B. D. Rainford and G. J. Daniell, Hyperfine Interact. **87**, 1129 (1994).

[53] S. K. Malik and D. T. Adroja, Phys. Rev. B **43**, 6295 (1991).

[54] P. Bonville *et al.*, Physica B **182**, 105 (1992).

[55] E. Bauer *et al.*, Z. Phys. B **94**, 359 (1994).

[56] A. Fujimori *et al.*, Phys. Rev. B **41**, 6783 (1990).

[57] P. C. Riedi *et al.*, Phys. Rev. B **199**, 558 (1994).

[58] O. Trovarelli, J. G. Sereni, G. Schmerber, and J. P. Kappler, Phys. Rev. B **49**, 15179 (1994).

[59] K. Katoh *et al.*, Physica B **230**, 159 (1997).

[60] M. J. Thornton *et al.*, Phys. Rev. B **54**, 4189 (1996).

[61] J. S. Lord *et al.*, J. Phys.: Condens. Matter **8**, 5475 (1996).

[62] B. D. Rainford, D. T. Adroja, A. J. Neville, and D. Fort, Physica B **206 & 207**, 209 (1995).

[63] K. Katoh, A. Ochiai, and T. Suzuki, Physica B **223 & 224**, 340 (1996).

[64] B.D.Rainford and D. T. Adroja, Triple axis neutron scattering experiments on CePdSb, to be published.

[65] P. G. de Gennes, Journal of Physical and Chemical Solids **4**, 223 (1958).

[66] H. G. Evertz and D. P. Landau, Phys. Rev. B **54**, 12302 (1996).

[67] M. E. Gouvêa, G. M. Wysin, A. R. Bishop, and F. G. Mertens, Phys. Rev. B **39**, 11840 (1989).

[68] D. G. Wiesler, H. Zabel, and S. M. Shapiro, Z. Phys. B **93**, 277 (1994).

[69] B. D. Rainford and D. T. Adroja, Physica B **194**, 365 (1994).

[70] M. Kasaya, H. Suzuki, and T. Yamag, J. Phys. Soc. Jap. **61**, 4187 (1992).

[71] K. H. Kim *et al.*, Phys. Rev. B **230**, 155 (1997).

[72] B. D. Rainford, unpublished calculation.

[73] G. Just and P. Paufler, J. Alloy. Comp. **232**, 1 (1996).

[74] F. Steglich *et al.*, Phys. Rev. Lett. **43**, 1892 (1979).

[75] M. J. Besnus *et al.*, Physica B **171**, 350 (1991).

[76] R. Felten, G. Weber, and H. Rietschel, J. Mag. Mag. Mat. **63 & 64**, 383 (1987).

[77] S. Dakin, Ph.D. thesis, Southampton University, 1992.

[78] J. Korringa, Physica **19**, 60 (1950).

[79] A. Loidl *et al.*, Physica B **156 & 157**, 794 (1989).

[80] C. Godart, A. M. Umarji, L. C. Gupta, and R. Vijayaraghavan, J. Mag. Mag. Mat. **63 & 64**, 326 (1987).

[81] M. B. Fontes *et al.*, Phys. Rev. B **53**, 11678 (1996).

[82] P. Haen *et al.*, J. Mag. Mag. Mat. **63 & 64**, 320 (1987).

[83] M. J. Besnus, J. P. Kappler, P. Lehmann, and A. Mayer, Solid State Commun. **55**, 779 (1987).

[84] L. P. Regnault, Phys. Rev. B **38**, 4481 (1988).

[85] A. Amato *et al.*, Phys. Rev. B **50**, 619 (1994).

[86] A. Amato *et al.*, Physica B **186-188**, 276 (1993).

[87] P. Haen *et al.*, J. Mag. Mag. Mat. **76 & 77**, 143 (1988).

[88] H. Aoki, S. Uji, A. K. Albessard, and Y. Onuki, Phys. Rev. Lett. **71**, 2110 (1993).

[89] J. Rossat-Mignod *et al.*, J. Mag. Mag. Mat. **76 & 77**, 376 (1988).

[90] M. J. Besnus, P. Lehmann, and A. Mayer, J. Mag. Mag. Mat. **63 & 64**, 323 (1987).

[91] P. Haen *et al.*, Physica B **163**, 519 (1990).

[92] J. M. Mignot *et al.*, Physica B **163**, 611 (1990).

[93] R. Djerbi *et al.*, J. Mag. Mag. Mat. **76**, 260 (1988).

[94] J. M. Mignot *et al.*, Physica B **171**, 357 (1991).

[95] S. J. Dakin. G. P. Rapson, and B. D. Rainford, J. Mag. Mag. Mat. **108**, 119 (1992).

[96] J. M. Mignot *et al.*, Solid State Commun. **77**, 317 (1991).

[97] B. D. Rainford, S. J. Dakin, and A. Severing, J. Mag. Mag. Mat. **108**, 117 (1992).

[98] M. J. Besnus *et al.*, Physica B **224**, 322 (1996).

[99] P. Haen *et al.*. J. Phys. Soc. Jpn **65**, 16 (1996).

[100] B.D.Rainford. D. Adroja, and P. Haen, Triple axis neutron scattering study of $CeRu_2Si_{1.0}Ge_{1.0}$., to be published.

[101] S. M. M. Evans, J. Phys. Cond. Mat. **2**, 9097 (1990).

[102] D. E. MacLaughlin *et al.*, Phys. Rev. B **37**, 3153 (1988).

[103] C. G. Windsor, *Pulsed Neutron Scattering* (Taylor & Francis, London, 1981).